

**THE DESIGN OF HOLE-TRANSPORT MATERIALS TO STABILIZE THE
PERFORMANCE OF PEROVSKITE SOLAR CELLS**

by

Valerie Anne Chiykowski

B.Sc., Queen's University, 2014

A THESIS SUBMITTED IN PARTIAL FULFILLMENT OF
THE REQUIREMENTS FOR THE DEGREE OF

DOCTOR OF PHILOSOPHY

in

THE FACULTY OF GRADUATE AND POSTDOCTORAL STUDIES

(CHEMISTRY)

THE UNIVERSITY OF BRITISH COLUMBIA

(VANCOUVER)

June 2019

© Valerie Anne Chiykowski, 2019

The following individuals certify that they have read, and recommend to the Faculty of Graduate and Postdoctoral Studies for acceptance, the dissertation entitled:

The Design of Hole-Transport Materials to Stabilize the Performance of Perovskite Solar Cells

submitted by Valerie A. Chiykowski in partial fulfillment of the requirements for

the degree of Doctor of Philosophy

in Chemistry

Examining Committee:

Curtis Berlinguette

Supervisor

Michael Wolf

Supervisory Committee Member

Laurel Schafer

Supervisory Committee Member

Mark MacLachlan

University Examiner

Peyman Servati

University Examiner

Additional Supervisory Committee Members:

Dan Bizzotto

Supervisory Committee Member

Abstract

Over six decades of photovoltaic research have led to the emergence of a highly efficient technology called perovskite solar cells (PSCs). Despite the recent sharp rise in power conversion efficiencies (PCEs) of this technology, PSCs have not yet been deployed at scale owing in part to the unsatisfactory stability of devices. The stability issues are due to the light absorbing layers being susceptible to dissolution and the hole-transport material (HTM) layers undergoing morphological changes under real life conditions. This dissertation seeks to suppress mechanisms of PSC degradation through the design of HTMs.

I designed a series of five structurally similar HTMs to study the effect of triphenylamine (TPA) location and number on the thermal stability (i.e., glass transition temperature, T_g) of the HTM layer. My studies demonstrate that where the TPA units are positioned about a spiro-carbon core can shift the T_g upwards of 30 °C.

I designed HTMs that can be electrochemically and thermally polymerized to yield an encapsulation layer for the PSC. I demonstrated that the polymerized HTM layer decreases film wettability and can be incorporated into a PSC device.

I interrogated a series of three structurally analogous donor-acceptor (D-A) architectures (i.e., monopodal, bipodal and tripodal architectures) to determine the role of molecular structure on the hole mobility of HTMs. From these experiments, I learned that “monopodal” D-A architectures yielded the highest hole mobilities because of the low computed reorganization energy, small polaron stabilization energy and hole extraction potential associated with this HTM.

Overall, I demonstrated three mechanisms to suppress either the degradation of the photoactive perovskite layer, the morphological changes to the HTM layer or the instability caused

by additives in HTM films. I suggest future design principles to yield stable PSC devices towards the commercialization of this technology.

Lay Summary

Solar energy is an important renewable energy source. Covering merely 0.16% of the earth's surface could provide enough electricity to meet the projected global demand of 2040, without any contribution from non-renewable sources such as oil and gas (though issues surrounding energy storage and distribution would have to be investigated in parallel to solar cell development). Solar panels must offer warranties of 20 years to be considered commercially viable for installation and application. The research in this dissertation strives to improve the stability of a particular solar cell technology, called perovskite solar cells, which exhibit high efficiencies and low costs of fabrication. Specifically, the experiments in this dissertation were designed to create new materials that do not: dissolve in water; change shape in heat; and rely on unstable dopants in order to conduct charge effectively.

Preface

Chapter 3 is adapted from the paper “Design Rules for High Mobility Xanthene-Based Hole-Transport Materials”, submitted for publication. The work was supervised by Prof. Aspuru-Guzik at the University of Toronto and Prof. Berlinguette. The project was designed and developed by myself. The computational screening was conducted by Dr. Daniel Tabor in the Aspuru-Guzik group. The synthesis, structural characterization, photophysical and electrochemical analysis of seven compounds were carried out by myself and Dr. Yang Cao in the Berlinguette group. The conductivity studies were performed by myself and David Dvorak in the Berlinguette Group. The mobility model was developed and carried out by Dr. Pascal Freiderich in the Aspuru-Guzik group. The perovskite solar cell studies were carried out by Dr. Hairen Tan in the Sargent group. The manuscript was written by myself and Dr. Daniel Tabor.

Chapter 4 is adapted from the paper “Precise Control of Thermal and Redox Properties of Organic Hole-Transport Materials”, *Angew. Chem. Int. Ed.*, **2018**, *57*, 15529-15533. The work was supervised by Prof. Aspuru-Guzik at the University of Toronto, Prof. Sargent at the University of Toronto and Prof. Berlinguette. The project was designed and developed by myself and Dr. Yang Cao in the Berlinguette group. The computational screening and calculations were conducted by Dr. Daniel Tabor in the Aspuru-Guzik group. The synthesis, structural characterization, photophysical and electrochemical analysis of seven compounds were carried out by myself and Dr. Yang Cao in the Berlinguette group. Hole mobility and perovskite solar cell studies were carried out by Dr. Hairen Tan in the Sargent group. The manuscript was written by myself, Dr. Daniel Tabor and Dr. Hairen Tan with contributions from Prof. Aspuru-Guzik, Prof. Sargent and Prof. Curtis Berlinguette.

Chapter 5 research was supervised by Prof. Sargent at the University of Toronto and Prof. Berlinguette. The project was designed and developed by myself. The synthesis, structural characterization, photophysical and electrochemical analysis of two compounds was carried out by myself. The conductivity studies were performed by myself and David Dvorak in the Berlinguette Group. Perovskite solar cells were fabricated and tested by Dr. Hairen Tan in the Sargent group.

Chapter 6 was supervised by Prof. Berlinguette. The project was designed and developed by myself. The computational calculations were carried out by Dr. Carolyn Virca in the Berlinguette group. The synthesis, structural characterization, photophysical and electrochemical analysis of three compounds was carried out by myself. The conductivity and hole mobility studies were performed by myself and David Dvorak in the Berlinguette Group.

Table of Contents

Abstract	iii
Lay Summary	v
Preface	vi
Table of Contents	viii
List of Tables	xiv
List of Figures	xv
List of Schemes	xix
List of Abbreviations	xx
Acknowledgments	xxvii
Dedication	xxviii
Chapter 1: Motivation and Outline	1
1.1 Motivation for research	1
1.2 Outline of dissertation.....	4
Chapter 2: Literature Review	7
2.1 Perovskite solar cells	7
2.1.1 Components and materials	7
2.1.2 Key Photovoltaic Metrics	9
2.2 Perovskite layer	10
2.2.1 Structure and role of the perovskite layer.....	10

2.3 Hole transport material layer	12
2.3.1 Roles and properties of hole transport materials.....	12
2.3.2 Instability of hole transport material layer	19
2.4 Solutions to perovskite solar cell instability using hole transport materials	21
2.4.1 Polymer hole transport materials for improved moisture stability of perovskite layer	21
2.4.2 High glass transition temperature hole transport materials for improved thermal stability of perovskite solar cells	23
2.4.3 Donor-acceptor hole transport materials for dopant-free perovskite solar cells	23
Chapter 3 : Tuning the Electrochemical and Electronic Properties of Spiro-Centred Hole Transport Materials through Substituent Identity	26
3.1 Introduction	26
3.2 Results and discussion	28
3.2.1 Computational screening	28
3.2.2 Synthesis	29
3.2.3 Electrochemical and photophysical characterization.....	29
3.2.4 Bulk thermal properties	32
3.2.5 Electrical properties	33
3.2.6 Bulk Simulation	34
3.2.7 Perovskite solar cell characterization	35

3.3 Conclusions	36
3.4 Experimental	37
3.4.1 Computational screening	37
3.4.2 Synthesis	37
3.4.3 Electrochemical and photophysical properties.....	43
3.4.4 Bulk thermal properties	43
3.4.5 Electrical properties	44
3.4.6 Bulk simulation	44
3.4.7 Perovskite solar cell characterization	45

Chapter 4 : Controlling the Thermal Stability and Electrochemistry of Hole-Transport

Material Films	47
4.1 Introduction	47
4.2 Results and discussion	49
4.2.1 Computational screening	49
4.2.2 Synthesis	53
4.2.3 Electrochemical and photophysical characterization.....	53
4.2.4 Bulk thermal properties	58
4.2.5 Electrical properties	58
4.2.6 Perovskite solar cell characterization	61
4.3 Conclusion	62

4.4 Experimental	63
4.4.1 Computational screening	63
4.4.2 Synthesis	64
4.4.3 Electrochemical and photophysical properties.....	68
4.4.4 Bulk thermal properties	68
4.4.5 Electrical properties	69
4.4.6 Perovskite solar cell characterization	69
Chapter 5 : Polymerizable Hole-Transport Materials for Improved Moisture Stability of Perovskite Solar Cells.....	71
5.1 Introduction	71
5.2 Results and discussion	73
5.2.1 Synthesis	73
5.2.2 Electrochemical and photophysical properties.....	76
5.2.3 Bulk thermal properties	78
5.2.4 Contact angle measurements	79
5.2.5 Electrical properties	80
5.2.6 Perovskite solar cell characterization	81
5.3 Conclusion.....	82
5.4 Experimental	83
5.4.1 Synthesis	83

5.4.2 Electrochemical and photophysical properties.....	86
5.4.3 Bulk thermal properties	86
5.4.4 Contact angle measurements	86
5.4.5 Electrical properties	87
5.4.6 Perovskite solar cell characterization	87

Chapter 6 : Effect of Donor-Acceptor Architecture on Hole-Transport Material Hole

Mobility.....	89
6.1 Introduction	89
6.2 Results and discussion	92
6.2.1 Synthesis	92
6.2.2 Electrical properties	94
6.2.3 Bulk thermal properties	95
6.2.4 Electrochemical and photophysical properties.....	97
6.2.5 Computed properties	100
6.3 Conclusions	101
6.4 Experimental	102
6.4.1 Synthesis	102
6.4.2 Electrical properties	106
6.4.3 Bulk thermal properties	107
6.4.4 Electrochemical and photophysical properties.....	107

6.4.5 Computed properties	108
Chapter 7: Conclusions and Future Directions.....	110
7.1 Conclusions	110
7.2 Future directions	111
References	115
Appendices	126
Appendix 1: Chapter 3	126
Appendix 2: Chapter 4	137
Appendix 3: Chapter 5	148
Appendix 4: Chapter 6	156

List of Tables

Table 2-1 Electrochemical and electron transport properties, and glass transition temperatures of organic HTMs.....	15
Table 3-1 Summary of computed reduction potentials and HOMO-LUMO energy gaps for the spiro-R series	28
Table 3-2 Summary of photophysical, electrochemical and bulk thermal properties for spiro-R series.....	31
Table 3-3 Conductivity data for spiro-OMeTAD and spiro-R series	34
Table 3-4 Perovskite solar cell data for spiro-OMeTAD and spiro-R series	36
Table 4-1 Calculated electronic frontier molecular orbital properties and contributions to reorganization energies (B3LYP/6-311+G(d,p) evaluated at B3LYP/6-31G(d) optimized geometries) of the HTM series and spiro-OMeTAD	52
Table 4-2 Electrochemical, bulk thermal and electrical properties of HTM series	54
Table 4-3 Summary of DPV oxidation peaks for HTM series.....	57
Table 4-4 Summary of spectroscopic and electrochemical properties for HTM series.	58
Table 4-5 Device characteristics for perovskite solar cells containing HTM series.	62
Table 5-1 Electrochemical, photophysical, and glass transition temperature data for HTMs.....	79
Table 5-2 Statistical performance data of HTMs in perovskite solar cell devices.	82
Table 6-1 Electrical, electrochemical, photophysical, and bulk thermal properties of TPA-1 , TPA-2 , and TPA-3	96
Table 6-2 Computed factors affecting hole mobility for TPA-1 , TPA-2 , and TPA-3	101

List of Figures

Figure 1-1 Power conversion efficiencies (PCEs) of select first, second, and third generation solar cell technologies with current certified record PCEs. Figure adapted from NREL Best Research-Cell Efficiencies Graph. ¹	2
Figure 1-2 (a) Schematic illustration of a conventional PSC (b) electron (e^-) and hole (h^+) flow through PSC components, and (c) molecular structure for organic HTM X60	3
Figure 1-3 Outline of organic HTM molecular design for dissertation chapters	4
Figure 2-1 Energy levels (e.g., valence band (VB) and conduction band (CB) of the perovskite and TiO_2-Cl , HOMO and LUMO levels of the HTM) relevant to various device performance parameters (e.g., V_{oc} and ΔG).....	8
Figure 2-2 $J-V$ and power density curves highlighting key performance metrics for a PSC	10
Figure 2-3 General perovskite (AMX_3) structure with examples of A (e.g., $CH_3NH_3^+$, $CH(NH_2)_2^+$ and Cs^+), M (e.g., Pb^{2+} and Sn^{2+}) and X (i.e., Cl^- , Br^- , I^-) identities.....	11
Figure 2-4 Examples of linear, starburst and spiro organic HTMs	14
Figure 2-5 MilliporeSigma pricing per gram of HTM.....	15
Figure 2-6 Morphological changes to the HTM layer above the T_g	20
Figure 2-7 Chemical structures of p-dopants ($LiTFSI$, $Zn(TFSI)_2$, FK209 and F4-TCNQ).....	21
Figure 2-8 Examples of polymer HTMs employed for improved PSC moisture stability	22
Figure 2-9 Common donor, pi and acceptor units employed for D-A HTMs.....	24
Figure 3-1 Molecular representations of the spiro-R series under investigation.....	26
Figure 3-2 Cyclic voltammograms for spiro-R series recorded in 0.1 M $n-NBu_4PF_6$ DCM solutions at room temperature. Data were collected at a scan rate of 50 mV/s. Dashed lines indicate E_{HOMO} values.	30

Figure 3-3 (a) UV-Vis absorption spectra and (b) emission spectra for spiro-R series dissolved in DCM.....	32
Figure 3-4 (a) Simulated (grey) and experimental (red) hole mobilities of spiro-OMeTAD and spiro-R series, (b) computed hole mobilities of the spiro-R series with the contributions by electronic coupling, reorganization energy, conformational disorder and electrostatic disorder..	35
Figure 4-1 Molecular representations of spiro-OMeTAD ⁶⁸ and the HTM series under investigation.	49
Figure 4-2 HOMO and LUMO orbitals of each molecule in the HTM series, calculated at the BP86/def2-SVP level of theory. Isosurfaces are at 0.03 and -0.03 values for the wavefunction..	50
Figure 4-3 Spin density difference maps for the HTM cations evaluated at the B3LYP/6-311+G(d,p) level of theory at the B3LYP/6-31G(d) cation adiabatic minima.	52
Figure 4-4 Cyclic voltammograms of HTM series in 0.1 M <i>n</i> -NBu ₄ PF ₆ DCM solutions, with a polished Pt working electrode, Pt wire counter electrode and Ag/AgCl reference electrode.....	54
Figure 4-5 Differential pulse voltammograms (DPVs) for HTM series normalized in amplitude to their first oxidation event. The number of electrons that contribute to each redox process was determined by integrating the area beneath the peak fitting. (a) The first deconvoluted oxidation events are shown in shaded colors to highlight the progressively anodic shift of E_{HOMO} for HTM-F (red), HTM-X (blue) and HTM-X' (green), respectively. Traces for (b) X60 (black) and (c) HTM-FX' (orange) are deconvoluted to highlight that the E_{HOMO} is linked to the TPA unit positioned on the fluorene unit.	56
Figure 4-6 (a) UV-Vis absorption spectra for HTM solutions (2.0×10^{-5} M) recorded in DCM. (b) Emission spectra for HTM series recorded in DCM excited at lowest energy absorption band recorded in Table 4-4.	57

Figure 4-7 Performance of perovskite solar cells with HTMs: (a) *J-V* curves of hole-only devices with **HTM** series; (b) *J-V* curves of solar cells with **HTM** series measured under solar simulator (100 mW cm⁻²); (c) Histogram of PCEs for 44 devices with **HTM-FX'**; (d) *J-V* curves of champion device with **HTM-FX'** scanned in reverse and forward directions (scanning rate of 20 mV/s)..... 60

Figure 4-8 (a) Steady-state PL and (b) time-resolved PL decay of perovskite films with **spiro-OMeTAD**, **X60** and **HTM-FX'** and (c) time-resolved PL decay of perovskite films with **HTM-F**, **HTM-X** and **HTM-X'** 61

Figure 5-1 Molecular structures of **VNPB**,²⁷ **HTM-FX'**^{26,119} and **spiro-VNPB**..... 72

Figure 5-2 Cyclic voltammograms (CVs) over 20 scans for **spiro-NPB** between 0.5-1.6 V vs NHE (grey), **spiro-VNPB** between 0.5-1.2 V vs NHE (teal) and **spiro-VNPB** between 0.5-1.6 V vs NHE (purple) recorded in 0.1 M *n*-NBu₄PF₆ DCM solutions at room temperature. Vertical arrows indicate increasing current response with subsequent scans suggestive of electropolymerization. Horizontal arrows indicate open-circuit potential..... 77

Figure 5-3 Differential pulse voltammograms (DPV) for **spiro-NPB** (black) and **spiro-VNPB** (teal) 77

Figure 5-4 Absorption profiles for **spiro-NPB** (black) and **spiro-VNPB** (teal) 78

Figure 5-5 Contact angle data of **spiro-OMeTAD**, **spiro-NPB**, **spiro-VNPB** and thermally polymerized **spiro-VNPB** over 30 minutes. 80

Figure 5-6 Sheet resistance data for **spiro-OMeTAD**, **spiro-NPB**, **spiro-VNPB** and thermally polymerized **spiro-VNPB**..... 81

Figure 6-1 Molecular representations of **TPA-1**, **TPA-2**, and **TPA-3** (collectively referred to as **TPA-X** series) which vary in D-A architectures. 91

Figure 6-2 a) Schematic of hole-only device for hole mobility measurements and b) hypothetical J - V curve of a hole-only device highlighting the ohmic and SCLC regimes for HTM hole mobility measurements.	95
Figure 6-3 Hole mobilities determined from SCLC region of hole-only devices containing spiro-OMeTAD , TPA-1 , TPA-2 , and TPA-3	95
Figure 6-4 Grazing incidence XRD data for TPA-1 , TPA-2 , and TPA-3 on glass.	97
Figure 6-5 Cyclic voltammograms (CVs) of TPA-1 , TPA-2 , and TPA-3 recorded in 0.1 M <i>n</i> -NBu ₄ PF ₆ DCM solutions at room temperature. Data were collected at a scan rate of 50 mV/s. ...	98
Figure 6-6 Visual representation of computed energies relevant to reorganization energy components (λ_1 and λ_2), hole extraction potential (HEP), and ionization potentials (IP) of neutral and charge HTM molecules.	98
Figure 6-7 (a) Experimental UV-Vis absorption, (b) experimental emission, and (c) theoretical absorption spectra for TPA-1 , TPA-2 , and TPA-3	99
Figure 6-8 Calculated frontier orbitals of optimized structures for TPA-1 , TPA-2 , and TPA-3 plotted at an absolute isovalue of 0.02.	100
Figure 7-1 Proposed architecture of future directions for PSCs where there the interface between the perovskite and HTM layers is manipulated by surface functionalization of the AMX ₃ perovskite structure and the incorporation of polymerizable HTM.	112
Figure 7-2 Proposed molecular structure of monopodal D-A HTM with spiro-core to increase T_g and opportunity to vary donor and acceptor identities and E_{HOMO}	113

List of Schemes

Scheme 2-1 Synthetic schemes for (a) spiro-OMeTAD and (b) X60	18
Scheme 3-1 Synthetic scheme for spiro-R series	29
Scheme 4-1 Synthetic scheme for HTM series.	53
Scheme 5-1 Synthetic scheme of spiro-VNPB and spiro-NPB	75
Scheme 6-1 Synthesis schemes for TPA-1 , TPA-2 , and TPA-3	93

List of Abbreviations

A	amp
Ag(TFSI)₂	silver bis(trifluoromethanesulfonyl)amide
AMX₃	general perovskite structure
AMX₃ · H₂O	general monohydrate perovskite sheet
A₂MX₆ · 2H₂O	general dihydrate perovskite octahedra
BPA	biphenylamine
B3LYP	Becke's three-parameter exchange functional (B3) and the Lee-Yang-Parr correlation functional (LYP)
¹³C	carbon-13
CB	conduction band
CH₃NH₃⁺	methylammonium
CH₃NH₃PbBr₃	methylammonium lead bromide
CH₃NH₃PbI₃	methylammonium lead bromide
Champion PCE	maximum power conversion efficiency achieved with a single device
cm	centimeter
CuBr	copper bromide
CuI	copper iodide
CuSCN	copper thiocyanate
CV	cyclic voltammogram
d	doublet
<i>d</i>	inter-electrode spacing
dir	direct
D-A	donor-acceptor
DCM	dichloromethane
DFT	density functional theory

DMSO	dimethylsulfoxide
DPV	differential pulse voltammetry
DSC	differential scanning calorimetry
DSSC	dye-sensitized solar cell
EI	electron impact
E_{HOMO}	highest occupied molecular orbital energy level
E_{LUMO}	lowest unoccupied molecular orbital energy level
$E_{\text{HOMO-LUMO}}$	energy gap between HOMO and LUMO energy levels
E_{F1}	first oxidation of fluorene TPAs
E_{F2}	second oxidation of fluorene TPAs
E_{X1}	first oxidation of xanthene TPAs
E_{X2}	second oxidation of xanthene TPAs
E_{Fermi}	Fermi level
E_{reorg}	reorganization energy
E^*_+	energy of neutral molecule at cation minimum geometry
E_+	energy of cation at cation minimum geometry
E^*	energy of cation at neutral minimum geometry
ESI	electron-spray ionization
ETL	electron transport layer
EtOAc	ethylacetate
eV	electron volts
F4-TCNQ	2,3,5,6-tetrafluoro-7,7,8,8-tetracyanoquinodimethane
FA	formamidinium
FF	fill factor
FK209	tris(2-(1H-pyrazol-1-yl)-4-tert-butylpyridine)cobalt(III) tri[hexafluorophosphate]

FTO	fluorine-doped tin oxide
G	Gibb's free energy or driving force
¹H	proton
HOMO	highest occupied molecular orbital
HPLC	high pressure liquid chromatography
HTM	hole-transport material
inv	inverse
ITO	indium-doped tin oxide
<i>J</i>	current density
<i>J_{sc}</i>	short-circuit current density
<i>J-V</i>	current density-voltage
<i>l</i>	length
LiTFSI	lithium(I) bis (trifluoromethylsulfonyl)imide
LUMO	lowest unoccupied molecular orbital
M	molar
MA	methylammonium
MeO-TPD	<i>N,N,N',N'</i> -tetrakis(4-methoxyphenyl)benzidine
MeOTPA-TPA	<i>N⁴,N⁴</i> -bis(4'-(bis(4-methoxyphenyl)amino)-[1,1'-biphenyl]-4-yl)- <i>N^{4'},N^{4'}</i> -bis(4-methoxyphenyl)-[1,1'-biphenyl]-4,4'-diamine
MeO-TPTE	<i>N⁴,N^{4'}</i> -([1,1'-biphenyl]-4,4'-diyl)bis(<i>N⁴,N^{4'},N^{4'}</i> -tris(4-methoxyphenyl)-[1,1'-biphenyl]-4,4'-diamine
MeO-TPTR	<i>N⁴</i> -(4'-(bis(4-methoxyphenyl)amino)-[1,1'-biphenyl]-4-yl)- <i>N⁴,N^{4'},N^{4'}</i> -tris-(4-methoxy phenyl)-[1,1'-biphenyl]-4,4'-diamine
MHz	megahertz
min	minute
mmol	millimole
mol	Mole

mV	millivolt
m/z	mass-to-charge ratio
<i>m-</i>	meta substituted
NiO_x	nickel oxide
nm	nanometer
<i>n</i>-Bu₄NPF₆	tetrabutylammonium hexafluorophosphate
NHE	normal hydrogen electrode
NMR	nuclear magnetic resonance
OLED	organic light-emitting diode
P3HT	poly(3-hexylthiophene-2,5-diyl)
<i>-o</i>	ortho substituted
<i>-p</i>	para substituted
PEDOT	poly(3,4-ethylenedioxythiophene)
PEPPSI-iPr	[1,3-Bis(2,6-Diisopropylphenyl)imidazol-2-ylidene](3-chloropyridyl)palladium(II) dichloride catalyst
PCE	power conversion efficiency
PL	photoluminescence
PMMA	poly(methyl methacrylate)
ppm	parts per million
PSC	perovskite solar cell
PSS	polystyrene sulfonate
PTFE	polytetrafluoroethylene
PTAA	poly(triaryl amine)
<i>P</i>_{in}	power input
<i>P</i>_{max}	power maximum
<i>P</i>_{out}	power output

R	resistance
rpm	rotations per min
s	second
S	Siemens
SCLC	space-charge limited current
SiO₂	silicon dioxide
spiro-F	<i>N</i> ² , <i>N</i> ² , <i>N</i> ² , <i>N</i> ² , <i>N</i> ⁷ , <i>N</i> ⁷ , <i>N</i> ⁷ , <i>N</i> ⁷ -octakis(4-fluorophenyl)spiro[fluorene-9,9'-xanthene]-2,2',7,7'-tetraamine
spiro-FOMe	<i>N</i> ² , <i>N</i> ² , <i>N</i> ⁷ , <i>N</i> ⁷ -tetrakis(4-fluorophenyl)- <i>N</i> ² , <i>N</i> ² , <i>N</i> ⁷ , <i>N</i> ⁷ -tetrakis(4-methoxyphenyl)spiro[fluorene-9,9'-xanthene]-2,2',7,7'-tetraamine
spiro-H	<i>N</i> ² , <i>N</i> ² , <i>N</i> ² , <i>N</i> ² , <i>N</i> ⁷ , <i>N</i> ⁷ , <i>N</i> ⁷ , <i>N</i> ⁷ -octaphenylspiro[fluorene-9,9'-xanthene]-2,2',7,7'-tetraamine
spiro-Me	<i>N</i> ² , <i>N</i> ² , <i>N</i> ² , <i>N</i> ² , <i>N</i> ⁷ , <i>N</i> ⁷ , <i>N</i> ⁷ , <i>N</i> ⁷ -octa- <i>p</i> -tolylspiro[fluorene-9,9'-xanthene]-2,2',7,7'-tetraamine
spiro-NPB	<i>N</i> ² , <i>N</i> ² , <i>N</i> ⁷ , <i>N</i> ⁷ -tetrakis(4-methoxyphenyl)- <i>N</i> ³ , <i>N</i> ⁶ -di(naphthalen-1-yl)- <i>N</i> ³ , <i>N</i> ⁶ -diphenylspiro[fluorene-9,9'-xanthene]-2,3',6',7'-tetraamine
spiro-OMeTAD	<i>N</i> ² , <i>N</i> ² , <i>N</i> ² , <i>N</i> ² , <i>N</i> ⁷ , <i>N</i> ⁷ , <i>N</i> ⁷ , <i>N</i> ⁷ -octakis(4-methoxyphenyl)-9,9'-spirobi[9H-fluorene]-2,2',7,7'-tetraamine
spiro-<i>p</i>,<i>o</i>-OMe	<i>N</i> ² , <i>N</i> ² , <i>N</i> ⁷ , <i>N</i> ⁷ -tetrakis(2-methoxyphenyl)- <i>N</i> ² , <i>N</i> ² , <i>N</i> ⁷ , <i>N</i> ⁷ -tetrakis(4-methoxyphenyl)spiro[fluorene-9,9'-xanthene]-2,2',7,7'-tetraamine
Spiro-Me	<i>N</i> ² , <i>N</i> ² , <i>N</i> ² , <i>N</i> ² , <i>N</i> ⁷ , <i>N</i> ⁷ , <i>N</i> ⁷ , <i>N</i> ⁷ -octa- <i>p</i> -thiomethylspiro[fluorene-9,9'-xanthene]-2,2',7,7'-tetraamine
spiro-TPD	<i>N</i> ² , <i>N</i> ² , <i>N</i> ⁷ , <i>N</i> ⁷ -tetraphenyl- <i>N</i> ² , <i>N</i> ² , <i>N</i> ⁷ , <i>N</i> ⁷ -tetra- <i>p</i> -tolyl-9,9'-spirobi[fluorene]-2,2',7,7'-tetraamine
Spiro-VNPB	<i>N</i> ² , <i>N</i> ² , <i>N</i> ⁷ , <i>N</i> ⁷ -tetrakis(4-methoxyphenyl)- <i>N</i> ³ , <i>N</i> ⁶ -di(naphthalen-1-yl)- <i>N</i> ³ , <i>N</i> ⁶ -bis(4-vinylphenyl)spiro[fluorene-9,9'-xanthene]-2,3',6',7'-tetraamine
ssDSSC	solid-state dye-sensitized solar cell
<i>t</i>	thickness
<i>T_c</i>	crystallization temperature

T_g	glass transition temperature
T_m	melting temperature
tBP	4-tert-butylpyridine
TD	time dependent
TiO₂	titanium dioxide
TiO₂-Cl	chlorine-doped compact titanium dioxide
TFSI	(trifluoromethane)sulfonimide
TLC	thin-layer chromatography
TPA	triphenylamine
TPD	<i>N,N'</i> -bis(3-methylphenyl)- <i>N,N'</i> -diphenylbenzidine
TPTE	<i>N</i> ⁴ , <i>N</i> ^{4'} -([1,1'-biphenyl]-4,4'-diyl)bis(<i>N</i> ⁴ , <i>N</i> ^{4'} -diphenyl- <i>N</i> ^{4'} -(<i>p</i> -tolyl)-[1,1'-biphenyl]-4,4'-diamine)
UV	ultraviolet
UV-Vis	ultraviolet-visible
V	voltage
V	volt
vac	vacuum
VB	valence band
VNPB	<i>N</i> ² , <i>N</i> ² , <i>N</i> ⁷ , <i>N</i> ⁷ -tetrakis(4-methoxyphenyl)- <i>N</i> ^{3'} , <i>N</i> ^{6'} -di(naphthalen-1-yl)- <i>N</i> ^{3'} , <i>N</i> ^{6'} -bis(4-vinylphenyl)spiro[fluorene-9,9'-xanthene]-2,3',6',7-tetraamine
V_{oc}	open-circuit voltage
W	watt
X60	<i>N</i> ² , <i>N</i> ² , <i>N</i> ^{2'} , <i>N</i> ^{2'} , <i>N</i> ⁷ , <i>N</i> ⁷ , <i>N</i> ^{7'} , <i>N</i> ^{7'} -octakis(4-methoxyphenyl)spiro[fluorene-9,9'-xanthene]-2,2',7,7'-tetraamine
Zn(TFSI)₂	zinc di[bis(trifluoromethylsulfonyl)imide]
μ_h	hole mobility

σ	conductivity
$\Delta E_{1/2}$	electronic coupling
ΔG	Gibbs free energy change
ϵ_0	vacuum permittivity
ϵ_r	dielectric constant
ϵ_{HOMO}	computed vertical oxidation potential
ϵ_{LUMO}	computed vertical ionization energy
λ_{max}	absorbance wavelength maximum
λ_{em}	emission wavelength maximum
μm	micrometer
δ	chemical shift (ppm)
$^{\circ}\text{C}$	degree Celsius
3D	three dimensional
2D	two dimensional

Acknowledgments

I would like to thank my research supervisor, Dr. Curtis P. Berlinguette. Thank you for allowing me to pursue research avenues and collaborations that I was impassioned about and I appreciate the opportunities provided to me by the way of conferences and meetings. I would like to acknowledge NSERC Create Sustainable Synthesis and NSERC PGSD for partial funding.

I would like to thank the excellent scientists I collaborated with: Dr. Daniel Tabor at Harvard University; Dr. Pascal Friedreich, Dr. Hairen Tan, Andrew Proppe, Dr. Edward Sargent and Dr. Alán Aspuru-Guzik at the University of Toronto; and Dr. Yang Cao, Dr. Carolyn Virca and David Dvorak at the University of British Columbia.

I would like to thank the entire Berlinguette group for support at group meetings and forming a community in and out of the lab. Thank you Angelica, Aiko, Rebecka, Damon, Mitch, Perry, Karen, Chris Brown and Kyle for the coffees and company throughout the rollercoaster that is graduate school. Thank you Ryan, Chris Voth and Ben Mowbray for the moving therapy on morning runs and helping me find an escape from my studies. Thank you to Kyle for countless lunches, coffees, strolls and runs and for being a patient sounding-board for all aspects of life. Thank you Carrie and Terri for providing support and love in the most motivating way. Thank you Rebecca, for being so supportive both in and out of the lab. I cannot imagine my graduate school experience without your intelligence, modesty and friendship, and nor would I ever dare to. Thank you Alex, for being by my side through the best and worst times and building a nice life for ourselves, warm in our home.

Finally, thank you to my family for believing in me when I was unable to believe in myself. Your support means everything.

Dedication

To my mom, for showing me what a strong woman looks like.

Chapter 1: Motivation and Outline

1.1 Motivation for research

Power conversion efficiencies (PCEs) of perovskite solar cells (PSCs) have increased from 13.0% to 22.7% since 2013 (Figure 1-1).¹ Despite this sharp rise in PCE, PSCs have not yet been deployed at scale.^{2,3} The primary reasons PSCs have not been commercialized are because of materials costs (e.g., gold electrodes are needed for state-of-the-art-devices),^{4,5} toxicity (e.g., lead is used in the light absorbing layer)⁶⁻⁸ and unsatisfactory stability (e.g., devices are notoriously unstable to moisture and air).^{6,9-11} The stability issues are due to the light absorbing layers being susceptible to dissolution^{12,13} and the hole transport material (HTM) layers undergoing morphological changes under real life conditions.^{14,15} With the goal of improved PSC stability in mind, the key outcomes of this dissertation are: encapsulation of the perovskite layer to prevent solvation upon moisture exposure; determination of a structure-property relationship for morphological stabilities (i.e., glass transition temperature, T_g) of HTM layers at elevated temperatures; and design of conductive HTMs without the requirement of additives.

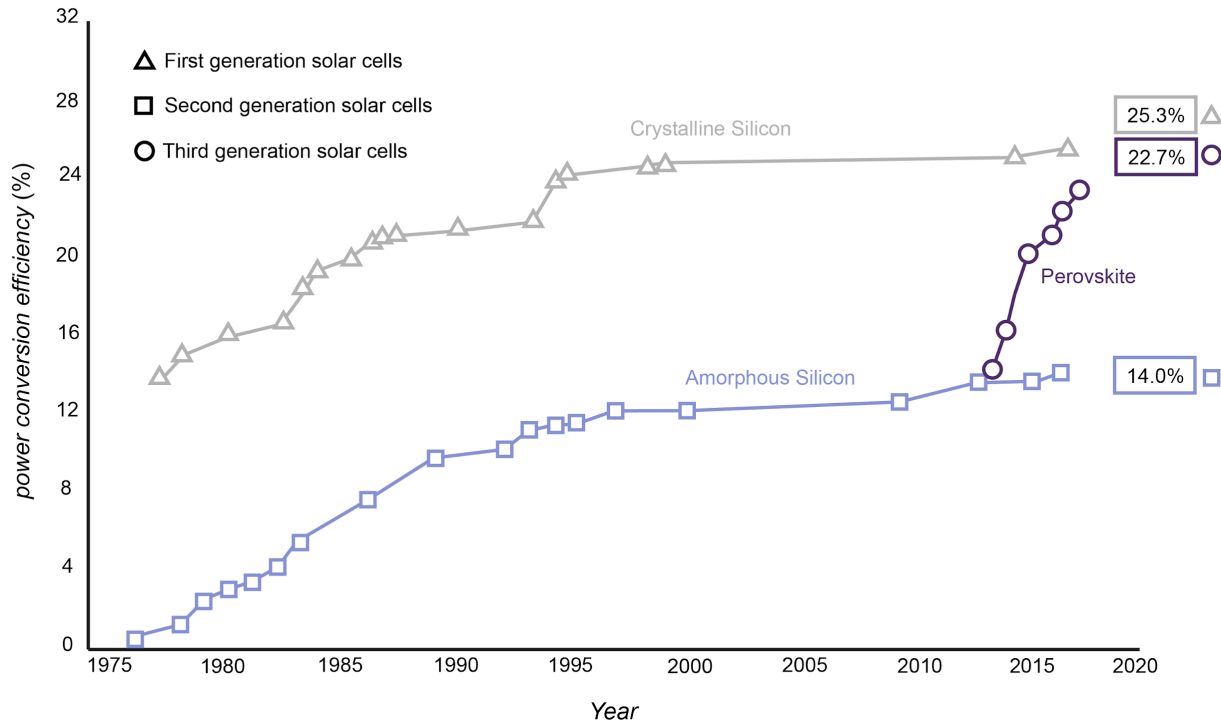


Figure 1-1 Power conversion efficiencies (PCEs) of select first, second, and third generation solar cell technologies with current certified record PCEs. Figure adapted from NREL Best Research-Cell Efficiencies Graph.¹

PSCs contain five layers: a perovskite layer; an electron transport layer (ETL); a conductive glass substrate; a hole transport material layer; and a metal counter-electrode (Figure 1-2a).^{16,17} The perovskite layer, typically a >500-nm film of inorganic-organic hybrid crystals (e.g., $\text{CH}_3\text{NH}_3\text{PbBr}_3$),^{18,19} absorbs the visible portion of the solar spectrum to generate electron-hole pairs (Figure 1-2b). The ETL (e.g., mesoscopic or compact titanium dioxide, TiO_2) extracts the photo-excited electrons from the perovskite and transports the electrons to the conductive glass substrate (e.g., indium-doped tin oxide, ITO or fluorine-doped tin oxide, FTO on glass).^{5,20} The HTM layer extracts holes from the perovskite layer and transports the holes to the counter-electrode, which is usually gold or silver.^{18,21} HTM layers are usually 100-200 nm films of redox-active organic compounds (e.g., **X60** in Figure 1-2c)^{22,23} or extended metal oxide solids (e.g., NiO_x).²⁴ The

objectives of this dissertation (Figure 1-3), and the corresponding literature review in **Chapter 2**, are confined to organic HTMs.

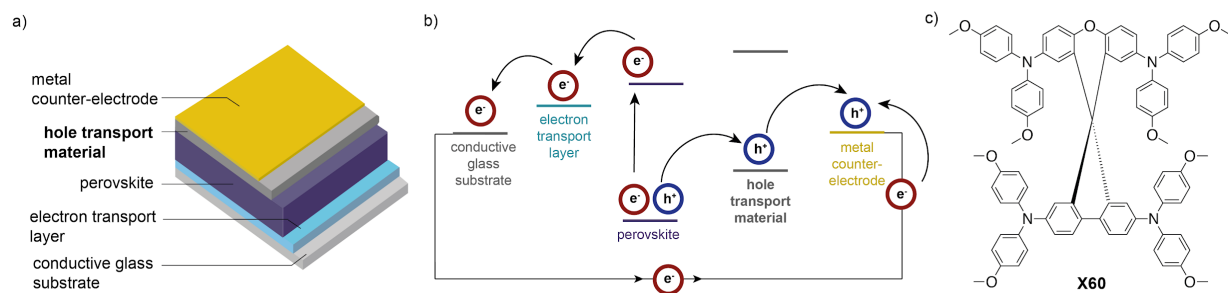


Figure 1-2 (a) Schematic illustration of a conventional PSC (b) electron (e^-) and hole (h^+) flow through PSC components, and (c) molecular structure for organic HTM X60

1.2 Outline of dissertation

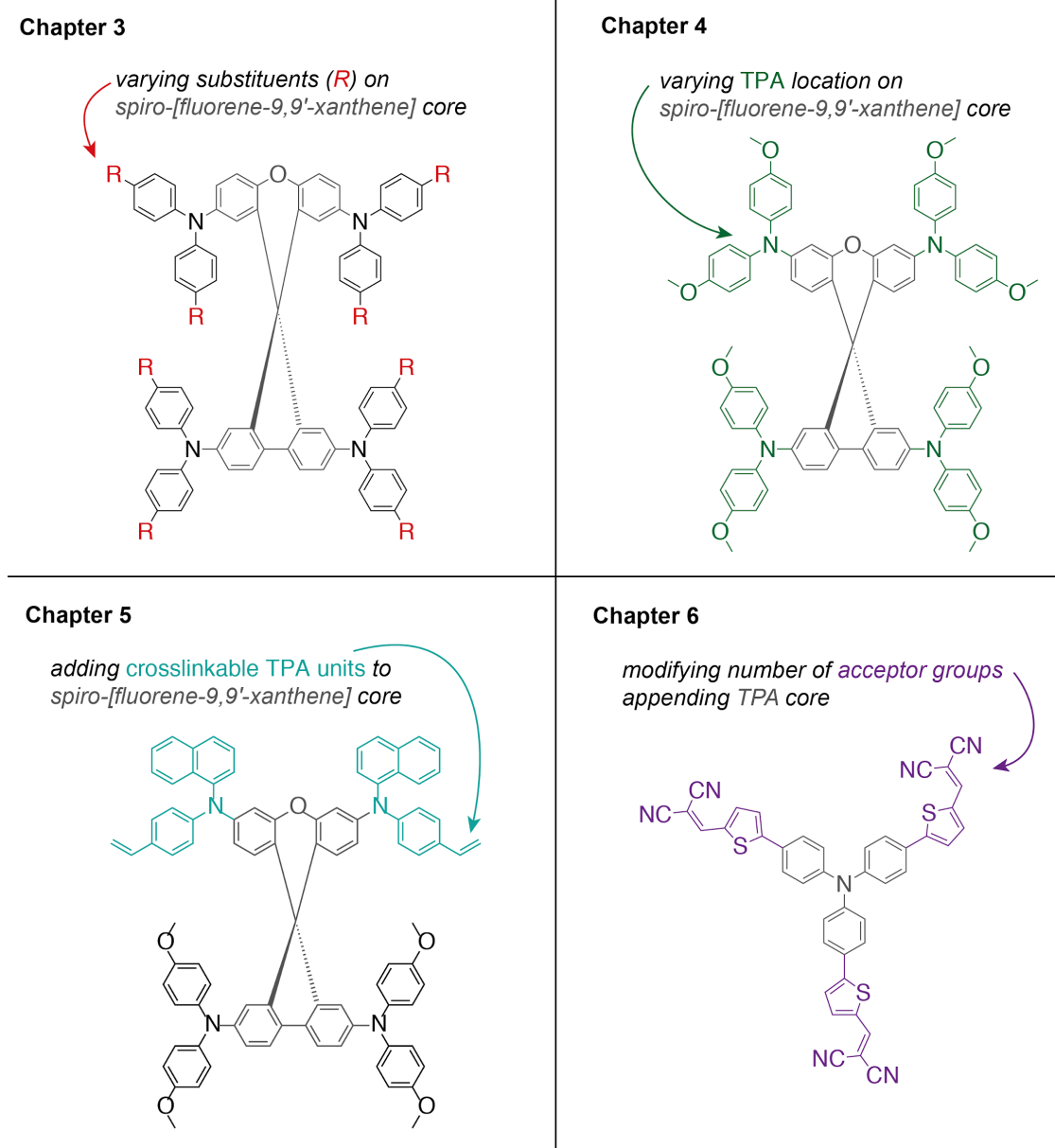


Figure 1-3 Outline of organic HTM molecular design for dissertation chapters

Chapter 3 describes how electrochemical and charge transport properties of HTMs can be modulated through substituent modification on the HTM molecule. How terminal substituents of HTMs affect the hole mobilities of HTMs is, quite surprisingly, not well understood. I therefore designed a series of HTMs with an **X60** core and seven different substitution patterns to test how

steric bulk and electronic factors impact the hole mobilities. This work yielded empirical evidence showing sterically bulky, non-polar substituents increased the hole mobilities of HTMs. This chapter also includes collaborative work outlining a computational model implicating the role of low conformational and electrostatic disorder exhibited by large, non-polar substituents for high hole mobility.

Chapter 4 describes how the location of the triphenylamine (TPA) groups about the **X60** core impacts the thermal stabilities of HTMs. There were few known design principles that teach how to modify spiro-based organic HTMs to modulate glass transition temperatures (T_g s) above 90 °C (this property is needed because the cell heats up during operation).²⁵ I discovered that the T_g of an HTM is linked to the location, and not number, of TPA units appended to the spiro-carbon core. My studies showed that where the TPA units were positioned about the spiro-carbon core could shift the T_g upwards of 30 °C. This design principle was published in *Angewandte Chemie International Edition* to help the field make more thermally stable PSC devices.²⁶

Chapter 5 describes my goal of using novel polymerizable HTMs that serve to encapsulate PSCs and protect them from moisture. Perovskite layers dissolve when exposed to moisture causing irreversible degradation of PSCs.^{6,12} Polymer HTMs can encapsulate the perovskite layer of PSCs, preventing water ingress into the cell.²⁷ I installed vinyl functionalities to the spiro-carbon core that are capable of undergoing thermal and electrochemical polymerization to form a polymeric HTM layer. This approach successfully lowered film wettability and illuminated a unique approach for making encapsulation layers.

Chapter 6 outlines my on-going exploration of designing “donor-acceptor” (D-A) HTMs with the goal of bypassing the need for dopants in the HTM films. While dopants are typically needed to get to appropriate hole conductivities, they are a source of device instability because

they are (i) hygroscopic and (ii) susceptible to migration during operation.²⁸⁻³⁰ I therefore designed, synthesized, and tested a series of D-A architectures in pursuit of HTMs with high hole mobilities. From these experiments, I learned that “monopodal” D-A architectures yielded the highest hole mobilities because of the low reorganization energy, small polaron stabilization energy and hole extraction potential calculated for this HTM. This achievement notwithstanding, PSCs exhibiting high PCEs with these candidate materials have not yet been realized.

A summary of this work and how it fits into the broader PSC community is provided in **Chapter 7**. I also discuss how the field can build on these results to make stable, high efficiency PSCs.

Chapter 2: Literature Review

2.1 Perovskite solar cells

Perovskite solar cells (PSCs) have been certified to produce a power conversion efficiency (PCE) approaching 23% (Figure 1-1). This value is striking in that it is approaching the performance of commercial silicon solar cells, which have been certified to exhibit a PCE of 25.3%. PSCs, however, can be fabricated at lower temperatures (i.e., $<150\text{ }^{\circ}\text{C}$)^{2,16,31} than the temperatures required for fabricating commercial silicon solar cells (i.e., $>1800\text{ }^{\circ}\text{C}$).^{32,33} The challenge is that while commercial silicon solar panels can last decades, the most stable PSCs do not last longer than six weeks without encapsulation.²⁸ Fundamentally new approaches are needed to make PSCs durable for commercially relevant time periods.

2.1.1 Components and materials

PSCs contain five layers: a perovskite layer; an electron transport layer (ETL); a conductive glass substrate; a hole transport material (HTM) layer; and a metal counter-electrode (Figure 2-1).^{16,17} The perovskite layer, typically a $>500\text{-nm}$ film of inorganic-organic hybrid crystals with the general structure AMX_3 (e.g., $\text{CH}_3\text{NH}_3\text{PbI}_3$),^{18,19} absorbs the visible portion of the solar spectrum to generate electron-hole pairs. The ETL (i.e., chlorine-doped compact titanium dioxide, $\text{TiO}_2\text{-Cl}$ herein) extracts the photo-excited electrons from the perovskite and transports the electrons to the conductive glass substrate (i.e., indium-doped tin oxide, ITO in this work).^{5,20} The HTM layer extracts holes from the perovskite layer and transports the holes to the counter-electrode, which is a sputter-deposited gold layer in this dissertation.^{18,21} HTM layers are usually 100-200 nm films of redox-active organic compounds (e.g., **X60** in Figure 1-2c)^{22,23} or extended metal oxide solids (e.g., NiO_x).²⁴ I focus on altering the molecular structure of organic HTMs related to **X60** while holding

the perovskite material, ETL, conductive glass substrate and counter-electrode material of the PSC constant.

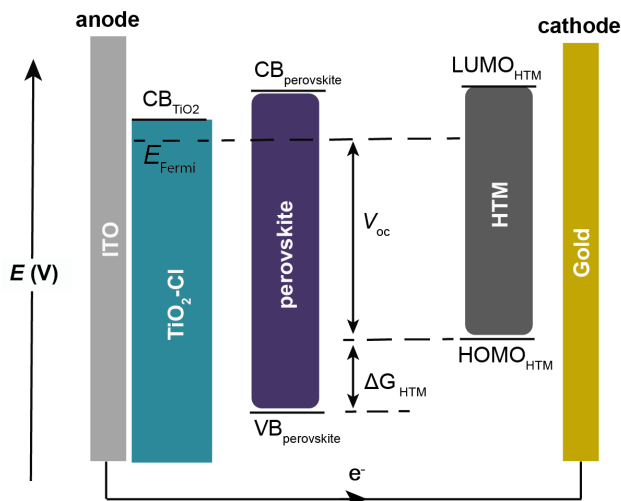


Figure 2-1 Energy levels (e.g., valence band (VB) and conduction band (CB) of the perovskite and $\text{TiO}_2\text{-Cl}$, HOMO and LUMO levels of the HTM) relevant to various device performance parameters (e.g., V_{oc} and ΔG)

During solar cell operation, photoexcitation of electrons from the valence band (VB) to conduction band (CB) of the perovskite generates electron-hole pairs (Figure 2-1).¹⁸ Electrons are then extracted from the CB of the perovskite and transported through the $\text{TiO}_2\text{-Cl}$ layer to the anode.²⁰ Electrons generate current by traveling through the $\text{TiO}_2\text{-Cl}$, ITO and circuit before returning back to the PSC at the gold counter-electrode. Holes extracted from the VB of the perovskite by the HTM layer are transported to the gold cathode. The relative positions of the band edges must be positioned appropriately for these processes to occur, and without significant energy losses (see Section 2.1.2).^{34,35}

2.1.2 Key Photovoltaic Metrics

The PCE is the ratio of maximum electrical power, P_{\max} , that can be extracted from the power of the incident solar radiation, P_{in} (Equation 2-1).

$$PCE = \frac{P_{\max}}{P_{\text{in}}} \times 100\% = \frac{J_{\text{sc}} \times V_{\text{oc}} \times FF}{P_{\text{in}}} \times 100\% \quad (\text{Equation 2-1})$$

P_{\max} is proportional to the short-circuit current (J_{sc}), open-circuit potential (V_{oc}) and fill factor (FF). J_{sc} is the maximum current measured when no voltage bias is applied against the cell (i.e., at short circuit), and corresponds to the y-intercept of the current-voltage (J - V) curve (Figure 2-2).³⁶ The V_{oc} is the voltage measured when no current is passed through the device (i.e., at open circuit) and corresponds to the x-intercept of the J - V curve.³⁷ V_{oc} corresponds approximately to the potential energy difference between the Fermi level (E_{Fermi}) of the TiO_2 -Cl and the highest-occupied molecular orbital (HOMO) level of the HTM (Figure 2-1).^{38,39} FF is the ratio between P_{\max} and $J_{\text{sc}} \times V_{\text{oc}}$ (Equation 2-2) and reflects the quality of the solar cell fabrication and J - V curve. Deviation from the ideal J - V curve ($FF < 1.0$) is caused by shunt and series resistance in the PSC. Series resistance is the loss of energy along the favoured charge flow pathway (e.g., high hole transfer resistance to the HTM, low mobility of holes through the HTM, low conductance of electrons through the ETL). Shunt resistance is the energy loss through parallel charge flow pathways (e.g., deleterious electron-hole pair recombination or excited-state electron transfer to the HTM).

$$FF = \frac{V_{\max} \times J_{\max}}{J_{\text{sc}} \times V_{\text{oc}}} = \frac{P_{\max}}{J_{\text{sc}} \times V_{\text{oc}}} \quad (\text{Equation 2-2})$$

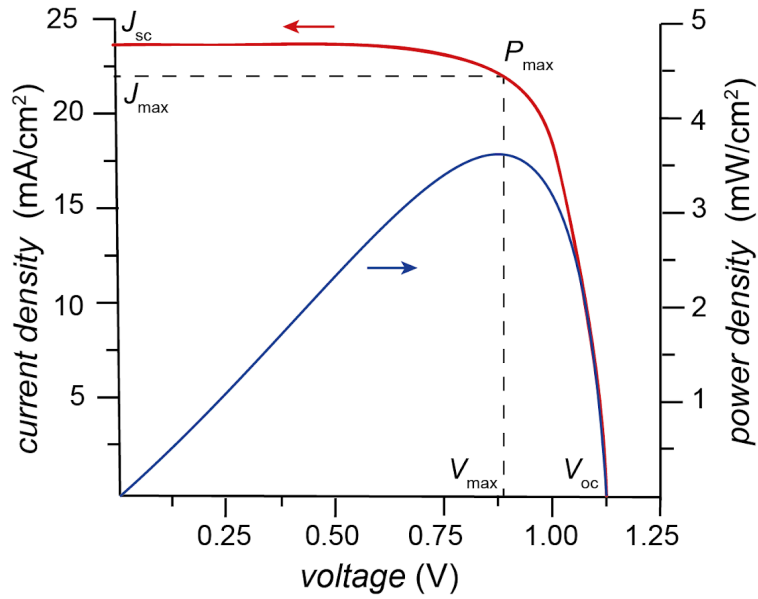


Figure 2-2 J - V and power density curves highlighting key performance metrics for a PSC

2.2 Perovskite layer

2.2.1 Structure and role of the perovskite layer

The light absorbing perovskite layer has the structure of AMX_3 where A is a large cation (e.g., Cs^+ , $CH_3NH_3^+$ or $HC(NH_2)_2^+$),^{19,40,41} M is a metal cation (e.g., Pb^{2+} or Sn^{2+}),^{42,43} and X is a halide (i.e., Cl⁻, Br⁻ or I⁻)^{44,45} (Figure 2-3). AMX_3 adopts an octahedral geometry repeating in all three dimensions. The perovskite formulation used in this work (i.e., $Cs_{0.05}HC(NH_2)_{20.81}CH_3NH_{30.14}PbI_{2.55}Br_{0.45}$) was selected because these films exhibit molar extinction coefficients greater than 10^5 cm^{-1} throughout the visible spectrum (it is characterized by an abrupt onset of absorption at 700 nm).^{46,47}

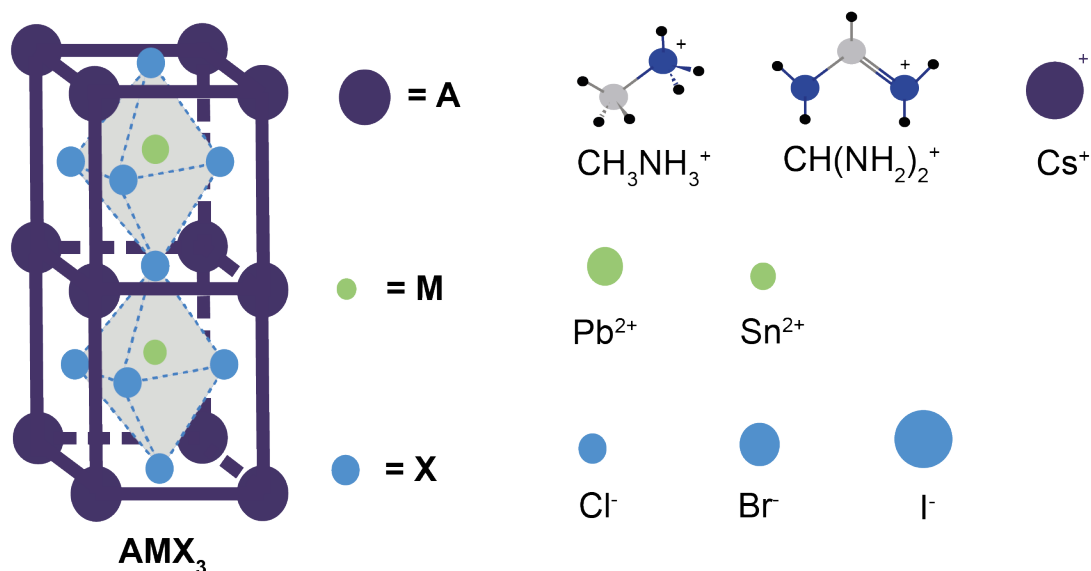


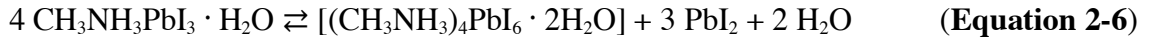
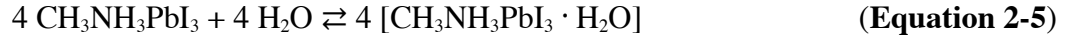
Figure 2-3 General perovskite (AMX_3) structure with examples of A (e.g., $CH_3NH_3^+$, $CH(NH_2)_2^+$ and Cs^+), M (e.g., Pb^{2+} and Sn^{2+}) and X (i.e., Cl^- , Br^- , I^-) identities

The perovskite structure (i.e., AMX_3) can react readily with water (acting as a Lewis base) to produce a Lewis acid (e.g., CH_3NH_3I) and a metal halide salt (e.g., PbI_2) (Equation 2-3).⁹ The Lewis acid can react to yield HI and CH_3NH_2 which is driven by dissolution in water (Equation 2-4). The final product, CH_3NH_2 , is volatile (i.e., boiling point of $-6\text{ }^\circ\text{C}$) and susceptible to evaporation, even prior to operation.¹¹



An alternative degradation pathway arises from the susceptibility of the 3D perovskite structure to monohydrate and dihydrate formation in the presence of water: The perovskite (e.g., $CH_3NH_3PbI_3$) can react with one equivalent of water to produce a monohydrate species (e.g., $CH_3NH_3PbI_3 \cdot H_2O$) or two equivalents of water to produce a dihydrate species (e.g., $(CH_3NH_3)_4PbI_6 \cdot 2H_2O$) (Equations 2-5 to 2-6).⁶ The first hydration results in the breakdown of 3D

perovskite into 2D perovskite sheets, while the second hydration results in the breakdown of 2D perovskite sheets into individual octahedra. The relative ratio of monohydrate to dihydrate species depends on the relative humidity of storage and the duration of moisture exposure. The degradation mechanisms of perovskites with water are irreversible and decrease the PCEs of PSCs over time.^{6,48}



2.3 Hole transport material layer

2.3.1 Roles and properties of hole transport materials

The HTM serves two key functions: hole extraction from the perovskite layer and hole transport to the gold cathode. The HTM must therefore be designed with appropriate energy levels, high conductivity, and high hole mobility, while being physically robust against elevated temperatures of a solar cell. The ideal HTM should therefore satisfy the following criteria:

- HOMO energy level positioned 70 mV more positive than the perovskite valance band,^{34,35}
- Conductivity greater than 10^{-5} S/cm;^{49,50}
- Hole mobility greater than 10^{-4} cm²/Vs;⁵⁰
- Glass transition temperature, T_g , greater than 90 °C.²⁵

It is difficult to modulate any one of these properties through structural modifications without impacting the others. Addressing this dynamic situation through rational molecular design is an overarching theme of this entire dissertation.

While HTMs can be broken down into inorganic (e.g., CuSCN, CuBr and NiO_x)^{24,51-54} and organic materials, this dissertation will be limited to the design and study of exclusively organic

HTMs. The primary reason for the focus on organic HTMs is that the structures can be more easily modulated through molecular design, enabling direct tuning of the four key properties listed above. Organic HTMs can be further divided into (i) linear, (ii) starburst or (iii) spiro architectures^{50,55} (Figure 2-4), with each class defined by different HOMO energy levels, hole mobilities, conductivities and glass transition temperatures.

Linear HTMs were originally developed for organic light emitting diodes (OLEDs) decades before their use in PSCs.^{14,56-59} Linear HTMs are molecules of repeating monomer units, ranging in size from small molecules (e.g., one unit) to polymers (e.g., >20 units). The HOMO levels and hole mobilities of linear HTMs are dependent on oligomer substituents and length, respectively. Triphenylamine (TPA) units are common monomers in linear HTMs because of reversible, facile redox chemistry and established synthetic chemistry (e.g., synthesized using Ullmann coupling or Buchwald-Hartwig coupling). The redox chemistry of these HTMs is exquisitely sensitive to substitution at the TPA unit. For example, the destabilized E_{HOMO} of **MeO-TPD** (i.e., -4.3 eV) relative to the E_{HOMO} of **TPD** (i.e., -5.3 eV) is due to the electron-donating strength of methoxy substituents stabilizing the oxidized form of the compound.⁶⁰ The higher E_{HOMO} of **MeO-TPD** results in a greater Gibbs free energy for hole extraction but a lower V_{oc} and, hence, PCE (Equation 2-1). The hole mobilities increase with increasing number of TPA units, which was demonstrated clearly by Xu *et al.* (e.g., 6.19×10^{-5} , 9.82×10^{-5} and 1.47×10^{-4} cm²/Vs for **MeO-TPD**, **MeO-TPTR**, and **MeO-TPTE**, respectively, in Figure 2-4.⁶¹ Finally, the cost to purchase commercially available HTMs also increases with linear HTM length (e.g., **TPA**, **TPD**, **TPTE** and **PTAA** which range from 3 to 2640 \$/g; see Figure 2-5). In other words, high hole mobility comes at a financial cost.⁶²

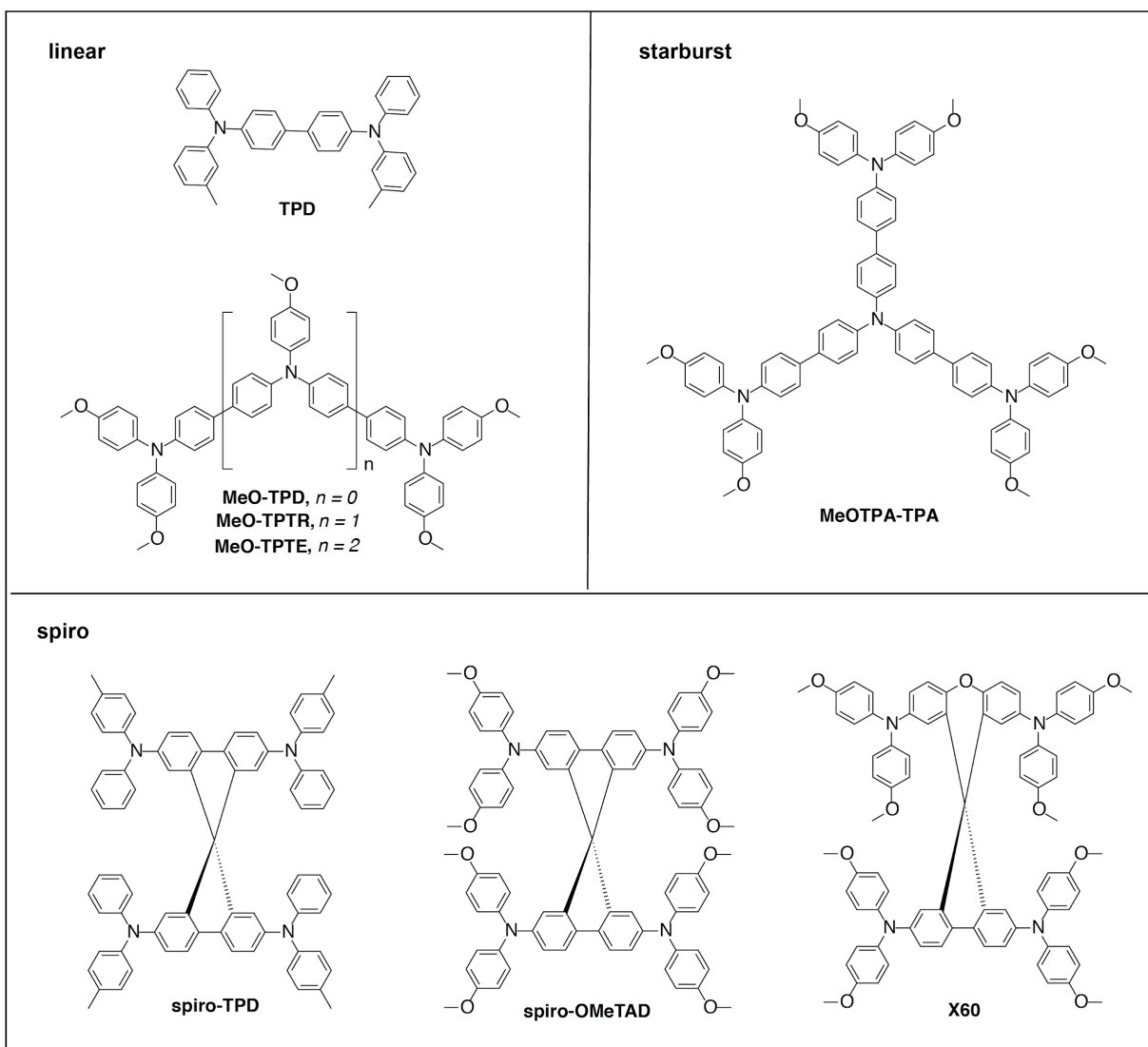


Figure 2-4 Examples of linear, starburst and spiro organic HTMs

Table 2-1 Electrochemical and electron transport properties, and glass transition temperatures of organic HTMs

Compound	E_{HOMO}	<i>hole mobility</i>	<i>conductivity</i>	T_g
	eV	$\text{cm}^2 \text{V}^{-1} \text{s}^{-1}$	S cm^{-1}	$^{\circ}\text{C}$
TPD	-5.3	-	-	60
MeO-TPD	-4.3	6.19×10^{-5}	$4.95 \times 10^{-7 a}$	71
MeO-TPTR	-4.33	9.82×10^{-5}	$2.75 \times 10^{-7 a}$	110
MeO-TPTE	-4.33	1.47×10^{-5}	$6.98 \times 10^{-7 a}$	137
MeOTPA-TPA	-5.13	1.08×10^{-4}	-	-
spiro-TPD	-5.3	-	-	115
spiro-OMeTAD	-5.11	2.00×10^{-4}	$4.61 \times 10^{-6 b}$	128
X60	-5.18	1.9×10^{-4}	$1.1 \times 10^{-4 c}$	107

Measured with ^a 3% FK209 ^b 20% LiTFSI ^c 20% LiTFSI and 3% FK209

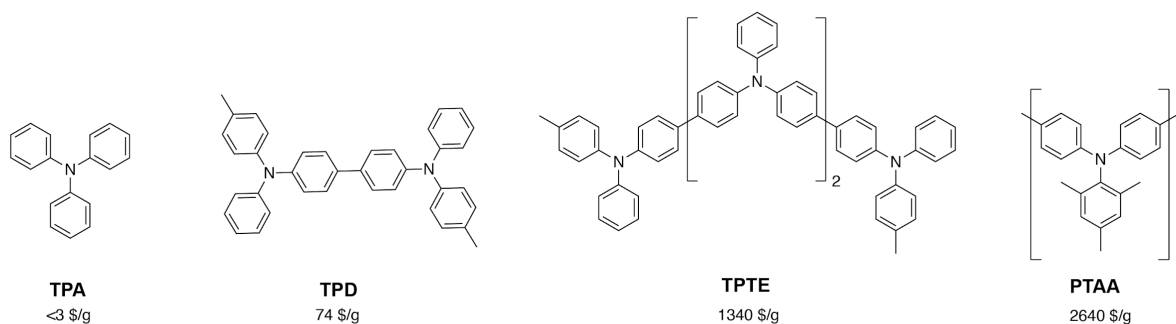


Figure 2-5 MilliporeSigma pricing per gram of HTM

Starburst structures, described as non-linear oligomers, typically have higher hole mobilities than analogous isomers with linear architectures. Ko *et al.* demonstrated this trend by designing starburst **MeOTPA-TPA** with a hole mobility of $1.08 \times 10^{-4} \text{ cm}^2/\text{Vs}$, while linear isomer **MeO-TPTE** exhibits a hole mobility of $1.54 \times 10^{-5} \text{ cm}^2/\text{Vs}$.⁶³ When comparing these linear and starburst HTMs, it is also evident that the E_{HOMO} is stabilized by 0.8 eV in the starburst configuration, which is favourable for increasing the V_{oc} and PCE when employed in a PSC device.

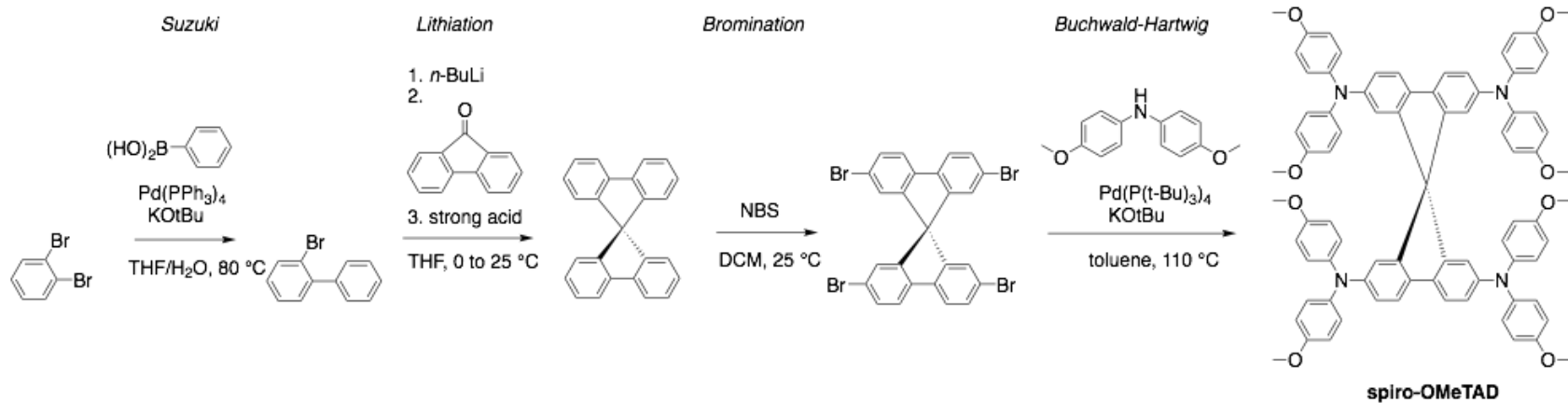
Sterically bulky spiro-centres increase the T_g of organic HTMs relative to homologous linear HTMs.^{64,65} Spiro HTMs are characterized by two π -systems juxtaposed across a tetrahedral sp^3 -hybridized atom (e.g., carbon, silicon). Naito and Miura demonstrated that steric bulk across a strained linkage led to more thermally stable films. Thermal stability tracks the T_g of the material.^{66,67} The T_g of linear **TPD** vs **spiro-TPD** is 60 °C vs 115 °C, respectively, and the T_g of linear **MeO-TPD** vs **spiro-OMeTAD** is 71 °C and 128 °C, respectively.⁵⁶ Solar cells are known to reach temperatures approaching 90 °C during operation, caused by solar exposure and thermal losses in the cell. The spiro-carbon core in both cases raises the T_g of the material above the 90 °C threshold necessary to avoid morphological changes during the operation of a PSC. Spiro-centres also increase the conductivity of organic HTMs relative to homologous linear HTMs. The conductivity of **spiro-OMeTAD** is approximately an order of magnitude higher than linear **MeO-TPD** ($4.61 \times 10^{-6} \text{ S/cm}$ vs $4.95 \times 10^{-7} \text{ S/cm}$ for **spiro-OMeTAD** and **MeO-TPD**, respectively).^{60,61}

Spiro-OMeTAD is a state-of-the-art HTM containing four redox active TPA groups substituting a spirobifluorene core.⁶⁸ **Spiro-OMeTAD** is difficult to synthesize because it requires: an air-sensitive Suzuki coupling; a moisture-sensitive lithiation reaction or Grignard generation; a bromination reaction; an air-sensitive Buchwald-Hartwig coupling; and chromatographic purification at most steps (Scheme 2-1a).⁶⁹⁻⁷¹ **X60**, however, can be synthesized in fewer steps and

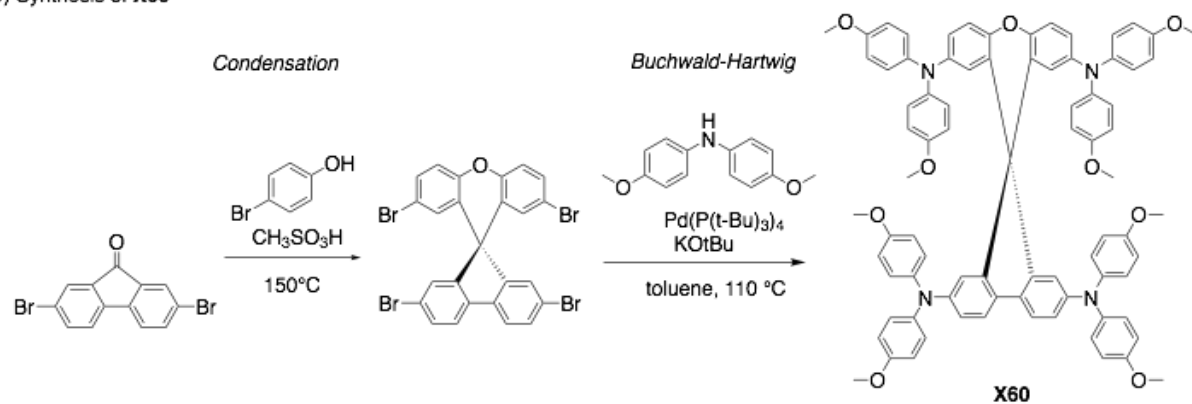
was reported in 2016 by Xu *et al.* and Maciejczyk *et al.* to generate similar PCEs to **spiro-OMeTAD** in a PSC.^{22,23} **X60** is an HTM that can be synthesized by a condensation reaction with >95% yield without a column, followed by a Buchwald-Hartwig coupling. **X60** rivals **spiro-OMeTAD** in performance (i.e., both >20% PCE in a PSC) but can be synthesized at a fifth of the cost.²² Moreover, the more accessible synthetic route for **X60** affords the opportunity to synthesize series of compounds to study structure-property relationships of HTMs without undertaking laborious syntheses. **X60** motivated the design of many HTMs studied in this dissertation (Figure 1-3).

Scheme 2-1 Synthetic schemes for (a) **spiro-OMeTAD** and (b) **X60**

a) Synthesis of **spiro-OMeTAD**



b) Synthesis of **X60**



2.3.2 Instability of hole transport material layer

In the HTM field, T_g is the temperature at which materials undergo a transition from the glassy, amorphous state, in which they exist following spin-coating at room temperature, to another morphology.^{59,72} Glass transition is an endothermic process (the absorption of heat by the material from the surroundings) that can be measured by a differential scanning calorimeter (DSC) as the point at which more heat flow is required to increase the temperature of bulk material at a sustained rate. The crystallization temperature, T_c , is the temperature at which an HTM film transitions from an amorphous phase to a crystalline phase. This phase change is exothermic and can be measured by a DSC as a decrease in the heat flow required to increase the temperature of a bulk material at a sustained rate.⁷³ Not all materials display a crystallization temperature if the regular, ordered stacking of molecules is not energetically favourable.

Morphological changes, pinholes and phase segregation of the HTM layer in a PSC can result from HTMs with low T_g values (Figure 2-6). Morphological changes to HTM films from the glassy, amorphous state occur above a material's T_g and can lead to small polycrystallite formation, decreased mechanical strength and phase segregation from dopants and additives. Grain boundaries between crystallites can trap charge carriers and lower the charge-transport properties of an HTM film.⁷⁴ Films may exhibit decreased mechanical strength which may result in defects in the form of pinholes at elevated temperatures.⁷⁵ Morphology changes can also result in phase segregation of the HTM from the added dopants which causes inconsistencies in film composition and conductivity.⁷⁶

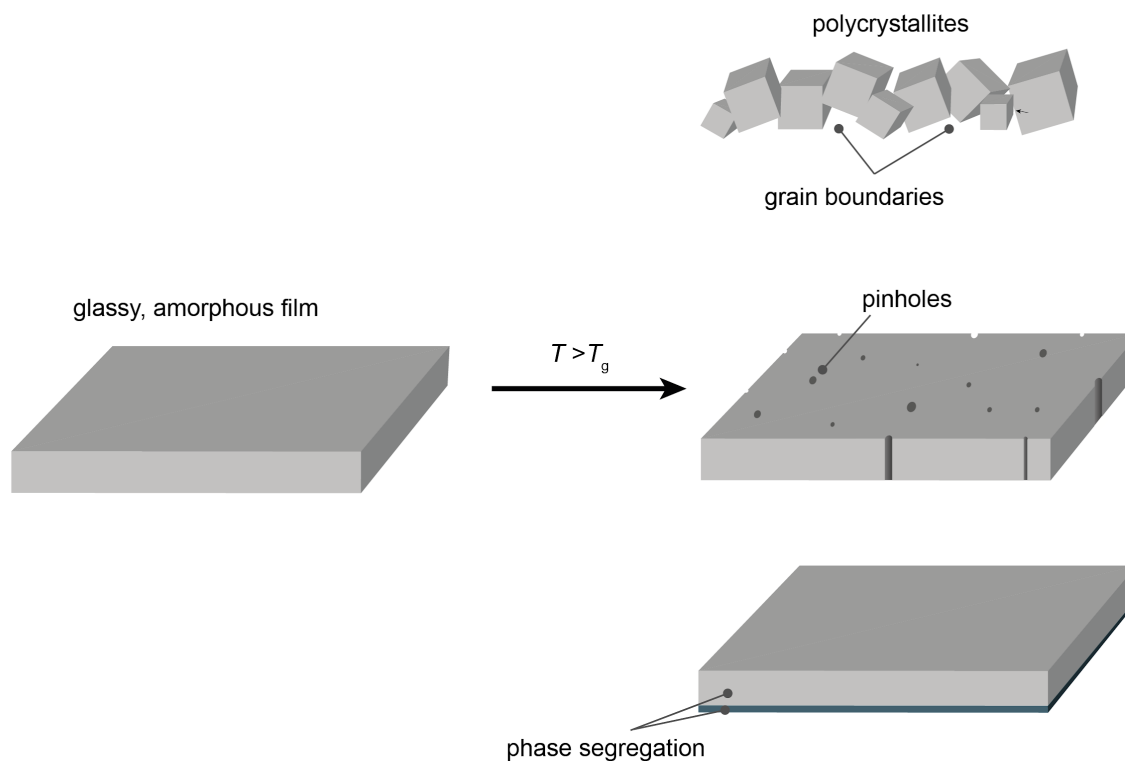


Figure 2-6 Morphological changes to the HTM layer above the T_g

The conductivity (σ) of a p-type semiconductor (e.g., an HTM film in a PSC) is proportional to the density of mobile holes (n_h), mobility of holes (μ_h) and elementary charge (e):

$$\sigma_h = n_h e \mu_h \quad \text{(Equation 2-7)}$$

Most HTM films are not intrinsically conductive, and hence, ancillary oxidants (i.e., dopants in Figure 2-7) are frequently added to induce chemical oxidation, increase the density of mobile holes, and maximize conductivity.^{77,78} Dopants either react directly with the HTM in a one or two electron redox reaction (this includes FK209 or $\text{Ag}(\text{TFSI})_2$, respectively) or indirectly with oxygen (in the case of LiTFSI) to yield oxidized equivalents of the HTM material (e.g., HTM^+).^{79,80}

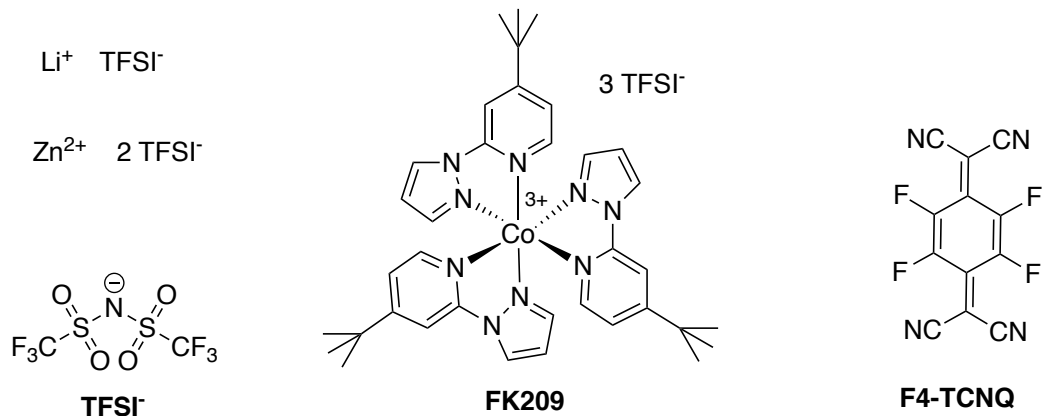


Figure 2-7 Chemical structures of p-dopants (LiTFSI , Zn(TFSI)_2 , FK209 and F4-TCNQ).

LiTFSI is the most commonly used dopant in the PSC field (Figure 2-7). A major challenge arises when employing LiTFSI because Li^+ is hygroscopic and can result in the ingress of water into the cell *via* the HTM layer.³⁰ Li^+ is also a small cation and can migrate toward the anode during cell operation.⁸¹ This ion migration results in inconsistencies in HTM film doping and conductivity which are diagnosed by the hysteresis of forward and backward J - V scans of the PSC.^{82,83} Alternative dopants to LiTFSI include other TFSI salts (e.g., FK209 and Zn(TFSI)_2 mentioned above) and organic molecular dopants (e.g., F4-TCNQ in Figure 2-7).^{28,29,84,85} Seo and coworkers demonstrated that PSCs doped with exclusively Zn(TFSI)_2 maintained PCEs above 20% following 600 h exposure at 50 °C and 40% relative humidity.²⁸

2.4 Solutions to perovskite solar cell instability using hole transport materials

2.4.1 Polymer hole transport materials for improved moisture stability of perovskite layer

There is little data available on modifying the HTM layer to improve PSC stability. In 2017, Kelly *et al.* investigated the use of **P3HT** nanowires in **PMMA** matrices as the HTM layers of a PSC.¹² The **P3HT** nanowires performed the role of an HTM and the **PMMA** matrix prevented the entry of water into the PSC. Liquid-phase water stability tests revealed that devices with 80:20

PMMA/P3HT compositions completely retained performance metrics (i.e., PCE, J_{sc} , V_{oc} and FF) following 60 s of exposure to water droplets on the surfaces of the devices. Vapour-phase water stability tests, however, revealed that the PCE dropped to 0% over seven days in a 99% humid environment regardless of the **PMMA** concentration. This decline in PCE implicates the importance of vapour-phase stability studies, in addition to studying the liquid-phase stability, to understand the durability of PSCs during moisture exposure.

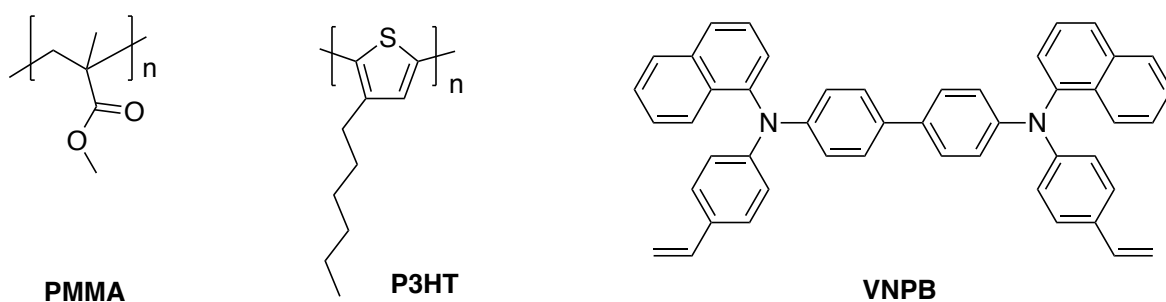


Figure 2-8 Examples of polymer HTMs employed for improved PSC moisture stability

Sargent and co-workers hypothesized that **VNPB** polymers could protect the perovskite layer of a PSC from the entry of water and suppress subsequent moisture degradation.²⁷ **VNPB** was thermally polymerized on the perovskite layer of a PSC to yield devices with 16.5% PCE. X-ray diffraction (XRD) was used to quantify degradation of the perovskite by measuring the amount of PbI_2 byproduct formed relative to the intact $CH_3NH_3PbI_3$ perovskite (Equation 2-3). XRD revealed that devices covered by **VNPB** degraded less than devices without the crosslinked HTM layer. This study demonstrates the potential for polymerizing molecular HTMs *in situ* to improve the stability of the perovskite layer against water ingress into PSCs. The **VNPB** structure inspired the novel spiro-centred HTMs developed in Chapter 5.

2.4.2 High glass transition temperature hole transport materials for improved thermal stability of perovskite solar cells

Increasing T_g through steric bulk (e.g., substituent changes and oligomer length) improves morphological stability and this incorporation of steric bulk is the inspiration for research outlined in Chapter 4. The use of bulky phenyl groups to increase T_g was demonstrated in 1996 by Sun *et al.* for a series of oligomeric HTMs: **MeO-TPD**; **MeO-TPTR**, and **MeO-TPTE** (Figure 2-4 and Table 2-1).^{86,87} The phenyl moieties of a TPA adopt pinwheel orientations that inhibit regular stacking of HTMs and increase the stabilities of amorphous films. Smaller substituents (e.g., halogens or alkyl groups) also increase the T_g of HTMs relative to otherwise homologous materials.⁶⁴ Naito demonstrated that increasing the size of halogen substituents results in steric disruptions to regular packing and increases the T_g of an HTM. Incorporation of electron-withdrawing halogens, however, significantly lowers the HOMO level for the HTM and decreases the free energy change necessary for hole extraction from the perovskite. Chapter 4 reveals design principles for improving the T_g values of spiro-centred HTMs more than 30 °C with judicious placement of bulky TPA units, without impacting the HOMO level of HTMs.

2.4.3 Donor-acceptor hole transport materials for dopant-free perovskite solar cells

It has been recognized that HTMs can have high conductivities without the use of dopants,⁸⁸ offering an opportunity to overcome the hygroscopic nature and diffusion of LiTFSI.⁸⁹ D-A materials have demonstrated >15% PCE in PSCs.⁸⁸⁻⁹⁰ Dopant-free HTMs typically are designed with large planar moieties to induce stacking,⁹⁰ and/or integration of donor-acceptor (D-A) structures.⁹¹ Large planar moieties improve stacking between HTM molecules and decrease the distance required for holes to be transported.^{88,92} Bi *et al.* has argued that the strong light

absorption properties characteristic to D-A HTMs could be beneficial in creating dual-light absorbing systems within the PSC.⁹³ This claim is in disagreement with convention where the HTM is designed to not absorb light.

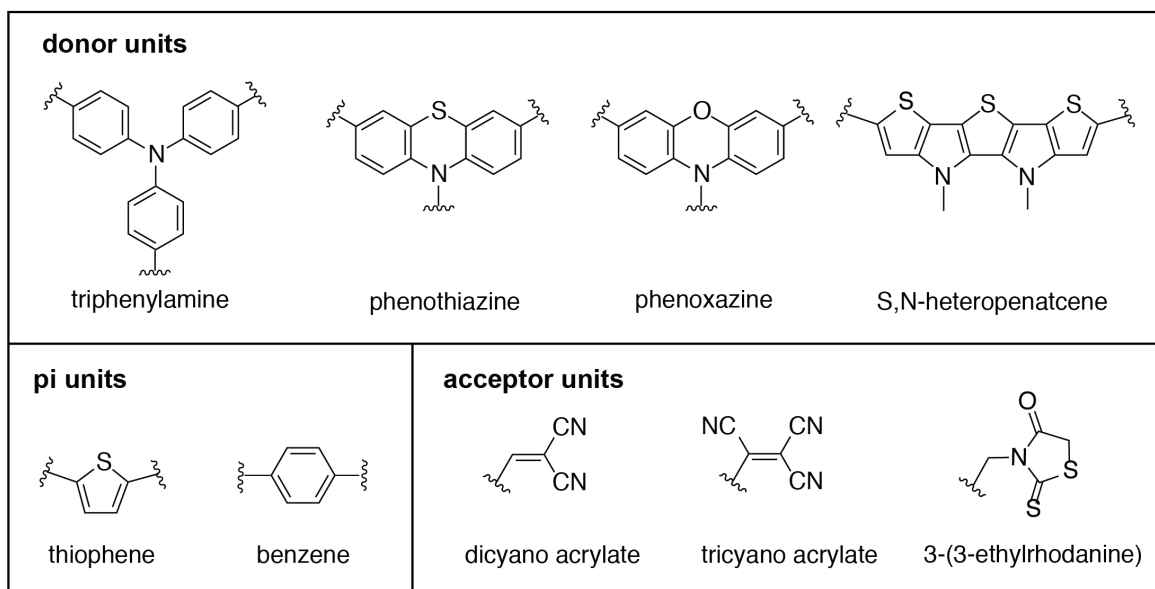


Figure 2-9 Common donor, pi and acceptor units employed for D-A HTMs

The molecular structure of D-A HTMs in the literature varies significantly in architecture (e.g., the number and identity of donor and acceptor groups) and organic class (e.g., linear or starburst). Yang *et al.* examined the effect of donor group identity between two monopodal D-A HTMs and determined that HTMs with benzo[1,2-b:4,5-b']dithiophene donor units yielded higher mobility films than a fluorinated alternative (i.e., 5,6-difluoro-2,1,3-benzothiadiazole).⁹⁴ Steck and coworkers compared thiophene and EDOT π -bridges in bipodal (A- π -D- π -A) HTMs and found that thiophene linkages yielded HTMs with minimal visible light absorption, often considered favourable for use in PSCs.⁹⁵ The effect of D-A architectures on the conductivities and hole mobilities of HTM films have not been previously investigated. In Chapter 6, three architectures

of D-A HTMs (i.e., monopodal, bipodal and tripodal structures) are investigated using computational and experimental techniques to design stable, dopant-free HTMs.

The HTM layer can be designed to overcome the unsatisfactory stability of PSCs in moisture and heat. HTMs can be designed to: encapsulate the perovskite layer to prevent solvation upon moisture exposure; suppress morphological changes at elevated cell temperatures; and eliminate hygroscopic and migrating additives in the device. Preventing these three degradation pathways for PSCs could be vital for guaranteeing stable PCEs for PSC commercialization.

Chapter 3 : Tuning the Electrochemical and Electronic Properties of Spiro-Centred Hole Transport Materials through Substituent Identity

3.1 Introduction

Spiro-OMeTAD has prevailed as a state-of-the-art hole transport material (HTM) since its discovery by Bach *et al.* in 1998.⁶⁸ The rigidity imparted by the spiro-carbon core causes an increase in glass transition temperature (T_g) relative to homologous linear HTMs.^{64,65} The spiro-carbon core therefore prevents morphological changes to the HTM during perovskite solar cell (PSC) operation. The four triphenylamine (TPA) units appended to the spiro-carbon core are incorporated to achieve reversible redox chemistry.⁹⁶

X60 was recently reported to be a viable alternative to **spiro-OMeTAD** (Figure 3-1).^{22,23} **X60** also contains four TPA units appending a strained spiro-carbon core but the asymmetric spiro[fluorene-9,9'-xanthene] core of **X60** can be synthesized in two steps - and at a fifth of the cost of the symmetric spirobifluorene core of **spiro-OMeTAD** (Scheme 2-1). **X60** reliably yields power conversion efficiencies (PCEs) greater than 20% in PSCs, values that are commensurate to those with **spiro-OMeTAD**.²⁶

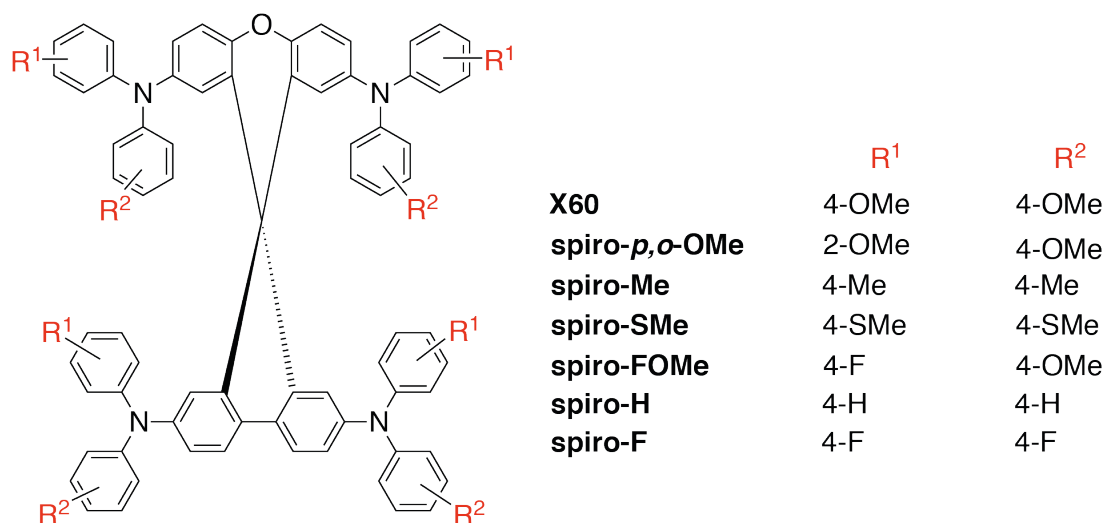


Figure 3-1 Molecular representations of the **spiro-R** series under investigation.

The effect of substituents on the charge transport properties of spiro-based HTMs remains poorly understood. **Spiro-OMeTAD** contains methoxy substituents, which were originally incorporated by Bach *et al.* to ensure an appropriate “matching of energy levels” between the valence band of the light absorbing layer (originally a ruthenium dye) to the highest occupied molecular orbital (HOMO) of the HTM.⁶⁸ Polander *et al.* demonstrated that the HOMO of the HTM must be at least 70 mV less positive than the valence band of a PSC for efficient hole extraction.^{34,35} The HOMO level (E_{HOMO}) of an HTM can be modulated through substituent identity and location, but how these substituents affect the hole mobilities of HTMs is not clearly defined. There is a pressing need to develop design rules for high mobility HTMs, while also retaining control over the E_{HOMO} .

The series of seven HTMs (**spiro-R**, Figure 3-1) was selected to contain modifications to the peripheral substituents appending the spiro[fluorene-9,9'-xanthene] core of **X60** to determine the role of substituent identity on hole mobility. We selected the series of seven analogous compounds from a computational screen of more than 25 compounds on the basis of appropriate HOMO level for use in a PSC. We systematically investigated the electrochemical, photophysical and charge transport properties of the series and compared HTM characteristics to those of **spiro-OMeTAD**. In parallel, we conducted a state-of-the-art multiscale simulation of the **spiro-R** hole mobilities and elucidated the role of substituents on hole mobility. Our computational model implicated the importance of low conformational and electrostatic disorder, common to large, non-polar substituents, for high hole mobility.

3.2 Results and discussion

3.2.1 Computational screening

Computational screening by Dr. Daniel Tabor of the Aspuru-Guzik group at the University of Toronto was used to select HTM substitution patterns on the basis of appropriate HOMO energy levels for hole extraction from the perovskite layer. A series of 25 molecules containing the spiro[fluorene-9,9'-xanthene] core was modelled by generating up to 20 conformers of each compound using B3LYP/6-31+G level of theory. The reduction potentials (ϵ_{HOMO} in Table 3-1) were calculated as an approximation of the HOMO energy levels (E_{HOMO}) of the HTMs. The valence band of the perovskite $\text{Cs}_{0.05}\text{FA}_{0.81}\text{MA}_{0.14}\text{PbI}_{2.55}\text{Br}_{0.45}$ used in our PSC studies is determined to be -5.82 eV in the solid state,²⁰ and minimum free energy change of 0.07 eV is necessary for hole extraction from the valence band of the perovskite to the HOMO of the HTM.^{34,35} Known compound **X60** deviated from experimental values by approximately 0.6 eV which is estimated to be a correction necessary going from a gaseous computation to experimental results. On this basis, HTMs with an ϵ_{HOMO} lower than -5.15 eV were anticipated to exhibit negligible hole extraction. Seven candidate materials were identified on this basis of ϵ_{HOMO} ; they are shown in Figure 3-1.

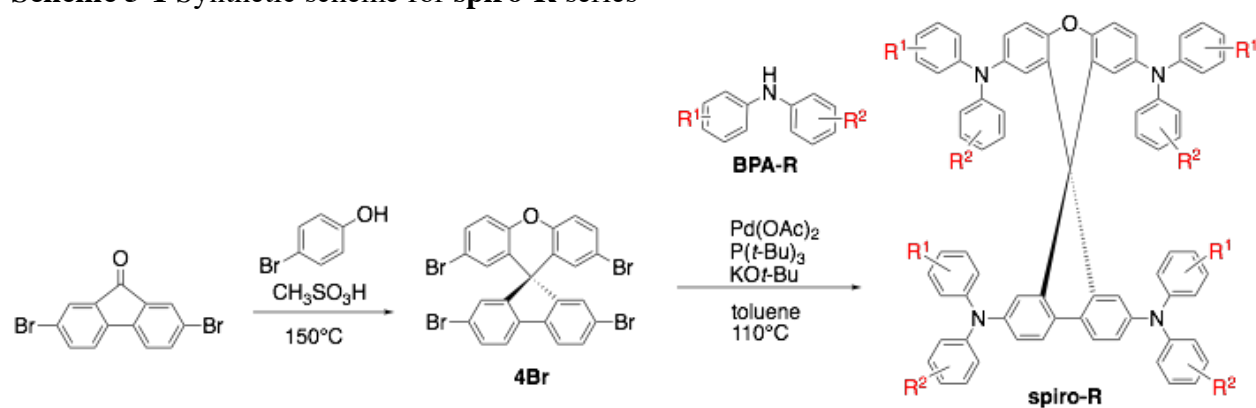
Table 3-1 Summary of computed reduction potentials and HOMO-LUMO energy gaps for the **spiro-R** series

compound	ϵ_{HOMO} (eV)	$\epsilon_{\text{HOMO-LUMO}}$ (eV)
X60	-4.49	3.66
spiro-<i>p,o</i>-OMe	-4.82	3.77
spiro-Me	-4.88	3.79
spiro-SMe	-5.09	3.60
spiro-FOMe	-4.96	3.72
spiro-H	-5.03	3.82
spiro-F	-5.37	3.78

3.2.2 Synthesis

The seven compounds were synthesized by coupling a one-pot condensation product with four equivalents of a secondary amine. The synthesis of the seven candidate HTM compounds followed a modified literature procedure where 2,7-dibromofluorenone was reacted with 4-bromophenol to yield a tetra-brominated product (**4Br**). **4Br** was isolated in >95% yield by a precipitation in methanol before undergoing four one-pot Buchwald-Hartwig couplings with four equivalents of secondary amine (**BPA-R**) (Scheme 3-1). **BPA-R** compounds were either purchased (in the case of **BPA-OMe**, **-Me** and **-H**) or synthesized (in the case of **BPA-*o,p*-OMe**, **-SMe**, **-FOMe** and **-F**). All intermediate and final compounds were characterized by ¹H nuclear magnetic resonance (NMR) spectroscopy, ¹³C NMR, low and high resolution mass spectrometry.

Scheme 3-1 Synthetic scheme for **spiro-R** series



3.2.3 Electrochemical and photophysical characterization

Cyclic voltammograms (CVs) were recorded for all HTMs in 0.1 M *n*-NBu₄PF₆ DCM solutions to experimentally determine the E_{HOMO} values for the series (Figure 3-2 and Table 3-2). CVs showed four peaks in current representing four electron transfer events for each compound, which matches the four TPA units present on each molecule. The E_{HOMO} of these materials occurred between 0.67 to 0.96 V vs NHE, with a clear trend that E_{HOMO} increases with increasing

electron-withdrawing character of substituents. The trend observed for the experimentally determined E_{HOMO} is fully supported by the ϵ_{HOMO} determined from density functional theory (DFT) calculations. The methoxy substituents on **X60** and **spiro-*p,o*-OMe** contributed to the lowest E_{HOMO} values measured for the series (0.67 and 0.69 vs NHE, respectively) because these substituents donate electron density toward the amine nitrogens and stabilize oxidized HTM molecules. Fluorine substituents were the most electron-withdrawing of the series owing to the high electronegativity of fluorine and, hence, **spiro-F** exhibited the highest E_{HOMO} measured at 0.96 V vs NHE.

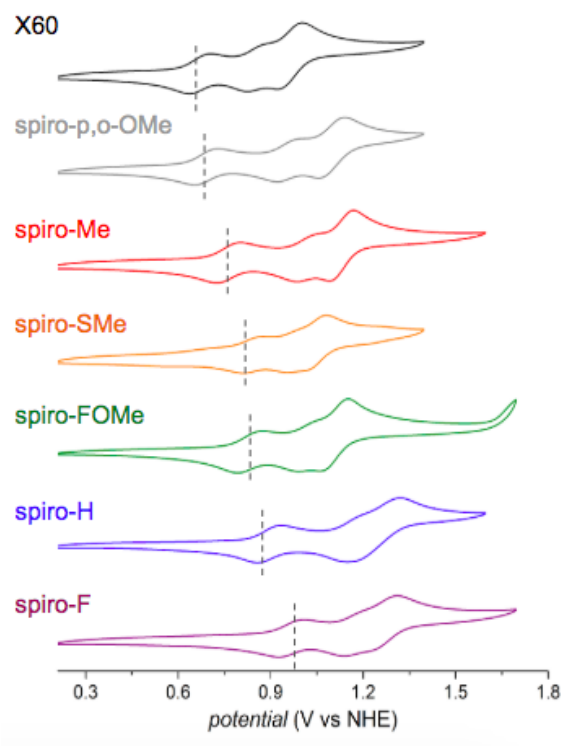


Figure 3-2 Cyclic voltammograms for **spiro-R** series recorded in 0.1 M $n\text{-NBu}_4\text{PF}_6$ DCM solutions at room temperature. Data were collected at a scan rate of 50 mV/s. Dashed lines indicate E_{HOMO} values.

Table 3-2 Summary of photophysical, electrochemical and bulk thermal properties for **spiro-R** series

compound	λ_{\max}^a (nm)	λ_{em}^b (nm)	$E_{\text{HOMO-LUMO}}^c$ (eV)	E_{HOMO}^d (V vs NHE)	E_{LUMO}^e (V vs NHE)	T_g^f (°C)	T_m^f (°C)
X60	306, 365	429	2.97	0.67	-2.30	107	>300
spiro-<i>p,o</i>-OMe	313, 354	413	3.07	0.69	-2.38	101	>300
spiro-Me	307, 388	414	3.02	0.77	-2.25	127	>300
spiro-SMe	327, 395	427	2.97	0.84	-2.13	125	270
spiro-FOMe	303, 381	416	3.02	0.84	-2.17	96	>300
spiro-H	306, 381	405	3.08	0.90	-2.18	98	>300
spiro-F	300, 376	405	3.06	0.96	-2.10	114	>300

^a Absorption maximum for HTM in DCM. ^b Excitation at higher energy λ_{\max} . ^c Determined from intersection of absorption and emission spectra. ^d The half-wave potential from the first oxidation of cyclic voltammograms of HTMs in DCM referenced to NHE with the addition of Fc/Fc⁺. ^e The LUMO determined from the addition of $E_{\text{HOMO-LUMO}}$ to E_{HOMO} . ^f Determined by differential scanning calorimetry (DSC).

All seven HTMs exhibited similar absorption profiles with maximum absorption peaks (λ_{\max}) between 300-327 nm and notable lower energy shoulders at 354-395 nm (Figure 3-3a and Table 3-2). The absorption bands in the UV region make these HTMs good candidates for either normal or inverted PSC devices as the HTMs would not compete with the photoactive layer for visible light absorption from solar radiation, regardless of the side of the device being illuminated. The emission data (Figure 3-3b) were collected to determine the bandgap ($E_{\text{HOMO-LUMO}}$) of each **spiro-R** compound from the intersection of the absorption and emission spectra. E_{LUMO} can be determined by adding the spectroscopically derived bandgap $E_{\text{HOMO-LUMO}}$ and the electrochemically derived E_{HOMO} . An E_{LUMO} smaller in magnitude than -2.00 V vs NHE is necessary to ensure that there is no deleterious flow of photoexcited electrons from the conduction band of the perovskite to the LUMO of the HTM and instead, only productive electron flow from the conduction band of the perovskite to the conduction band of the TiO₂-Cl.⁹⁷ All experimental E_{LUMO} values were smaller

in magnitude than -2.10 V vs NHE and, therefore, electron transfer to the HTM will be suppressed (Table 3-2).

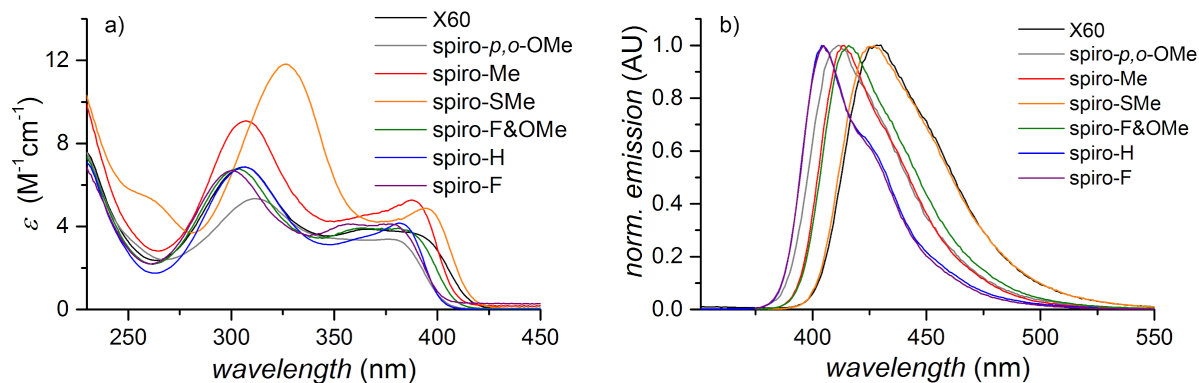


Figure 3-3 (a) UV-Vis absorption spectra and (b) emission spectra for **spiro-R** series dissolved in DCM

3.2.4 Bulk thermal properties

The seven compounds exhibited glass transition and melting temperatures above the maximum operating temperature of a PSC (i.e., 90 °C).⁵⁰ The glass transition temperature (T_g) and melting temperature (T_m) were determined using differential scanning calorimetry (DSC) for each material in the series (Table 3-2). The T_g values for all seven HTMs were measured between 96-127 °C. The T_m values were all above 270 °C for the **spiro-R** series. An HTM should exhibit a T_g and T_m greater than 90 °C to avoid morphological and phase changes to the glassy, amorphous HTM film as the temperature of a PSC increases during operation due to solar irradiation and thermal losses in the cell. All seven HTMs displayed suitable bulk thermal properties for PSC application and are not expected to undergo morphological or phase changes during operation.

3.2.5 Electrical properties

Conductivity measurements were performed for each of the **spiro-R** films with 20 mol% LiTFSI dopant and 250 mol% tBP additive. LiTFSI is the most commonly used dopant in the PSC field and is employed to increase the number of charge carriers and conductivity of an HTM film.^{79,80} tBP was added to all films to increase film uniformities by suppressing phase segregation between dopant molecules and HTMs during spin coating.⁷⁶ Four parallel gold electrodes were deposited uniformly on each of the spin-coated films and a current was applied from 2×10^{-9} to 1×10^{-7} A through the two outer contacts. The responding voltage was measured between the two inner contacts. The conductivity values tabulated in Table 3-3 were calculated from the slope of the current vs. voltage plots, and the film thicknesses were determined by optical profilometry. The three highest conductivities of 5.8×10^{-5} , 6.9×10^{-5} and 2.5×10^{-4} S/cm were measured for **X60**, **spiro-SMe** and **-Me**, respectively which are the HTMs containing the largest substituents of the series. The asymmetrically substituted **spiro-FOMe** exhibited the lowest conductivity (1.9×10^{-6} S/cm). **Spiro-F**, containing polar fluorine substituents, exhibited the second lowest conductivity of the series (i.e., 1.6×10^{-5} S/cm).

Table 3-3 Conductivity data for **spiro-OMeTAD** and **spiro-R** series

compound	conductivity (S/cm)
spiro-OMeTAD	$1.2 \pm 0.2 \times 10^{-4}$
X60	$5.8 \pm 0.1 \times 10^{-5}$
spiro-<i>p,o</i>-OMe	$3.7 \pm 0.7 \times 10^{-5}$
spiro-Me	$2.5 \pm 0.6 \times 10^{-4}$
spiro-SMe	6.9×10^{-5}
spiro-FOMe	1.9×10^{-6}
spiro-H	$2.8 \times 10^{-5} \pm 2.8 \times 10^{-6}$
spiro-F	1.6×10^{-5}

Conductivity measured for films composed of HTM, 20 mol% LiTFSI and 250 mol% tBP

3.2.6 Bulk Simulation

The hole mobilities of the **spiro-R** series were calculated from experimentally determined conductivities by assuming a constant charge carrier density for all HTMs. The agreement between experimentally determined hole mobilities and computationally derived values (Figure 3-4a) lends credence to us gleaned design principles from our mobility model. The hole mobilities were computed as a product of the electronic coupling, reorganization energy, conformational disorder and electrostatic disorder. Conformational disorder is due to geometrical differences between the molecules in the amorphous structure. Electrostatic disorder is due to the electrostatic interaction between molecules with their amorphous environment. The contributions by conformational disorder and electrostatic disorder appear to vary most significantly between compounds in the series and impact the mobilities the greatest of the four factors. Conformational disorder was minimized by increasing the steric bulk of substituents which implicated the importance of large substituents (e.g., methyl, methoxy and thiomethyl groups) on HTM hole mobility. The

electrostatic disorder was impacted by the polarities of the substituents where dense, polar and asymmetric substituents negatively impacted the computed electrostatic disorder and hole mobility values. In particular, symmetric substitution of large, non-polar moieties (e.g., methyl groups in the case of **spiro-Me**) can effectively lower both conformational disorder and electrostatic disorder to yield higher hole mobilities than smaller, polar substituents.

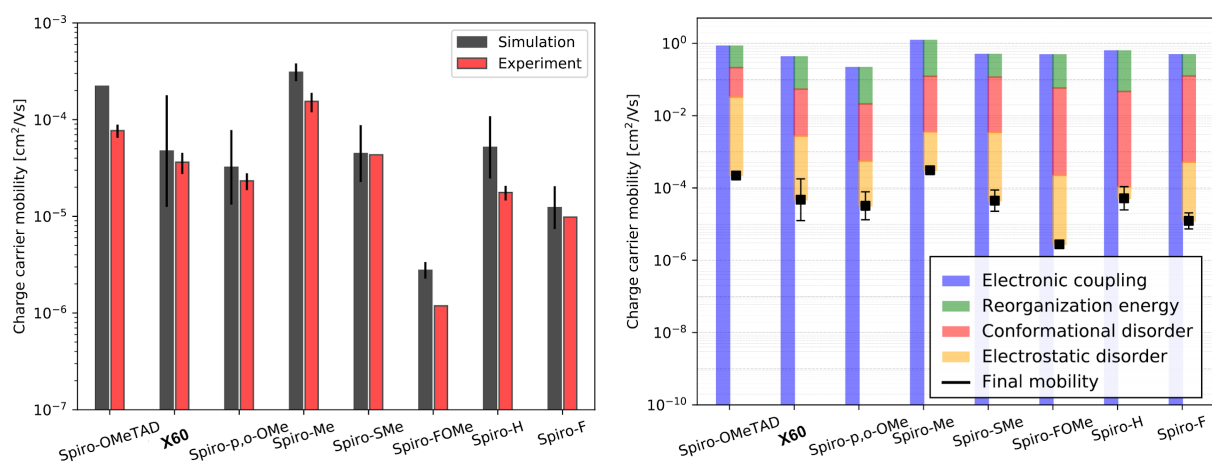


Figure 3-4 (a) Simulated (grey) and experimental (red) hole mobilities of **spiro-OMeTAD** and **spiro-R** series, (b) computed hole mobilities of the **spiro-R** series with the contributions by electronic coupling, reorganization energy, conformational disorder and electrostatic disorder.

3.2.7 Perovskite solar cell characterization

PSC studies were carried out by Dr. Hairen Tan of the Sargent group at the University of Toronto. Each of the HTMs was then tested in a PSC with the device architecture: glass/ITO/TiO₂-Cl/perovskite/HTM/Au. All HTMs were doped with 20 mol% LiTFSI to increase the number of charge carriers and the conductivities of the films. Table 3-4 summarizes the performance of PSCs fabricated with identical methods for each HTM. **X60** demonstrated a PCE of 20.9% in a PSC which was commensurate with state-of-the-art HTM **spiro-OMeTAD** (PCE of 21.2%). The six other HTMs yielded PCEs of 3.5% or below. We had anticipated that the V_{oc} values of PSCs would

increase with increasing electron-withdrawing strength of substituents and stabilizing of HTM E_{HOMO} but this trend was not observed. We hypothesized that the poor conductivities and hole mobilities of the majority of the materials (e.g., **spiro-FOMe** and **-F**) resulted in the poor overall device metrics and prevented V_{oc} values from reflecting the energy difference between the E_{Fermi} of the $\text{TiO}_2\text{-Cl}$ and the E_{HOMO} of the HTM.

Table 3-4 Perovskite solar cell data for **spiro-OMeTAD** and **spiro-R** series

compound	V_{oc} (V)	J_{sc} (mA/cm ²)	FF	PCE (%)
Spiro-OMeTAD	1.12	23.4	0.80	21.2
X60	1.12	23.4	0.79	20.9
spiro-<i>p,o</i>-OMe	1.03	13.5	0.75	3.5
spiro-Me	0.68	0.16	0.34	0.04
spiro-SMe	0.92	1.25	0.34	0.39
spiro-FOMe	0.77	0.04	0.20	0.01
spiro-H	0.75	0.3	0.14	0.04

PSCs prepared with $\text{Cs}_{0.05}\text{FA}_{0.81}\text{MA}_{0.14}\text{PbI}_{2.55}\text{Br}_{0.45}$ perovskite mixture and 20 mol% LiTFSI dopant/250 mol% tBP additive in HTM layer

3.3 Conclusions

Relatively bulky, non-polar substituents (e.g. methyl substituents) yield high hole mobility materials. We were able to draw this conclusion by screening a library of 25 HTM compounds which differed in both substituent identity and position about the core. We selected seven candidate materials on the basis of computed ϵ_{HOMO} values. We studied the effect of both substituent identity and location on the electrochemical, photophysical and charge transport properties of seven candidate HTMs. Owing to the agreement between experimental and simulated hole mobility data, we were able to extract design principles for high hole mobility HTMs from

our model. Sterically bulky, non-polar substituents are beneficial for decreasing the conformational and electrostatic disorder to yield high hole mobility materials.

3.4 Experimental

3.4.1 Computational screening

Cores were assembled from spiro[fluorene-9,9'-xanthene] moieties. To each of these cores, there were various modifications in the positions and the functional groups attached to the triphenylamine (TPA) units and the TPA substitution positions themselves. Each molecule was then subject to the same computational pipeline. Conformers were generated using the RDKit package. These conformers were optimized at the B3LYP/def2-SV(P) level of theory and the frontier molecular orbital (i.e., HOMO and LUMO) energies obtain were obtained. The Gaussian0930 package was used for these electronic structure calculations.

3.4.2 Synthesis

All reagents were obtained from MilliporeSigma, Alfa Aesar or Fisher Scientific and used as received. All reactions were performed using toluene that was passed through a solvent purification system prior to use. Standard inert atmosphere and Schlenk techniques were carried out under nitrogen. All reactions and purifications were carried out in the dark. Purification by column chromatography was performed using silica (Silicycle: Ultrapure Flash Silica). Analytical thin-layer chromatography (TLC) was performed on aluminum-backed sheets pre-coated with silica 60 F-254 adsorbent (250 μm thick; Silicycle, QC, Canada) and visualized under UV light. Routine ^1H and ^{13}C NMR spectra were collected on a Bruker AV300 or Bruker AV400 inv/dir instrument at ambient temperatures, operating at 400 MHz and 100 MHz, respectively. Chemical

shifts (δ) are reported in parts per million (ppm) using the residual signals δ 7.26 and 77.0 for CDCl_3 , δ 2.05 and 29.8 for acetone- d_6 and δ 2.50 and 39.4 for DMSO- d_6 as internal references for ^1H and ^{13}C , respectively.

4Br (2,2',7,7'-tetrabromospiro[fluorene-9,9'-xanthene]): 2,7-dibromo-9-flourenone (1.08 g, 3.20 mmol), 4-bromophenol (5.53 g, 32.0 mmol) and methane sulfonic acid (0.82 mL, 12.8 mmol) were mixed at 150 °C for 18 h under N_2 . The reaction mixture was cooled to room temperature and product was precipitated with the addition of MeOH. Separation by filtration and rinsing with MeOH yielded 2.09 g (96.5%) of product as white powder. ^1H NMR (300 MHz, Acetone- d_6) δ = 8.01 (d, J = 8.1 Hz, 1 H), 7.69 (dd, J = 8.2, 1.8 Hz, 1H), 7.49 (dd, J = 8.8, 2.4 Hz, 1H), 7.44 (d, J = 1.7 Hz, 1 H), 7.31 (d, J = 8.8 Hz, 1H), 6.53 (d, J = 2.4 Hz, 1H). ^{13}C NMR (100 MHz, Acetone- d_6): δ = 155.5, 150.0, 137.6, 132.2, 130.4, 129.0, 124.8, 122.9, 122.0, 119.2, 116.2 ppm. HRMS (EI) m/z : 643.76141 [(M^+)] calcd for $\text{C}_{25}\text{H}_{12}\text{O}_7\text{Br}_4$ m/z : 643.76216.

BPA-*p,o*-OMe (2-Methoxy-*N*-(4-methoxyphenyl)aniline): 2-iodoanisole (1.00 g, 4.27 mmol), *p*-anisidine (0.53 g, 4.27 mmol), palladium acetate (0.061 g, 0.30 mmol), tri-*tert*-butylphosphine (0.110 g, 0.491 mmol) and potassium *tert*-butoxide (1.03 g, 10.7 mmol) were added to toluene (15 ml) under N_2 . The reaction mixture was stirred at reflux for 16 h. The reaction mixture was cooled to room temperature. Purification by silica column chromatography (SiO_2 : hexanes/EtOAc, 8:1) yielded 0.807 g (81%) of pale yellow solid product. ^1H NMR (400 MHz, CDCl_3) δ = 7.12, (d, J = 8.8 Hz, 1 H), 7.04 (dd, J = 7.7, 1.7 Hz, 1H), 7.05-6.77 (m, 6H), 5.97 (s, 1H). ^{13}C NMR (100 MHz, Acetone- d_6): δ = 155.8, 147.8, 135.9, 135.5, 123.2, 121.4, 119.0, 115.1, 113.1, 110.7, 56.0 ppm. HRMS (EI) m/z : 230.1190 [(M^+)] calcd for $\text{C}_{14}\text{H}_{16}\text{NO}_2$ m/z : 230.1181.

BPA-SMe (Bis(4-(thiomethyl)phenyl)amine): (4-bromophenyl)methylsulfane (2.03 g, 10.0 mmol), 4-(methylthioaniline) (1.39 g, 10.0 mmol), palladium acetate (0.112 g, 0.50 mmol), tri-

tert-butylphosphine (0.100 g, 0.5 mmol) and potassium *tert*-butoxide (1.68 g, 15.0 mmol) were added to toluene (15 mL) under N₂. The reaction mixture was stirred at reflux for 16 h. The reaction mixture was cooled to room temperature. Purification by silica column chromatography (SiO₂: hexanes/EtOAc, 10:1) yielded 1.55 g (44%) of yellow/brown solid product. ¹H NMR (400 MHz, CDCl₃) δ = 7.20 (d, *J* = 8.6 Hz, 4H), 6.94 (d, *J* = 8.6 Hz, 4H), 5.62 (br, 1H), 2.42 (s, 6H). ¹³C NMR (101 MHz, CDCl₃) δ = 141.3, 129.9, 129.3, 118.6, 77.5, 77.2, 76.8, 17.9. HRMS (ESI) *m/z*: 262.0721 [(M+)] calcd for C₁₄H₁₆NS₂ *m/z*: 262.0724.

BPA-FOMe (4-Fluoro-*N*-(4-methoxyphenyl)aniline): 4-bromoanisole (2.81 g, 15.0 mmol), 4-fluoroaniline (1.67 g, 15.0 mmol), palladium acetate (0.168 g, 0.75 mmol), tri-*tert*-butylphosphine (0.151 g, 0.75 mmol) and potassium *tert*-butoxide (2.53 g, 22.5 mmol) were added to toluene (15 ml) under N₂. The reaction mixture was stirred at reflux for 16 h. The reaction mixture was cooled to room temperature. Purification by silica column chromatography (SiO₂: hexanes/EtOAc, 10:1) yielded 1.60 g (49.1%) of pale yellow waxy solid product.

BPA-F (bis(4-fluorophenyl)amine): 4-bromo-fluorobenzene (3.15 g, 18 mmol), 4-fluoroaniline (2.00 g, 18 mmol), palladium acetate (0.29 g, 1.4 mmol), tri-*tert*-butylphosphine (0.32 g, 1.4 mmol) and potassium *tert*-butoxide (2.00 g, 90 mmol) were added to toluene (15 ml) under N₂. The reaction mixture was stirred at reflux for 16 h. The reaction mixture was cooled to room temperature. Purification by silica column chromatography (SiO₂: hexanes/EtOAc, 5:1) yielded 2.29 g (62%) of dark brown oil product. ¹H NMR (400 MHz, CDCl₃) δ = 6.97, (d, *J* = 1.1 Hz, 8 H), 5.46 (s, 1H). ¹³C NMR (100 MHz, Acetone-d₆): δ = 159.1, 156.7, 140.0, 119.6, 119.5, 116.2, 116.0 ppm. HRMS (EI) *m/z*: 205.07029 [(M+)] calcd for C₁₂H₉NF₂ *m/z*: 205.07031.

X60 (*N2,N2,N2',N2',N7,N7,N7',N7'*-octakis(4-methoxyphenyl)spiro[fluorene-9,9'-xanthene]-2,2',7,7'-tetraamine): bis(4-methoxyphenyl)amine (1.14 g, 5.00 mmol), **4Br** (0.678 g, 1.00 mmol),

palladium acetate (0.018 g, 0.08 mmol), tri-*tert*-butylphosphine (0.018 g, 0.08 mmol) and potassium *tert*-butoxide (0.45 g, 5.00 mmol) were added to toluene (15 ml) under N₂. The reaction mixture was stirred at reflux for 16 h. The reaction mixture was cooled to room temperature. Purification by silica column chromatography (SiO₂: hexanes/EtOAc, 4:1) yielded 0.731 g (59%) of product as pale green solid. ¹H NMR (400 MHz, CDCl₃) δ = matched literature. ¹³C NMR (100 MHz, CDCl₃): δ = 155.7, 155.4, 154.9, 147.8, 146.8, 143.3, 141.7, 141.4, 133.1, 125.6, 125.5, 124.4, 124.2, 122.8, 121.9, 119.8, 118.7, 117.4, 114.6, 114.5. 55.6, 54.4. HRMS (ESI) *m/z*: 1241.5085 [(M+H)] calcd for C₈₁H₆₉N₄O₉ *m/z*: 1241.5065.

spiro-*p,o*-OMe (*N2,N2',N7,N7'*-tetrakis(2-methoxyphenyl)-*N2,N2',N7,N7'*-tetrakis(4-methoxyphenyl)spiro[fluorene-9,9'-xanthene]-2,2',7,7'-tetraamine): 2-methoxy-*N*-(4-methoxyphenyl)aniline (1.27 g, 5.50 mmol), **4Br** (0.800 g, 1.23 mmol), palladium acetate (0.020 g, 0.1 mmol), tri-*tert*-butylphosphine (0.022 g, 0.1 mmol) and potassium *tert*-butoxide (0.50 g, 5.50 mmol) were added to toluene (15 mL) under N₂. The reaction mixture was stirred at reflux for 16 h. The reaction mixture was cooled to room temperature. Purification by silica column chromatography (SiO₂: hexanes/EtOAc, 4:1) yielded 0.686 g (45%) of product as pale green solid. ¹H NMR (400 MHz, CD₂Cl₂) δ = 7.24 (d, *J* = 9.0 Hz, 2H), 7.12 (m, 4H), 8.97 (m, 4H), 6.85 (m, 14H), 6.71 (m, 18H), 6.16 (d, *J* = 2.7 Hz, 2H), 3.73 (d, *J* = 15.4 Hz, 12H), 3.46 (d, *J* = 12.9 Hz, 12H). ¹³C NMR (100 MHz, CD₂Cl₂): δ = 155.7, 155.6, 155.5, 155.0, 154.7, 147.7, 146.5, 143.2, 141.5, 141.0, 135.9, 135.8, 132.4, 129.3, 129.0, 126.2, 126.1, 125.9, 124.8, 122.8, 121.5, 121.4, 121.3, 119.7, 119.3, 119.1, 116.6, 116.3, 114.3, 114.2, 113.3, 113.1, 55.7, 55.6, 55.5, 55.5, 54.8. HRMS (ESI) *m/z*: 1240.4989 [(M+H)] calcd for C₈₁H₆₈N₄O₉ *m/z*: 1240.4986.

spiro-Me (*N2,N2,N2',N2',N7,N7,N7',N7'*-octa-*p*-tolylspiro[fluorene-9,9'-xanthene]-2,2',7,7'-tetraamine): di-*p*-tolylamine (1.46 g, 7.4 mmol), **4Br** (1.00 g, 1.5 mmol), palladium acetate (0.024

g, 0.12 mmol), tri-*tert*-butylphosphine (0.027 g, 0.12 mmol) and potassium *tert*-butoxide (0.71 g, 5.00 mmol) were added to toluene (15 mL) under N₂. The reaction mixture was stirred at reflux for 16 h. The reaction mixture was cooled to room temperature. Purification by silica column chromatography (SiO₂: hexanes/EtOAc, 15:1) yielded 0.910 g (22%) of product as light brown solid. ¹H NMR (400 MHz, Acetone-d₈) δ = 7.46 (d, *J* = 8.3 Hz, 2H), 7.09-6.99 (m, 20H), 6.86 (d, *J* = 8.4 Hz, 8H), 6.82 (dd, *J* = 8.3, 2.3 Hz, 4H), 6.76 (d, *J* = 8.4 Hz, 8H), 6.39 (d, *J* = 2.6 Hz, 2H), 4.72 (s, 12H), 5.10 (s, 12H). ¹³C NMR (100 MHz, CDCl₃): δ = 155.7, 155.4, 154.9, 147.8, 146.8, 143.3, 141.7, 141.4, 133.1, 125.6, 125.5, 124.4, 124.2, 122.8, 121.9, 119.8, 118.7, 117.4, 114.6, 114.5, 77.5, 77.2, 76.8, 55.6, 54.4. HRMS (ESI) *m/z*: 1113.5469 [(M+H)] calcd for C₈₁H₆₉N₄O *m/z*: 1113.5471.

spiro-SMe: (*N2,N2,N2',N2',N7,N7,N7',N7'*-octa-*p*-thiomethylspiro[fluorene-9,9'-xanthene]-2,2',7,7'-tetraamine): bis(4-(methylthio)phenylamine) (0.915 g, 3.5 mmol), **4Br** (0.454 g, 0.70 mmol), palladium acetate (0.040 g, 0.18 mmol), tri-*tert*-butylphosphine (0.036 g, 0.18 mmol) and potassium *tert*-butoxide (0.561 g, 5.00 mmol) were added to toluene (15 mL) under N₂. The reaction mixture was stirred at reflux for 16 h. The reaction mixture was cooled to room temperature. Purification by silica column chromatography (SiO₂: hexanes/EtOAc, 12:1) yielded 0.451 g (47%) of product as yellow solid. ¹H NMR (400 MHz, CDCl₃) δ = 7.38 (d, *J* = 8.2 Hz, 2H), 7.17 – 7.07 (m, 16H), 7.05 – 6.77 (m, 24H), 6.36 (d, *J* = 2.6 Hz, 2H), 2.46 (s, 12H), 2.42 (s, 12H).

spiro-FOMe (*N²,N²,N⁷,N⁷*-tetrakis(4-fluorophenyl)-*N²,N²,N⁷,N⁷*-tetrakis(4-methoxyphenyl)spiro[fluorene-9,9'-xanthene]-2,2',7,7'-tetraamine): *N*-(4-fluorophenyl)aniline (0.760 g, 3.5 mmol), **4Br** (0.454 g, 0.70 mmol), palladium acetate (0.18 g, 0.18 mmol), tri-*tert*-butylphosphine (0.036 g, 0.18 mmol) and potassium *tert*-butoxide (0.561 g, 5.0 mmol) were added

to toluene (15 mL) under N₂. The reaction mixture was stirred at reflux for 16 h. The reaction mixture was cooled to room temperature. Purification by silica column chromatography (SiO₂: hexanes/EtOAc, 20:1 to 10:1) yielded 0.620 g (74.2%) of product as pale brown solid. ¹H NMR (400 MHz, CDCl₃) δ = 7.33 (d, 2H, *J* = 8.0 Hz), 6.98 (d, 2H, *J* = 8.0 Hz), 6.93- 6.76 (m, 38H), 6.33 (d, 2H, *J* = 2.7 Hz), 3.80 (s, 6H), 3.76 (s, 6H). ¹³C NMR (101 MHz, CDCl₃): δ 159.6, 159.3 (d, *J* = 60.6 Hz), 159.0, 156.9 (d, *J* = 59.3 Hz), 156.0, 155.7, 155.6, 147.6, 147.2, 144.6 (d, *J* = 2.5 Hz), 144.2 (d, *J* = 2.7 Hz), 143.1, 141.0, 140.8, 133.5, 126.2, 125.6, 125.5, 124.8, 124.7 (d, *J* = 7.8 Hz), 123.2, 123.0 (d, *J* = 7.7 Hz), 122.6, 120.1, 119.2, 117.8, 115.9 (d, *J* = 22.5 Hz), 115.7 (d, *J* = 22.4 Hz), 114.8, 114.7, 55.6, 55.6, 54.4.

spiro-H (*N*²,*N*²,*N*²,*N*²,*N*⁷,*N*⁷,*N*⁷,*N*⁷-octaphenylspiro[fluorene-9,9'-xanthene]-2,2',7,7'-tetraamine): diphenylamine (1.96 g, 11.6 mmol), **4Br** (1.50 g, 2.3 mmol), palladium acetate (0.037 g, 0.18 mmol), tri-*tert*-butylphosphine (0.045 g, 0.18 mmol) and potassium *tert*-butoxide (1.11 g, 11.6 mmol) were added to toluene (30 mL) under N₂. The reaction mixture was stirred at reflux for 16 h. The reaction mixture was cooled to room temperature. Purification by silica column chromatography (SiO₂: hexanes/EtOAc, 12:1) yielded 1.35 g (59%) of product as light brown solid. ¹H NMR (400 MHz, Acetone-*d*₆) δ = 7.52 (d, 2H, *J* = 8.0 Hz), 7.32-7.18 (m, 16H), 7.10-7.00 (m, 8H), 6.97 (dd, 8H, *J* = 7.5, 1.2 Hz), 6.92-6.85 (m, 10H), 6.41 (d, 2H, *J* = 2.6 Hz). HRMS (ESI) *m/z*: 1001.4203 [(M+Na)] calcd for C₇₁H₅₄N₄ONa *m/z*: 1001.4195.

spiro-F (*N*²,*N*²,*N*²,*N*²,*N*⁷,*N*⁷,*N*⁷,*N*⁷-octakis(4-fluorophenyl)spiro[fluorene-9,9'-xanthene]-2,2',7,7'-tetraamine): bis(4-fluorophenyl)amine (0.414 g, 2.0 mmol), **4Br** (0.300 g, 0.45 mmol), palladium acetate (0.012 g, 0.072 mmol), tri-*tert*-butylphosphine (0.018 g, 0.072 mmol) and potassium *tert*-butoxide (0.100 g, 0.87 mmol) were added to toluene (15 mL) under N₂. The reaction mixture was stirred at reflux for 16 h. The reaction mixture was cooled to room temperature. Purification by

silica column chromatography (SiO₂: hexanes/EtOAc, 15:1) yielded 0.204 g (39%) of product as light brown solid. ¹H NMR (400 MHz, CDCl₃) δ = 7.36 (d, *J* = 8.8 Hz, 2H), 7.01 (d, *J* = 8.8 Hz, 2H), 6.89-6.77 (m, 38H), 6.26 (d, *J* = 2.6 Hz, 2H). ¹³C NMR (101 MHz, Chloroform-*d*) δ 160.0, 159.6, 157.6, 157.2, 155.5, 147.5, 147.4, 144.0, 144.0, 143.8, 142.9, 133.8, 129.2, 128.4, 125.6, 125.5, 125.4, 125.3, 124.4, 124.3, 123.5, 123.2, 120.4, 119.7, 118.1, 116.3, 116.1, 115.9, 54.5. HRMS (ESI) *m/z*: 1145.3438 [(M+Na)] calcd for C₇₁H₄₆N₄OF₈Na *m/z*: 1145.3442.

3.4.3 Electrochemical and photophysical properties

Solution-phase electrochemical data were recorded with a CHI660D potentiostat using a platinum wire counter electrode, Ag/AgCl reference electrode, and a platinum working electrode. A 0.1 M *n*-NBu₄PF₆ DCM solution at ambient temperature was used for all HTMs. Ag/AgCl in saturated KCl was used as the reference electrode and was calibrated versus the normal hydrogen electrode (NHE) by addition of Fc/Fc⁺ as an internal reference. CVs were acquired for 0.5 mM solutions of each HTM at a scan rate of 50 mV s⁻¹.

Solution UV-vis absorption spectra were recorded using a Cary 5000 UV-vis spectrophotometer. Photoluminescence (PL) spectra were recorded with a Cary Eclipse. All samples were measured in a 1 cm cell at room temperature with DCM as the solvent. Concentration of 2 × 10⁻⁵ M and 1 × 10⁻⁵ M were used for solution absorption and emission measurements, respectively.

3.4.4 Bulk thermal properties

DSC curves of compounds were collected using a Netzsch DSC 214 Polyma instrument under a nitrogen protective atmosphere. For each measurement, two aluminum crucibles were used, one as empty reference and the other for sample measurement. A customized heating program was

developed to include a 5 min hold at the initial temperature of 50 °C and four consecutive heating-cooling cycles ($T_{\min} = 50$ °C, $T_{\max} = 300$ °C, 10 K/min). Data from the last 3 heating segments were used to identify the T_m and extrapolate the T_g of the material.

3.4.5 Electrical properties

Four parallel Au electrodes with a spacing of 0.75 mm and length of 23 mm were used to measure the film conductivities in the dark and under ambient conditions. A Keithley 2400 sourcemeter was used to force current through the outer electrodes while sensing the voltage across the inner two electrodes. A linear fit of each measurement was used to determine the resistance, R , and the geometry of samples was then used to calculate the conductivity, σ , according to the equation

$$\sigma = \frac{d}{Rlt} \quad \text{(Equation 3-1)}$$

where l is the electrode length, d is the inter-electrode spacing and t is the film thickness. The film thickness was measured using a Bruker DektakXT profilometer.

3.4.6 Bulk simulation

For simulation of thin film properties such as HOMO/LUMO energy distributions and hole mobility, we used the multiscale modeling approach described by Friederich *et al.*^{98,99} This approach includes the parameterization of molecule-specific force fields, the generation of atomically-resolved morphologies using a Monte Carlo simulated annealing protocol,¹⁰⁰ the analysis of the electronic structure of the molecules in their amorphous environment,¹⁰¹ the calculation of electronic couplings, reorganization energies, energy disorder and, finally, the calculation of the hole mobility using an effective medium model.¹⁰² We generated and analyzed three morphologies (each with approximately 1000 molecules) for all seven materials to have

sufficient statistics for the calculation of the hole mobility which sensitively depends on the energy disorder or the width of the distribution of HOMO energies.

3.4.7 Perovskite solar cell characterization

The planar perovskite solar cells were fabricated according to our previous work.²⁰ Briefly, pre-patterned ITO coated glass substrates were sequentially cleaned using detergent, acetone, and isopropanol. The TiO₂-Cl electron transport layers were spin-coated on ITO substrates from the colloidal nanocrystal solutions, and annealed on a hot plate at 150 °C for 30 min in ambient air. After the substrates had cooled, we transferred the substrates immediately to a nitrogen-filled glovebox for the deposition of perovskite films. The Cs_{0.05}FA_{0.81}MA_{0.14}PbI_{2.55}Br_{0.45} precursor solution (1.4 M) was prepared in a mixed solvent of DMF and DMSO with a volume ratio of 4:1. The molar ratios of PbI₂/PbBr₂ and FAI/MABr were both fixed at 0.85:0.15, molar ratio of CsI/(FAI+MABr) is 0.05:0.95, and the molar ratio of (FAI+MABr+CsI)/(PbI₂+PbBr₂) was fixed at 1:1. The perovskite films were deposited onto the TiO₂-Cl substrates with two-step spin coating procedures. The first step was 2000 rpm for 10 s with an acceleration of 200 rpm/s. The second step was 6000 rpm for 20 s with a ramp-up of 2000 rpm/s. Chlorobenzene (100 μL) was dropped on the spinning substrate during the second spin-coating step at 10 s before the end of the procedure. The substrate was then immediately transferred on a hotplate and heated at 100 °C for 20 min. After cooling down to room temperature, the hole-transport layer was subsequently deposited on top of the perovskite film by spin coating at 4000 rpm for 30 s using a chlorobenzene solution which contained 72.3 mg/mL of HTMs and 28.8 μL/mL of tBP, as well as 520 mg/mL of LiTFSI in acetonitrile). Finally, 100 nm Au contact was deposited on top of HTMs by electron-beam evaporation in an Angstrom Engineering deposition system.

Current density-voltage (J - V) characteristics were measured using a Keithley 2400 source meter under illumination of a solar simulator (Newport, Class A) at the light intensity of 100 mW cm^{-2} as verified using a certified reference solar cell (Newport). A spectral mismatch factor of 1 was used for all J - V measurements. Unless otherwise stated, the instantaneous J - V curves were measured with a scanning rate of 50 mV s^{-1} from 1.2 V to -0.1 V . The active area was determined using an aperture shade mask (0.049 cm^2) placed in front of the solar cell to avoid overestimation of the photocurrent density.

Chapter 4 : Controlling the Thermal Stability and Electrochemistry of Hole-Transport Material Films

4.1 Introduction

Hole-transport materials (HTMs) are a key component of organic light-emitting diodes (OLEDs)^{59,103,104} and solid-state solar cell devices.^{105,106} High performance HTMs for perovskite solar cells (PSCs) should exhibit high glass transition temperatures (T_g) to suppress the formation of grain boundaries in glassy films which can impede effective charge transfer.^{49,107} It is imperative that the HTM contains an appropriately positioned and reversible redox couple to mediate charge extraction from the photo-oxidized perovskite material, and be capable of conducting charge through the charge transport layer.^{35,108} These materials should also have high temporal stability under elevated temperatures and humidity.^{27,109,110}

Organic HTMs are amenable to low-temperature solution processing while also being capable of mediating high power conversion efficiencies (PCEs).^{50,111} **Spiro-OMeTAD**⁶⁸ (Figure 4-1) is a widely-used organic HTM and is capable of reaching PCEs greater than 20% when integrated in PSCs.^{20,112} The **spiro-OMeTAD** molecule teaches how a spiro-carbon center can impart a rigid 3D structure that leads to a high T_g (125 °C).¹¹³ The redox-active TPA substituents functionalized with methoxy groups also yield reversible redox couples at potentials appropriate for use in a PSC.¹¹⁴ This combination of structural and electrochemical properties contributes to the high hole mobilities (2×10^{-4} to 5×10^{-5} cm² V⁻¹s⁻¹) that have proven so effective for **spiro-OMeTAD**.¹¹⁵

As described in Chapter 2, **X60** is an HTM disclosed in early 2016^{22,23} which contains an asymmetric fluorene-9,9'-xanthene core functionalized with TPA groups, analogous to that of **spiro-OMeTAD**, to generate hole-transport properties that produce high PCEs in the PSCs.^{22,23,114} The simple reaction chemistry associated with spiro-based **X60** inspired us to elucidate how each

of the TPA units appending the unsymmetric spiro-core affects the HTM properties and the corresponding performance in a PSC. I discovered that the TPA units positioned about the highly conjugated fluorene fragment are the electrochemically relevant units (i.e., associated with the redox couple that represents the HOMO energy level, E_{HOMO}) while those positioned on the xanthene moiety affect the structural and bulk thermal properties.²⁶ I was able to resolve this structure-property relationship by placing TPA groups exclusively on the fluorene (**HTM-F**) or the xanthene (**HTM-X**) units of the core. These results pointed to the xanthene substituents governing the bulk thermal properties, prompting me to test how *para*- and *meta*-substitution of TPAs at the xanthene moiety (i.e., **HTM-X** and **HTM-X'**, respectively) affects the T_g s of these films. This decoupling of the E_{HOMO} levels and bulk thermal properties (e.g., T_g) yielded **HTM-FX'** which is characterized by a strikingly high T_g of 137 °C. This HTM was found to be capable of generating a PCE of 20.8% in a PSC, a value that compares favorably with those measured for **spiro-OMeTAD** and **X60** under the same experimental conditions. Moreover, devices containing **HTM-FX'** could be prepared with a notably high level of reproducibility. This identification of how the TPAs impact the redox activity, thermal properties and device characteristics will guide the design of new high-performance HTMs.

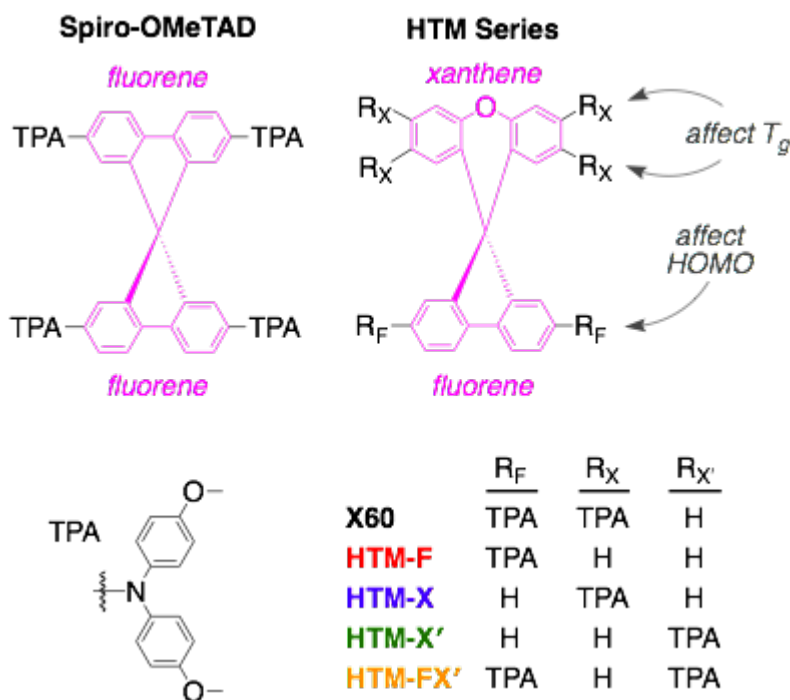


Figure 4-1 Molecular representations of **spiro-OMeTAD**⁶⁸ and the **HTM** series under investigation.

4.2 Results and discussion

4.2.1 Computational screening

Computational screening was carried out by Dr. Daniel Tabor of the Aspuru-Guzik group at the University of Toronto. Replacing one of the two fluorene units in **spiro-OMeTAD** with a xanthene unit to form **X60**^{22,23} results in a break in molecular symmetry and enables analysis of which specific TPA groups affect the redox properties and thermal properties of HTMs. Computational methods were used to screen the five HTMs in Figure 4-1 containing this unsymmetrical core for appropriate frontier orbital energy levels, low reorganization energies and photophysical properties. The frontier orbitals were modeled (Figure 4-2) and the computed reduction potentials corresponding to the first oxidation event (ϵ_{HOMO}) were predicted to all exhibit suitable reduction potentials for hole extraction from the perovskite layer.

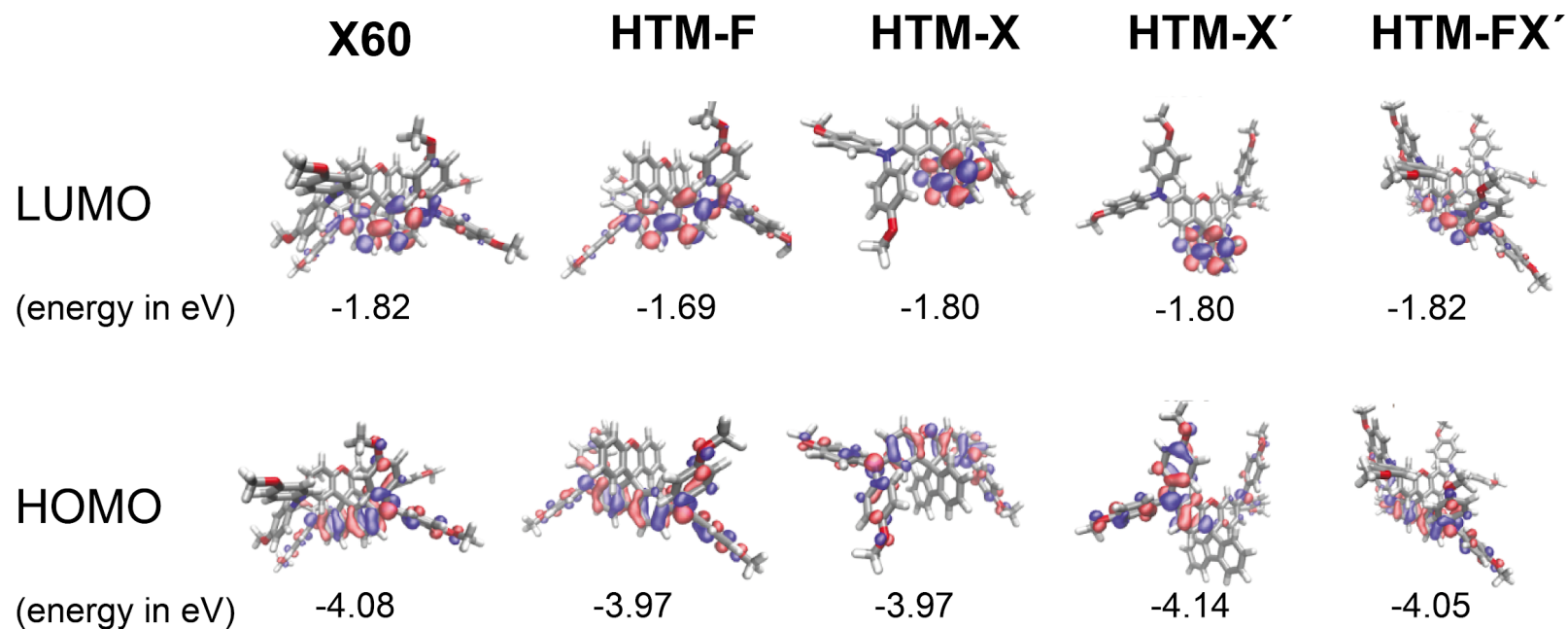


Figure 4-2 HOMO and LUMO orbitals of each molecule in the **HTM** series, calculated at the BP86/def2-SVP level of theory. Isosurfaces are at 0.03 and -0.03 values for the wavefunction.

The reorganization energies (E_{reorg}) for the entire **HTM** series (Table 4-1) were calculated using density functional theory (DFT) and evaluated using Nelsen's four point method.^{23,116,117} HTMs containing TPA moieties at the R_x or $R_{x'}$ positions of the HTM scaffold were predicted to exhibit smaller E_{reorg} values that are favourable for efficient hole transport according to Marcus theory.¹¹⁸ When considering each component term of the E_{reorg} calculation independently (Table 4-1), both the vertical ionization and the adiabatic ionization energies are substantially higher for compounds functionalized at exclusively the fluorene or xanthene units relative to **X60** and **HTM-FX'** (substituted at both the fluorene and xanthene units) due to less diffuse hole delocalization (Figure 4-3). The net relative effect of these two terms largely cancel out in a reorganization energy calculation thereby yielding similar E_{reorg} values across the series. The vertical electron affinity of the cation at the adiabatic cation minimum appears to be the more dominant factor that affects E_{reorg} , and **HTM-F** was found to contain the largest relative contribution from this term. Modeling the spin-density differences of the adiabatic minima for the singly oxidized molecules of the series (Figure 4-3) provides a visualization of the hole on an oxidized HTM and reveals differences in hole delocalization within the series. Fluorene was confirmed to be a highly conjugated unit and the positions of TPA groups on the xanthene moieties affect the electronic structure of the oxygen bridge. All computed E_{reorg} values were relatively low, between 0.14-0.20 eV and close to that of **spiro-OMeTAD** (0.14 eV).

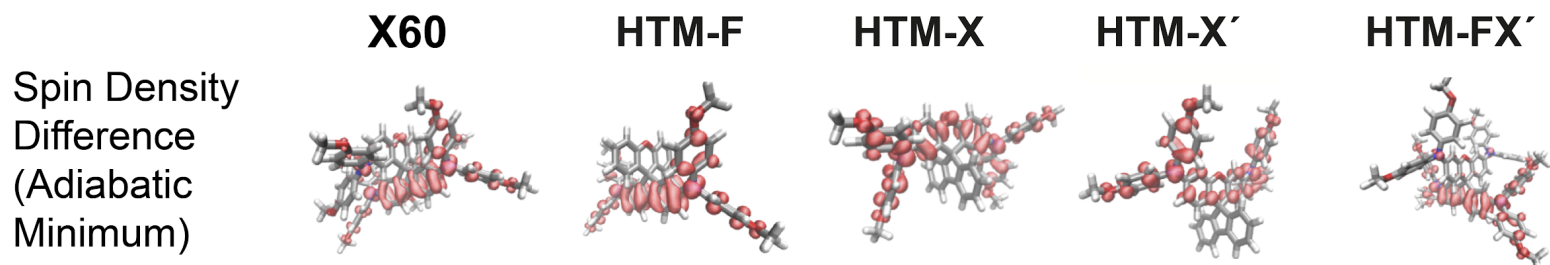


Figure 4-3 Spin density difference maps for the **HTM** cations evaluated at the B3LYP/6-311+G(d,p) level of theory at the B3LYP/6-31G(d) cation adiabatic minima.

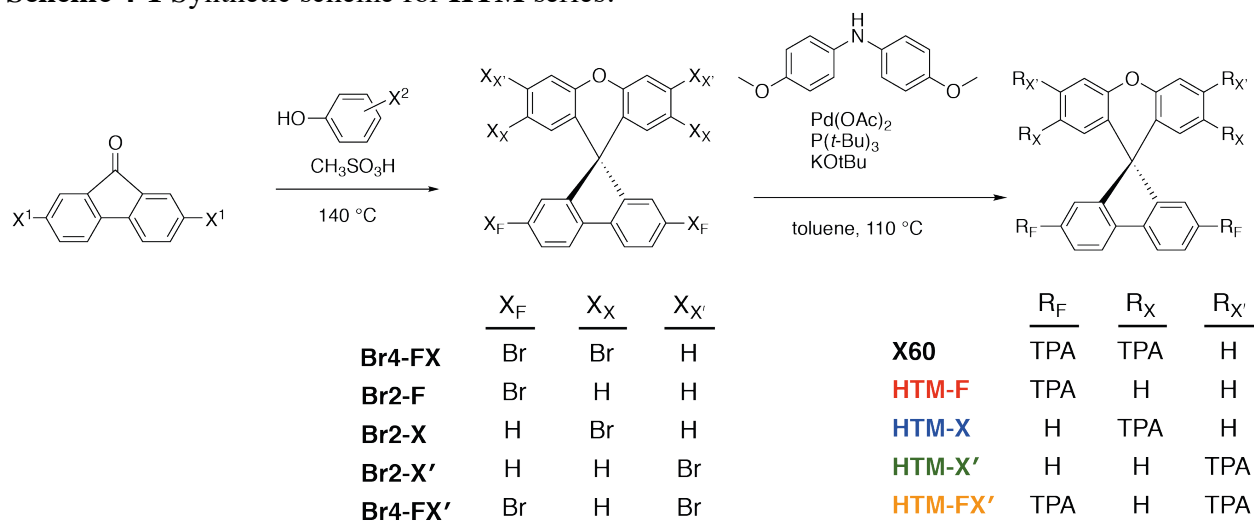
Table 4-1 Calculated electronic frontier molecular orbital properties and contributions to reorganization energies (B3LYP/6-311+G(d,p) evaluated at B3LYP/6-31G(d) optimized geometries) of the **HTM** series and **spiro-OMeTAD**

Compound	ϵ_{HOMO} (eV)	ϵ_{LUMO} (eV)	$\epsilon_{\text{HOMO-LUMO}}$ (eV)	E^*_+ (eV)	E_+ (eV)	E^* (eV)	E_{reorg} (eV)
X60	-4.54	-1.06	3.48	0.076	5.321	5.400	0.154
HTM-F	-4.60	-1.12	3.48	0.108	5.429	5.525	0.205
HTM-X	-4.65	-1.20	3.46	0.081	5.523	5.598	0.152
HTM-FX'	-4.52	-1.03	3.48	0.072	5.273	5.359	0.158
HTM-X'	-4.90	-1.14	3.76	0.071	5.739	5.812	0.144
Spiro-OMeTAD	-4.52	-1.06	3.48	0.059	5.235	5.319	0.143

4.2.2 Synthesis

The preparation of **X60** followed a modified literature procedure where 2,7-dibromofluorenone is reacted with 4-bromophenol to yield a tetra-brominated product that, in turn, undergoes a Pd-catalyzed Buchwald-Hartwig coupling with excess 4,4'-dimethoxyphenylamine to yield the product.²³ This procedure was adapted to access the rest of the **HTM** series (Scheme 4-1) using either non-brominated fluorenone for **HTM-X** and **HTM-X'** and/or 3-bromophenol for **HTM-FX'** and **HTM-X'**. All compounds in the **HTM** series were prepared in merely two reaction steps under relatively benign reaction conditions and a single column purification step. By contrast, the **spiro-OMeTAD** core alone requires a multi-step synthesis involving air and moisture-sensitive reagents, hazardous lithiation reactions and several time-consuming column chromatographic purification steps.⁶⁸

Scheme 4-1 Synthetic scheme for **HTM** series.



4.2.3 Electrochemical and photophysical characterization

Cyclic voltammograms (CVs) for each HTM were recorded in 0.1 M *n*-NBu₄PF₆ DCM solutions to determine the E_{HOMO} for the series (Table 4-2 and Figure 4-4). The E_{HOMO} values for

HTMs bearing TPAs on the fluorene (**X60**, **HTM-F** and **HTM-FX'**) were all found to be ~ 0.66 V vs NHE, which is slightly more positive than **spiro-OMeTAD** (0.63 V vs NHE) and therefore appropriate for energy alignment with the perovskite layer.

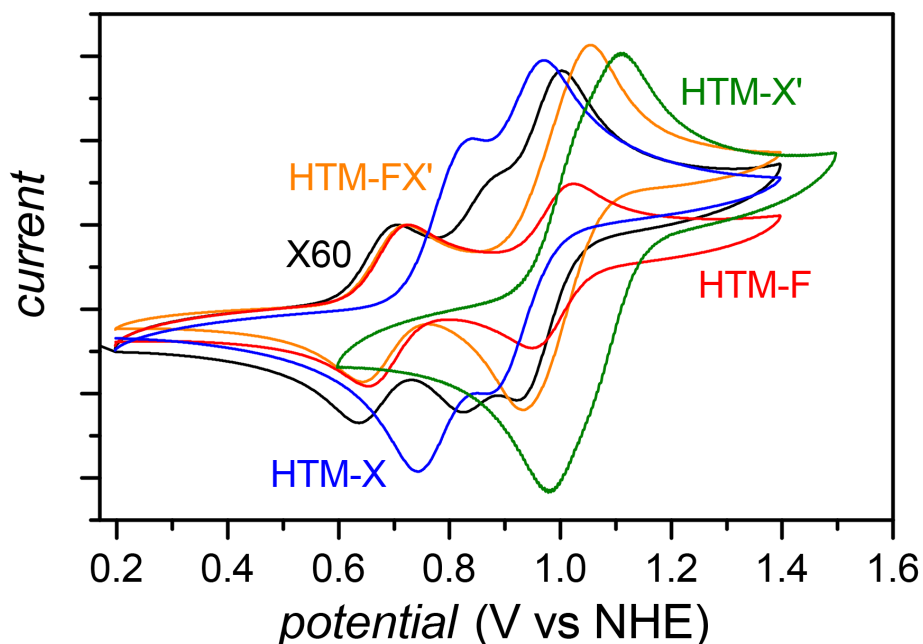


Figure 4-4 Cyclic voltammograms of **HTM** series in 0.1 M $n\text{-NBu}_4\text{PF}_6$ DCM solutions, with a polished Pt working electrode, Pt wire counter electrode and Ag/AgCl reference electrode.

Table 4-2 Electrochemical, bulk thermal and electrical properties of **HTM** series

Compound	E_{HOMO}^a (V vs NHE)	ϵ_{HOMO}^b (eV)	T_g^c ($^{\circ}\text{C}$)	Hole Mobility ($\times 10^{-4} \text{ cm}^2 \text{ V}^{-1} \text{ s}^{-1}$) ^d
Spiro-OMeTAD	0.63	-5.13	125	6.9
X60	0.67	-5.17	107	1.4
HTM-F	0.67	-5.17	104	0.4
HTM-X	0.76	-5.26	94	0.5
HTM-FX'	0.66	-5.16	137	4.8
HTM-X'	0.97	-5.47	130	0.3

^a The half-wave potential corresponding to the first oxidation process in the cyclic voltammogram. Measured in DCM and referenced to NHE by addition of ferrocene. ^b $\epsilon_{HOMO} = -(E_{HOMO} + 4.50 \text{ eV})$. ^c Determined by differential scanning calorimetry (DSC). All T_m values determined to be >300 $^{\circ}\text{C}$ and above the detection limits of the instrument. ^d Determined by space-charge-limit current (SCLC) method from doped HTMs.

Differential pulse voltammetry (DPV) was used to deconvolute and quantify each of the successive oxidation events for the series (Figure 4-5 and Table 4-3). The number of oxidation events tracked the number of TPA units on the HTM, and we were able to assign the redox activity to specific TPA units by taking a number of different observations into account. For example, the E_{HOMO} levels for the HTMs with only *para*- or *meta*-substituted xanthene TPAs (**HTM-X** and **HTM-X'**, respectively) are higher than that of the HTM with only fluorene TPAs (**HTM-F**) and reflect a lower degree of electronic coupling based on successive oxidation of their two TPA groups (Figure 4-5a). This conjecture is fully supported by the trend in computed ϵ_{HOMO} values (Table 4-3). The first reduction potentials (E_{HOMO}) for **X60** and **HTM-FX'** can therefore be linked to the first oxidations of the fluorene TPAs (E_{F1}), in that the first oxidation event of **X60** and **HTM-FX'** matches that measured for **HTM-F** (0.67 V vs NHE). The second oxidation event for **X60** at 0.87 V vs NHE is attributed to the first oxidation of the xanthene TPAs (E_{X1}) by benchmarking against **HTM-X** (0.78 V vs NHE). The third and fourth oxidation events of **X60** are assigned using the second Faradaic events for **HTM-F** (E_{F2}) and **HTM-X** (E_{X2}) according to their electronic coupling ($\Delta E_{1/2}$ in Figure 4-5) with the first two oxidations. Similarly, all four oxidation events for **HTM-FX'** have been resolved even though the second, third and fourth oxidation features overlapped significantly and appeared to be a three-electron process (0.8 to 1.1 V vs NHE). My assignments of the redox activity for each TPA unit, which were corroborated by modeling the degree of hole delocalization of the cationic HTM species (Figure 4-3), clearly show that the redox activity relevant to the HOMO level is confined to the TPA groups appended to the fluorene units for **X60** and **HTM-FX'**. This finding indicates that the xanthene units can be modified without compromising the E_{HOMO} levels corresponding to the fluorene TPA units.

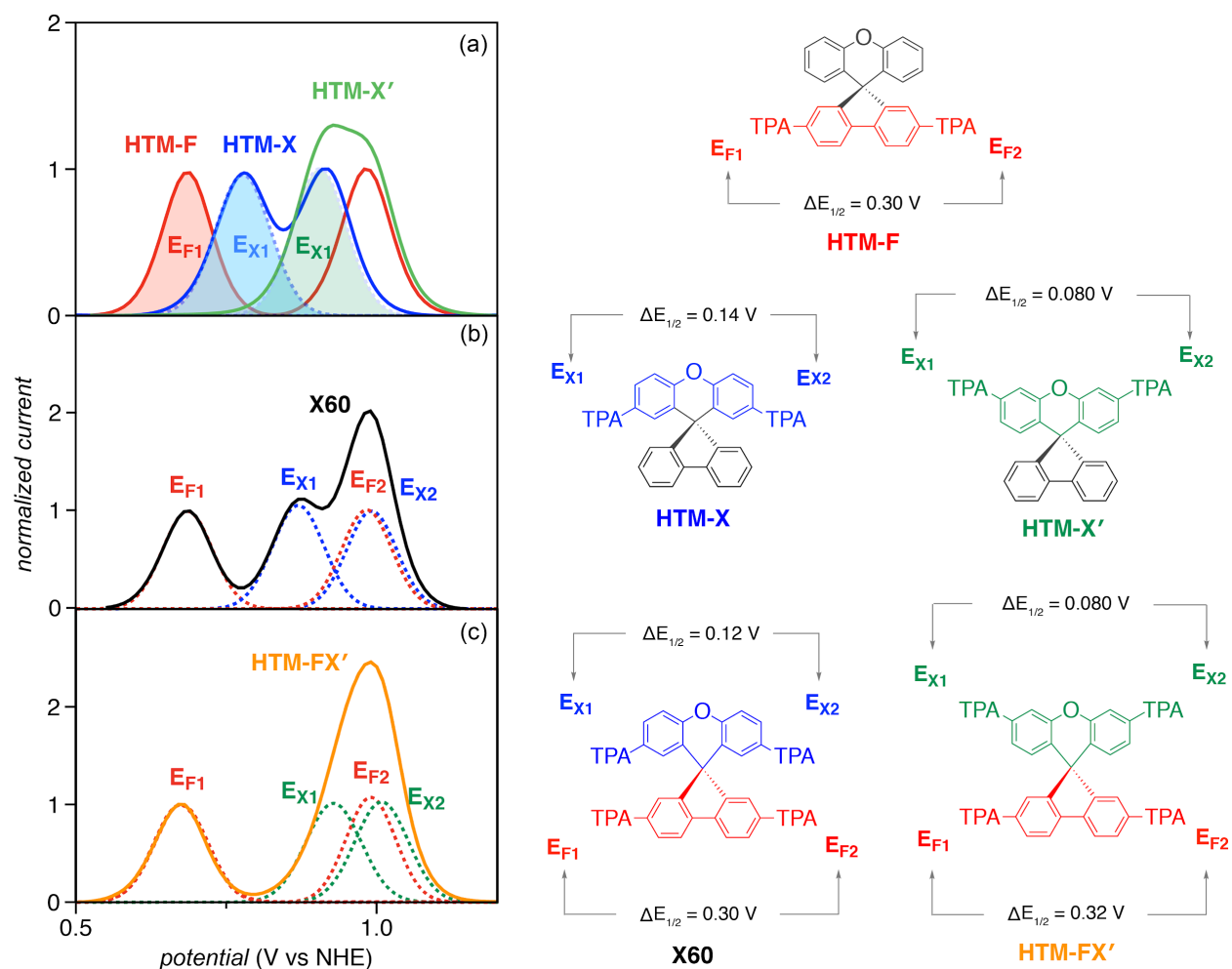


Figure 4-5 Differential pulse voltammograms (DPVs) for HTM series normalized in amplitude to their first oxidation event. The number of electrons that contribute to each redox process was determined by integrating the area beneath the peak fitting. (a) The first deconvoluted oxidation events are shown in shaded colors to highlight the progressively anodic shift of E_{HOMO} for **HTM-F** (red), **HTM-X** (blue) and **HTM-X'** (green), respectively. Traces for (b) **X60** (black) and (c) **HTM-FX'** (orange) are deconvoluted to highlight that the E_{HOMO} is linked to the TPA unit positioned on the fluorene unit.

Table 4-3 Summary of DPV oxidation peaks for **HTM** series

Compound	E_{F1} (V vs NHE)	E_{F2}	$\Delta E_{1/2}$ (mV)	E_{X1} (V vs NHE)	E_{X2}	$\Delta E_{1/2}$ (mV)
X60	0.685	0.983	297	0.869	0.991	122
HTM-F	0.685	0.982	296	-	-	-
HTM-X	-	-	-	0.777	0.915	138
HTM-FX'	0.672	0.989	317	0.927	1.007	80
HTM-X'	-	-	-	0.905	0.987	82

The similar UV-visible absorption and emission maxima (Figure 4-6 and Table 4-4) of **X60**, **HTM-F**, and **HTM-FX'** confirm the similar electronic structures of the compounds' frontier orbitals. All HTMs under study exhibit limited light absorption in the visible region which may be beneficial in maximizing light absorption by the perovskite layer (Figure 4-6a).

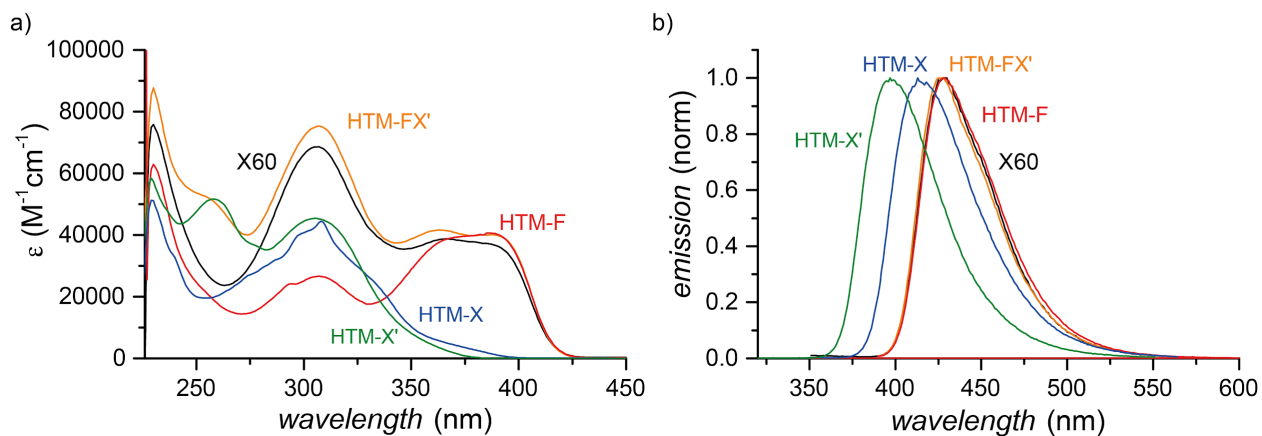


Figure 4-6 (a) UV-Vis absorption spectra for **HTM** solutions (2.0×10^{-5} M) recorded in DCM. (b) Emission spectra for **HTM** series recorded in DCM excited at lowest energy absorption band recorded in Table 4-4.

Table 4-4 Summary of spectroscopic and electrochemical properties for **HTM** series.

Compound	λ_{\max}^a (nm)	λ_{em}^b (nm)	$E_{\text{HOMO-LUMO}}^c$ (eV)
X60	392, 305	428	2.97
HTM-F	391, 307	428	3.07
HTM-X	308	413	2.97
HTM-FX'	398, 304	428	3.02
HTM-X'	304	396	3.02

^a Absorption maximum for HTM in DCM. ^b Excitation at higher energy λ_{\max} . ^c Determined from the intersection point of absorption and emission spectra.

4.2.4 Bulk thermal properties

The melting point (T_m) and T_g of each HTM measured by differential scanning calorimetry (DSC) are tabulated in Table 4-2. The T_m and T_g values for every member of the series were measured to be >300 °C and >93 °C, respectively. A T_g value higher than 90°C is required to avoid morphology changes during solar cell operation.⁴⁹ There is no apparent trend between number of TPA units and glass transition temperature (e.g., T_g (**X60**) = 107 °C *c.f.* T_g (**HTM-F**) = 104 °C). However, substitution at the *meta*-position of the xanthene moiety was found to increase T_g by over 30 °C (e.g., T_g (**HTM-X'**) = 130 °C *c.f.* T_g (**HTM-X**) = 94 °C). This striking increase in T_g through *meta*-substitution of the xanthene was also observed in the case of **HTM-FX'** (T_g = 137 °C *c.f.* 107 °C for **X60**).

4.2.5 Electrical properties

The current-voltage (J - V) characteristics of “hole-only” devices with various HTMs are shown in Figure 4-7a and are used to determine the hole mobilities of the HTMs under study. The HTMs are doped with tBP and LiTFSI. The hole mobilities tabulated in Table 4-2 were determined

using the space-charge-limited current (SCLC) method. The mobilities of **spiro-OMeTAD**, **X60** and **HTM-FX'** obtained here are comparable to the previous reported values.^{23,115,119} The mobility of **HTM-FX'** is close to that of **spiro-OMeTAD** and is much higher than that of all other HTM compounds in the series under study. While the E_{HOMO} level of **HTM-FX'** is similar to **X60**, the higher mobility is ascribed to the *meta*-substitution affecting the chemical structure or electronic delocalization. The low hole mobilities of **HTM-X** and **HTM-X'** may be due to the E_{HOMO} levels being too stabilized for efficient doping by LiTFSI. Given that the extent of hole doping for **HTM-F** and **X60** by LiTFSI is expected to be similar based on the similarities in E_{HOMO} , the low mobility of **HTM-F** is attributed to the higher E_{reorg} value (0.21 eV) relative to the other HTMs (<0.16 eV).

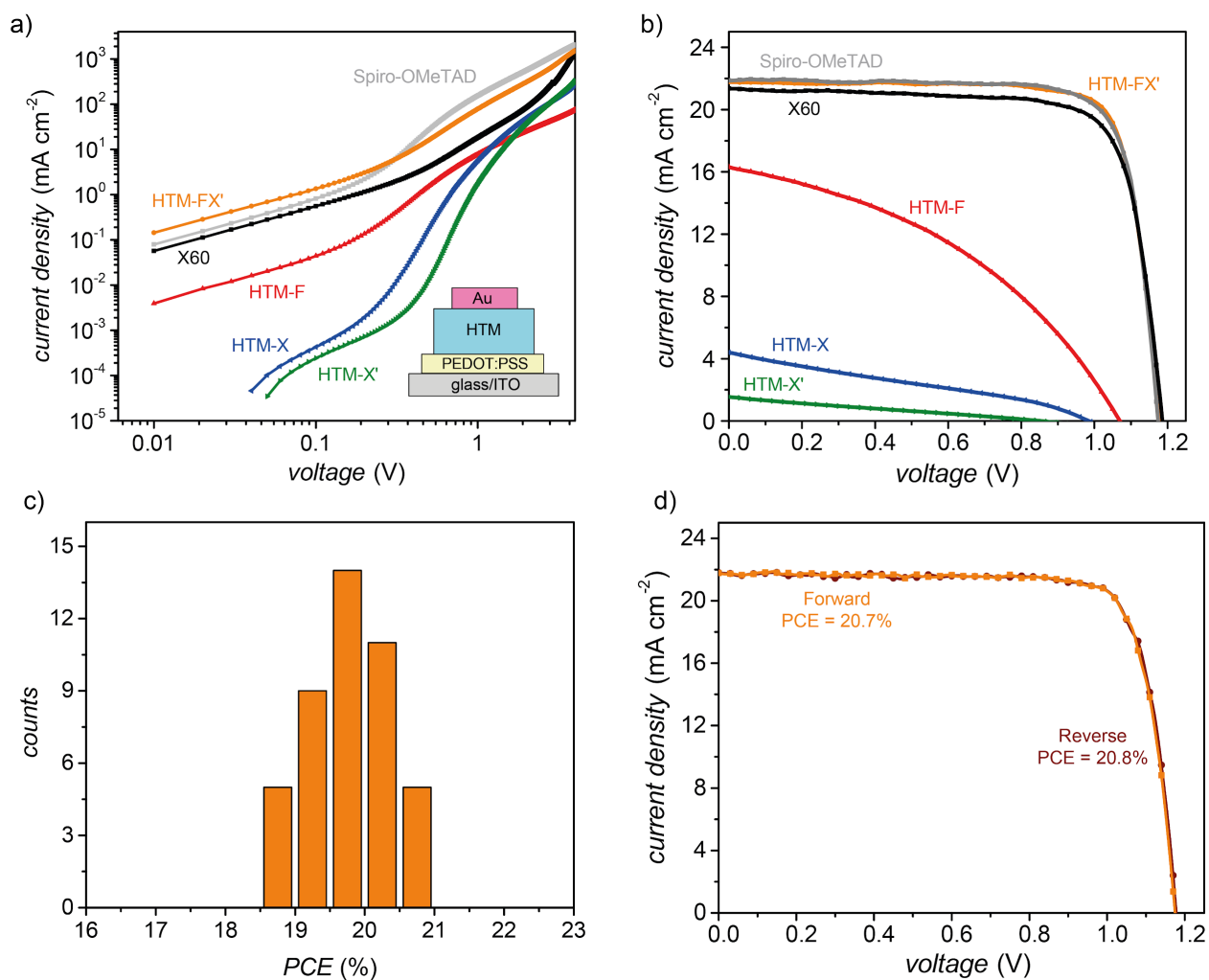


Figure 4-7 Performance of perovskite solar cells with HTMs: (a) J - V curves of hole-only devices with **HTM** series; (b) J - V curves of solar cells with **HTM** series measured under solar simulator (100 mW cm^{-2}); (c) Histogram of PCEs for 44 devices with **HTM-FX'**; (d) J - V curves of champion device with **HTM-FX'** scanned in reverse and forward directions (scanning rate of 20 mV/s).

The HTMs exhibited similar charge extraction kinetics and effective photoluminescence quenching for all HTMs as revealed by time-resolved and steady-state photoluminescence (PL) measurements (Figure 4-7). Hole extraction from the perovskite layer to each of the HTMs in this study was not found to be a limiting factor, except for **HTM-X'** which showed incomplete PL quenching (Figure 4-7a and c). The HTMs exhibit similar charge extraction kinetics between **spiro-OMeTAD**, **X60**, and **HTM-FX'** (Figure 4-7b) while the initial PL decay rates in HTMs with only two TPA moieties follow the trend of **HTM-F** > **HTM-X** > **HTM-X'**.

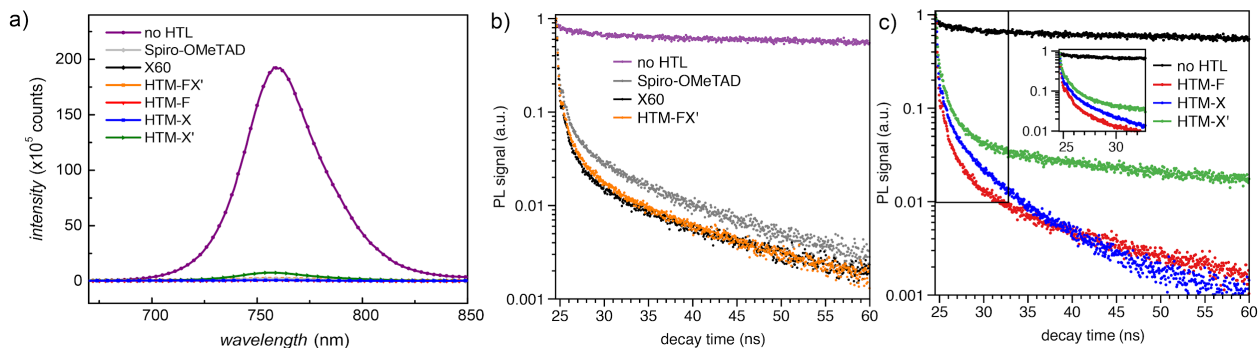


Figure 4-8 (a) Steady-state PL and (b) time-resolved PL decay of perovskite films with **spiro-OMeTAD**, **X60** and **HTM-FX'** and (c) time-resolved PL decay of perovskite films with **HTM-F**, **HTM-X** and **HTM-X'**.

4.2.6 Perovskite solar cell characterization

Each of the HTMs were then tested in planar PSCs with the device architecture: glass/ITO/TiO₂-Cl/perovskite/HTM/Au by Dr. Hairen Tan of the Sargent group at the University of Toronto. Table 4-5 summarizes the statistical performance of devices fabricated with otherwise-identical device processing for each HTM, and the *J-V* curves of champion devices for each HTM are shown in Figure 4-7b. Champion PCE values indicate the maximum power conversion efficiency achieved with a single device. PSCs containing **HTM-F**, **HTM-X**, and **HTM-X'** all generated low PCE values. This observation is attributed to the low hole mobilities (Figure 4-7a) precluding effective transport of carriers through the HTM layers. **X60** results in PCEs that are lower than **spiro-OMeTAD** and the best device yielded a PCE of 19.5% which is comparable to a previous report.²³ **HTM-FX'** exhibited slightly higher PCEs than **X60** (20.8% vs 19.5%, respectively) and the small performance enhancement can be attributed to the higher hole mobility imparted by the change of TPA substitution pattern on the xanthene unit (4.8 vs 1.4×10^{-4} cm²V⁻¹s⁻¹, respectively). **HTM-FX'** produced a device performance that rivals that of **spiro-OMeTAD**. PSCs containing **HTM-FX'** exhibit excellent reproducibility, as indicated by the

narrow PCE distribution over 44 devices (Figure 4-7c). Moreover, PSCs containing **HTM-FX'** also show negligible hysteresis in the J - V measurements (Figure 4-7d). These results highlight that *meta*-substitution of the xanthene groups to be an important handle for achieving high-efficiency PSCs.

Table 4-5 Device characteristics for perovskite solar cells containing **HTM** series.

Compound	V_{oc} (V)	J_{sc} (mA cm ⁻²)	FF (%)	PCE (%)	Champion PCE (%)
Spiro-OMeTAD	1.16 ± 0.02	21.9 ± 0.3	77.7 ± 1.7	19.7 ± 0.5	20.4
X60	1.16 ± 0.01	21.2 ± 0.3	74.0 ± 2.3	18.2 ± 0.7	19.5
HTM-FX'	1.17 ± 0.01	21.7 ± 0.3	77.5 ± 2.0	19.7 ± 0.6	20.8
HTM-F	1.08 ± 0.02	14.7 ± 0.9	40.6 ± 1.9	6.5 ± 0.5	7.0
HTM-X	0.88 ± 0.11	3.8 ± 0.6	31.6 ± 2.2	1.1 ± 0.2	1.3
HTM-X'	0.77 ± 0.06	1.4 ± 0.1	26.1 ± 1.3	0.2 ± 0.1	0.3

Statistical performance of 41 **spiro-OMeTAD** devices, 24 **X60** devices, 44 **HTM-FX'** devices, 8 **HTM-F** devices, and 4 devices for each **HTM-X** and **HTM-X'**, is shown here.

4.3 Conclusion

Breaking the symmetric core of **spiro-OMeTAD** by replacing one of the two fluorene units with a xanthene unit to form **X60**²³ enabled us to experimentally resolve how the positions of TPA groups about the core affect the redox properties and glass transition temperatures of HTMs relevant to high efficiency PSCs. TPA groups positioned on the highly conjugated fluorene moiety

renders the HTM easier to oxidize, which, in turn, increases the free energy change for hole-extraction from the perovskite layer. The glass transition temperatures, however, are governed by the TPAs about the xanthene unit: substitution at the *meta*-position raises the T_g by 30 °C over those substituted at the *para*-position. The synergistic effects of a positively shifted E_{HOMO} and high glass transition temperature in **HTM-FX'** yielded a device power conversion efficiency of 20.8%, which is commensurate with current state-of-the-art PSCs. Electrochemical, photophysical and structural findings were fully supported by computational analysis of the frontier orbitals and reorganization energies of the neutral HTMs and spin density difference maps of cationic species, thereby highlighting the role predictive tools can play in screening future state-of-the-art HTMs. This set of design principles that enables selective control of redox and mesoscopic properties will be elaborated on in future chapters in pursuit of robust higher performance PSCs and can be used to inform the rational design and accelerated discovery of high efficiency materials with robust performance during cell operation.

4.4 Experimental

4.4.1 Computational screening

Up to 20 conformers were generated for each molecule using MMFF94 force field¹²⁰ with the RDKit package.¹²¹ Each conformer was then used as the starting point for a set of DFT calculations. Geometry optimizations were performed at both the B3LYP/6-31G(d) and BP86/def2-SVP levels of theory. The HOMO and LUMO levels were calculated at the B3LYP/6-311+G(d,p) level of theory at the B3LYP/6-31G(d) minima. These gaps are shown in Table 4-1. Vertical excitation energies were obtained using time-dependent (TD) DFT at the B3LYP/def2-TZVP, CAM-B3LYP/def2-TZVP, ω B97X-D/def2-TZVP and levels of theory, with the first 15

states obtained. The resulting spectra are plotted in Figure A4-11. Reorganization energy (E_{reorg}) for hole transfer were calculated using the Nelsen four point method^{23,116,117} at both the B3LYP/6-31G(d) and ω B97X-D/6-31G(d) levels of theory:

$$E_{\text{reorg}} = [M^+(0) - M(0)] + [M^+(+) - M(+)] \quad \text{(Equation 4-1)}$$

Where $M(0)$ and $M(+)$ are the neutral and oxidized HTMs with a neutral geometry and $M^+(0)$ and $M^+(+)$ are the neutral and oxidized HTMs with the oxidized geometry.

In addition, the HOMO and LUMO orbitals were obtained for the neutral molecules and spin density differences were determined for the radical cations at both the neutral and the cation minimum geometry. The ground state electronic structure energy calculations were performed with the QChem 4.2 suite.¹²² The excited-state calculations for the modeled UV-Vis spectra, the orbital plots and the spin density difference maps were generated with Gaussian09, revision D.01¹²³ with VMD employed for visualization.¹²⁴

4.4.2 Synthesis

All reagents were obtained from MilliporeSigma, Alfa Aesar or Fisher Scientific and used as received. All reactions were performed using toluene from a solvent purification system. Standard inert atmosphere and Schlenk techniques were carried out under nitrogen. All reactions and purification were carried out in the dark. Purification by column chromatography was performed using silica (Silicycle: Ultrapure Flash Silica). Analytical thin-layer chromatography (TLC) was performed on aluminum-backed sheets pre-coated with silica 60 F-254 adsorbent (250 μm thick; Silicycle, QC, Canada) and visualized under UV light. Routine ^1H and ^{13}C NMR spectra were collected on a Bruker AV400 inv/dir instrument at ambient temperatures, operating at 300 MHz and 100 MHz, for ^1H and ^{13}C nuclei, respectively. Chemical shifts (δ) are reported in parts per million (ppm) using the residual signals δ 7.26 and 77.0 for CDCl_3 , δ 2.05 and 29.8 for acetone-

δ 2.50 and 39.4 for DMSO- d_6 as internal references for ^1H and ^{13}C , respectively. Standard abbreviations indicating multiplicity are used as follows: s = singlet; d = doublet; t = triplet; m = multiplet.

Br4-FX (2,2',7,7'-tetrabromospiro[fluorene-9,9'-xanthene]): 2,7-dibromo-9-flourenone (1.08 g, 3.20 mmol), 4-bromophenol (5.53 g, 32.0 mmol) and methane sulfonic acid (0.82 mL, 12.8 mmol) were mixed at 140 °C for 18 h under N_2 . The reaction mixture was cooled to room temperature and product was precipitated with the addition of MeOH. Separation by filtration and rinsing with MeOH yielded 2.09 g (96.5%) of product as white powder. ^1H NMR (400 MHz, CDCl_3): δ = 8.01 (d, 2H, J = 8.1 Hz), 7.69 (dd, 2H, J = 8.2, 1.8 Hz), 7.49 (dd, 2H, J = 8.8, 2.4 Hz), 7.44 (d, 2H, J = 1.7 Hz), 7.31 (d, 2H, J = 8.8 Hz), 6.53 (d, 2H, J = 2.4 Hz). ^{13}C NMR (100 MHz, CDCl_3): δ = 155.5, 150.0, 137.6, 132.2, 130.4, 129.0, 124.8, 122.9, 122.0, 119.2, 116.2. HRMS (EI): m/z = 643.76141 [M^+] (calcd for $[\text{C}_{25}\text{H}_{12}\text{OBr}_4]^+$: m/z = 643.76216).

Br4-FX' (2,3',6',7-tetrabromospiro[fluorene-9,9'-xanthene]): Compound was prepared following a modified literature procedure for **Br4-X**. ^1H NMR (400 MHz, CD_2Cl_2): δ = 7.73 (d, 2H, J = 8.2 Hz), 7.60 (dd, 2H, J = 8.2, 1.8 Hz), 7.38 (dd, 2H, J = 8.8, 2.4 Hz), 7.28 (d, 2H, J = 1.8 Hz), 7.17 (d, 2H, J = 8.8 Hz), 6.49 (d, 2H, J = 2.4 Hz). ^{13}C NMR (100 MHz, CD_2Cl_2): δ = 156.1, 150.5, 138.2, 132.6, 132.6, 130.8, 129.4, 125.2, 123.2, 122.6, 119.6, 116.4. HRMS (EI): m/z = 643.76192 [M^+] (calcd for $[\text{C}_{25}\text{H}_{12}\text{OBr}_4]^+$: m/z = 643.76216).

Br2-F (2,7-dibromospiro[fluorene-9,9'-xanthene]): Compound was prepared following a modified literature procedure for **Br4-X**. ^1H NMR (400 MHz, CDCl_3): δ = 7.63 (d, 2H, J = 8.1 Hz), 7.50 (dd, 2H, J = 8.1, 1.8 Hz), 7.31 – 7.13 (m, 6H), 6.92 – 6.78 (m, 2H), 6.38 (dt, 2H, J = 7.8, 1.1 Hz). Characterization data has been previously reported.¹²⁵

Br2-X (2',7'-dibromospiro[fluorene-9,9'-xanthene]): Compound was prepared following a modified literature procedure for **Br4-X**. ¹H NMR (400 MHz, CDCl₃): δ = 7.93 – 7.79 (m, 2H), 7.44 (tt, 2H, *J* = 7.5, 1.2 Hz), 7.35 – 7.24 (m, 6H), 7.15 (dd, 2H, *J* = 14.5, 1.0 Hz), 6.49 (dd, 2H, *J* = 2.4, 1.0 Hz). HRMS (EI): *m/z* = 487.94118 [M⁺] (calcd for [C₂₅H₁₄O₇Br₂]⁺: *m/z* = 487.94114).

Br2-X' (3',6'-dibromospiro[fluorene-9,9'-xanthene]): Compound was prepared following a modified literature procedure for **Br4-X**. ¹H NMR (400 MHz, CDCl₃): δ = 7.80 (dt, 2H, *J* = 7.6, 0.9 Hz), 7.49 – 7.34 (m, 4H), 7.23 (td, 2H, *J* = 7.5, 1.1 Hz), 7.12 (dt, 2H, *J* = 7.6, 0.9 Hz), 6.91 (dd, 2H, *J* = 8.4, 2.0 Hz), 6.26 (d, 2H, *J* = 8.4 Hz). ¹³C NMR (101 MHz, CDCl₃): δ = 154.4, 151.7, 139.7, 129.5, 128.8, 128.4, 127.0, 125.7, 123.9, 121.2, 120.3, 120.1, 77.5, 77.2, 76.8, 53.7. HRMS (EI): *m/z* = 487.94119 [M⁺] (calcd for [C₂₅H₁₄O₇Br₂]⁺: *m/z* = 487.94114).

X60 (N₂,N₂,N₂',N₂',N₇,N₇,N₇',N₇'-octakis(4-methoxyphenyl)spiro[fluorene-9,9'-xanthene]-2,2',7,7'-tetraamine): bis(4-methoxyphenyl)amine (1.14 g, 5.00 mmol), **Br4-FX** (0.678 g, 1.00 mmol), palladium acetate (0.018 g, 0.080 mmol), tri-*tert*-butylphosphine (0.018 g, 0.080 mmol) and potassium *tert*-butoxide (0.45 g, 5.0 mmol) were added to toluene (15 mL) under N₂. The reaction mixture was stirred at reflux for 16 h. The reaction mixture was cooled to room temperature. Purification by silica column chromatography (SiO₂: hexanes/EtOAc, 4:1; *R_f* = 0.24) yielded 0.731 g (59.2%) of product as pale green solid. ¹H NMR (400 MHz, CDCl₃): δ = matched literature. ¹³C NMR (100 MHz, CDCl₃): δ = 155.7, 155.4, 154.9, 147.8, 146.8, 143.3, 141.7, 141.4, 133.1, 125.6, 125.5, 124.4, 124.2, 122.8, 121.9, 119.8, 118.7, 117.4, 114.6, 114.5, 55.6, 54.4. HRMS (ESI): *m/z* = 1241.5085 [M+H]⁺ (calcd for [C₈₁H₆₉N₄O₉]⁺: *m/z* = 1241.5065).

HTM-FX' (N₂,N₂,N₃',N₃',N₆',N₆',N₇,N₇'-octakis(4-methoxyphenyl)spiro[fluorene-9,9'-xanthene]-2,3',6',7'-tetraamine): Compound was prepared following a modified literature procedure for **X60**.^{23,119} Purification by silica column chromatography (SiO₂: hexanes/EtOAc, 5:1;

$R_f = 0.21$) yielded product as pale green solid in 78.2% yield. ^1H NMR (400 MHz, acetone- d_6): $\delta = 7.50$ (d, 2H, $J = 9.0$ Hz), 7.05 – 6.96 (m, 8H), 6.95 – 6.84 (m, 16H), 6.78 (dd, 12H, $J = 7.9, 4.4$ Hz), 6.41 (dd, 2H, $J = 8.5, 2.4$ Hz), 6.38 – 6.31 (m, 4H), 3.75 (d, 24H, $J = 3.4$ Hz). ^{13}C NMR (100 MHz, acetone- d_6): $\delta = 157.3, 156.8, 156.7, 152.6, 149.8, 148.9, 141.8, 141.3, 133.6, 128.7, 127.7, 126.8, 121.3, 120.6, 118.8, 118.0, 116.0, 115.6, 115.4, 107.7, 55.7, 55.7, 54.2$. HRMS (ESI): $m/z = 1240.4988$ [M] $^+$ (calcd for [$\text{C}_{81}\text{H}_{68}\text{N}_4\text{O}_9$] $^+$: $m/z = 1240.4986$).

HTM-F (N2,N2,N7,N7-tetrakis(4-methoxyphenyl)spiro[fluorene-9,9'-xanthene]-2,7-diamine): Compound was prepared following a modified literature procedure for **X60**.²³ ^1H NMR (400 MHz, CDCl_3): $\delta = 7.46 - 7.40$ (m, 2H), 7.15 (ddd, 2H, $J = 8.5, 7.1, 1.6$ Hz), 7.06 (dd, 2H, $J = 8.2, 1.3$ Hz), 6.94 – 6.80 (m, 14H), 6.75 – 6.63 (m, 8H), 6.60 (dd, 2H, $J = 7.8, 1.6$ Hz), 3.75 (s, 12H).

HTM-X (N2',N2',N7',N7'-tetrakis(4-methoxyphenyl)spiro[fluorene-9,9'-xanthene]-2',7'-diamine): Compound was prepared following a modified literature procedure for **X60**.²³ ^1H NMR (400 MHz, CDCl_3): $\delta = 7.55$ (d, 2H, $J = 7.5$ Hz), 7.26 – 7.14 (m, 8H), 7.02 (d, 2H, $J = 8.9$ Hz), 6.79 – 6.67 (m, 8H), 6.60 (d, 6H, $J = 9.0$ Hz), 6.06 (d, 2H, $J = 2.8$ Hz), 3.72 (s, 12H). ^{13}C NMR (100 MHz, CDCl_3): $\delta = 155.1, 155.0, 146.6, 143.5, 141.2, 139.7, 128.0, 127.6, 125.4, 125.0, 122.3, 121.4, 120.1, 117.2, 114.4, 55.6, 54.7$. HRMS (ESI): $m/z = 786.3083$ [$\text{M}+\text{H}$] $^+$ (calcd for [$\text{C}_{53}\text{H}_{42}\text{N}_2\text{O}_5$] $^+$: $m/z = 786.3094$).

HTM-X' (N3',N3',N6',N6'-tetrakis(4-methoxyphenyl)spiro[fluorene-9,9'-xanthene]-3',6'-diamine): Compound was prepared following a modified literature procedure for **X60**.²³ ^1H NMR (400 MHz, CDCl_3): $\delta = 7.75$ (dt, 2H, $J = 7.5, 1.0$ Hz), 7.34 (m, 2H), 7.24 – 7.23 (m, 4H), 7.03 (d, 8H, $J = 8.9$ Hz), 6.79 (d, 8H, $J = 8.9$ Hz), 6.59 (d, 2H, $J = 2.4$ Hz), 6.31 (dd, 2H, $J = 8.6, 2.4$ Hz), 6.14 (d, 2H, $J = 8.6$ Hz), 3.77 (s, 12H). ^{13}C NMR (100 MHz, CDCl_3): $\delta = 156.2, 155.5, 152.1, 148.7, 140.6, 139.8, 128.3, 128.1, 127.6, 127.2, 125.8, 119.9, 116.4, 115.1, 114.8, 106.9, 77.5,$

77.2, 76.8, 55.6). HRMS (ESI): $m/z = 786.3089$ [M+H]⁺ (calcd for [C₅₃H₄₂N₂O₅]⁺: $m/z = 786.3094$).

4.4.3 Electrochemical and photophysical properties

Solution-phase UV-Vis absorption spectra were collected on a Cary 5000 spectrophotometer. Photoluminescence spectra were recorded with a Cary Eclipse fluorimeter. All samples were measured in a 1-cm quartz cell at room temperature in HPLC grade DCM. The concentrations of the DCM solutions of analytes for UV-Vis and photoluminescence measurements were approximately $2 \times 10^{-5} \text{ mol}\cdot\text{L}^{-1}$ and $1 \times 10^{-5} \text{ mol}\cdot\text{L}^{-1}$, respectively. Solution-phase electrochemical data were recorded with a CHI660D potentiostat at room temperature using a platinum wire counter electrode and a platinum working electrode. Ag/AgCl in saturated KCl was used as the reference electrode and was calibrated versus the normal hydrogen electrode (NHE) by the addition of Fc⁺/Fc. A 0.1 M *n*-NBu₄PF₆ electrolyte solution in DCM was used for all HTMs. CV data were acquired for 0.5 mM solutions of each HTM at a scan rate of 50 mV s⁻¹. DPV data were collected with the same instrument, electrodes and electrolyte conditions with an amplitude of 0.05 V, a pulse width of 0.05 s, sampling period of 0.5 s and pulse period of 0.5 s.

4.4.4 Bulk thermal properties

DSC curves of compounds were collected using a Netzsch DSC 214 Polyma instrument under a nitrogen protective atmosphere. For each measurement, two aluminum crucibles were used, one for material measurement and the other as empty reference. A customized heating program was developed to include a 5 min hold at the initial temperature of 50 °C, and four continuous cycles between to 50 °C and 300 °C with a heating/cooling rate of 10 K/min and 5 min holds at 50 °C

and 300 °C. Data from the heating segment of last 3 cycles were used to identify the T_m and extrapolate the T_g of the material.

4.4.5 Electrical properties

The hole-only devices were fabricated with a structure of glass/ITO/PEDOT:PSS/HTMs/Au according to previous literature.²⁰ The HTMs were doped with tBP and LiTFSI. The dopant concentration was kept constant for all HTMs and the same as used in PSCs. Hole mobility was investigated by the space-charge-limit current (SCLC) method, which can be described as the following equation: $\mu = (8d^3J)/(9\epsilon_0\epsilon_rV^2)$, where μ is the hole mobility, J is the current density, ϵ_0 is the vacuum permittivity, ϵ_r is the dielectric constant of the material (normally taken to approach 3 for organic semiconductors), V is the applied bias, and d is the film thickness.¹¹⁵ The applied bias was measured from 0 to 5 V.

Current density-voltage (J - V) characteristics were measured using a Keithley 2400 source meter under illumination of a solar simulator (Newport, Class A) at the light intensity of 100 mW cm⁻² as verified using a certified reference solar cell (Newport). A spectral mismatch factor of 1 was used for all J - V measurements. Unless otherwise stated, the instantaneous J - V curves were measured with a scanning rate of 50 mV s⁻¹ (voltage step of 10 mV and delay time of 200 ms) from 1.2 V to -0.1 V. The active area was determined using an aperture shade mask (0.049 cm²) placed in front of the solar cell to avoid overestimation of the photocurrent density. No excess encapsulation or preconditioning procedure was used.

4.4.6 Perovskite solar cell characterization

The planar perovskite solar cells were fabricated according to previous work.²⁰ Briefly, pre-patterned indium tin oxide (ITO) coated glass substrates were sequentially cleaned using detergent,

acetone, and isopropanol. The TiO₂-Cl electron transport layers were spin-coated on ITO substrates from the colloidal nanocrystal solutions, and annealed on a hot plate at 150 °C for 30 min in ambient air. After the substrates had cooled, substrates were transferred immediately to a nitrogen-filled glovebox for the deposition of perovskite films. The Cs_{0.05}FA_{0.81}MA_{0.14}PbI_{2.55}Br_{0.45} precursor solution (1.4 M) was prepared in a mixed solvent of DMF and DMSO with a volume ratio of 4:1. The molar ratios of PbI₂/PbBr₂ and FAI/MABr were both fixed at 0.85:0.15, molar ratio of CsI/(FAI+MABr) is 0.05:0.95, and the molar ratio of (FAI+MABr+CsI)/(PbI₂+PbBr₂) was fixed at 1:1. The perovskite films were deposited onto the TiO₂-Cl substrates with two-step spin coating procedures. The first step was 2000 rpm for 10 s with an acceleration of 200 rpm/s. The second step was 6000 rpm for 20 s with a ramp-up of 2000 rpm/s. Chlorobenzene (100 μL) was dropped on the spinning substrate during the second spin-coating step at 10 s before the end of the procedure. The substrate was then immediately transferred on a hotplate and heated at 100 °C for 20 min. After cooling down to room temperature, the hole-transport layer was subsequently deposited on top of the perovskite film by spin coating at 4000 rpm for 30 s using a chlorobenzene solution which contained 72.3 mg/mL of HTMs and 28.8 μL/mL of tBP, as well as 17.5 μL/mL of LiTFSI (520 mg/mL in acetonitrile). Finally, 100 nm Au contact was deposited on top of the HTM film by electron-beam evaporation in an Angstrom Engineering deposition system.

Chapter 5 : Polymerizable Hole-Transport Materials for Improved Moisture Stability of Perovskite Solar Cells

5.1 Introduction

There are many challenges that remain for perovskite solar cells (PSCs) to be a commercially-deployed technology.^{2,3} One key challenge is the sensitivity of the photo-active perovskite layer to water. Water drives the conversion of the 3-dimensional AMX_3 structure into 2-dimensional monohydrate sheets (i.e., $AMX_3 \cdot H_2O$) and eventually into isolated dihydrate octahedra formulated as $A_2MX_6 \cdot 2H_2O$ (Equations 2-3 and 2-4).⁶ One solution to this problem is to encapsulate the PSC to simply prevent water from entering the device. Hwang and coworkers achieved negligible decreases in the PCEs of PSCs over 30 days in ambient environment by coating the entire solar cell with hydrophobic Teflon (polytetrafluoroethylene, PTFE) ¹²⁶ while Dong *et al.* demonstrated the use of silica (SiO_2) encapsulation of PSCs for stabilized PCEs in 65% humid environments.¹²⁷ The use of carbon films,¹²⁸ epoxy resins,¹²⁹ and HTM design for PSC encapsulation have also been investigated as engineering approaches to improving PSC stability. All these approaches add extra components and weight to the solar cell.

One potentially powerful approach is to use polymeric HTM films to preclude water from reaching the perovskite layer. Kelly *et al.* investigated the use of hole-transporting **P3HT** nanowires in hydrophobic **PMMA** matrices as the HTM layer of a PSC and saw improved stability of devices in liquid phase stability studies.¹² Others have employed **PEDOT:PSS** mixtures as the hole-transporting layer. ^{43,130} Solution deposition of polymers can be challenging, however, because the low solubilities of these high molecular weight materials creating processing challenges. To overcome this issue, the photo-driven, electrochemical and thermal polymerization of solution-deposited monomers *in situ* provides an alternative means of accessing polymer HTM

layers. UV-active cinnamate-based moieties have been appended to traditional triphenylamine (TPA)-based HTMs to obtain photo-crosslinkable HTMs.¹³¹ Zhu *et al.* electrochemically polymerized carbazole-containing monomers on indium-doped tin oxide (ITO) conductive glass for HTM layers in inverted PSC architectures.¹¹⁰ Sargent and coworkers thermally crosslinked monomers of **VNPB** (Figure 5-1), which were capable of reaching PCEs of 16.5% in a PSC.²⁷ Only a handful of *in situ* polymerization approaches and functionalities have been explored, providing the opportunity to design HTMs with the desirable properties of state-of-the-art HTMs and new crosslinkable functionalities.

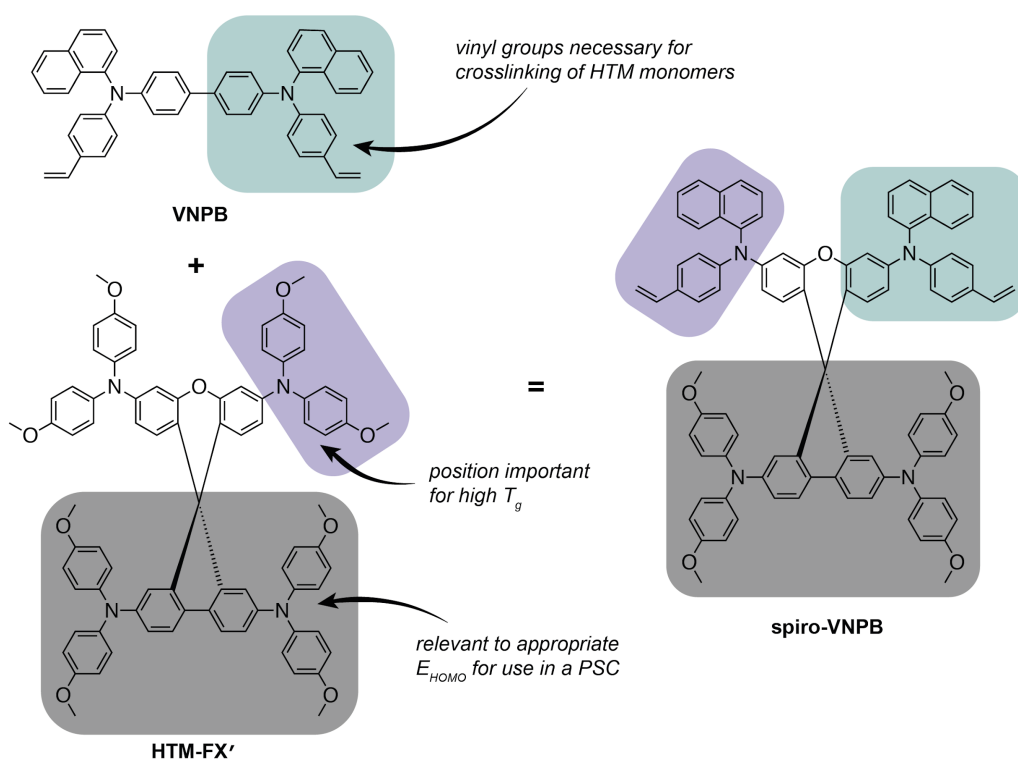


Figure 5-1 Molecular structures of **VNPB**,²⁷ **HTM-FX**^{26,119} and **spiro-VNPB**.

The challenges of designing HTMs with crosslinkable functionality are to maintain: appropriate redox potentials for charge extraction; high glass transition temperatures; and high conductivities for use in PSCs. We recently demonstrated the importance of methoxy-substituted

TPA units flanking fluorene moieties to maintain a highest occupied molecular orbital (HOMO) energy level (E_{HOMO}) at 0.69 V vs NHE and ensure sufficient (i.e., >70 mV) free energy change for hole extraction from the perovskite valence band.²⁶ We also determined, in work reported in Chapter 4, that *meta*-substitution on the xanthene portion of the spiro[fluorene-9,9'-xanthene] core of **HTM-FX'** improved the thermal stability of the material (characterized by glass transition temperature, T_g) relative to *para*-substitution.

We set out to develop a polymerizable HTM that exhibits similar electrochemistry and thermal stability as state-of-the-art HTMs, as well as low wettability as a film intended for PSC encapsulation. **spiro-VNPB** was designed to contain: the redox-active TPA units of **HTM-FX'**; the thermal stability (i.e., $T_g > 90$ °C) of **HTM-FX'**; and the crosslinkable functionality of **VNPB**. Hence, styrene-containing aryl amines were installed in the *meta*-position on the xanthene to create polymerizable **spiro-VNPB** with high T_g values ($T_g = 151$ °C). We hypothesized that **spiro-VNPB** could be polymerized by electrochemical and thermal means to produce polymerized **spiro-VNPB** with lower film wettability than control compound **spiro-NPB** as determined by time-resolved contact angle measurements. We also aimed to demonstrate the use of polymerized **spiro-VNPB** in an operating PSC.

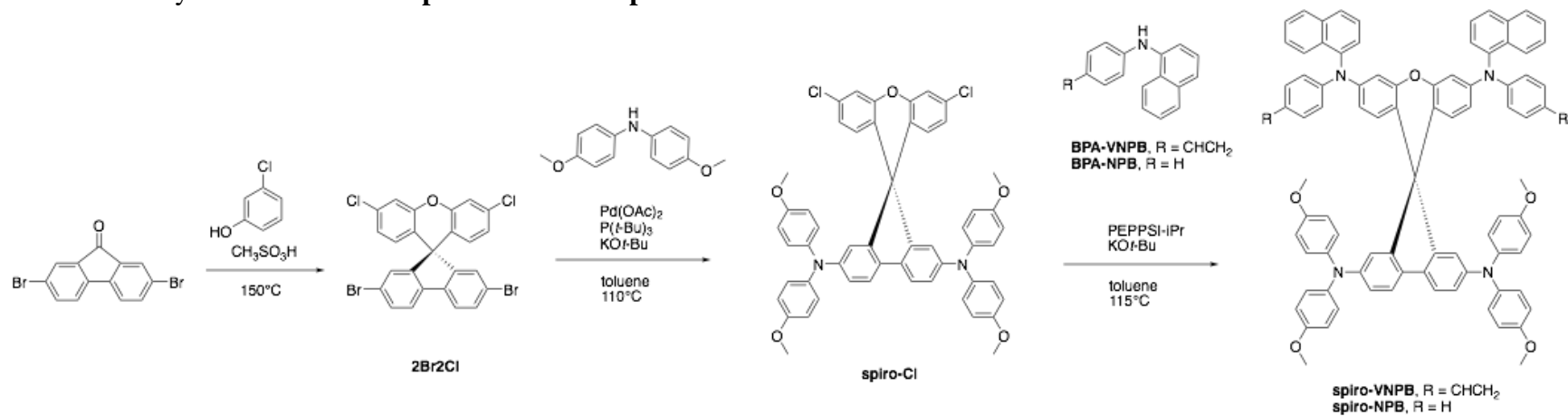
5.2 Results and discussion

5.2.1 Synthesis

The spiro[fluorene-9,9'-xanthene] core was synthesized with bromide and chloride substituents on the different halves for subsequent selective coupling at the fluorene and xanthene portions of the molecule (Scheme 5-1). Syntheses of **spiro-VNPB** and **spiro-NPB** proceeded similar to that of **HTM-FX'** with the spiro[fluorene-9,9'-xanthene] core being synthesized in >95%

yield in a condensation reaction. Selective Buchwald-Hartwig coupling at the aryl bromide was achieved with different conditions (i.e., 100 °C with palladium acetate and tri-*tert*-butylphosphine ligands) than at the aryl chloride (i.e., 110 °C with PEPPSI-*i*Pr catalyst). As such, methoxy-substituted TPA units were installed on the fluorene moiety for similar electrochemistry as **HTM-FX'** and vinyl-functionalized TPA units were installed at the *meta*-position of the xanthene moiety for greater thermal stability and the opportunity to polymerize HTM monomers.

Scheme 5-1 Synthetic scheme for **spiro-VNPB** and **spiro-NPB**



5.2.2 Electrochemical and photophysical properties

The electrochemical properties of **spiro-NPB** and **spiro-VNPB** in 0.1 M *n*-NBu₄PF₆ DCM solutions were tested by cyclic voltammetry (Figure 5-2). The cyclic voltammograms (CVs) recorded on **spiro-NPB** revealed four Faradaic events, which we attribute to the oxidation of the four aryl amine groups appended to the spiro core. The CVs were reproducible over 20 scans. In the case of **spiro-VNPB**, an oxidative scan produced two reversible oxidation events at 0.71 and 0.95 V vs NHE followed by an irreversible oxidation at higher potentials. Successive CV cycling between 0.5 V and 1.6 V range led to a progressively increasing current response, indicative of conductive polymer deposition on the working electrode at higher potentials. We observed a purple film deposited on the working electrode following the 20 scans between 0.5 V and 1.6 V vs NHE or when collecting differential pulse voltammograms of **spiro-VNPB** above 1.2 V vs NHE (Figure 5-3). No polymerization was observed when **spiro-VNPB** was subjected to cycling over a narrower range of 0.5-1.2 V vs NHE (Figure 5-2). These results point to the electropolymerization and deposition of **spiro-VNPB** occurring when the vinyl-containing aryl amine units are oxidized at potentials above 1.2 V vs NHE.

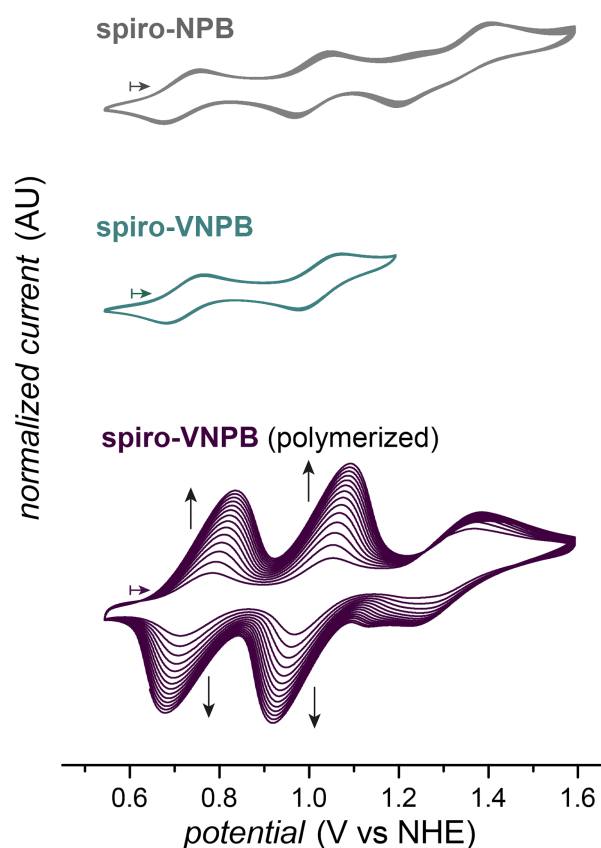


Figure 5-2 Cyclic voltammograms (CVs) over 20 scans for **spiro-NPB** between 0.5-1.6 V vs NHE (grey), **spiro-VNPB** between 0.5-1.2 V vs NHE (teal) and **spiro-VNPB** between 0.5-1.6 V vs NHE (purple) recorded in 0.1 M $n\text{-NBu}_4\text{PF}_6$ DCM solutions at room temperature. Vertical arrows indicate increasing current response with subsequent scans suggestive of electropolymerization. Horizontal arrows indicate open-circuit potential.

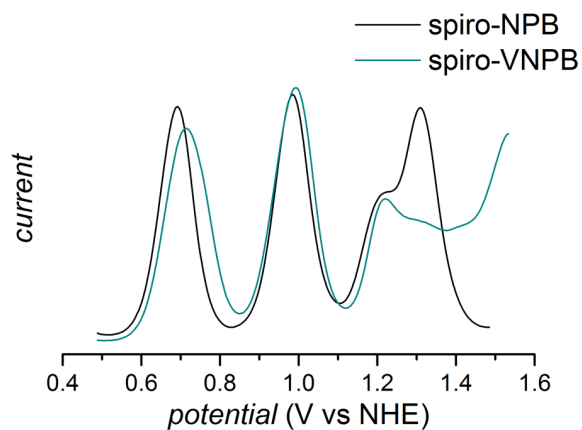


Figure 5-3 Differential pulse voltammograms (DPV) for **spiro-NPB** (black) and **spiro-VNPB** (teal)

The E_{HOMO} for **spiro-NPB** and **spiro-VNPB** were measured to be 0.71 and 0.72 V, respectively. These E_{HOMO} values indicated that the free energy change for charge extraction from the perovskite layer is similar to **HTM-FX'** ($E_{\text{HOMO}} = 0.67$ V vs NHE). The UV-visible absorption and emission maxima (Figure 5-4 and Table 5-1) of **spiro-VNPB** and **spiro-NPB** confirm that all materials under study absorb minimally in the visible region which may be beneficial in maximizing the solar absorption by the perovskite layer in a PSC. Absorption and emission onsets are the same for both materials and, hence, the bandgap ($E_{\text{HOMO-LUMO}}$) determined from the intersection of these two spectra are identical for the two materials.

5.2.3 Bulk thermal properties

The T_g values of 147 °C and 151 °C for **spiro-NPB** and **spiro-VNPB**, respectively, were determined by differential scanning calorimetry (DSC; Table 5-1), and satisfy the key requirement that the T_g must be greater than 90 °C to remain in the amorphous phase during device operation. Both of these values are also higher than that measured for commercially available **X60** ($T_g = 107$ °C) owing to the bulky aryl amine groups being positioned at the *meta*-position of the xanthene moiety.²⁶

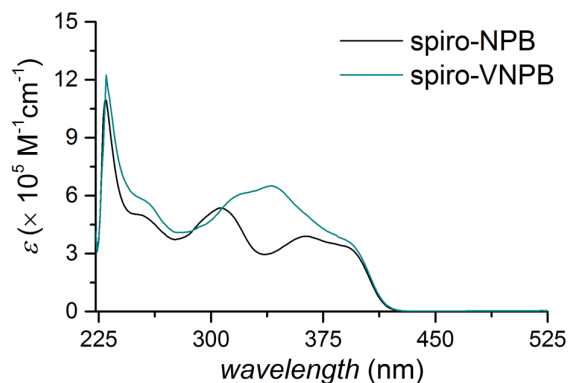


Figure 5-4 Absorption profiles for **spiro-NPB** (black) and **spiro-VNPB** (teal)

Table 5-1 Electrochemical, photophysical, and glass transition temperature data for **spiro-NPB** and **spiro-VNPB**

Compound	E_{HOMO}^a (V vs NHE)	λ_{max}^b (nm)	λ_{em}^c (nm)	T_g^d (°C)
spiro-NPB	0.71	362, 306	428	147
spiro-VNPB	0.72	316, 339, 392	428	151

^a The half-wave potential corresponding to the first and second oxidation processes in the cyclic voltammogram. Measured in DCM and referenced to NHE by addition of ferrocene. ^b Absorption maxima for HTM in DCM. ^c Excitation at higher energy λ_{max} in DCM. ^d Determined by DSC. Both T_m values determined to be >300 °C and above the detection limits of our instrument.

5.2.4 Contact angle measurements

The contact angle of a water droplet on the surface of a film reports the wettability of a material.^{132,133} The retention of a water droplet on the surface of a film indicates low wettability and the ability to prevent liquid water ingress below the encapsulation layer. Contact angle measurements of water droplets on spin-coated **spiro-OMeTAD**, **spiro-NPB**, non-polymerized **spiro-VNPB** and polymerized **spiro-VNPB** films on glass substrates were carried to determine the wettability of the various HTM films. Photographic images of the droplets (backlit for contrast) were captured and contact angles were measured using inhouse software. **Spiro-OMeTAD**, **spiro-NPB** and thermally polymerized **spiro-VNPB** held water droplets with similar contact angles of 70, 73 and 72°, respectively; however, the droplets collapsed within seconds to wet the glass substrates below and delaminate the films from the surface. A contact angle of 79 ° was observed for thermally polymerized **spiro-VNPB** films which retained water droplets (>60 °) throughout the 30-min experiment. The overall decrease in size of the water droplet implicates evaporation as the cause for the contact angle decrease (Figure 5-5).

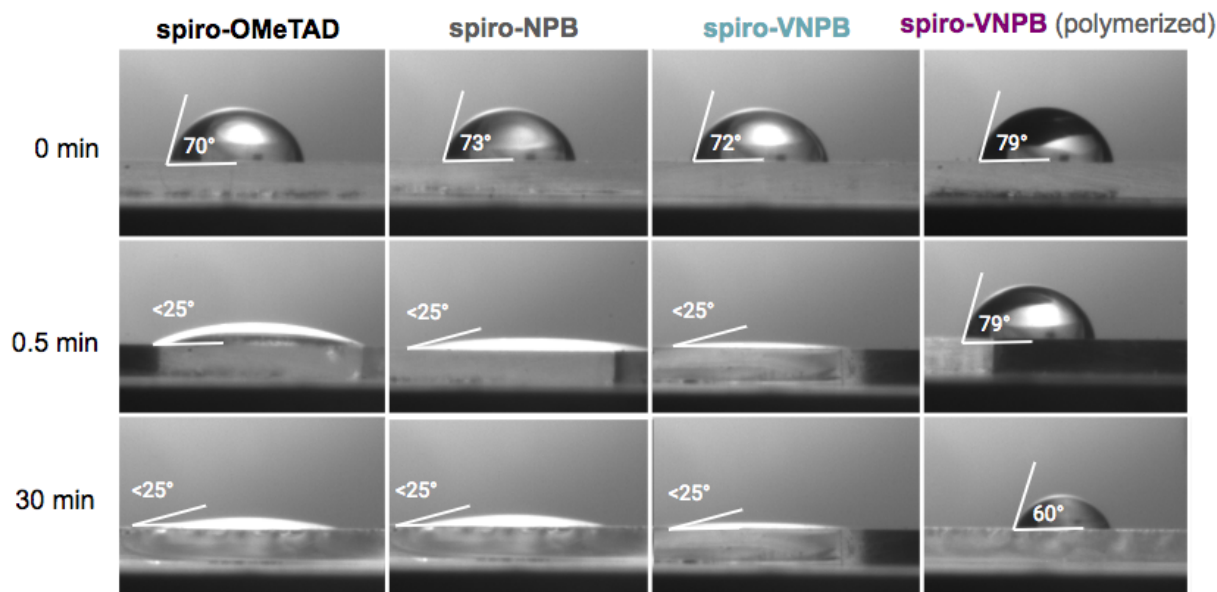


Figure 5-5 Contact angle data of **spiro-OMeTAD**, **spiro-NPB**, **spiro-VNPB** and thermally polymerized **spiro-VNPB** over 30 minutes.

5.2.5 Electrical properties

We measured the sheet resistivity of ~ 100 nm thick films of **spiro-OMeTAD**, **spiro-NPB**, non-polymerized **spiro-VNPB** and thermally polymerized **spiro-VNPB** (5 min at 150 °C) spin-coated on glass substrates with 20 mol% LiTFSI dopant and 250 mol% tBP additive, during 180 min of air exposure (Figure 5-6) to test the feasibility of these films as charge transport layers in PSCs. **Spiro-OMeTAD** was significantly less resistive than **spiro-NPB**, **spiro-VNPB** and thermally polymerized **spiro-VNPB**. The high resistivity of **spiro-NPB**, **spiro-VNPB** and thermally polymerized **spiro-VNPB** indicated that the naphthyl substituents appended to the xanthene moiety are more insulating than the phenyl substituents common to both **spiro-OMeTAD** and **X60**. The high resistivity of these novel materials may limit their use as the sole HTM layer in PSCs. Thermally polymerized **spiro-VNPB** exhibited lower sheet resistivity than molecular **spiro-VNPB** which supports the polymerization of this material for PSC encapsulation.

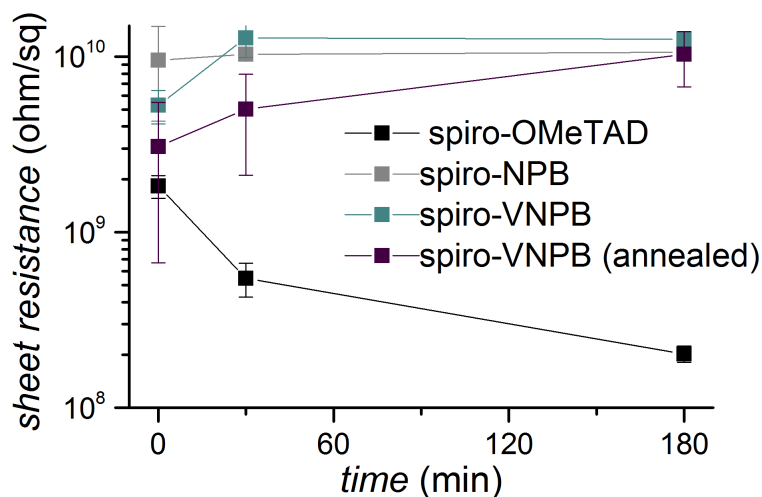


Figure 5-6 Sheet resistance data for **spiro-OMeTAD**, **spiro-NPB**, **spiro-VNPB** and thermally polymerized **spiro-VNPB**

5.2.6 Perovskite solar cell characterization

PSC studies were carried out by Dr. Hairen Tan of the Sargent group at the University of Toronto. **Spiro-VNPB** was incorporated into a perovskite device by annealing a 10-nm thick layer above the perovskite layer and below a hole-transporting **spiro-OMeTAD** layer (Table 5-2). PSCs with the **spiro-VNPB** encapsulating layer yielded PCEs of 6.1% while devices containing exclusively **spiro-OMeTAD** yielded PCEs of 18.0%. This 12% difference in PCEs was attributed to the higher sheet resistivity of annealed **spiro-VNPB** relative to **spiro-OMeTAD**. The deleterious impact of high sheet resistivity was confirmed by constructing PSCs with exclusively **spiro-VNPB** which yielded PCEs of merely 1.2%. The high resistivity and low PCE yielded by **spiro-VNPB** prompts research into polymerizable HTMs with higher conductivity imparted by stable dopants (e.g., F4-TCNQ) or optimized encapsulation layer thickness (e.g., <10 nm).

Table 5-2 Statistical performance data of **spiro-OMeTAD** and **spiro-VNPB** in perovskite solar cell devices.

material	V_{oc} (V)	J_{sc} (mA/cm ²)	FF	PCE (%)
spiro-OMeTAD	1.10	21.4	0.77	18.0
spiro-VNPB / spiro-OMeTAD	0.93	13.9	0.47	6.1
spiro-VNPB (thermally polymerized)	1.03	3.1	0.39	1.2

Spiro-VNPB was thermally polymerized at 150 °C for 15 minutes. Data collected for Cs_{0.05}FA_{0.81}MA_{0.14}PbI_{2.55}Br_{0.45} perovskite layer on TiO₂-Cl under of 100 mW cm⁻² lamp.

5.3 Conclusion

We designed **spiro-VNPB** to contain: the redox active TPA units and thermal stability (i.e., $T_g > 90$ °C) of **HTM-FX'**; and the crosslinking functionality of **VNPB**. We discovered that **spiro-VNPB** could be polymerized either electrochemically (at potentials greater than 1.2 V vs NHE), or thermally (at temperatures above 120 °C). Contact angle measurements demonstrated that thermal polymerization of **spiro-VNPB** decreased the wettability of films and prevented the penetration of water through the HTM film, relative to films of **spiro-OMeTAD**, **spiro-NPB** and non-polymerized **spiro-VNPB**. The lower wettability of polymerized **spiro-VNPB** demonstrated that it could be used as an encapsulation layer to potentially improve the moisture stability of PSCs. PSCs fabricated with **spiro-VNPB** as an encapsulation layer and **spiro-OMeTAD** as an HTM layer resulted in PCEs of 6.1%. Further research into optimizing the encapsulation process (i.e., conductivity, layer thickness and polymerization method) is ongoing.

5.4 Experimental

5.4.1 Synthesis

All reagents were obtained from MilliporeSigma, Alfa Aesar or Fisher Scientific and used as received. All reactions were performed using toluene from a solvent purification system prior to use. Standard inert atmosphere and Schlenk techniques were carried out under nitrogen. All reactions and purification were carried out in the dark. Purification by column chromatography was performed using silica (Silicycle: Ultrapure Flash Silica). Analytical thin-layer chromatography (TLC) was performed on aluminum-backed sheets pre-coated with silica 60 F-254 adsorbent (250 μm thick; Silicycle, QC, Canada) and visualized under UV light. Routine ^1H and ^{13}C NMR spectra were collected on a Bruker AV400 inv/dir instrument at ambient temperatures, operating at 300 MHz and 100 MHz, for ^1H and ^{13}C nuclei, respectively. Chemical shifts (δ) are reported in parts per million (ppm) using the residual signals δ 7.26 and 77.0 for CDCl_3 , δ 2.05 and 29.8 for Acetone- d_6 and δ 2.50 and 39.4 for DMSO- d_6 as internal references for ^1H and ^{13}C , respectively. Standard abbreviations indicating multiplicity are used as follows: s = singlet; d = doublet; t = triplet; m = multiplet.

Y2Br2Cl (2,7-dibromo-3',6'-dichlorospiro[fluorene-9,9'-xanthene]): 2,7-dibromo-9-flourenone (1.50 g, 4.43 mmol), 3-chlorophenol (5.50 g, 45.0 mmol) and methane sulfonic acid (1.7 mL, 17.5 mmol) were mixed at 140 $^\circ\text{C}$ for 18 h under N_2 . The reaction mixture was cooled to room temperature and product was precipitated with the addition of MeOH. Separation by filtration and rinsing with MeOH yielded 2.36 g (95.4%) of product as white powder. ^1H NMR (400 MHz, CDCl_3): δ = 7.63 (d, J = 8.1 Hz, 2H), 7.52 (dd, J = 8.1, 1.8 Hz, 2H), 7.28 – 7.16 (d, 2H), 6.82 (dd, J = 8.5, 2.1 Hz, 2H), 6.30 (d, J = 8.5 Hz, 2H). ^{13}C NMR (100 MHz, CDCl_3): δ = 155.9, 151.2,

137.5, 134.2, 131.8, 129.0, 128.9, 124.4, 122.6, 121.6, 117.4, 77.3, 77.0, 76.7. HRMS (EI): $m/z = 555.86333$ [M]⁺ (calcd for [C₂₅H₁₂Br₂Cl₂O]⁺: $m/z = 555.86319$).

Y592Cl (3',6'-dichloro-*N2,N2,N7,N7*-tetrakis(4-methoxyphenyl)spiro[fluorene-9,9'-xanthene]-2,7-diamine): **Y2Br2Cl** (0.80 g, 1.43 mmol), bis(4-methoxyphenyl)amine (0.66 g, 2.87 mmol), palladium acetate (0.023 g, 0.11 mmol), tri-*tert*-butylphosphine (0.023 g, 0.11 mmol) and potassium *tert*-butoxide (0.34 g, 0.64 mmol) were added to toluene (15 mL) under N₂. The reaction mixture was stirred at reflux for 16 h. The reaction mixture was cooled to room temperature. Purification by silica column chromatography (SiO₂: hexanes/EtOAc, 4:1; $R_f = 0.31$) yielded 1.11 g (91.0%) of product as yellow powder. ¹H NMR (400 MHz, Acetone-d₆) $\delta = 7.61$ (d, $J = 8.4$ Hz, 2H), 7.16 (d, $J = 8.4$ Hz, 2H), 7.01 (dd, $J = 8.4, 2.2$ Hz, 2H), 6.95 – 6.74 (m, 18H), 6.68 (d, $J = 2.1$ Hz, 2H), 6.59 (d, $J = 8.4$ Hz, 2H), 3.74 (s, 12H). ¹³C NMR (101 MHz, Acetone-d₆) $\delta = 206.3, 157.2, 157.1, 155.8, 152.3, 149.5, 141.8, 141.7, 134.0, 133.4, 130.2, 127.2, 127.2, 125.3, 125.1, 121.7, 121.5, 121.0, 120.9, 118.2, 117.6, 117.5, 115.6, 115.6, 55.8, 54.4, 30.6, 30.4, 30.2, 30.0, 29.8, 29.6, 29.4, 29.3$. HRMS (ESI): $m/z = 854.2305$ [M+H]⁺ (calcd for [C₅₃H₄₀N₂Cl₂O₅]⁺: $m/z = 854.2314$).

spiro-VNPB (*N2,N2,N7,N7*-tetrakis(4-methoxyphenyl)-*N3',N6'*-di(naphthalen-1-yl)-*N3',N6'*-bis(4-vinylphenyl)spiro[fluorene-9,9'-xanthene]-2,3',6',7-tetraamine): **Y59-Cl** (1.12 g, 1.31 mmol), *N*-(4-vinylphenyl)naphthalen-1-amine (0.80 g, 3.27 mmol), PEPPSI-*iPr* (0.089 g, 0.13 mmol), and potassium *tert*-butoxide (0.50 g, 5.2 mmol) were added to toluene (15 mL) under N₂. The reaction mixture was stirred at reflux for 16 h. The reaction mixture was cooled to room temperature. Purification by silica column chromatography (SiO₂: hexanes/EtOAc, 4:1; $R_f = 0.22$) yielded 0.65 g (40.7 %) of product as pale yellow powder. ¹H NMR (400 MHz, Acetone-d₆)

$\delta = 7.94$ (d, $J = 8.1$ Hz, 2H), 7.88(dd, $J = 8.4, 2.2$ Hz, 2H), 7.58 – 7.40 (m, 4H), 7.44 – 7.09 (m, 12H), 6.99 – 6.83 (m, 12H), 6.83 – 6.68 (m, 12H), 6.64 (d, $J=8.2$ Hz, 2H), 6.60 (dd, $J = 8.1, 1.1$ Hz, 2H), 6.50 (s, 2H), 6.44 (d, $J = 8.2$ Hz, 2H), 5.61 (dd, $J = 17.6, 1.1$ Hz, 2H), 5.07 (dd, $J = 10.9, 1.1$ Hz, 2H), 3.73 (s, 12H). ^{13}C NMR (101 MHz, Acetone- d_6) $\delta = 206.3, 157.0, 156.4, 152.8, 149.1, 149.0, 148.6, 143.8, 141.9, 137.4, 136.5, 133.6, 132.6, 132.2, 129.9, 129.6, 129.2, 129.2, 128.4, 128.2, 128.0, 127.7, 127.5, 127.4, 127.2, 126.3, 124.8, 122.6, 121.40, 120.8, 120.0, 118.5, 118.0, 115.6, 112.5, 110.0, 55.9, 30.6, 30.4, 30.2, 30.0, 29.8, 29.6, 29.4$. HRMS (ESI): $m/z = 1273.5260$ [M+H] $^+$ (calcd for [C₈₉H₆₉N₄O₉] $^+$: $m/z = 1273.5268$).

spiro-NPB (*N2,N2,N7,N7-tetrakis(4-methoxyphenyl)-N3',N6'-di(naphthalen-1-yl)-N3',N6'-diphenylspiro[fluorene-9,9'-xanthene]-2,3',6',7-tetraamine*) **Y59-Cl** (0.55 g, 0.64 mmol), *N*-phenylnaphthalen-1-amine (0.35 g, 1.61 mmol), PEPPSI-*i*Pr (0.044 g, 0.064 mmol), and potassium *tert*-butoxide (0.247 g, 2.6 mmol) were added to toluene (15 mL) under N₂. The reaction mixture was stirred at reflux for 16 h. The reaction mixture was cooled to room temperature. Purification by silica column chromatography (SiO₂: hexanes/EtOAc, 4:1; $R_f = 0.22$) yielded 0.32 g (41.5 %) of product as pale brown solid. ^1H NMR (400 MHz, Acetone- d_6) δ 7.92 (d, $J = 8.2$ Hz, 2H), 7.88 (d, $J = 8.5$ Hz, 2H), 7.83 (d, $J = 8.3$ Hz, 2H), 7.47 (m, 6H), 7.35 (m, 4H), 7.30 (m, 8H), 7.17 (d, $J = 8.4$ Hz, 4H), 6.96 (d, $J = 7.8$ Hz, 4H), 6.88 (m, 8H), 6.74 (m, 12H), 6.54 (dd, $J = 8.6, 2.2$ Hz, 2H), 6.47 – 6.37 (m, 4H), 3.71 (s, 12H). ^{13}C NMR (101 MHz, Acetone- d_6) δ 206.3, 157.0, 156.5, 152.8, 149.3, 149.1, 148.9, 144.0, 141.8, 138.6, 136.5, 133.6, 132.3, 130.2, 129.9, 129.6, 129.2, 129.1, 128.4, 127.9, 127.6, 127.5, 127.3, 127.1, 126.3, 124.8, 123.3, 123.2, 121.4, 120.7, 119.5, 118.5, 117.4, 115.6, 109.3, 55.9, 54.4. HRMS (ESI): $m/z = 1221.4987$ [M+H] $^+$ (calcd for [C₈₅H₆₅N₄O₅] $^+$: $m/z = 1221.4955$).

5.4.2 Electrochemical and photophysical properties

Solution UV-Vis absorption spectra were collected on a Cary 5000 spectrophotometer. Photoluminescence spectra were recorded with a Cary Eclipse fluorimeter. All samples were measured in a 1-cm quartz cell at room temperature in HPLC grade DCM. The concentrations of the DCM solutions of analytes for UV-Vis and photoluminescence measurements were 2×10^{-5} mol L⁻¹ and 1×10^{-5} mol L⁻¹, respectively. Solution electrochemical data were recorded with a CHI660D potentiostat at room temperature using a platinum wire counter electrode and a platinum working electrode. Ag/AgCl in saturated KCl was used as the reference electrode and was calibrated versus the normal hydrogen electrode (NHE) by the addition of Fc⁺/Fc. A 0.1 M *n*-NBu₄PF₆ DCM solution was used for all HTMs. CV data were acquired for 0.5 mM solutions of each HTM at a scan rate of 50 mV s⁻¹.

5.4.3 Bulk thermal properties

DSC curves of compounds were collected using a Netzsch DSC 214 Polyma instrument under a nitrogen protective atmosphere. For each measurement, two aluminum crucibles were used, one for material measurement and the other as empty reference. A customized heating program was developed to include a 5 min hold at the initial temperature of 50 °C, and four continuous cycles between to 50 °C and 300 °C with a heating/cooling rate of 10 K/min and 5 min holds at 50 °C and 300 °C. Data from the heating segment of last 3 cycles were used to identify the T_m and extrapolate the T_g of the material.

5.4.4 Contact angle measurements

Contact angles were measured using a camera capture of a water droplet on an HTM surface spin-coated (at 3000 rpm for 45 seconds) on glass substrates. Images were taken following

deposition of a single 10 μL droplet of deionized water on the HTM surface. When droplets were stable on HTM surface (angle $>25^\circ\text{C}$), the image was further analyzed by inhouse software. Images were captured after 30 minutes to assess droplet stability on the film surface.

5.4.5 Electrical properties

Four parallel Au electrodes with a spacing of 0.75 mm and length of 23 mm were used to measure the film conductivities in the dark and under ambient conditions. A Keithley 2400 sourcemeter was used to force current through the outer electrodes while sensing the voltage across the inner two electrodes. A linear fit of each measurement was used to determine the resistance, R . The film thickness was measured using a Bruker DektakXT profilometer.

5.4.6 Perovskite solar cell characterization

The planar perovskite solar cells were fabricated according to our previous work.²⁰ Briefly, pre-patterned indium tin oxide (ITO) coated glass substrates were sequentially cleaned using detergent, acetone, and isopropanol. The $\text{TiO}_2\text{-Cl}$ electron transport layers were spin-coated on ITO substrates from the colloidal nanocrystal solutions, and annealed on a hot plate at 150°C for 30 min in ambient air. After the substrates had cooled, we transferred the substrates immediately to a nitrogen-filled glovebox for the deposition of perovskite films. The $\text{Cs}_{0.05}\text{FA}_{0.81}\text{MA}_{0.14}\text{PbI}_{2.55}\text{Br}_{0.45}$ precursor solution (1.4 M) was prepared in a mixed solvent of DMF and DMSO with a volume ratio of 4:1. The molar ratios of $\text{PbI}_2/\text{PbBr}_2$ and FAI/MABr were both fixed at 0.85:0.15, molar ratio of $\text{CsI}/(\text{FAI}+\text{MABr})$ is 0.05:0.95, and the molar ratio of $(\text{FAI}+\text{MABr}+\text{CsI})/(\text{PbI}_2+\text{PbBr}_2)$ was fixed at 1:1. The perovskite films were deposited onto the $\text{TiO}_2\text{-Cl}$ substrates with two-step spin coating procedures. The first step was 2000 rpm for 10 s

with an acceleration of 200 rpm/s. The second step was 6000 rpm for 20 s with a ramp-up of 2000 rpm/s. Chlorobenzene (100 μL) was dropped on the spinning substrate during the second spin-coating step at 10 s before the end of the procedure. The substrate was then immediately transferred on a hotplate and heated at 100 $^{\circ}\text{C}$ for 20 min. After cooling down to room temperature, the hole-transport layer was subsequently deposited on top of the perovskite film by spin coating at 4000 rpm for 30 s using a chlorobenzene solution which contained 72.3 mg/mL of HTMs and 28.8 $\mu\text{L}/\text{mL}$ of tBP, as well as 17.5 $\mu\text{L}/\text{mL}$ of LiTFSI (520 mg/mL in acetonitrile). Finally, 100 nm Au contact was deposited on top of HTM films by electron-beam evaporation in an Angstrom Engineering deposition system.

Current density-voltage (J - V) characteristics were measured using a Keithley 2400 source meter under illumination of a solar simulator (Newport, Class A) at the light intensity of 100 mW cm^{-2} as verified using a certified reference solar cell (Newport). A spectral mismatch factor of 1 was used for all J - V measurements. Unless otherwise stated, the instantaneous J - V curves were measured with a scanning rate of 50 mV s^{-1} from 1.2 V to -0.1 V. The active area was determined using an aperture shade mask (0.049 cm^2) placed in front of the solar cell to avoid overestimation of the photocurrent density.

Chapter 6 : Effect of Donor-Acceptor Architecture on Hole-Transport Material Hole Mobility

6.1 Introduction

Perovskite solar cells (PSCs) rely on hole-transport materials (HTMs) to selectively conduct holes from the photoactive perovskite layer to the cathode. HTM layers are usually 100-200 nm thick films of extended metal oxide solids (e.g., NiO_x)^{24,134,135} or redox-active organic compounds (e.g., **spiro-OMeTAD**).^{68,136} Organic HTMs are attractive due to their readily modifiable structures that enable acute control of the frontier energy levels, light absorption, and thermal stability.^{77,137}

Organic HTMs typically require doping in order to optimize conductivity and to realize high device power conversion efficiencies (PCEs).^{79,138} Doping is most frequently achieved through chemical oxidation with an ancillary oxidant. LiTFSI is an ionic dopant added to HTM layers that has been utilized in PSC devices to yield PCEs greater than 20%.^{136,139} However, lithium ions are hygroscopic and can therefore draw water into the PSC, causing dissolution of the photoactive perovskite layer.¹² Lithium ions are also susceptible to migration through an HTM film during PSC operation, leading to inconsistencies in the film morphology and conductivity over time.^{85,140} Another common ionic dopant is FK209, which can also yield PCEs that are >20%.^{141,142} Seo *et al.* recently demonstrated that $\text{Zn}(\text{TFSI})_2$ is a stable dopant, but it is currently sold at 10 times the price of LiTFSI from distributors such as MilliporeSigma.^{28,143} Molecular dopants, such as F4-TCNQ, avoid the hygroscopic nature of lithium ions, but still exhibit a 30% decrease in device PCE over eight days of stability studies.²⁹ This scenario provides the impetus to make “dopant-free” HTMs, which do not require hygroscopic, migratory and/or expensive additives that compromise device stability and deployment.

Donor-acceptor (D-A) HTMs are a promising class of molecules because they can yield high conductivities without dopants.^{93,144} D-A HTMs contain at least one electron-rich donor (e.g., triphenylamine or S,N-heteropentacene) and at least one electron-withdrawing acceptor group (e.g., dicyanoacrylate or 3-(3-ethylrhodanine)).⁹³ D-A molecules typically provide predictable redox chemistry at the donor unit and strong light absorption properties owing to the allowed HOMO-LUMO (i.e., D-A) electronic transitions.^{91,145} It is currently not clear why these D-A materials exhibit high conductivities without the use of dopants, but I submit that the ability for these molecules to exist in a charge-separated form when exposed to visible light may be integral to yielding a “pseudo-doped” species when photoexcited.

The work reported in this chapter seeks to develop a structure-property relationship between the D-A architecture (e.g., monopodal, bipodal, and tripodal architectures) and hole mobility. Previous research has been limited to only comparing the effect of varying the donor, π -bridge, or acceptor identities between *similar* D-A architectures. Yang *et al.* examined the effect of donor group identity between two structurally-similar (monopodal) D-A HTMs and determined that HTMs with benzo[1,2-b:4,5-b']dithiophene donor units yielded higher mobility films than a fluorinated alternative (i.e., 5,6-difluoro-2,1,3-benzothiadiazole).⁹⁴ Steck and coworkers compared thiophene and EDOT π -bridges between donor and acceptor moieties in structurally-similar (bipodal) A-D-A HTMs and found that thiophene linkages yielded HTMs with minimal visible light absorption, which likely allowed for greater light absorption by the perovskite layer.⁹⁵ A variety of other D-A HTMs have been disclosed in literature but to the best of my knowledge, no study has been conducted on the effect of structurally-dissimilar D-A architectures on the hole mobilities of HTMs.

In this chapter, I report on-going investigations of monopodal, bipodal, and tripodal D-A architectures to determine which form exhibits the highest hole mobility. I conducted a controlled study of three homologous D-A HTMs bearing monopodal, bipodal, or tripodal architectures (**TPA-1**, **TPA-2**, and **TPA-3**, respectively; Figure 6-1). Triphenylamine (TPA) was selected as the donor unit because it is electron-rich and displays the reversible redox chemistry necessary for hole extraction and hole transport by the HTM.^{146,147} Thiophene was used as the π -bridge and dicyanoacrylate was used as the acceptor group. Preliminary results reveal that **TPA-1** exhibited the highest hole mobility of the series. I provide herein a comprehensive summary of the electrochemical, thermal, and photophysical properties in tandem with computational data (e.g., reorganization energy, polaron stabilization energy, hole extraction potential) in pursuit of understanding why this topology yields the highest hole mobility.

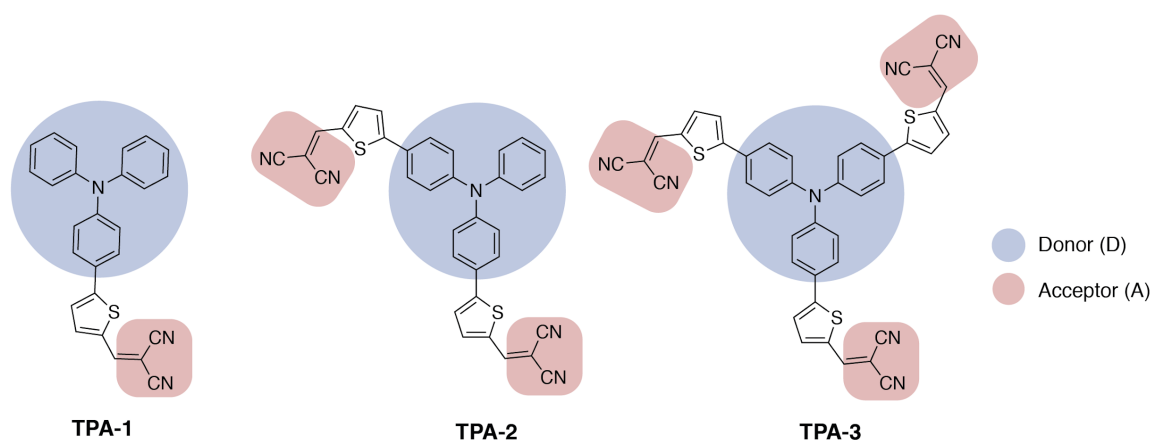


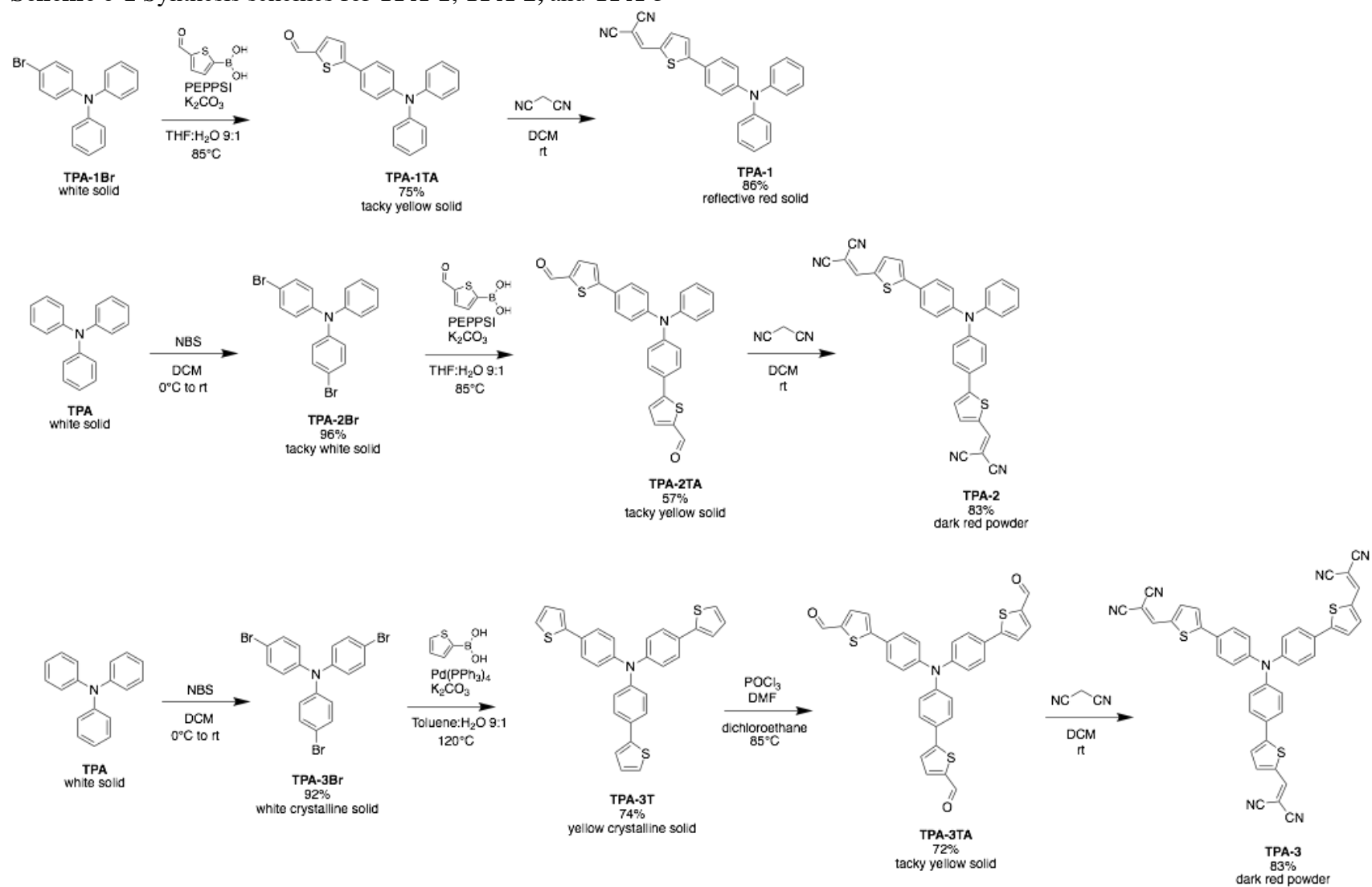
Figure 6-1 Molecular representations of **TPA-1**, **TPA-2**, and **TPA-3** (collectively referred to as **TPA-X** series) which vary in D-A architectures.

6.2 Results and discussion

6.2.1 Synthesis

The number of acceptor groups had a significant impact on the ease of synthesis for the three HTMs (collectively referred to as **TPA-X**) in the series. Different synthetic approaches were used for each material based on the increasing difficulty of coupling one, two, or three aldehyde-substituted thiophene groups (electron-withdrawing units) by Suzuki coupling (Scheme 6-1). In the case of **TPA-3**, the Suzuki coupling of three equivalents of (5-formylthiophen-2-yl)boronic acid to a tri-brominated TPA was low yielding (<20% isolated yield for the penultimate product) and, hence, this step was amended to the coupling of 2-thienylboronic acid (74% isolated yield) followed by an acylation reaction (72% isolated yield) for an overall yield of 53% for the penultimate product. The general synthetic pathway for all three HTMs, however, started with a mono-, di- or tri-brominated TPA, followed by the installation of the pi-bridge and aldehyde group in one or two steps, and finished with a Knoevenagel condensation to append the cyanoacrylate acceptor group in place of the aldehyde (Scheme 6-1). For characterization, purified HTMs were dissolved in toluene and spin-coated on glass or indium-doped tin oxide (ITO) on glass substrates at 2000-3000 rpm for ~100 nm thick films, as determined by optical profilometry.

Scheme 6-1 Synthesis schemes for **TPA-1**, **TPA-2**, and **TPA-3**



6.2.2 Electrical properties

Hole mobility is the intrinsic ability of a material to transport holes through a film and is independent of factors such as doping and oxidation by air. I prepared “hole-only devices” (i.e., ITO/PEDOT:PSS/HTM/Au; Figure 2a) to measure the hole mobilities of HTM films using the space-charge limited current (SCLC) method (Figure 2b). Films were prepared by spin-coating dissolved solutions of poly(3,4-ethylenedioxythiophene):polystyrene sulfonate (PEDOT:PSS) and then **TPA-X** series on etched ITO substrates. Gold contacts were deposited by sputtering to complete the hole-only devices. Hole mobility (μ_h) is calculated from quadratic (SCLC) region of current-voltage (J - V) plots where current is controlled by the charge carriers injected by contacts and is not impacted by the number of charge carriers present in the film from doping or ambient oxidation of the material. The μ_h can be extracted from the slope of the SCLC region using Equation 6-1:

$$\mu_h = (8d^3J)/(9\varepsilon_0\varepsilon_rV^2) \quad \text{(Equation 6-1)}$$

where d is the film thickness, J is the current density, ε_0 is the vacuum permittivity, ε_r is the dielectric constant of the material (normally assumed to be 3 for organic semiconductors), and V is the applied bias. An HTM with intrinsically high hole mobility will ensure sustained current in a cell and will contribute to higher fill factors (FFs). The measurements on the **TPA-X** series were found to be in the range of 2.88×10^{-5} - 4.49×10^{-4} cm²/Vs (Figure 6-3). **TPA-1** produced the highest hole mobility (4.49×10^{-4} cm²/Vs) for the series, and is commensurate with the state-of-the-art HTM **spiro-OMeTAD** without the use of dopants.

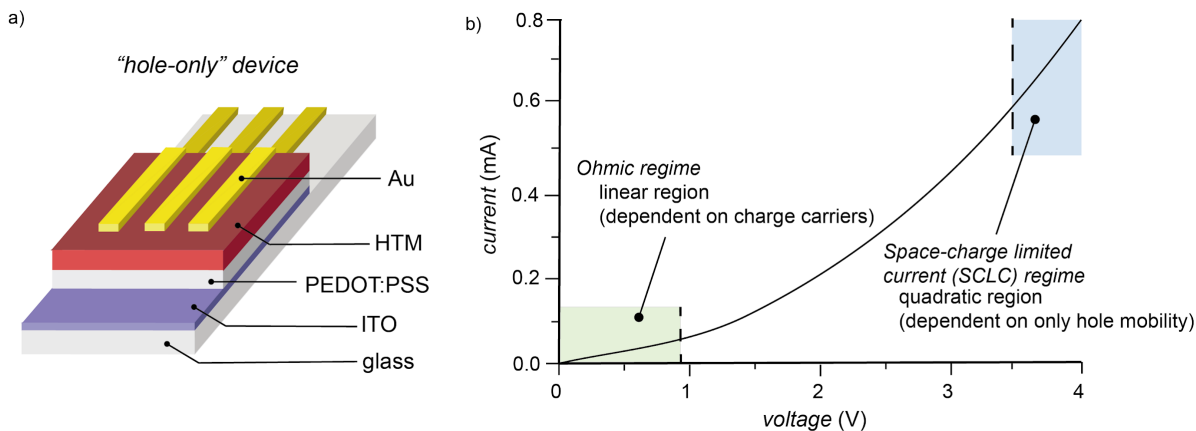


Figure 6-2 a) Schematic of hole-only device for hole mobility measurements and b) hypothetical $J-V$ curve of a hole-only device highlighting the ohmic and SCLC regimes for HTM hole mobility measurements.

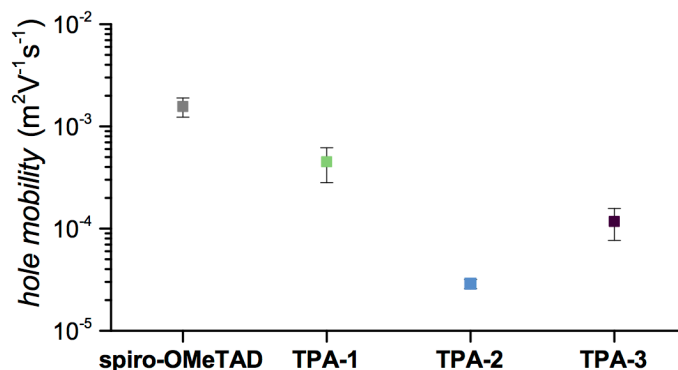


Figure 6-3 Hole mobilities determined from SCLC region of hole-only devices containing **spiro-OMeTAD**, **TPA-1**, **TPA-2**, and **TPA-3**.

6.2.3 Bulk thermal properties

I then set out to resolve why **TPA-1** yields the highest hole mobility for this series of amorphous HTM films. I investigated the glass transition temperature (the temperature at which a bulk material transitions from glassy, amorphous phase to a different phase) by measuring the

endothermic phase transition with differential scanning calorimetry (DSC). The trend shows that increasing the number of acceptor units increases the glass transition temperatures (T_g) of the bulk HTMs: The T_g s of **TPA-1**, **TPA-2**, and **TPA-3** were 59, 116, and 127 °C, respectively (Table 6-1). These T_g values, along with grazing incidence X-ray diffraction (XRD) data (Figure 6-4), indicate that all three HTMs are amorphous glasses when deposited by spin-coating at room temperature. On this basis, we can rule out different phases being responsible for the differences in hole mobilities. It is also worth noting that **TPA-1** has a T_g of 59 °C, which is typically too low for use in devices (values of >90 °C are needed for stable operation). The less conductive **TPA-2** and **TPA-3** films however, both exhibited higher T_g values (116 and 127 °C, respectively) appropriate for use in a PSC.

Table 6-1 Electrical, electrochemical, photophysical, and bulk thermal properties of **TPA-1**, **TPA-2**, and **TPA-3**

Compound	<i>hole mobility</i> (m ² /Vs)	IP_v (eV)	ϵ_{HOMO}^a (V vs NHE)	E_{HOMO}^b (V vs NHE)	λ_{max}^c (nm)	λ_{em}^d (nm)	T_g^e (°C)
TPA-1	4.49×10 ⁻⁴	6.56	1.14	1.19	517	649	59
TPA-2	2.88×10 ⁻⁵	6.74	1.24	1.24	519	642	116
TPA-3	1.17×10 ⁻⁴	6.92	1.34	1.26	504	641	127

^a The computed $IP(v)$ and ϵ_{HOMO} were conducted using B3LYP/6-31G(d,p) level of theory and ϵ_{HOMO} was referenced against experimental data for **TPA-2**. ^b The half-wave potential corresponding to the first and second oxidation processes in the cyclic voltammogram measured in DCM and referenced to NHE by addition of ferrocene. ^c Absorption maximum for HTM in DCM. ^d Excitation at higher energy λ_{max} in DCM. ^e Determined by differential scanning calorimetry (DSC). All T_m values determined to be >300 °C and above the detection limits of our instrument.

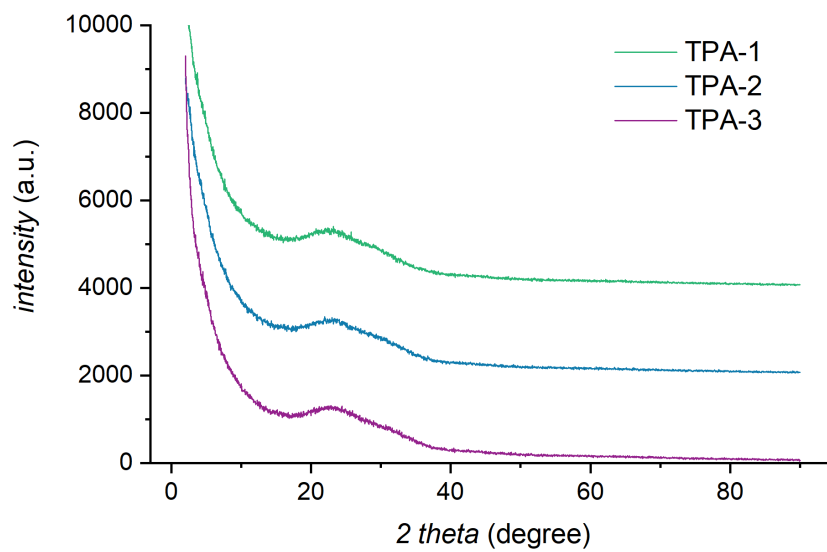


Figure 6-4 Grazing incidence XRD data for **TPA-1**, **TPA-2**, and **TPA-3** on glass

6.2.4 Electrochemical and photophysical properties

Increasing the number of electron-withdrawing acceptor groups increased the highest occupied molecular orbital energy level (E_{HOMO}) of the **TPA-X** series: 1.19, 1.24, and 1.26 V vs NHE for **TPA-1**, **TPA-2** and **TPA-3**, respectively (cyclic voltammogram (CV) data in Table 6-1 and Figure 6-5). The computed highest occupied molecular orbital (HOMO) energy levels (ϵ_{HOMO}) were 1.14, 1.24 and 1.35 V vs NHE. The low E_{HOMO} of **TPA-1** is proportional to the adiabatic ionization potential (IP_a), which is the difference in energy between the optimized neutral molecule (i.e., HTM) and oxidized molecule (i.e., HTM⁺; Figure 6-6). The IP_a is proportional to a number of properties related to hole mobility, including reorganization energy and small polaron stabilization energy. It should be noted that the electron-withdrawing substituents result in more stabilized E_{HOMO} values than typically observed for non-D-A HTMs (i.e., 0.67 V vs NHE for state-of-the-art HTM **spiro-OMeTAD**). The stabilized E_{HOMO} values may preclude use in PSCs because HOMOs may not be sufficiently high in energy (i.e., >70 mV less positive than perovskite valence

band) to participate in a one-electron redox chemistry relevant for hole extraction from the perovskite conduction band.

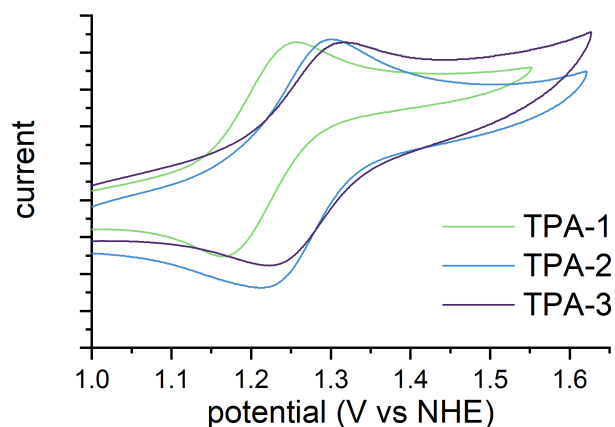


Figure 6-5 Cyclic voltammograms (CVs) of TPA-1, TPA-2, and TPA-3 recorded in 0.1 M $n\text{-NBu}_4\text{PF}_6$ DCM solutions at room temperature. Data were collected at a scan rate of 50 mV/s.

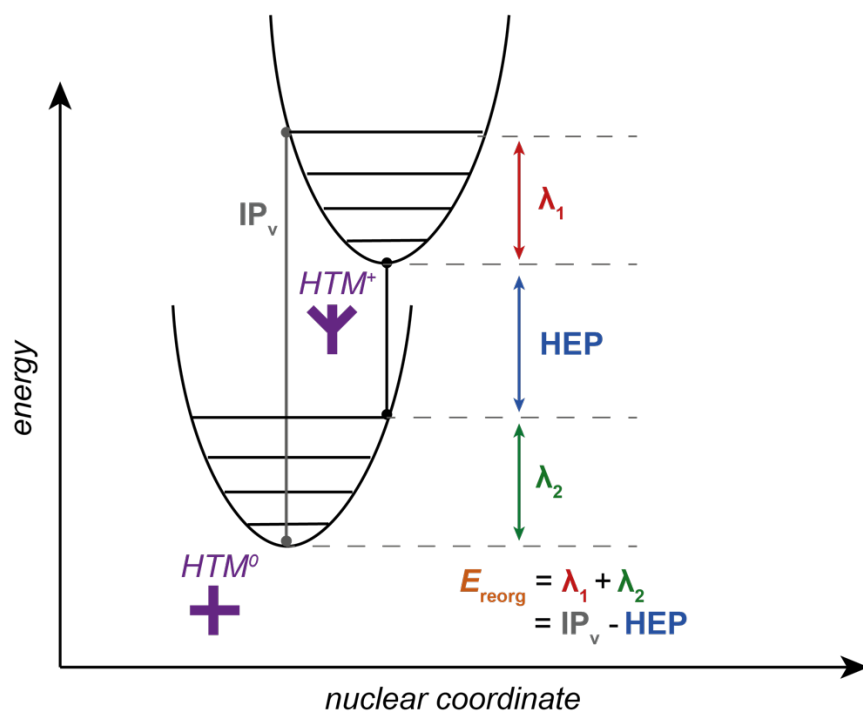


Figure 6-6 Visual representation of computed energies relevant to reorganization energy components (λ_1 and λ_2), hole extraction potential (HEP), and ionization potentials (IP) of neutral and charge HTM molecules.

Increasing the number of acceptor units increased the molar extinction coefficients (ϵ) of **TPA-X** HTMs (Figure 6-7a). The increase in ϵ is fully supported by time-dependent density functional theory (TD-DFT) calculations, which reported increasing oscillator strength of the HOMO-LUMO (D-A) transition from **TPA-1** to **TPA-3** (Figure 6-7c). The agreement between experimental and theoretical spectra confirmed the modelling used for **TPA-1**, **TPA-2**, and **TPA-3** and the parameters relating to hole mobility extracted from the models (i.e., reorganization energies, small polaron stabilization energies, and hole extraction potentials). The increase in vertical ionization potential (IP_v in Table 6-1) from **TPA-1** to **TPA-3** is proportional to a number of properties related to hole mobility, including reorganization energy and small polaron stabilization energy.

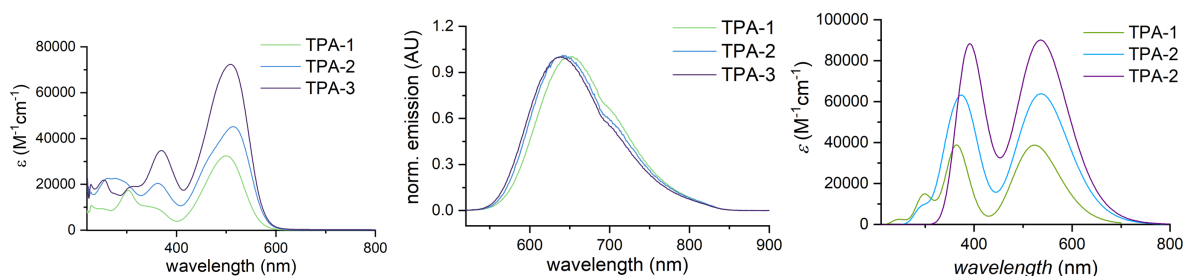


Figure 6-7 (a) Experimental UV-Vis absorption, (b) experimental emission, and (c) theoretical absorption spectra for **TPA-1**, **TPA-2**, and **TPA-3**.

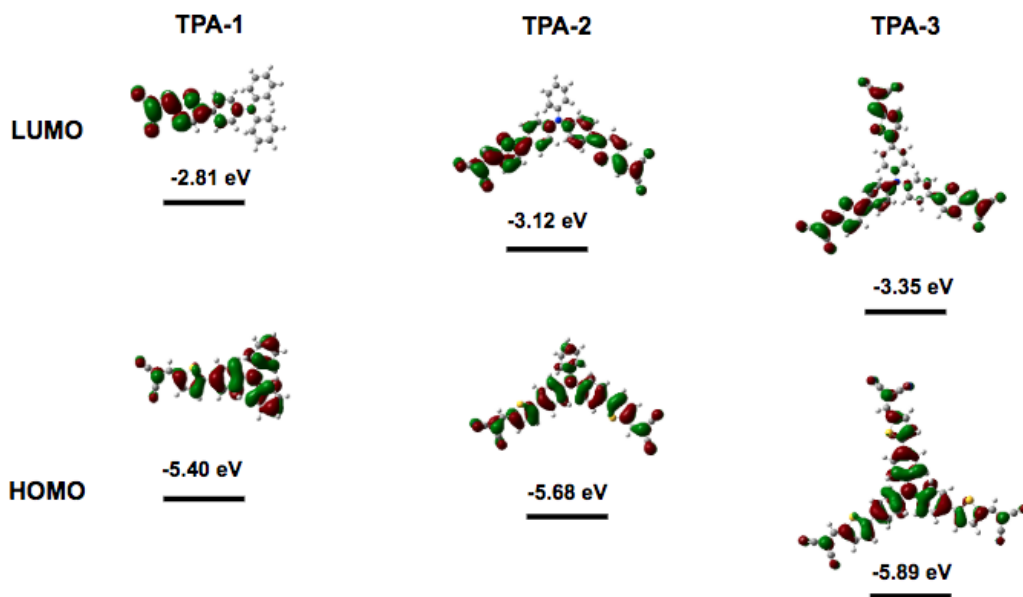


Figure 6-8 Calculated frontier orbitals of optimized structures for **TPA-1**, **TPA-2**, and **TPA-3** plotted at an absolute isovalue of 0.02.

6.2.5 Computed properties

Reorganization energy, small polaron stabilization energy, and hole extraction potential (Figure 6-6) are three factors that affect hole mobility and were computed and tabulated in Table 6-2. Reorganization energy (E_{reorg}) is the amount of energy required to modify an HTM from neutral geometry to oxidized geometry. According to Marcus theory, the rate of charge transfer is exponentially proportional to E_{reorg} and, hence, a low E_{reorg} will contribute to faster hole transfer and higher hole mobility. The E_{reorg} values computed for **TPA-1**, **TPA-2**, and **TPA-3** were 0.23, 0.40, and 0.43 eV, respectively. The small polaron stabilization energy (λ_1) estimates the self-trapping energy of holes on an HTM molecule and is inversely proportional to hole mobility. The small polaron stabilization energies for **TPA-1**, **TPA-2**, and **TPA-3** are 0.11, 0.19, and 0.27 eV, respectively. Lastly, the hole extraction potential (HEP) must be small to avoid electron-hole pair

recombination and to promote charge dissociation with minimal Coulombic interactions. The hole extraction potentials for **TPA-1**, **TPA-2**, and **TPA-3** are 6.33, 6.34, and 6.48 eV, respectively. The reorganization energies, small polaron stabilization energies and hole extraction potentials all predicted that **TPA-1** would demonstrate the highest hole mobility of the series under study, thereby supporting my experimental results.

Table 6-2 Computed factors affecting hole mobility for **TPA-1**, **TPA-2**, and **TPA-3**

Compound	E_{reorg} (eV)	small polaron stabilization energy (eV)	hole extraction potential (eV)
TPA-1	0.23	0.11	6.33
TPA-2	0.40	0.19	6.34
TPA-3	0.43	0.27	6.48

6.3 Conclusions

This study provides the first systematic analysis of hole mobility, photophysical, electrochemical, and bulk thermal properties for a series of D-A HTM analogues. Significant differences in hole mobility were experimentally determined, and **TPA-1** exhibited the highest hole mobility of the series ($4.49 \times 10^{-4} \text{ cm}^2/\text{Vs}$). Increasing the number of acceptor units imparted measurable increases in E_{HOMO} values and the ϵ values of the **TPA-X** series under study. The high hole mobility of **TPA-1** was explained by the low computed reorganization energy, small polaron stabilization energy, and hole extraction potential of this HTM. More HTMs should be designed with the under-investigated monopodal structure of **TPA-1**, but with a focus on destabilizing the E_{HOMO} through the addition of less electron-withdrawing acceptor groups and increasing T_g with steric bulk to ensure efficient function in a PSC.

6.4 Experimental

6.4.1 Synthesis

All reagents were obtained from MilliporeSigma, Alfa Aesar or Fisher Scientific and used as received. All reactions were performed using toluene that was passed through a solvent purification system prior to use. Standard inert atmosphere and Schlenk techniques were carried out under nitrogen. All reactions and purification were carried out in the dark. Purification by column chromatography was performed using silica (Silicycle: Ultrapure Flash Silica). Analytical thin-layer chromatography (TLC) was performed on aluminum-backed sheets pre-coated with silica 60 F-254 adsorbent (250 μm thick; Silicycle, QC, Canada) and visualized under UV light. Routine ^1H and ^{13}C NMR spectra were collected on a Bruker AV300 or Bruker AV400 inv/dir instrument at ambient temperatures, operating at 400 MHz and 100 MHz, respectively. Chemical shifts (δ) are reported in parts per million (ppm) using the residual signals δ 7.26 and 77.0 for CDCl_3 , δ 2.05 and 29.8 for acetone- d_6 and δ 2.50 and 39.4 for $\text{DMSO-}d_6$ as internal references for ^1H and ^{13}C , respectively. Work on this project is ongoing and full characterization by ^1H NMR, ^{13}C NMR and high resolution mass spectrometry is lacking at the time of submission.

TPA-1TA (5-(4-(diphenylamino)phenyl)thiophene-2-carbaldehyde): 4-bromo-N,N-diphenylamine (0.200 g, 0.62 mmol), (5-formylthiophen-2-yl)boronic acid (0.126 g, 0.80 mmol), palladium tetrakis(triphenylphosphine) (0.036 g, 0.030 mmol) and potassium acetate (0.200 g, 2.04 mmol) were added sequentially to 25 mL of sparged THF/ H_2O (9:1, v/v) under N_2 . The reaction mixture was stirred and left at reflux for 16 h, then cooled to room temperature. THF was then removed *in vacuo*. A crude mixture was extracted with 20 mL of distilled water and 3 \times 20 mL DCM. The organic phase was collected, dried over MgSO_4 and reduced under pressure. Purification by silica column chromatography (SiO_2 : hexanes/DCM of 9:1, R_f = 0.37) yielded

0.145 g (75.4%) of product as an orange solid. ¹H NMR (300 MHz, Acetone-*d*₆) δ 9.91 (s, 1H), 7.93 (d, *J* = 4.0 Hz, 1H), 7.73 – 7.65 (m, 2H), 7.56 (d, *J* = 4.0 Hz, 1H), 7.41 – 7.31 (m, 4H), 7.20 – 7.12 (m, 6H), 7.08 – 7.00 (m, 2H).

TPA-1 (2-((5-(4-(diphenylamino)phenyl)thiophen-2-yl)methylene)malononitrile): **TPA-1TA** (0.167 g, 0.47 mmol), malononitrile (0.037 g, 0.56 mmol) and piperidine (1 mL) were added to acetonitrile (20 mL) under N₂. The mixture was stirred and left at reflux for 16 h, then cooled to room temperature and solvent was removed *in vacuo*. Purification by silica column chromatography (SiO₂: hexanes/EtOAc of 4:1, R_f = 0.31) yielded 0.171 g (86.1%) of product as a metallic red solid. ¹H NMR (300 MHz, Acetone-*d*₆) δ 8.37 (s, 1H), 7.95 (d, *J* = 4.1 Hz, 1H), 7.77 – 7.70 (m, 2H), 7.65 (d, *J* = 4.2 Hz, 1H), 7.43 – 7.33 (m, 4H), 7.22 – 7.13 (m, 6H), 7.09 – 7.01 (m, 2H).

TPA-2Br (4-bromo-*N*-(4-bromophenyl)-*N*-phenylaniline): triphenylamine (1.50 g, 6.12 mmol) and *N*-bromosuccinimide (2.29 g, 12.85 mmol) was added to dichloromethane (20 mL) under N₂ at 0 °C. Reaction mixture was brought to room temperature and was stirred for 16 h. The reaction mixture was quenched with distilled water (20 mL) and extracted with 3 × 20 mL DCM. The organic phase was collected, dried over MgSO₄ and solvent was removed *in vacuo*. Purification by silica column chromatography (SiO₂: hexanes/DCM of 4:1, R_f = 0.45) yielded 2.33 g (96.1%) of product as a white solid.

TPA-2TA (5,5'-((phenylazanediyl)bis(4,1-phenylene))bis(thiophene-2-carbaldehyde)): **TPA-2Br** (0.200 g, 0.50 mmol), (5-formylthiophen-2-yl)boronic acid (0.170 g, 1.01 mmol), palladium tetrakis(triphenylphosphine) (0.086 g, 0.070 mmol) and potassium acetate (0.299 g, 3.05 mmol) were added sequentially to 25 mL of sparged THF/H₂O (9:1, *v/v*) under N₂. The reaction mixture was stirred and left at reflux for 16 h, then cooled to room temperature. THF was then removed *in*

vacuo. A crude mixture was extracted with 20 mL of distilled water and 3 × 20 mL DCM. The organic phase was collected, dried over MgSO₄ and reduced under pressure. Purification by silica column chromatography (SiO₂: hexanes/EtOAc of 3:1, R_f = 0.21) yielded 0.133 g (57.1%) of product as a tacky yellow solid. ¹H NMR (300 MHz, Acetone-*d*₆) δ 9.93 (s, 2H), 7.95 (d, *J* = 4.0 Hz, 2H), 7.83 – 7.75 (m, 4H), 7.60 (d, *J* = 4.0 Hz, 2H), 7.48 (d, *J* = 4.0 Hz, 2H), 7.27-7.12 (m, 7H)

TPA-2 (2,2'-((((phenylazanediy)bis(4,1-phenylene))bis(thiophene-5,2-diyl))bis(methaneylylidene))dimalononitrile): **TPA-2TA** (0.130 g, 0.28 mmol), malononitrile (0.044 g, 0.67 mmol) and piperidine (2 mL) were added to acetonitrile (20 mL) under N₂. The mixture was stirred and left at reflux for 16 h, then cooled to room temperature and solvent was removed *in vacuo*. Purification by silica column chromatography (SiO₂: hexanes/EtOAc of 2:1, R_f = 0.68) yielded 0.131 g (83.3%) of product as a purple-red solid. ¹H NMR (300 MHz, Acetone-*d*₆) δ 8.40 (d, *J* = 0.6 Hz, 2H), 7.97 (d, *J* = 4.1 Hz, 2H), 7.84 – 7.79 (m, 4H), 7.71 (d, *J* = 4.1 Hz, 2H), 7.45 (t, 2H), 7.28 – 7.18 (m, 7H).

TPA-3Br (tris(4-bromophenyl)amine): triphenylamine (1.50 g, 6.12 mmol) and N-bromosuccinimide (3.81 g, 21.4 mmol) was added to dichloromethane (20 mL) under N₂ at 0 °C. Reaction mixture was brought to room temperature and was stirred for 16 h. The reaction mixture was quenched with distilled water (20 mL) and extracted with 3 × 20 mL DCM. The organic phase was collected, dried over MgSO₄ and solvent was removed *in vacuo*. Evaporation yielded 2.70 g (91.9%) of product as a white solid.

TPA-3T (tris(4-(thiophen-2-yl)phenyl)amine): **TPA-3Br** (0.500 g, 1.05 mmol), thiophen-2-ylboronic acid (0.725 g, 3.45 mmol), palladium tetrakis(triphenylphosphine) (0.362 g, 0.300 mmol) and potassium bicarbonate (0.333 g, 3.14 mmol) were added sequentially to 25 mL of sparged toluene/H₂O (10:1, *v/v*) under N₂. The reaction mixture was stirred and left at reflux for

16 h, then cooled to room temperature. THF was then removed *in vacuo*. A crude mixture was extracted with 20 mL of distilled water and 3 × 20 mL DCM. The organic phase was collected, dried over MgSO₄ and reduced under pressure. Purification by silica column chromatography (SiO₂: hexanes/EtOAc of 7:1, R_f = 0.36) yielded 0.382 g (73.6%) of product as a yellow crystalline solid.

TPA-3TA (5,5',5''-(nitrilotris(benzene-4,1-diyl))tris(thiophene-2-carbaldehyde)): **TPA-3T** (0.385 g, 0.78 mmol) was dissolved in 1,2-dichlorobenzene (20 mL). Phosphorous oxychloride (0.718 g, 4.7 mmol, 0.44 mL) and DMF (0.513 g, 7.04 mmol, 0.55 mL) were added dropwise by syringe. Mixture was heated to 85 °C for 7 h, then reaction was cooled to room temperature. 0.1 M Na₂CO₃ (30 mL) was added slowly and allowed to reaction for 30 min. A crude mixture was extracted with 3 × 20 mL DCM. The organic phase was collected, dried over MgSO₄ and reduced under pressure. Purification by silica column chromatography (SiO₂: DCM, R_f = 0.62) yielded 0.323 g (72.4%) of product as a yellow crystalline solid. ¹H NMR (300 MHz, Acetone-*d*₆) δ 9.93 (s, 3H), 7.96 (d, *J* = 4.0 Hz, 3H), 7.76 (dd, *J* = 16.3, 8.7 Hz, 6H), 7.62 (d, *J* = 4.0 Hz, 3H), 7.21 (d, *J* = 8.7 Hz, 6H), 7.02 (d, *J* = 8.7 Hz, 3H).

TPA-3 (2,2',2''-(((nitrilotris(benzene-4,1-diyl))tris(thiophene-5,2-diyl))tris(methaneylylidene))trimalononitrile): **TPA-3TA** (0.250 g, 0.40 mmol), malononitrile (0.095 g, 1.44 mmol) and piperidine (2 mL) were added to acetonitrile (20 mL) under N₂. The mixture was stirred and left at reflux for 16 h, then cooled to room temperature and solvent was removed *in vacuo*. Purification by silica column chromatography (SiO₂: hexanes/EtOAc of 2:1, R_f = 0.57) yielded 0.159 g (83.1%) of product as a purple-red solid. ¹H NMR (300 MHz, Acetone-*d*₆) δ 8.42 (s, 3H), 7.99 (d, *J* = 4.1 Hz, 3H), 7.87 (d, *J* = 8.7 Hz, 6H), 7.75 (d, *J* = 4.1 Hz, 3H), 7.32 (d, *J* = 8.7 Hz, 6H).

6.4.2 Electrical properties

For conductivity measurements, four parallel Au electrodes with a spacing of 0.75 mm and length of 23 mm were used to measure the film conductivities in the dark and under ambient conditions. A Keithley 2400 source meter was used to force current through the outer electrodes while sensing the voltage across the inner two electrodes. A linear fit of each measurement was used to determine the resistance, R , and the sample geometry was then used to calculate the conductivity, σ , according to the equation

$$\sigma = \frac{d}{Rlt} \quad \text{(Equation 6-2)}$$

where l is the electrode length, d is the inter-electrode spacing and t is the film thickness. The film thickness was measured using a Bruker DektakXT profilometer. Light soaking chamber was manufactured in house. The light source is a 1000 W metal halide lamp with 1 sun exposure (wavelength range: ~390-750 nm). A built-in fan is used to keep temperatures below 45°C as measured by a thermocouple.

The hole-only devices were fabricated with a structure of glass/ITO/PEDOT:PSS/HTMs/Au according to previous literature. The HTMs were doped with tBP and LiTFSI. The dopant concentration was kept constant for all HTMs and the same as used in PSCs. Hole mobility was investigated by the space-charge-limit current (SCLC) method, which can be described with the **Equation 6-1**

where μ is the hole mobility, J is the current density, ϵ_0 is the vacuum permittivity, ϵ_r is the dielectric constant of the material (normally taken to approach 3 for organic semiconductors), V is the applied bias, and d is the film thickness. The applied bias was measured from 0 to 5 V.

6.4.3 Bulk thermal properties

DSC curves of compounds were collected using a Netzsch DSC 214 Polyma instrument under a nitrogen protective atmosphere. For each measurement, two aluminum crucibles were used, one for material measurement and the other as empty reference. A customized heating program was developed to include a 5 min hold at the initial temperature of 50 °C, and four continuous cycles between to 50 °C and 300 °C with a heating/cooling rate of 10 K/min and 5 min holds at 50 °C and 300 °C. Data from the heating segment of last 3 cycles were used to identify the T_m (melting point) and extrapolate the T_g (glass transition temperature) of the material.

X-ray diffraction measurements were performed with a Rigaku Smartlab diffractometer in parallel beam geometry using Cu K α radiation. The data were collected with a 0.04° step size from 2-90° at a rate of 1.6 s/step. A 0.3° grazing incidence angle was used.

6.4.4 Electrochemical and photophysical properties

Solution electrochemical data were recorded with a CHI660D potentiostat at room temperature using a platinum wire counter electrode and a platinum working electrode. Ag/AgCl in saturated KCl was used as the reference electrode and was calibrated versus the normal hydrogen electrode (NHE) by the addition of Fc⁺/Fc. A 0.1 M *n*-NBu₄PF₆ DCM solution was used for all HTMs. CV data were acquired for 0.5 mM solutions of each HTM at a scan rate of 50 mV s⁻¹.

Solution UV-Vis absorption spectra were collected on a Cary 5000 spectrophotometer. Photoluminescence spectra were recorded with a Cary Eclipse fluorimeter. All samples were measured in a 1-cm quartz cell at room temperature in HPLC grade DCM. The concentrations of the DCM solutions of analytes for UV-Vis and photoluminescence measurements were 2 × 10⁻⁵ mol L⁻¹ and 1 × 10⁻⁵ mol L⁻¹, respectively.

6.4.5 Computed properties

DFT calculations were performed for all molecules in the gas phase using B3LYP/6-31G(d,p) in Gaussian 09. Vibrational frequencies were computed to ensure structures were optimized to energy minima and the total energy of each compound was taken from the total thermal and electronic energy. Theoretical UV-vis absorption spectra were obtained from the results of TD-DFT calculations and orbital images were generated using the cubegen utility. To approximate the geometry of the **TPA-X** molecules within an HTM film, the rotational angle between the phenyl rings was held fixed at approximately 10°. The geometric restriction was taken as a reasonable estimate of the reduced mobility of the TPA cores in a film due to the good agreement of the computed oxidation potentials and absorption spectra with empirical data. The oxidation potentials were calculated using isodesmic reactions with the empirical oxidation potential of **TPA-2** as the reference potential. Systematic errors in computing oxidation potentials are eliminated through the use of isodesmic reactions.^{Ref1} ΔG for the isodesmic reactions can be calculated using the change in free energy of the reaction



$$\Delta G = G_{\text{products}} - G_{\text{reactants}} \quad \text{(Equation 6-5)}$$

Where $\mathbf{TPA-X}_{\text{neut}}$ and $\mathbf{TPA-X}_{\text{ox}}$ are the neutral and oxidized **TPA-X** compound of interest and $\mathbf{TPA-2}^+$ and **TPA-2** are the oxidized and neutral **TPA-2** molecule. ΔG for the isodesmic reaction is then used to calculate the oxidation potential E_0 using the equation:

$$E_0 = -\Delta G/F + E_0^{\text{ref}} \quad \text{(Equation 6-6)}$$

Where F is Faraday's constant and E_0^{ref} is the oxidation potential of the reference compound ($E_0^{\text{ref}} = 1.24 \text{ V vs SHE}$). The oxidation potential of **TPA-2** is accurate by design as a result of using the

empirical oxidation potential of **TPA-2** as the reference potential. Reorganization energies (E_{reorg}) for hole transfer were calculated according to:

$$E_{\text{reorg}} = \lambda_1 + \lambda_2 = [M^+(0) - M(0)] + [M^+(+) - M(+)] \quad \text{(Equation 6-7)}$$

Where $M(0)$ and $M(+)$ are the neutral and oxidized HTMs with a neutral geometry and $M^+(0)$ and $M^+(+)$ are the neutral and oxidized HTMs with the oxidized geometry. The small polaron stabilization energy (SPE) was calculated as the energy difference between the adiabatic and vertical ionization potentials ($\text{IP}_{(a)} - \text{IP}_{(v)}$).^{Ref1} The hole extraction potential is the potential difference between the electronic band gap, estimated as the HOMO-LUMO gap, and the first singlet excited state.^{Ref2} It was calculated using

$$E_b = \Delta_{\text{H-L}} - E_1 \quad \text{(Equation 6-8)}$$

Where $\Delta_{\text{H-L}}$ is the HOMO-LUMO energy gap and E_1 is the energy of the first singlet excited state.

Chapter 7: Conclusions and Future Directions

7.1 Conclusions

The main objectives of this thesis were to suppress degradation of the perovskite layer and the hole transport material (HTM) layer to improve the commercial viability of perovskite solar cells (PSCs). My experiments were designed to address moisture-induced degradation of the photoactive perovskite layer,^{148,149} thermal instability of HTM film morphologies,¹⁵⁰ and issues associated with the diffusion of dopants, which are added to improve HTM film conductivity.^{28,151} The experiments in this dissertation outlined how to develop HTMs that can encapsulate photoactive perovskite layers to provide protection against water exposure, and how to design HTMs that circumvent morphological changes and dopant diffusion.

Chapter 3 described how the highest occupied molecular orbital (HOMO) energy levels and hole mobilities could be modulated with the substituents appended to a spiro[fluorene-9,9'-xanthene] core. I designed and synthesized a series of seven spiro-centred HTMs with substituents which vary in steric bulk, electron-withdrawing strength and location about the HTM. Sterically bulky, non-polar substituents increased the hole mobilities of HTMs by decreasing conformational and electrostatic disorder. These experimental results were supported by a computational model developed from bulk multi-dimensional simulations of approximately 1000 molecules.

Chapter 4 defined a previously unreported structure-property relationship whereby the location of triphenylamine (TPA) units appended to a spiro-carbon core significantly impacted the glass transition temperatures (T_g s) of HTMs. T_g s must be maintained above 90° C to prevent morphological changes to the HTM layer during PSC operation, and I found that the location of TPA groups around a spiro[fluorene-9,9'-xanthene]) core influences both the T_g and HOMO level of the HTM.²⁶ We leveraged this structure-property relationship to improve the morphological

stability of films while ensuring sufficient free energy change for hole-extraction from the perovskite. These design principles were applied in subsequent projects to ensure morphologically stable HTMs with appropriate energetics for hole extraction.

Chapter 5 showcased an HTM with polymerizable functionality to form an encapsulation layer in a PSC to prevent the ingress of water into the cell. I designed a novel HTM that could undergo thermal or electrochemical polymerization, which successfully lowered film wettability. However, the material only exhibited a 6.1% power conversion efficiency (PCE) in PSC proof-of-concept experiments, and hence, further optimization of the encapsulation process and long-term stability studies remain to be conducted.

Chapter 6 contributed to a research effort which develops donor-acceptor (D-A) HTMs that do not require dopants to achieve useful conductivities ($> 1 \times 10^{-4}$ S/cm). A series containing monopodal, bipodal, and tripodal D-A HTMs was developed and investigated using physical and computational methods. The monopodal D-A HTM demonstrated the highest hole mobility because of the low computed reorganization energy, small polaron stabilization energy and hole extraction potential. These HTMs may be a useful new class of dopant-free PSCs, but more work is required.

7.2 Future directions

Spiro-VNPB in Chapter 5 was designed with styrene groups to undergo thermal polymerization to yield films less resistant to water penetration over time. The low conductivity of **spiro-VNPB**, however, resulted in PSCs with 1% PCE. I propose the investigation of **spiro-VNPB** at a styrene-functionalized perovskite surface to create a monolayer of crosslinked HTM at the perovskite/HTM interface. The interface between the perovskite and HTM layer must be optimized to increase the efficiency of hole extraction following light-absorption. Following

preparation of the 500-700 nm thick perovskite layer with the desired bulk AMX_3 composition for high performance, the organic cation (A) at the surface could be replaced with a styrene-functionalized ammonium (Figure 7-1). The styrene-functionalized ammonium could, in turn, be exploited to crosslink with a thin layer of **spiro-VNPB** by thermal annealing. A 200-nm layer of a champion HTM (e.g., **HTM-FX'** or **spiro-OMeTAD**) could be deposited on top of the thermally polymerized **spiro-VNPB** layer. This should improve both the perovskite/HTM interface by providing a covalent linkage between the perovskite and HTM and prevent the penetration of water by incorporating a polymerized network.

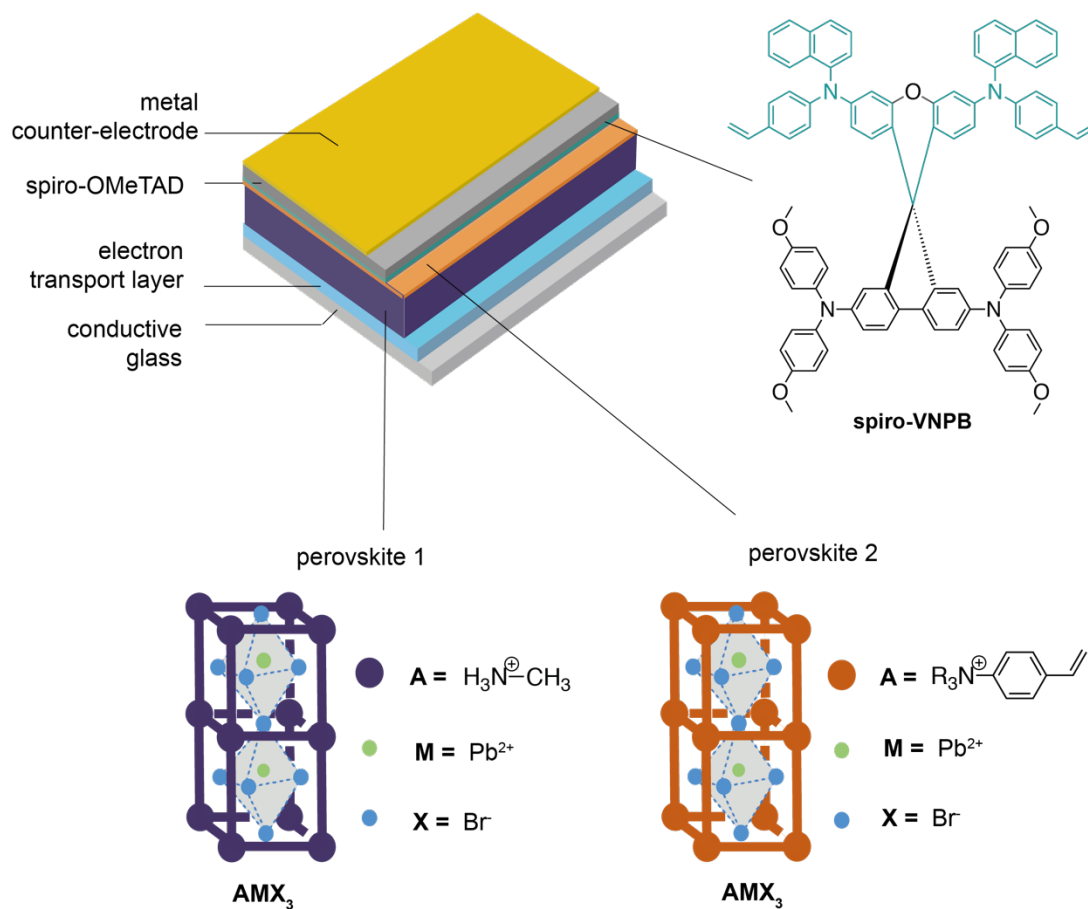


Figure 7-1 Proposed architecture of future directions for PSCs where the interface between the perovskite and HTM layers is manipulated by surface functionalization of the AMX_3 perovskite structure and the incorporation of polymerizable HTM.

The monopodal donor-acceptor (D-A) architecture of **TPA-1** in **Chapter 6** exhibited high hole mobility without the use of dopants, the high redox potential (>1.2 V vs NHE) conferred limited free energy change for hole extraction and the low T_g (59 °C) precluded use in a PSC. Computational screening could be employed to predict the effects of more weakly electron-withdrawing acceptor groups on the redox potential of candidate compounds (Figure 7-2). Laborious synthesis and characterization would only need to be performed on materials that have been predicted to exhibit greater than 70 mV more positive HOMO level than the perovskite conduction band to ensure sufficient free energy change for charge extraction.

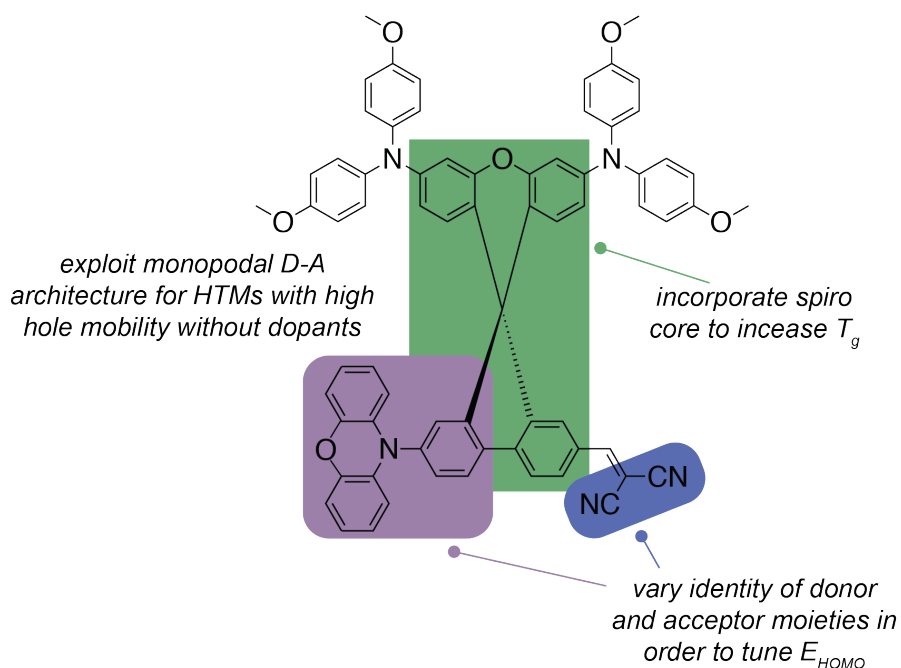


Figure 7-2 Proposed molecular structure of monopodal D-A HTM with spiro-core to increase T_g and opportunity to vary donor and acceptor identities and E_{HOMO} .

The high T_g imparted by the spiro-carbon core relative to isomeric linear HTMs and the high hole mobility of monopodal D-A HTMs could potentially be combined to design thermally stable, dopant-free HTMs.^{64,65} The incorporation of more rigid structures within the D-A

architecture should increase the T_g values of the HTMs studied above 90 °C (this property is needed for practical operation). Greater rigidity can be incorporated in either the donor group (e.g., bridged TPA units) or by creating a D-A architecture across a spiro-carbon core. Additionally, shortening the D-A molecule by eliminating the pi-bridge could restrict the conformational freedom of the molecule and increase the T_g values of these HTMs.

Over 2000 publications on improving the stability of PSCs have been published, but many challenges remain. I hope that the approaches laid out in this dissertation will engender higher PSC stability to advance PSCs into commercial production and use.

References

- (1) National Renewable Energy Laboratory. PV Research Cell Record Efficiency Chart. <https://www.nrel.gov/pv/assets/pdfs/pv-efficiency-chart.20190103.pdf>. (Accessed December 18th, 2018)
- (2) Rong, Y.; Hu, Y.; Mei, A.; Tan, H.; Saidaminov, M. I.; Seok, S. I.; McGehee, M. D.; Sargent, E. H.; Han, H. Challenges for Commercializing Perovskite Solar Cells. *Science* **2018**, *361* (6408).
- (3) Qiu, L.; Ono, L. K.; Qi, Y. Advances and Challenges to the Commercialization of Organic–inorganic Halide Perovskite Solar Cell Technology. *Materials Today Energy* **2018**, *7*, 169–189.
- (4) Kim, H.-S.; Lee, C.-R.; Im, J.-H.; Lee, K.-B.; Moehl, T.; Marchioro, A.; Moon, S.-J.; Humphry-Baker, R.; Yum, J.-H.; Moser, J. E.; et al. Lead Iodide Perovskite Sensitized All-Solid-State Submicron Thin Film Mesoscopic Solar Cell with Efficiency Exceeding 9%. *Sci. Rep.* **2012**, *2*, 591.
- (5) Etgar, L.; Gao, P.; Xue, Z.; Peng, Q.; Chandiran, A. K.; Liu, B.; Nazeeruddin, M. K.; Grätzel, M. Mesoscopic CH₃NH₃PbI₃/TiO₂ Heterojunction Solar Cells. *J. Am. Chem. Soc.* **2012**, *134* (42), 17396–17399.
- (6) Leguy, A. M. A.; Hu, Y.; Campoy-Quiles, M.; Alonso, M. I.; Weber, O. J.; Azarhoosh, P.; van Schilfgaarde, M.; Weller, M. T.; Bein, T.; Nelson, J.; et al. Reversible Hydration of CH₃NH₃PbI₃ in Films, Single Crystals, and Solar Cells. *Chem. Mater.* **2015**, *27* (9), 3397–3407.
- (7) Yi, C.; Luo, J.; Meloni, S.; Boziki, A.; Ashari-Astani, N.; Grätzel, C.; Zakeeruddin, S. M.; Röthlisberger, U.; Grätzel, M. Entropic Stabilization of Mixed A-Cation ABX₃ Metal Halide Perovskites for High Performance Perovskite Solar Cells. *Energy Environ. Sci.* **2016**, *9* (2), 656–662.
- (8) Molina-Ontoria, A.; Zimmermann, I.; Garcia-Benito, I.; Gracia, P.; Roldán-Carmona, C.; Aghazada, S.; Grätzel, M.; Nazeeruddin, M. K.; Martín, N. Benzotrithiophene-Based Hole-Transporting Materials for 18.2 % Perovskite Solar Cells. *Angew. Chem. Int. Ed.* **2016**, *55* (21), 6270–6274.
- (9) Niu, G.; Guo, X.; Wang, L. Review of Recent Progress in Chemical Stability of Perovskite Solar Cells. *J. Mater. Chem. A Mater. Energy Sustain.* **2015**, *3* (17), 8970–8980.
- (10) Noel, N. K.; Stranks, S. D.; Abate, A.; Wehrenfennig, C.; Guarnera, S.; Haghighirad, A.-A.; Sadhanala, A.; Eperon, G. E.; Pathak, S. K.; Johnston, M. B.; et al. Lead-Free Organic–inorganic Tin Halide Perovskites for Photovoltaic Applications. *Energy Environ. Sci.* **2014**, *7* (9), 3061–3068.
- (11) Wang, D.; Wright, M.; Elumalai, N. K.; Uddin, A. Stability of Perovskite Solar Cells. *Sol. Energy Mater. Sol. Cells* **2016**, *147*, 255–275.
- (12) Kundu, S.; Kelly, T. L. Improving the Moisture Stability of Perovskite Solar Cells by Using PMMA/P3HT Based Hole-Transport Layers. *Mater. Chem. Front.* **2017**, *2* (1), 81–89.
- (13) Habisreutinger, S. N.; Leijtens, T.; Eperon, G. E.; Stranks, S. D.; Nicholas, R. J.; Snaith, H. J. Carbon Nanotube/polymer Composites as a Highly Stable Hole Collection Layer in Perovskite Solar Cells. *Nano Lett.* **2014**, *14* (10), 5561–5568.
- (14) Koene, B. E.; Loy, D. E.; Thompson, M. E. Asymmetric Triaryldiamines as Thermally Stable Hole Transporting Layers for Organic Light-Emitting Devices. *Chem. Mater.* **1998**, *10* (8), 2235–2250.

- (15) Leijtens, T.; Ding, I.-K.; Giovenzana, T.; Bloking, J. T.; McGehee, M. D.; Sellinger, A. Hole Transport Materials with Low Glass Transition Temperatures and High Solubility for Application in Solid-State Dye-Sensitized Solar Cells. *ACS Nano* **2012**, *6* (2), 1455–1462.
- (16) Zuo, C.; Bolink, H. J.; Han, H.; Huang, J.; Cahen, D.; Ding, L. Advances in Perovskite Solar Cells. *Adv. Sci.* **2016**, *3* (7), 1500324.
- (17) Fu, Q.; Tang, X.; Huang, B.; Hu, T.; Tan, L.; Chen, L.; Chen, Y. Recent Progress on the Long-Term Stability of Perovskite Solar Cells. *Adv. Sci.* **2018**, *5* (5), 1700387.
- (18) Lee, M. M.; Teuscher, J.; Miyasaka, T.; Murakami, T. N.; Snaith, H. J. Efficient Hybrid Solar Cells Based on Meso-Superstructured Organometal Halide Perovskites. *Science* **2012**, *338* (6107), 643–647.
- (19) Kojima, A.; Teshima, K.; Shirai, Y.; Miyasaka, T. Organometal Halide Perovskites as Visible-Light Sensitizers for Photovoltaic Cells. *J. Am. Chem. Soc.* **2009**, *131* (17), 6050–6051.
- (20) Tan, H.; Jain, A.; Voznyy, O.; Lan, X.; García de Arquer, F. P.; Fan, J. Z.; Quintero-Bermudez, R.; Yuan, M.; Zhang, B.; Zhao, Y.; et al. Efficient and Stable Solution-Processed Planar Perovskite Solar Cells via Contact Passivation. *Science* **2017**, *355* (6326), 722–726.
- (21) Domanski, K.; Correa-Baena, J.-P.; Mine, N.; Nazeeruddin, M. K.; Abate, A.; Saliba, M.; Tress, W.; Hagfeldt, A.; Grätzel, M. Not All That Glitters Is Gold: Metal-Migration-Induced Degradation in Perovskite Solar Cells. *ACS Nano* **2016**, *10* (6), 6306–6314.
- (22) Maciejczyk, M.; Ivaturi, A.; Robertson, N. SFX as a Low-Cost “Spiro” Hole-Transport Material for Efficient Perovskite Solar Cells. *J. Mater. Chem. A Mater. Energy Sustain.* **2016**, *4* (13), 4855–4863.
- (23) Xu, B.; Bi, D.; Hua, Y.; Liu, P.; Cheng, M.; Grätzel, M.; Kloo, L.; Hagfeldt, A.; Sun, L. A Low-Cost Spiro[fluorene-9,9'-Xanthene]-Based Hole Transport Material for Highly Efficient Solid-State Dye-Sensitized Solar Cells and Perovskite Solar Cells. *Energy Environ. Sci.* **2016**, *9* (3), 873–877.
- (24) Park, J. H.; Seo, J.; Park, S.; Shin, S. S.; Kim, Y. C.; Jeon, N. J.; Shin, H.-W.; Ahn, T. K.; Noh, J. H.; Yoon, S. C.; et al. Efficient CH₃NH₃PbI₃ Perovskite Solar Cells Employing Nanostructured P-Type NiO Electrode Formed by a Pulsed Laser Deposition. *Adv. Mater.* **2015**, *27* (27), 4013–4019.
- (25) Zhou, X.; He, J.; Liao, L. S.; Lu, M.; Ding, X. M.; Hou, X. Y.; Zhang, X. M.; He, X. Q.; Lee, S. T. Real-Time Observation of Temperature Rise and Thermal Breakdown Processes in Organic LEDs Using an IR Imaging and Analysis System. *Adv. Mater.* **2000**, *12* (4), 265–269.
- (26) Chiykowski, V. A.; Cao, Y.; Tan, H.; Tabor, D. P.; Sargent, E. H.; Aspuru-Guzik, A.; Berlinguette, C. P. Precise Control of Thermal and Redox Properties of Organic Hole-Transport Materials. *Angew. Chem. Int. Ed.* **2018**, *57* (47), 15529–15533.
- (27) Xu, J.; Voznyy, O.; Comin, R.; Gong, X.; Walters, G.; Liu, M.; Kanjanaboos, P.; Lan, X.; Sargent, E. H. Crosslinked Remote-Doped Hole-Extracting Contacts Enhance Stability under Accelerated Lifetime Testing in Perovskite Solar Cells. *Adv. Mater.* **2016**, *28* (14), 2807–2815.
- (28) Seo, J.-Y.; Kim, H.-S.; Akin, S.; Stojanovic, M.; Simon, E.; Fleischer, M.; Hagfeldt, A.; Zakeeruddin, S. M.; Grätzel, M. Novel P-Dopant toward Highly Efficient and Stable Perovskite Solar Cells. *Energy Environ. Sci.* **2018**, *11* (10), 2985–2992.
- (29) Huang, L.; Hu, Z.; Xu, J.; Zhang, K.; Zhang, J.; Zhang, J.; Zhu, Y. Efficient and Stable

- Planar Perovskite Solar Cells with a Non-Hygroscopic Small Molecule Oxidant Doped Hole Transport Layer. *Electrochim. Acta* **2016**, *196*, 328–336.
- (30) Pellaroque, A.; Noel, N. K.; Habisreutinger, S. N.; Zhang, Y.; Barlow, S.; Marder, S. R.; Snaith, H. J. Efficient and Stable Perovskite Solar Cells Using Molybdenum Tris(dithiolene)s as P-Dopants for Spiro-OMeTAD. *ACS Energy Lett.* **2017**, *2* (9), 2044–2050.
- (31) Mrinalini, M.; Islavath, N.; Prasanthkumar, S.; Giribabu, L. Stipulating Low Production Cost Solar Cells All Set to Retail...! *Chem. Rec.* **2018**, *19*, 661–675.
- (32) Louwen, A.; van Sark, W.; Schropp, R.; Faaij, A. A Cost Roadmap for Silicon Heterojunction Solar Cells. *Sol. Energy Mater. Sol. Cells* **2016**, *147*, 295–314.
- (33) Pizzini, S. Towards Solar Grade Silicon: Challenges and Benefits for Low Cost Photovoltaics. *Sol. Energy Mater. Sol. Cells* **2010**, *94* (9), 1528–1533.
- (34) Westbrook, R. J. E.; Sanchez-Molina, D. I.; Manuel Marin-Beloqui, D. J.; Bronstein, D. H.; Haque, D. S. A. Effect of Interfacial Energetics on Charge Transfer from Lead Halide Perovskite to Organic Hole Conductors. *J. Phys. Chem. C* **2018**, *122* (2), 1326–1332.
- (35) Polander, L. E.; Pahner, P.; Schwarze, M.; Saalfrank, M.; Koerner, C.; Leo, K. Hole-Transport Material Variation in Fully Vacuum Deposited Perovskite Solar Cells. *APL Materials* **2014**, *2* (8), 081503.
- (36) Park, N.-G.; Segawa, H. Research Direction toward Theoretical Efficiency in Perovskite Solar Cells. *ACS Photonics* **2018**, *5* (8), 2970–2977.
- (37) Hagfeldt, A.; Boschloo, G.; Sun, L.; Kloo, L.; Pettersson, H. Dye-Sensitized Solar Cells. *Chem. Rev.* **2010**, *110* (11), 6595–6663.
- (38) Gong, X.; Sun, Q.; Liu, S.; Liao, P.; Shen, Y.; Grätzel, C.; Zakeeruddin, S. M.; Grätzel, M.; Wang, M. Highly Efficient Perovskite Solar Cells with Gradient Bilayer Electron Transport Materials. *Nano Lett.* **2018**, *18* (6), 3969–3977.
- (39) Guo, J.-J.; Meng, X.-F.; Niu, J.; Yin, Y.; Han, M.-M.; Ma, X.-H.; Song, G.-S.; Zhang, F. A Novel Asymmetric Phthalocyanine-Based Hole Transporting Material for Perovskite Solar Cells with an Open-Circuit Voltage above 1.0 V. *Synth. Met.* **2016**, *220*, 462–468.
- (40) Hazarika, A.; Zhao, Q.; Gaulding, E. A.; Christians, J. A.; Dou, B.; Marshall, A. R.; Moot, T.; Berry, J. J.; Johnson, J. C.; Luther, J. M. Perovskite Quantum Dot Photovoltaic Materials beyond the Reach of Thin Films: Full-Range Tuning of A-Site Cation Composition. *ACS Nano* **2018**, *12* (10), 10327–10337.
- (41) Cai, Y.; Xie, L.; Zhang, Z.; Zhou, Y.; Liu, H.; Lu, X.; Gao, X.; Gao, J.; Shu i, L.; Wu, S.; et al. Tuning the A-Site Cation and X-Site Anion Composition of CH₃NH₃PbI₃ Perovskite Material for Efficient Planar Perovskite Solar Cells. *Electrochim. Acta* **2019**, *293*, 371–379.
- (42) Liu, X.; Yan, K.; Tan, D.; Liang, X.; Zhang, H.; Huang, W. Solvent Engineering Improves Efficiency of Lead-Free Tin-Based Hybrid Perovskite Solar Cells beyond 9%. *ACS Energy Lett.* **2018**, 2701–2707.
- (43) Chi, D.; Huang, S.; Zhang, M.; Mu, S.; Zhao, Y.; Chen, Y.; You, J. Composition and Interface Engineering for Efficient and Thermally Stable Pb-Sn Mixed Low-Bandgap Perovskite Solar Cells. *Adv. Funct. Mater.* **2018**, *358*, 1804603.
- (44) Yang, S. J.; Kim, M.; Ko, H.; Sin, D. H.; Sung, J. H.; Mun, J.; Rho, J.; Jo, M.-H.; Cho, K. Visualization and Investigation of Charge Transport in Mixed-Halide Perovskite via Lateral-Structured Photovoltaic Devices. *Adv. Funct. Mater.* **2018**, *28* (41), 1804067.
- (45) Balakrishna, R. G.; Kobosko, S. M.; Kamat, P. V. Mixed Halide Perovskite Solar Cells.

- Consequence of Iodide Treatment on Phase Segregation Recovery. *ACS Energy Lett.* **2018**, *3* (9), 2267–2272.
- (46) Qiu, X.; Cao, B.; Yuan, S.; Chen, X.; Qiu, Z.; Jiang, Y.; Ye, Q.; Wang, H.; Zeng, H.; Liu, J.; et al. From Unstable CsSnI₃ to Air-Stable Cs₂SnI₆: A Lead-Free Perovskite Solar Cell Light Absorber with Bandgap of 1.48 eV and High Absorption Coefficient. *Sol. Energy Mater. Sol. Cells* **2017**, *159*, 227–234.
- (47) Xiao, J.-W.; Liu, L.; Zhang, D.; De Marco, N.; Lee, J.-W.; Lin, O.; Chen, Q.; Yang, Y. The Emergence of the Mixed Perovskites and Their Applications as Solar Cells. *Adv. Energy Mater.* **2017**, *7* (20), 1700491.
- (48) Yang, J.; Kelly, T. L. Decomposition and Cell Failure Mechanisms in Lead Halide Perovskite Solar Cells. *Inorg. Chem.* **2017**, *56* (1), 92–101.
- (49) Wu, J.; Lan, Z.; Lin, J.; Huang, M.; Huang, Y.; Fan, L.; Luo, G. Electrolytes in Dye-Sensitized Solar Cells. *Chem. Rev.* **2015**, *115* (5), 2136–2173.
- (50) Agarwala, P.; Kabra, D. A Review on Triphenylamine (TPA) Based Organic Hole Transport Materials (HTMs) for Dye Sensitized Solar Cells (DSSCs) and Perovskite Solar Cells (PSCs): Evolution and Molecular Engineering. *J. Mater. Chem. A Mater. Energy Sustain.* **2017**, *5* (4), 1348–1373.
- (51) Sun, L.; Ichinose, K.; Sekiya, T.; Sugiura, T.; Yoshida, T. Cathodic Electrodeposition of P-CuSCN Nanorod and Its Dye-Sensitized Photocathodic Property. *Phys. Procedia* **2011**, *14*, 12–24.
- (52) O'Regan, B.; Schwartz, D. T. Large Enhancement in Photocurrent Efficiency Caused by UV Illumination of the Dye-Sensitized Heterojunction TiO₂/RuLL'NCS/CuSCN: Initiation and Potential Mechanisms. *Chem. Mater.* **1998**, *10* (6), 1501–1509.
- (53) Tennakone, K.; Senadeera, G. K. R.; De Silva, D. B. R. A.; Kottegoda, I. R. M. Highly Stable Dye-Sensitized Solid-State Solar Cell with the Semiconductor 4CuBr 3S(C₄H₉)₂ as the Hole Collector. *Appl. Phys. Lett.* **2000**, *77* (15), 2367–2369.
- (54) Tennakone, K.; G R R; Wijayantha, K. G. U. The Suppression of the Recombination of Photogenerated Carriers in a Dye-Sensitized Nano-Porous Solid-State Photovoltaic Cell. *Semicond. Sci. Technol.* **1999**, *11* (11), 1737.
- (55) Urieta-Mora, J.; García-Benito, I.; Molina-Ontoria, A.; Martín, N. Hole Transporting Materials for Perovskite Solar Cells: A Chemical Approach. *Chem. Soc. Rev.* **2018**, *47*, 8541–8571.
- (56) Kuwahara, A.; Naka, S.; Okada, H.; Onnagawa, H. Carrier Mobility of Organic Thin Films Using Lateral Electrode Structure with Optical Slits. *Appl. Phys. Lett.* **2006**, *89* (13), 132106.
- (57) Shirota, Y. Photo- and Electroactive Amorphous Molecular Materials—Molecular Design, Syntheses, Reactions, Properties, and Applications. *J. Mater. Chem.* **2005**, *15* (1), 75–93.
- (58) Kuwabara, Y.; Ogawa, H.; Inada, H.; Noma, N.; Shirota, Y. Thermally Stable Multilayered Organic Electroluminescent Devices Using Novel Starburst Molecules, 4,4',4''-Tri(N-Carbazolyl)triphenylamine (TCTA) and 4,4',4''-Tris(3-Methylphenylphenylamino)triphenylamine (m-MTDATA), as Hole-Transport Materials. *Adv. Mater.* **1994**, *6* (9), 677–679.
- (59) O'Brien, D. F.; Burrows, P. E.; Forrest, S. R.; Koene, B. E.; Loy, D. E.; Thompson, M. E. Hole Transporting Materials with High Glass Transition Temperatures for Use in Organic Light-Emitting Devices. *Adv. Mater.* **1998**, *10* (14), 1108–1112.
- (60) Xu, B.; Tian, H.; Bi, D.; Gabrielsson, E.; Johansson, E. M. J.; Boschloo, G.; Hagfeldt, A.;

- Sun, L. Efficient Solid State Dye-Sensitized Solar Cells Based on an Oligomer Hole Transport Material and an Organic Dye. *J. Mater. Chem. A Mater. Energy Sustain.* **2013**, *1* (46), 14467–14470.
- (61) Xu, B.; Tian, H.; Lin, L.; Qian, D.; Chen, H.; Zhang, J.; Vlachopoulos, N.; Boschloo, G.; Luo, Y.; Zhang, F.; et al. Integrated Design of Organic Hole Transport Materials for Efficient Solid-State Dye-Sensitized Solar Cells. *Adv. Energy Mater.* **2015**, *5* (3), 1401185.
- (62) Hole Transport Materials - Hole Transport (HT) & Hole Injection Layer (HIL) Materials | Sigma-Aldrich <https://www.sigmaaldrich.com/materials-science/material-science-products.html?TablePage=19352383> (Accessed Dec 16, 2018).
- (63) Choi, H.; Paek, S.; Lim, N.; Lee, Y. H.; Nazeeruddin, M. K.; Ko, J. Efficient Perovskite Solar Cells with 13.63 % Efficiency Based on Planar Triphenylamine Hole Conductors. *Chemistry* **2014**, *20* (35), 10894–10899.
- (64) Naito, K. Quantitative Relations between Glass Transition Temperatures and Thermodynamic Parameters for Various Materials: Molecular Design for Nonpolymeric Organic Dye Glasses with Thermal Stability. *Chem. Mater.* **1994**, *6* (12), 2343–2350.
- (65) Naito, K.; Miura, A. Molecular Design for Nonpolymeric Organic Dye Glasses with Thermal Stability: Relations between Thermodynamic Parameters and Amorphous Properties. *J. Phys. Chem.* **1993**, *97* (23), 6240–6248.
- (66) Kwak, J.; Lyu, Y.-Y.; Noh, S.; Lee, H.; Park, M.; Choi, B.; Char, K.; Lee, C. Hole Transport Materials with High Glass Transition Temperatures for Highly Stable Organic Light-Emitting Diodes. *Thin Solid Films* **2012**, *520* (24), 7157–7163.
- (67) Daškevičiūtė, Š.; Sakai, N.; Franckevičius, M.; Daškevičienė, M.; Magomedov, A.; Jankauskas, V.; Snaith, H. J.; Getautis, V. Nonspiro, Fluorene-Based, Amorphous Hole Transporting Materials for Efficient and Stable Perovskite Solar Cells. *Adv. Sci.* **2018**, *5* (4), 1700811.
- (68) Bach, U.; Lupo, D.; Comte, P.; Moser, J. E.; Weissörtel, F.; Salbeck, J.; Spreitzer, H.; Grätzel, M. Solid-State Dye-Sensitized Mesoporous TiO₂ Solar Cells with High Photon-to-Electron Conversion Efficiencies. *Nature* **1998**, *395*, 583.
- (69) Ramakrishna, J.; Venkatakrishnan, P. Bigger and Brighter Fluorenes: Facile π -Expansion, Brilliant Emission and Sensing of Nitroaromatics. *Chem. Asian J.* **2017**, *12* (2), 181–189.
- (70) Poriel, C.; Ferrand, Y.; Juillard, S.; Le Maux, P.; Simonneaux, G. Synthesis and Stereochemical Studies of Di and Tetra 9,9'-Spirobifluorene Porphyrins: New Building Blocks for Catalytic Material. *Tetrahedron* **2004**, *60* (1), 145–158.
- (71) Schmidt, H. C.; Larsen, C. B.; Wenger, O. S. Electron Transfer around a Molecular Corner. *Angew. Chem. Int. Ed.* **2018**, *57* (22), 6696–6700.
- (72) Nakar, R.; Cho, A.-N.; Berton, N.; Faure-Vincent, J.; Tran Van, F.; Park, N.-G.; Schmalz, B. Triphenylamine 3,6-Carbazole Derivative as Hole-Transporting Material for Mixed Cation Perovskite Solar Cells. *Chem. Pap.* **2018**, *72* (7), 1779–1787.
- (73) Toda, A.; Tomita, C.; Hikosaka, M.; Saruyama, Y. An Application of Temperature Modulated Differential Scanning Calorimetry to the Exothermic Process of Poly(ethylene Terephthalate) Crystallization. *Polymer* **1997**, *38* (11), 2849–2852.
- (74) Strohhriegl, P.; Grazulevicius, J. V. Charge-Transporting Molecular Glasses. *Adv. Mater.* **2002**, *14* (20), 1439–1452.
- (75) Shirota, Y.; Kuwabara, Y.; Inada, H.; Wakimoto, T.; Nakada, H.; Yonemoto, Y.; Kawami, S.; Imai, K. Multilayered Organic Electroluminescent Device Using a Novel Starburst Molecule, 4,4',4'-tris(3-methylphenylphenylamino)triphenylamine, as a Hole Transport

- Material. *Appl. Phys. Lett.* **1994**, *65* (7), 807–809.
- (76) Wang, S.; Sina, M.; Parikh, P.; Uekert, T.; Shahbazian, B.; Devaraj, A.; Meng, Y. S. Role of 4-Tert-Butylpyridine as a Hole Transport Layer Morphological Controller in Perovskite Solar Cells. *Nano Lett.* **2016**, *16* (9), 5594–5600.
- (77) Xi, H.; Tang, S.; Ma, X.; Chang, J.; Chen, D.; Lin, Z.; Zhong, P.; Wang, H.; Zhang, C. Performance Enhancement of Planar Heterojunction Perovskite Solar Cells through Tuning the Doping Properties of Hole-Transporting Materials. *ACS Omega* **2017**, *2* (1), 326–336.
- (78) Ye, T.; Wang, J.; Chen, W.; Yang, Y.; He, D. Improved Performance and Reproducibility of Perovskite Solar Cells by Well-Soluble Tris(pentafluorophenyl)borane as a P-Type Dopant. *ACS Appl. Mater. Interfaces* **2017**, *9* (21), 17923–17931.
- (79) Abate, A.; Leijtens, T.; Pathak, S.; Teuscher, J.; Avolio, R.; Errico, M. E.; Kirkpatrick, J.; Ball, J. M.; Docampo, P.; McPherson, I.; et al. Lithium Salts as “Redox Active” P-Type Dopants for Organic Semiconductors and Their Impact in Solid-State Dye-Sensitized Solar Cells. *Phys. Chem. Chem. Phys.* **2013**, *15* (7), 2572–2579.
- (80) Cappel, U. B.; Daeneke, T.; Bach, U. Oxygen-Induced Doping of Spiro-MeOTAD in Solid-State Dye-Sensitized Solar Cells and Its Impact on Device Performance. *Nano Lett.* **2012**, *12* (9), 4925–4931.
- (81) Li, Z.; Xiao, C.; Yang, Y.; Harvey, S. P.; Kim, D. H.; Christians, J. A.; Yang, M.; Schulz, P.; Nanayakkara, S. U.; Jiang, C.-S. Extrinsic Ion Migration in Perovskite Solar Cells. *Energy Environ. Sci.* **2017**, *10* (5), 1234–1242.
- (82) Li, Z.; Tinkham, J.; Schulz, P.; Yang, M.; Kim, D. H.; Berry, J.; Sellinger, A.; Zhu, K. Acid Additives Enhancing the Conductivity of Spiro-OMeTAD Toward High-Efficiency and Hysteresis-Less Planar Perovskite Solar Cells. *Adv. Energy Mater.* **2017**, *7* (4), 1601451.
- (83) Liu, X.; Li, B.; Zhang, N.; Yu, Z.; Sun, K.; Tang, B.; Shi, D.; Yao, H.; Ouyang, J.; Gong, H. Multifunctional RbCl Dopants for Efficient Inverted Planar Perovskite Solar Cell with Ultra-High Fill Factor, Negligible Hysteresis and Improved Stability. *Nano Energy* **2018**, *53*, 567–578.
- (84) Hawash, Z.; Ono, L. K.; Qi, Y. Recent Advances in Spiro-MeOTAD Hole Transport Material and Its Applications in Organic-Inorganic Halide Perovskite Solar Cells. *Adv. Mater. Interfaces* **2018**, *5* (1), 1700623.
- (85) Jung, M.-C.; Raga, S. R.; Ono, L. K.; Qi, Y. Substantial Improvement of Perovskite Solar Cells Stability by Pinhole-Free Hole Transport Layer with Doping Engineering. *Sci. Rep.* **2015**, *5*, 9863.
- (86) Tokito, S.; Tanaka, H.; Noda, K.; Okada, A.; Taga, Y. Thermal Stability in Oligomeric triphenylamine/tris(8-Quinolinolato) Aluminum Electroluminescent Devices. *Appl. Phys. Lett.* **1997**, *70* (15), 1929–1931.
- (87) Tanaka, H.; Tokito, S.; Taga, Y.; Okada, A. Novel Hole-Transporting Materials Based on Triphenylamine for Organic Electroluminescent Devices. *Chem. Commun.* **1996**, *0* (18), 2175–2176.
- (88) Zhang, F.; Yi, C.; Wei, P.; Bi, X.; Luo, J.; Jacopin, G.; Wang, S.; Li, X.; Xiao, Y.; Zakeeruddin, S. M.; et al. A Novel Dopant-Free Triphenylamine Based Molecular “Butterfly” Hole-Transport Material for Highly Efficient and Stable Perovskite Solar Cells. *Adv. Energy Mater.* **2016**, *6* (14), 1600401.
- (89) Li, X.; Tang, X.; Yang, Y.; Ye, T.; Wu, D.; Wang, H.; Li, J.; Wang, X. A Dopant-Free Polymer as Hole-Transporting Material for Highly Efficient and Stable Perovskite Solar Cells. *Prog. Photovoltaics Res. Appl.* **2018**, *131*, 6050.

- (90) Kazim, S.; Javier Ramos, F.; Gao, P.; Nazeeruddin, M. K.; Grätzel, M.; Ahmad, S. A Dopant Free Linear Acene Derivative as a Hole Transport Material for Perovskite Pigmented Solar Cells. *Energy Environ. Sci.* **2015**, *8* (6), 1816–1823.
- (91) Katono, M.; Wielopolski, M.; Marszalek, M.; Bessho, T.; Moser, J.-E.; Humphry-Baker, R.; Zakeeruddin, S. M.; Grätzel, M. Effect of Extended π -Conjugation of the Donor Structure of Organic D–A– π –A Dyes on the Photovoltaic Performance of Dye-Sensitized Solar Cells. *J. Phys. Chem. C* **2014**, *118* (30), 16486–16493.
- (92) Chiang, C.-H.; Wu, C.-G. A Method for the Preparation of Highly Oriented MAPbI₃ Crystallites for High-Efficiency Perovskite Solar Cells to Achieve an 86% Fill Factor. *ACS Nano* **2018**, *12* (10), 10355–10364.
- (93) Bi, D.; Mishra, A.; Gao, P.; Franckevičius, M.; Steck, C.; Zakeeruddin, S. M.; Nazeeruddin, M. K.; Bäuerle, P.; Grätzel, M.; Hagfeldt, A. High-Efficiency Perovskite Solar Cells Employing a S,N-Heteropentacene-Based D-A Hole-Transport Material. *ChemSusChem* **2016**, *9* (5), 433–438.
- (94) Liu, Y.; Hong, Z.; Chen, Q.; Chen, H.; Chang, W.-H.; Yang, Y. M.; Song, T.-B.; Yang, Y. Perovskite Solar Cells Employing Dopant-Free Organic Hole Transport Materials with Tunable Energy Levels. *Adv. Mater.* **2016**, *28* (3), 440–446.
- (95) Steck, C.; Franckevičius, M.; Zakeeruddin, S. M.; Mishra, A.; Bäuerle, P.; Grätzel, M. A–D–A-Type S,N-Heteropentacene-Based Hole Transport Materials for Dopant-Free Perovskite Solar Cells. *J. Mater. Chem. A Mater. Energy Sustain.* **2015**, *3* (34), 17738–17746.
- (96) Chiykowski, V. A.; Lam, B.; Du, C.; Berlinguette, C. P. On How Electron Density Affects the Redox Stability of Phenothiazine Sensitizers on Semiconducting Surfaces. *Chem. Commun.* **2017**, *53* (17), 2547–2550.
- (97) Ye, M.; He, C.; Icozzia, J.; Liu, X.; Cui, X.; Meng, X.; Rager, M.; Hong, X.; Liu, X.; Lin, Z. Recent Advances in Interfacial Engineering of Perovskite Solar Cells. *J. Phys. D Appl. Phys.* **2017**, *50* (37), 373002.
- (98) Friederich, P.; Gómez, V.; Sprau, C.; Meded, V.; Strunk, T.; Jenne, M.; Magri, A.; Symalla, F.; Colsmann, A.; Ruben, M.; et al. Rational In Silico Design of an Organic Semiconductor with Improved Electron Mobility. *Adv. Mater.* **2017**, *29* (43), 1703505.
- (99) Friederich, P.; Meded, V.; Poschlad, A.; Neumann, T.; Rodin, V.; Stehr, V.; Symalla, F.; Danilov, D.; Lüdemann, G.; Fink, R. F.; et al. Molecular Origin of the Charge Carrier Mobility in Small Molecule Organic Semiconductors. *Adv. Funct. Mater.* **2016**, *26* (31), 5757–5763.
- (100) Neumann, T.; Danilov, D.; Lennartz, C.; Wenzel, W. Modeling Disordered Morphologies in Organic Semiconductors. *J. Comput. Chem.* **2013**, *34* (31), 2716–2725.
- (101) Friederich, P.; Symalla, F.; Meded, V.; Neumann, T.; Wenzel, W. Ab Initio Treatment of Disorder Effects in Amorphous Organic Materials: Toward Parameter Free Materials Simulation. *J. Chem. Theory Comput.* **2014**, *10* (9), 3720–3725.
- (102) Massé, A.; Friederich, P.; Symalla, F.; Liu, F.; Nitsche, R.; Coehoorn, R.; Wenzel, W.; Bobbert, P. A. Ab Initio Charge-Carrier Mobility Model for Amorphous Molecular Semiconductors. *Phys. Rev. B Condens. Matter* **2016**, *93* (19), 195209.
- (103) Mesta, M.; Carvelli, M.; de Vries, R. J.; van Eersel, H.; van der Holst, J. J. M.; Schober, M.; Furno, M.; Lüssem, B.; Leo, K.; Loebel, P.; et al. Molecular-Scale Simulation of Electroluminescence in a Multilayer White Organic Light-Emitting Diode. *Nat. Mater.* **2013**, *12* (7), 652–658.

- (104) Liang, X.; Wang, K.; Zhang, R.; Li, K.; Lu, X.; Guo, K.; Wang, H.; Miao, Y.; Xu, H.; Wang, Z. Tetra-Carbazole Substituted Spiro[fluorene-9,9'-Xanthene]-Based Hole-Transporting Materials with High Thermal Stability and Mobility for Efficient OLEDs. *Dyes Pigm.* **2017**, *139*, 764–771.
- (105) Calió, L.; Kazim, S.; Grätzel, M.; Ahmad, S. Hole-Transport Materials for Perovskite Solar Cells. *Angew. Chem. Int. Ed.* **2016**, *55* (47), 14522–14545.
- (106) Bakr, Z. H.; Wali, Q.; Fakharuddin, A.; Schmidt-Mende, L.; Brown, T. M.; Jose, R. Advances in Hole Transport Materials Engineering for Stable and Efficient Perovskite Solar Cells. *Nano Energy* **2017**, *34* (Supplement C), 271–305.
- (107) Wang, Y.; Su, T.-S.; Tsai, H.-Y.; Wei, T.-C.; Chi, Y. Spiro-Phenylpyrazole/Fluorene as Hole-Transporting Material for Perovskite Solar Cells. *Sci. Rep.* **2017**, *7* (1), 7859.
- (108) Krishna, A.; Sabba, D.; Yin, J.; Bruno, A.; Antila, L. J.; Soci, C.; Mhaisalkar, S.; Grimsdale, A. C. Facile Synthesis of a Hole Transporting Material with a Silafluorene Core for Efficient Mesoscopic CH₃NH₃PbI₃ Perovskite Solar Cells. *J. Mater. Chem. A Mater. Energy Sustain.* **2016**, *4* (22), 8750–8754.
- (109) Kou, C.; Feng, S.; Li, H.; Li, W.; Li, D.; Meng, Q.; Bo, Z. Molecular “Flower” as the High-Mobility Hole-Transport Material for Perovskite Solar Cells. *ACS Appl. Mater. Interfaces* **2017**, *9* (50), 43855–43860.
- (110) Wang, Y.; Zhang, S.; Wu, J.; Liu, K.; Li, D.; Meng, Q.; Zhu, G. Electropolymerization Porous Aromatic Framework Film As a Hole-Transport Layer for Inverted Perovskite Solar Cells with Superior Stability. *ACS Appl. Mater. Interfaces* **2017**, *9* (50), 43688–43695.
- (111) Rakstys, K.; Saliba, M.; Gao, P.; Gratia, P.; Kamaraukas, E.; Paek, S.; Jankauskas, V.; Nazeeruddin, M. K. Highly Efficient Perovskite Solar Cells Employing an Easily Attainable Bifluorenylidene-Based Hole-Transporting Material. *Angew. Chem. Int. Ed.* **2016**, *55* (26), 7464–7468.
- (112) Bi, D.; Tress, W.; Dar, M. I.; Gao, P.; Luo, J.; Renevier, C.; Schenk, K.; Abate, A.; Giordano, F.; Correa Baena, J.-P.; et al. Efficient Luminescent Solar Cells Based on Tailored Mixed-Cation Perovskites. *Sci Adv* **2016**, *2* (1), e1501170.
- (113) Pudzich, R.; Fuhrmann-Lieker, T.; Salbeck, J. Spiro Compounds for Organic Electroluminescence and Related Applications. In *Emissive Materials Nanomaterials*; Springer Berlin Heidelberg: Berlin, Heidelberg, **2006**; 83–142.
- (114) Zhang, J.; Xu, B.; Yang, L.; Ruan, C.; Wang, L.; Liu, P.; Zhang, W.; Vlachopoulos, N.; Kloos, L.; Boschloo, G.; et al. The Importance of Pendant Groups on Triphenylamine-Based Hole Transport Materials for Obtaining Perovskite Solar Cells with over 20% Efficiency. *Adv. Energy Mater.* **2018**, *8* (2), 1701209
- (115) Snaith, H. J.; Grätzel, M. Enhanced Charge Mobility in a Molecular Hole Transporter via Addition of Redox Inactive Ionic Dopant: Implication to Dye-Sensitized Solar Cells. *Appl. Phys. Lett.* **2006**, *89* (26), 262114.
- (116) Deng, W.-Q.; Goddard, W. A. Predictions of Hole Mobilities in Oligoacene Organic Semiconductors from Quantum Mechanical Calculations. *J. Phys. Chem. B* **2004**, *108* (25), 8614–8621.
- (117) Nelsen, S. F.; Blackstock, S. C.; Kim, Y. Estimation of Inner Shell Marcus Terms for Amino Nitrogen Compounds by Molecular Orbital Calculations. *J. Am. Chem. Soc.* **1987**, *109* (3), 677–682.
- (118) Marcus, R. A. On the Theory of Oxidation-Reduction Reactions Involving Electron Transfer. I. *J. Chem. Phys.* **1956**, *24* (5), 966–978.

- (119) Liu, K.; Yao, Y.; Wang, J.; Zhu, L.; Sun, M.; Ren, B.; Xie, L.; Luo, Y.; Meng, Q.; Zhan, X. Spiro[fluorene-9,9'-Xanthene]-Based Hole Transporting Materials for Efficient Perovskite Solar Cells with Enhanced Stability. *Mater. Chem. Front.* **2016**, *1* (1), 100–110.
- (120) Tosco, P.; Stiefl, N.; Landrum, G. Bringing the MMFF Force Field to the RDKit: Implementation and Validation. *J. Cheminform.* **2014**, *6* (1), 37.
- (121) Landrum, G. RDKit <http://www.rdkit.org/> (Accessed Nov 27, 2017).
- (122) Shao, Y.; Gan, Z.; Epifanovsky, E.; Gilbert, A. T. B.; Wormit, M.; Kussmann, J.; Lange, A. W.; Behn, A.; Deng, J.; Feng, X.; et al. Advances in Molecular Quantum Chemistry Contained in the Q-Chem 4 Program Package. *Mol. Phys.* **2015**, *113* (2), 184–215.
- (123) Frisch, M. J.; Trucks, G. W.; Schlegel, H. B.; Scuseria, G. E. G09 Gaussian Inc. Wallingford, CT **2009**.
- (124) Humphrey, W.; Dalke, A.; Schulten, K. VMD: Visual Molecular Dynamics. *J. Mol. Graph.* **1996**, *14* (1), 33–38, 27–28.
- (125) Bi, D.; Xu, B.; Gao, P.; Sun, L.; Grätzel, M.; Hagfeldt, A. Facile Synthesized Organic Hole Transporting Material for Perovskite Solar Cell with Efficiency of 19.8%. *Nano Energy* **2016**, *23* (Supplement C), 138–144.
- (126) Hwang, I.; Jeong, I.; Lee, J.; Ko, M. J.; Yong, K. Enhancing Stability of Perovskite Solar Cells to Moisture by the Facile Hydrophobic Passivation. *ACS Appl. Mater. Interfaces* **2015**, *7* (31), 17330–17336.
- (127) Dong, Q.; Liu, F.; Wong, M. K.; Tam, H. W.; Djurišić, A. B.; Ng, A.; Surya, C.; Chan, W. K.; Ng, A. M. C. Encapsulation of Perovskite Solar Cells for High Humidity Conditions. *ChemSusChem* **2016**, *9* (18), 2597–2603.
- (128) Wei, H.; Xiao, J.; Yang, Y.; Lv, S.; Shi, J.; Xu, X.; Dong, J.; Luo, Y.; Li, D.; Meng, Q. Free-Standing Flexible Carbon Electrode for Highly Efficient Hole-Conductor-Free Perovskite Solar Cells. *Carbon N. Y.* **2015**, *93*, 861–868.
- (129) Tvingstedt, K.; Malinkiewicz, O.; Baumann, A.; Deibel, C.; Snaith, H. J.; Dyakonov, V.; Bolink, H. J. Radiative Efficiency of Lead Iodide Based Perovskite Solar Cells. *Sci. Rep.* **2014**, *4*, 6071.
- (130) Liu, D.; Li, Y.; Yuan, J.; Hong, Q.; Shi, G.; Yuan, D.; Wei, J.; Huang, C.; Tang, J.; Fung, M.-K. Improved Performance of Inverted Planar Perovskite Solar Cells with F4-TCNQ Doped PEDOT:PSS Hole Transport Layers. *J. Mater. Chem. A Mater. Energy Sustain.* **2017**, *5* (12), 5701–5708.
- (131) Zhang, Y.-D.; Hreha, R. D.; Jabbour, G. E.; Kippelen, B.; Peyghambarian, N.; Marder, S. R. Photo-Crosslinkable Polymers as Hole-Transport Materials for Organic Light-Emitting Diodes. *J. Mater. Chem.* **2002**, *12* (6), 1703–1708.
- (132) Sharma, A.; Reiter, G. Instability of Thin Polymer Films on Coated Substrates: Rupture, Dewetting, and Drop Formation. *J. Colloid Interface Sci.* **1996**, *178* (2), 383–399.
- (133) Sun, T.; Wang, G.; Liu, H.; Feng, L.; Jiang, L.; Zhu, D. Control over the Wettability of an Aligned Carbon Nanotube Film. *J. Am. Chem. Soc.* **2003**, *125* (49), 14996–14997.
- (134) Wang, K.-C.; Jeng, J.-Y.; Shen, P.-S.; Chang, Y.-C.; Diao, E. W.-G.; Tsai, C.-H.; Chao, T.-Y.; Hsu, H.-C.; Lin, P.-Y.; Chen, P.; et al. P-Type Mesoscopic Nickel Oxide/organometallic Perovskite Heterojunction Solar Cells. *Sci. Rep.* **2014**, *4*, 4756.
- (135) Kim, J. H.; Liang, P.-W.; Williams, S. T.; Cho, N.; Chueh, C.-C.; Glaz, M. S.; Ginger, D. S.; Jen, A. K.-Y. High-Performance and Environmentally Stable Planar Heterojunction Perovskite Solar Cells Based on a Solution-Processed Copper-Doped Nickel Oxide Hole-Transporting Layer. *Adv. Mater.* **2015**, *27* (4), 695–701.

- (136) Nguyen, W. H.; Bailie, C. D.; Unger, E. L.; McGehee, M. D. Enhancing the Hole-Conductivity of Spiro-OMeTAD without Oxygen or Lithium Salts by Using spiro(TFSI)₂ in Perovskite and Dye-Sensitized Solar Cells. *J. Am. Chem. Soc.* **2014**, *136* (31), 10996–11001.
- (137) Ren, J.; Qu, J.; Chen, J.; Li, Z.; Cui, Y.; Wang, H.; Yu, Z.; Hao, Y. Fluorinated Dopant-Free Hole-Transporting Material for Efficient and Stable Perovskite Solar Cells with Carbon Cathode. *J. Power Sources* **2018**, *401*, 29–36.
- (138) Wang, S.; Yuan, W.; Meng, Y. S. Spectrum-Dependent Spiro-OMeTAD Oxidization Mechanism in Perovskite Solar Cells. *ACS Appl. Mater. Interfaces* **2015**, *7* (44), 24791–24798.
- (139) Namatame, M.; Yabusaki, M.; Watanabe, T.; Ogomi, Y.; Hayase, S.; Marumoto, K. Direct Observation of Dramatically Enhanced Hole Formation in a Perovskite-Solar-Cell Material Spiro-OMeTAD by Li-TFSI Doping. *Appl. Phys. Lett.* **2017**, *110* (12), 123904.
- (140) Hawash, Z.; Ono, L. K.; Raga, S. R.; Lee, M. V.; Qi, Y. Air-Exposure Induced Dopant Redistribution and Energy Level Shifts in Spin-Coated Spiro-MeOTAD Films. *Chem. Mater.* **2015**, *27* (2), 562–569.
- (141) Koh, T. M.; Dharani, S.; Li, H.; Prabhakar, R. R.; Mathews, N.; Grimsdale, A. C.; Mhaisalkar, S. G. Cobalt Dopant with Deep Redox Potential for Organometal Halide Hybrid Solar Cells. *ChemSusChem* **2014**, *7* (7), 1909–1914.
- (142) Li, M.-H.; Hsu, C.-W.; Shen, P.-S.; Cheng, H.-M.; Chi, Y.; Chen, P.; Guo, T.-F. Novel Spiro-Based Hole Transporting Materials for Efficient Perovskite Solar Cells. *Chem. Commun.* **2015**, *51* (85), 15518–15521.
- (143) MilliporeSigma. Zinc di[bis(trifluoromethylsulfonyl)imide] 720755 <https://www.sigmaaldrich.com/catalog/product/aldrich/720755?lang=en®ion=CA> (Accessed Mar 18, 2019).
- (144) Liu, Y.; Chen, Q.; Duan, H.-S.; Zhou, H.; Yang, Y.; Chen, H.; Luo, S.; Song, T.-B.; Dou, L.; Hong, Z.; et al. A Dopant-Free Organic Hole Transport Material for Efficient Planar Heterojunction Perovskite Solar Cells. *J. Mater. Chem. A Mater. Energy Sustain.* **2015**, *3* (22), 11940–11947.
- (145) Mathew, S.; Yella, A.; Gao, P.; Humphry-Baker, R.; Curchod, B. F. E.; Ashari-Astani, N.; Tavernelli, I.; Rothlisberger, U.; Nazeeruddin, M. K.; Grätzel, M. Dye-Sensitized Solar Cells with 13% Efficiency Achieved through the Molecular Engineering of Porphyrin Sensitizers. *Nat. Chem.* **2014**, *6* (3), 242–247.
- (146) Chiykowski, V. A.; Lam, B.; Du, C.; Berlinguette, C. P. Comparative Analysis of Triarylamine and Phenothiazine Sensitizer Donor Units in Dye-Sensitized Solar Cells. *Chem. Commun.* **2017**, *53* (15), 2367–2370.
- (147) Wu, J.-T.; Hsiang, T.-L.; Liou, G.-S. Synthesis and Optical Properties of Redox-Active Triphenylamine-Based Derivatives with Methoxy Protecting Groups. *J. Mater. Chem.* **2018**, *6* (48), 13345–13351.
- (148) Niu, G.; Li, W.; Meng, F.; Wang, L.; Dong, H.; Qiu, Y. Study on the Stability of CH₃NH₃PbI₃ Films and the Effect of Post-Modification by Aluminum Oxide in All-Solid-State Hybrid Solar Cells. *J. Mater. Chem. A Mater. Energy Sustain.* **2014**, *2* (3), 705–710.
- (149) Zhu, Z.; Zhao, D.; Chueh, C.-C.; Shi, X.; Li, Z.; Jen, A. K.-Y. Highly Efficient and Stable Perovskite Solar Cells Enabled by All-Crosslinked Charge-Transporting Layers. *Joule* **2018**, *2* (1), 168–183.
- (150) Rolston, N.; Bush, K. A.; Printz, A. D.; Gold-Parker, A.; Ding, Y.; Toney, M. F.; McGehee,

- M. D.; Dauskardt, R. H. Engineering Stress in Perovskite Solar Cells to Improve Stability. *Adv. Energy Mater.* **2018**, *8* (29), 1802139.
- (151) Gao, L.-L.; Zhang, K.-J.; Chen, L.; Chen, N.; Li, C.-X.; Li, C.-J.; Yang, G.-J. Small Molecule-Driven Directional Movement Enabling Pin-Hole Free Perovskite Film via Fast Solution Engineering. *Nanoscale* **2017**, *9* (41), 15778–15785.

Appendices

Appendix 1: Chapter 3

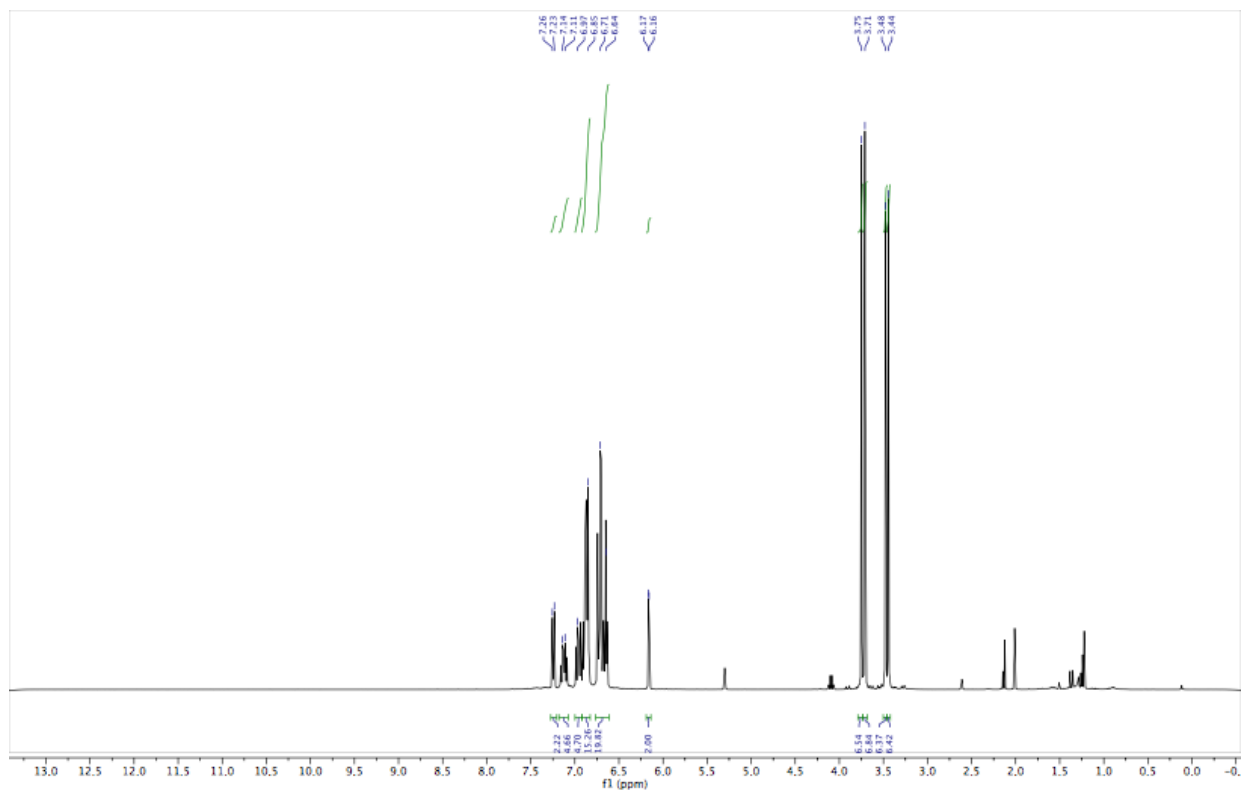


Figure A3-1 ^1H NMR of spiro-*p,o*-OMe in CD_2Cl_2 at ambient temperature.

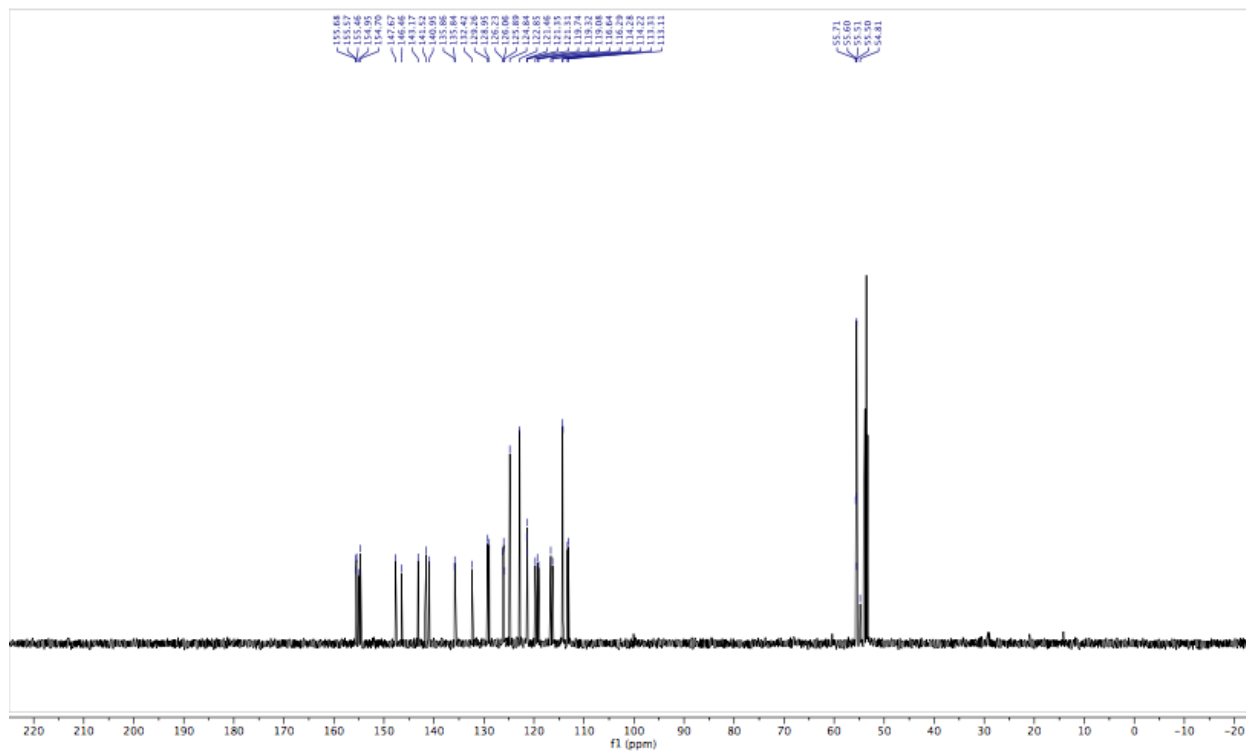


Figure A3-2 ^{13}C NMR of spiro-*p,o*-OMe in CD_2Cl_2 at ambient temperature.

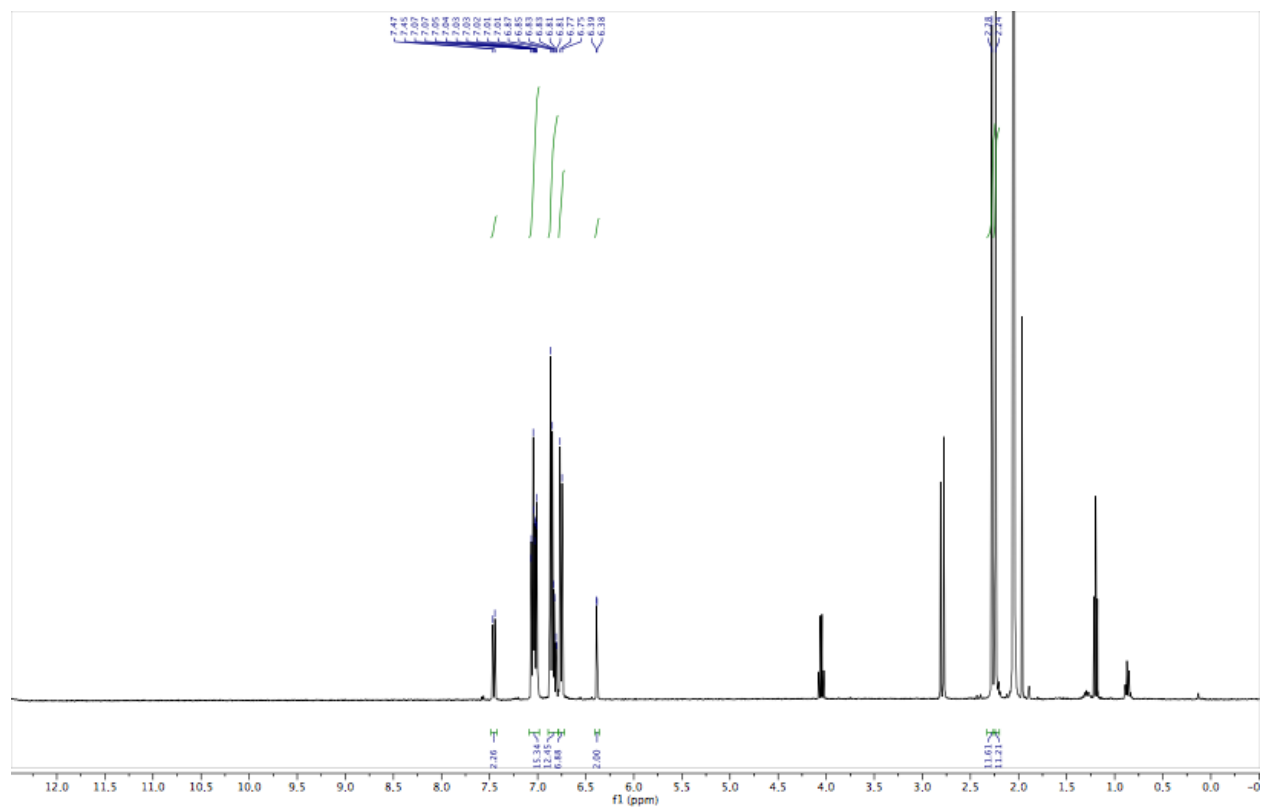


Figure A3-3 ^1H NMR of spiro-Me in CD_2Cl_2 at ambient temperature.

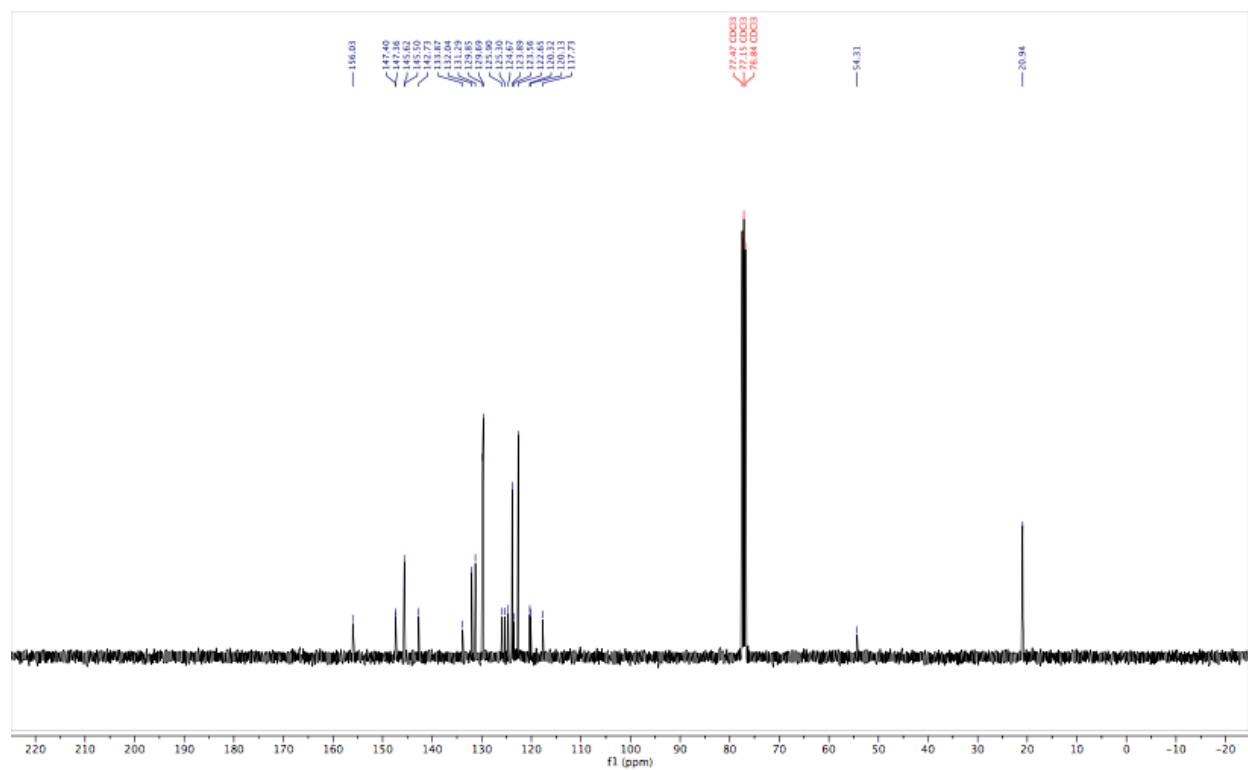


Figure A3-4 ^{13}C NMR of spiro-Me in CD_2Cl_2 at ambient temperature.

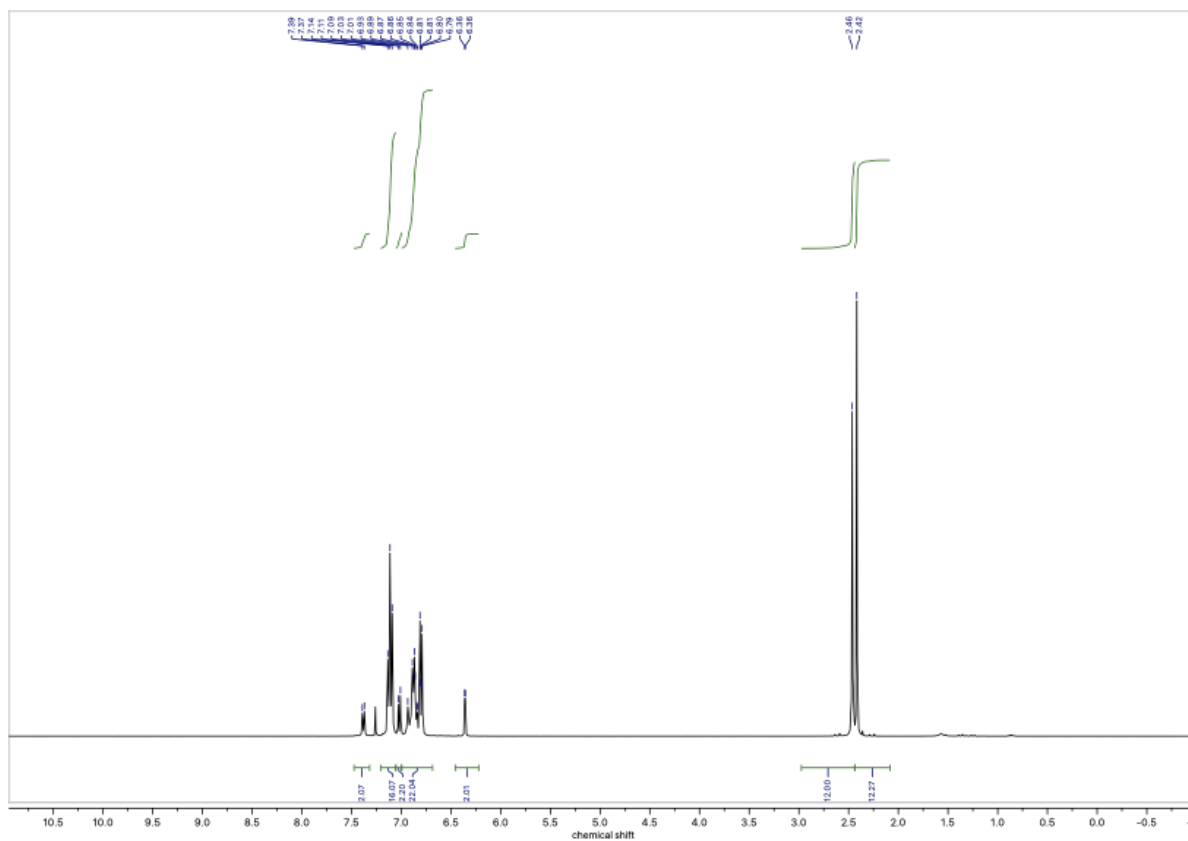


Figure A3-5 ^1H NMR of spiro-SMe in CDCl_3 at ambient temperature.

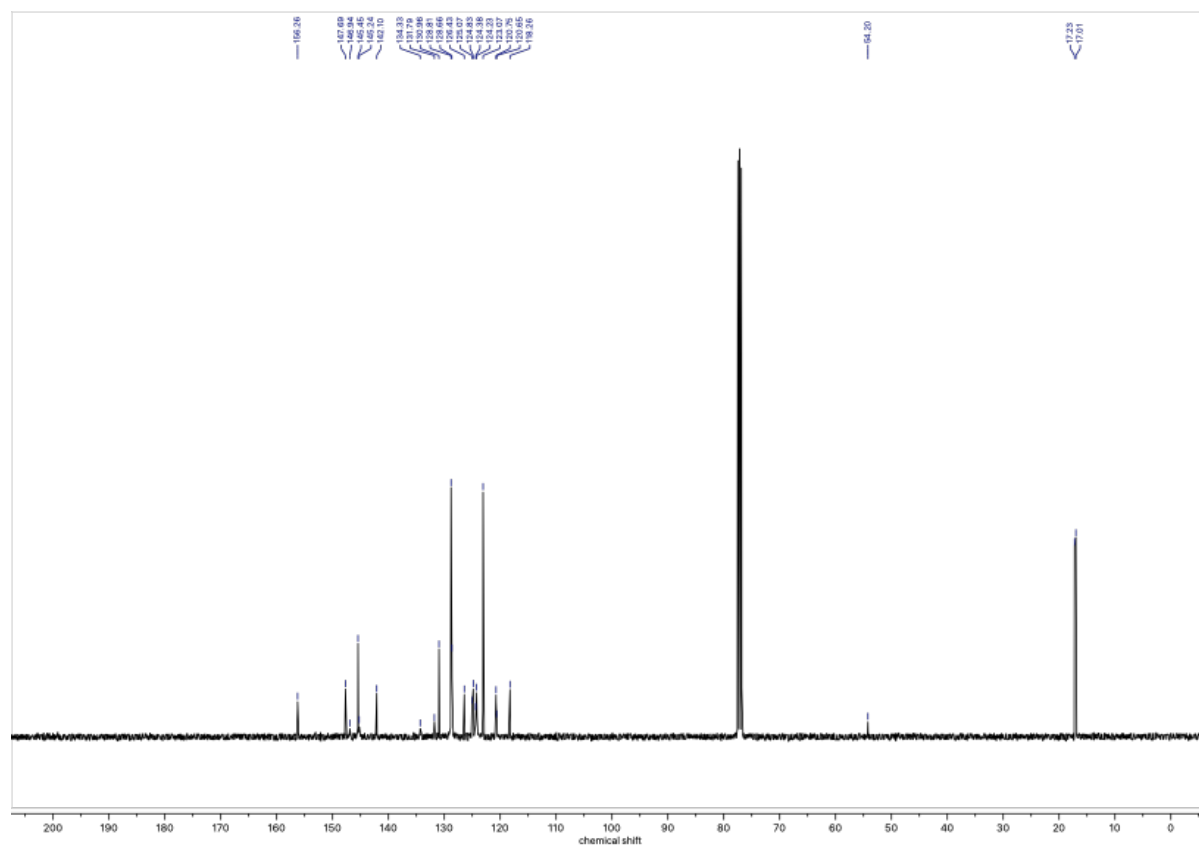


Figure A3-6 ^{13}C NMR of **spiro-SMe** in CDCl_3 at ambient temperature.

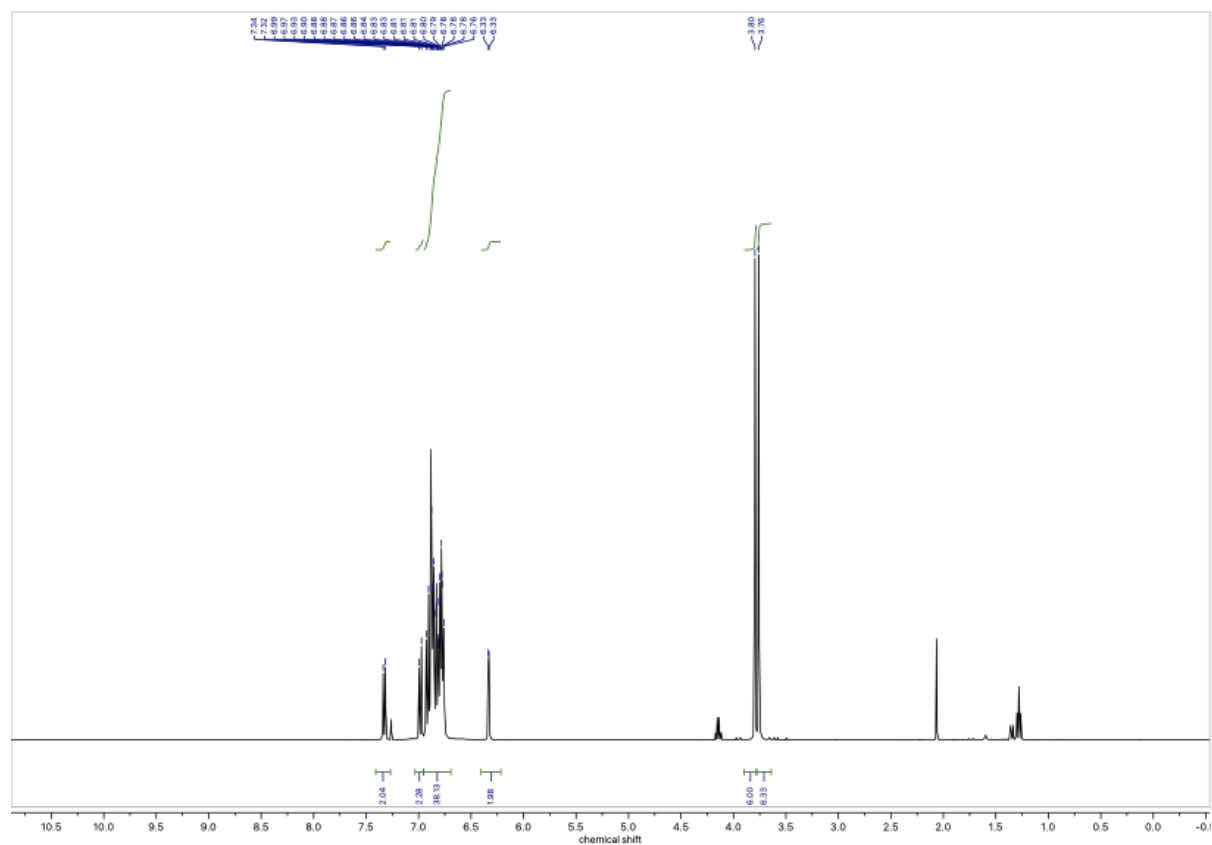


Figure A3-7 ¹H NMR of spiro-FOMe in CDCl₃ at ambient temperature.

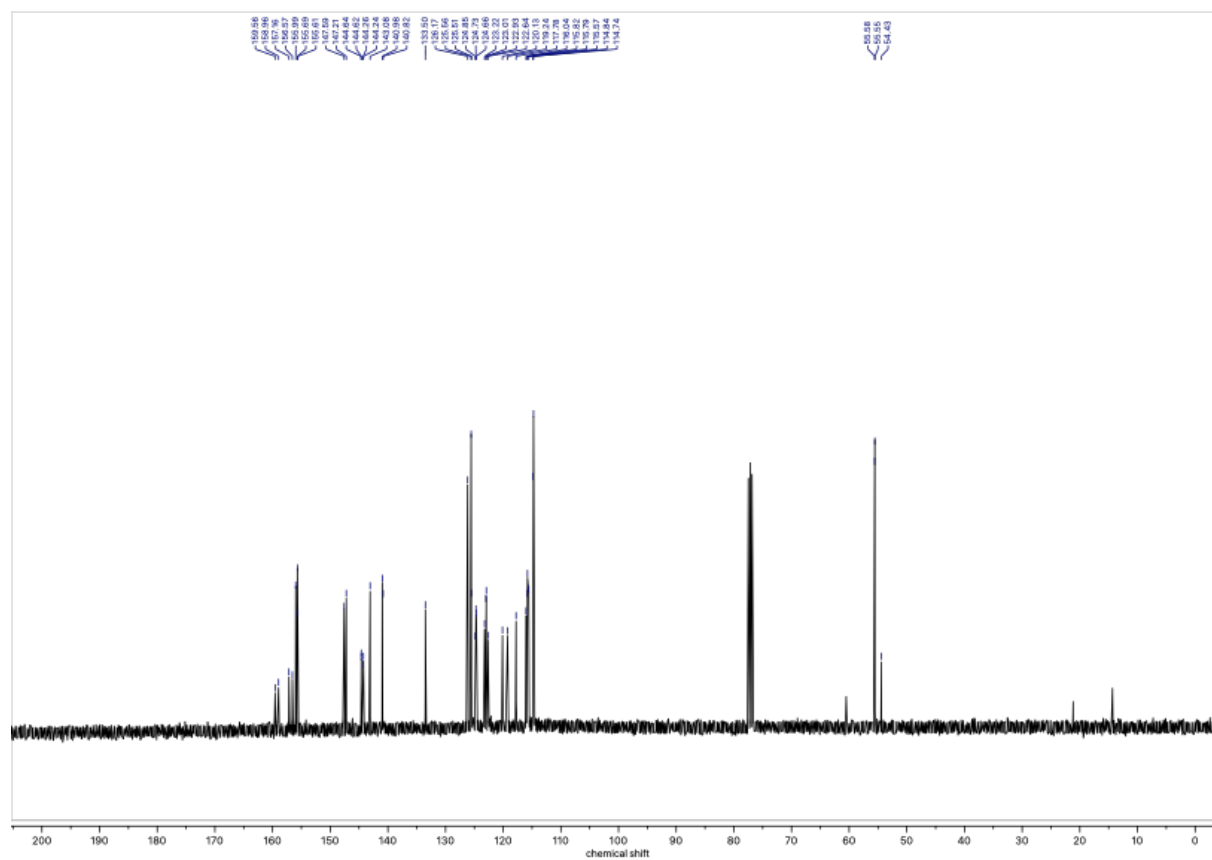


Figure A3-8 ^{13}C NMR of spiro-FOMe in CDCl_3 at ambient temperature.

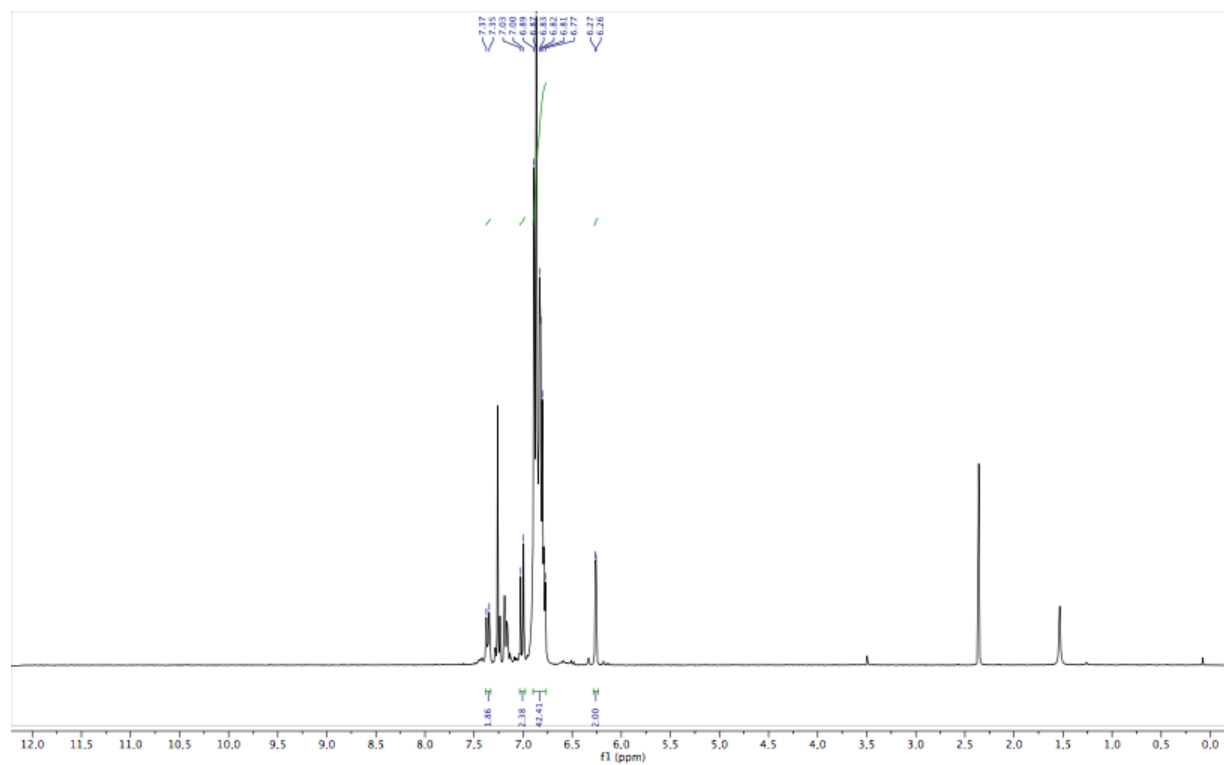


Figure A3-9 ¹H NMR of **spiro-F** in CD₂Cl₂ at ambient temperature.

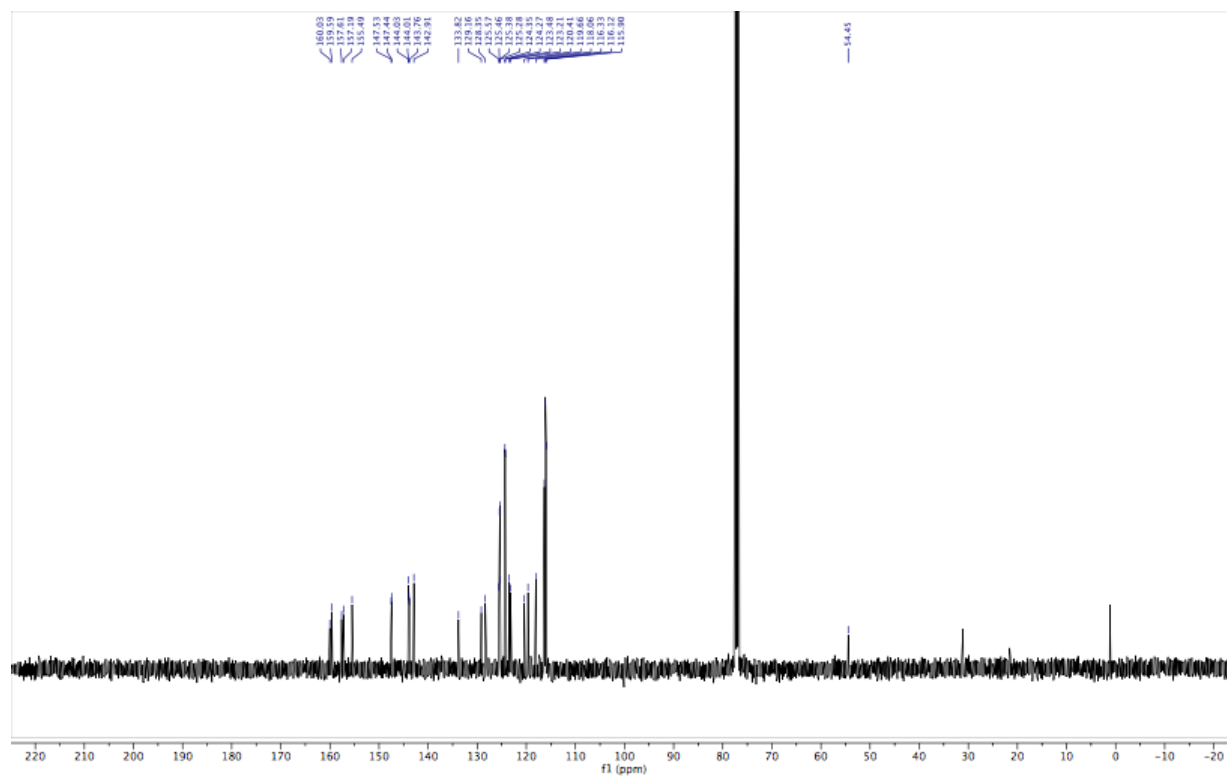


Figure A3-10 ^{13}C NMR of **spiro-F** in CD_2Cl_2 at ambient temperature.

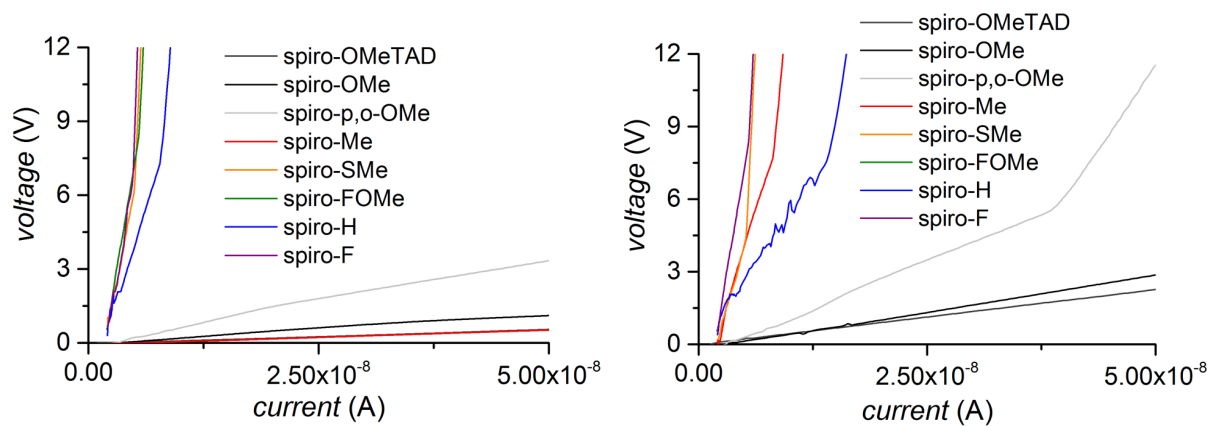


Figure A3-11 Resistance data for **spiro-OMeTAD** and **spiro-R** series with (a) 20% Li^+ and (b) 20% Li^+ and 3% Co(III) doping

Table A3-1 Conductivity data for **spiro-OMeTAD** and **spiro-R** series

compound	Conductivity 20% Li ⁺ (S/cm)	Conductivity 20% Li ⁺ and 3% Co(III) (S/cm)
Spiro-OMeTAD	1.23×10^{-4}	1.67×10^{-4}
X60	5.81×10^{-5}	2.11×10^{-4}
spiro-<i>p,o</i>-OMe	3.72×10^{-5}	2.20×10^{-5}
spiro-Me	2.47×10^{-4}	1.17×10^{-5}
spiro-SMe	6.92×10^{-5}	3.75×10^{-6}
spiro-FOMe	1.90×10^{-6}	4.32×10^{-5}
spiro-H	2.82×10^{-5}	7.43×10^{-6}
spiro-F	1.57×10^{-5}	1.67×10^{-4}

Table A3-2 Perovskite solar cell data for **spiro-R** series doped with LiTFSI and Co(III)TFSI

compound	V_{oc} (V)	J_{sc} (mA/cm ²)	FF	PCE (%)
spiro-Me	0.87	0.21	0.28	0.05
spiro-SMe	0.83	3.35	0.27	0.79
spiro-FOMe	0.93	0.29	0.27	0.07

Perovskite solar cells prepared with Cs_{0.05}FA_{0.81}MA_{0.14}PbI_{2.55}Br_{0.45} perovskite mixture, 20% LiTFSI dopant, 3% Co(III)TFSI and 250% tert-butylpyridine.

Appendix 2: Chapter 4

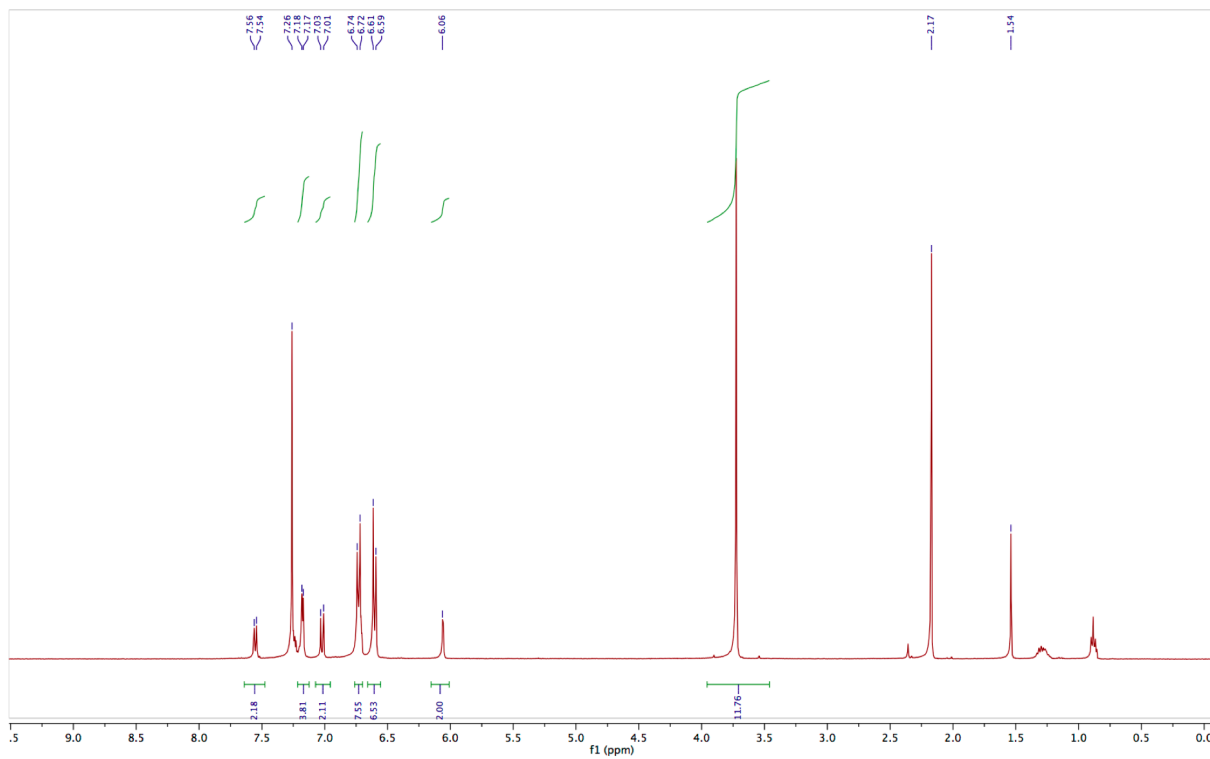


Figure A4-1 ¹H NMR of **HTM-X** in CDCl₃ at ambient temperature.

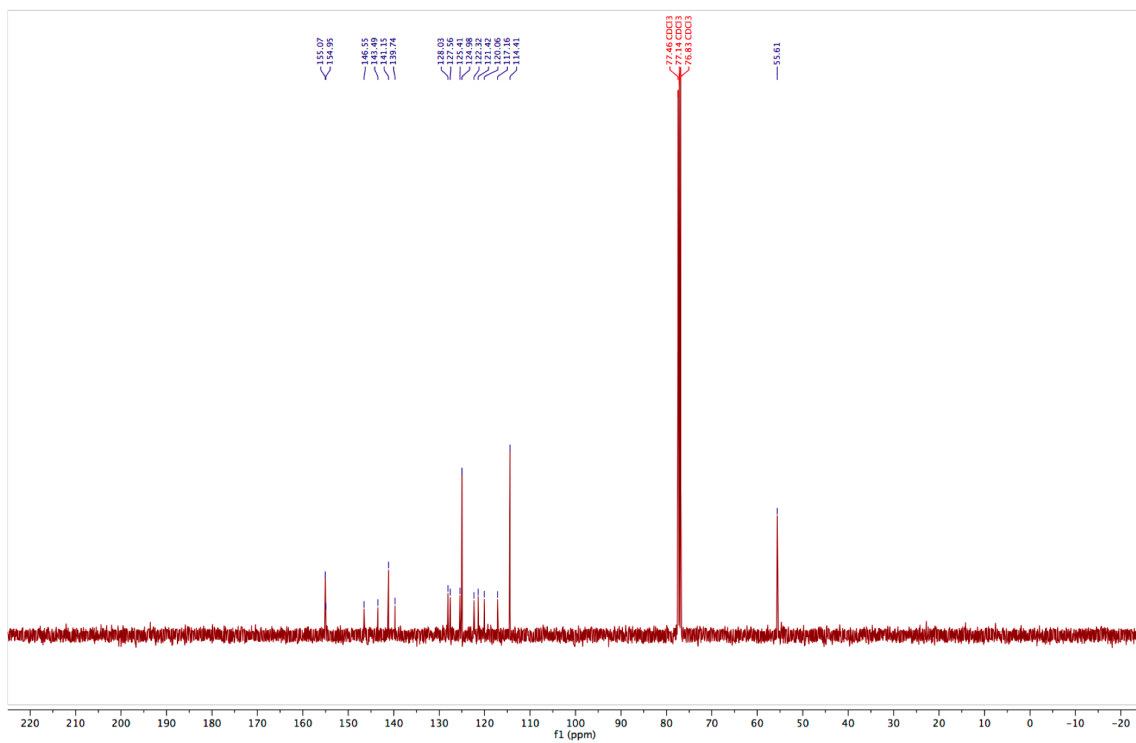


Figure A4-2 $^{13}\text{C}\{^1\text{H}\}$ NMR of **HTM-X** in CDCl_3 at ambient temperature

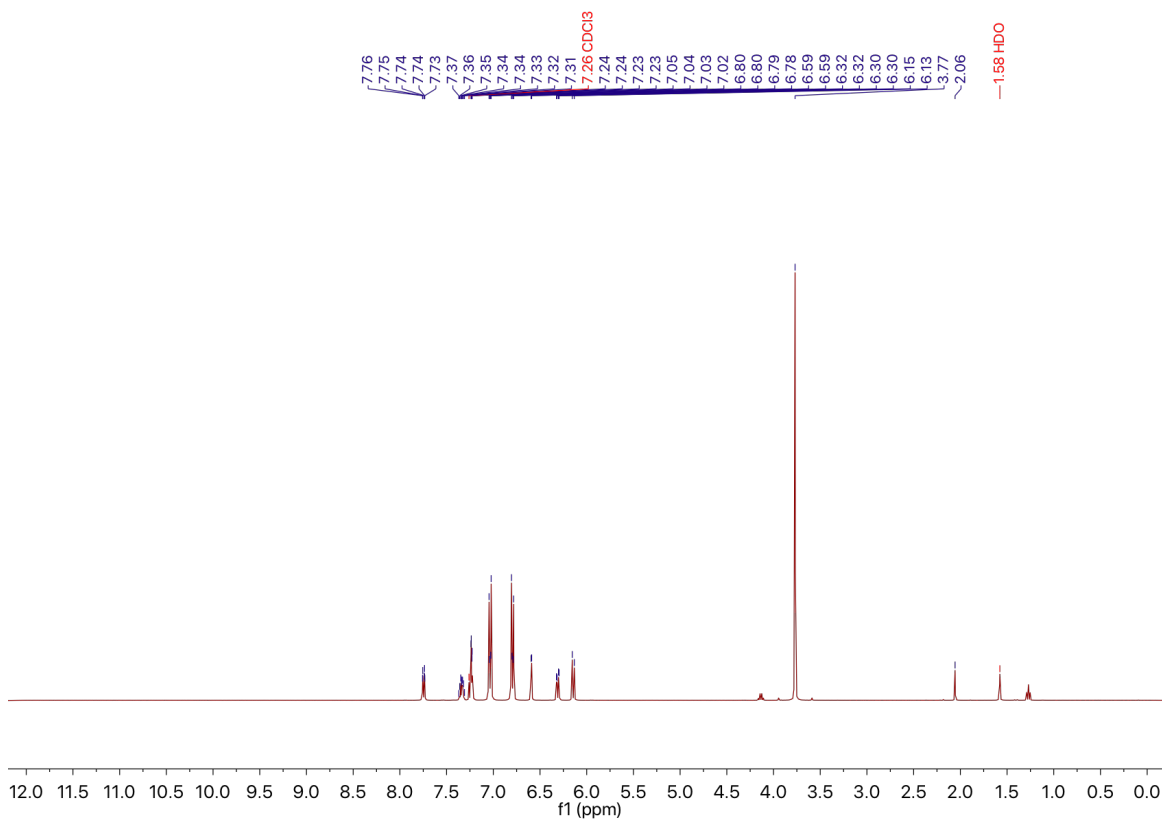


Figure A4-3 ^1H NMR of **HTM-X'** in CDCl_3 at ambient temperature.

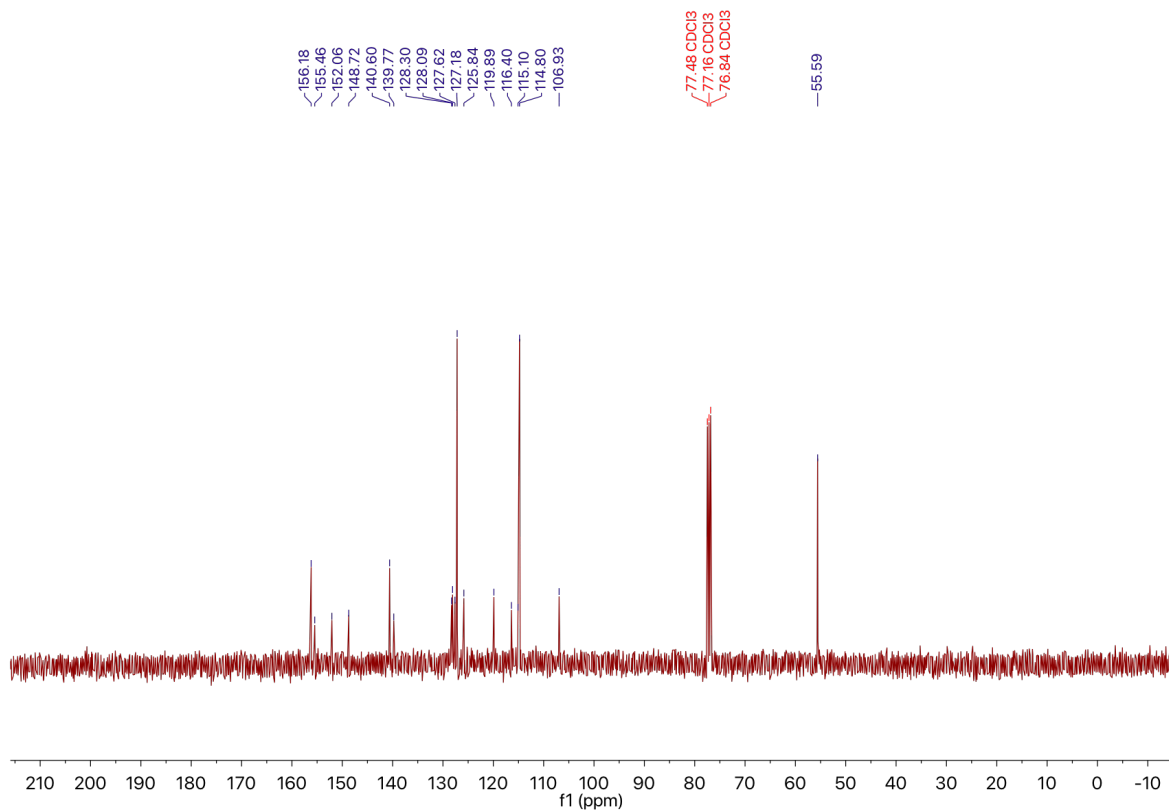


Figure A4-4 $^{13}\text{C}\{^1\text{H}\}$ NMR of HTM-X' in CDCl_3 at ambient temperature

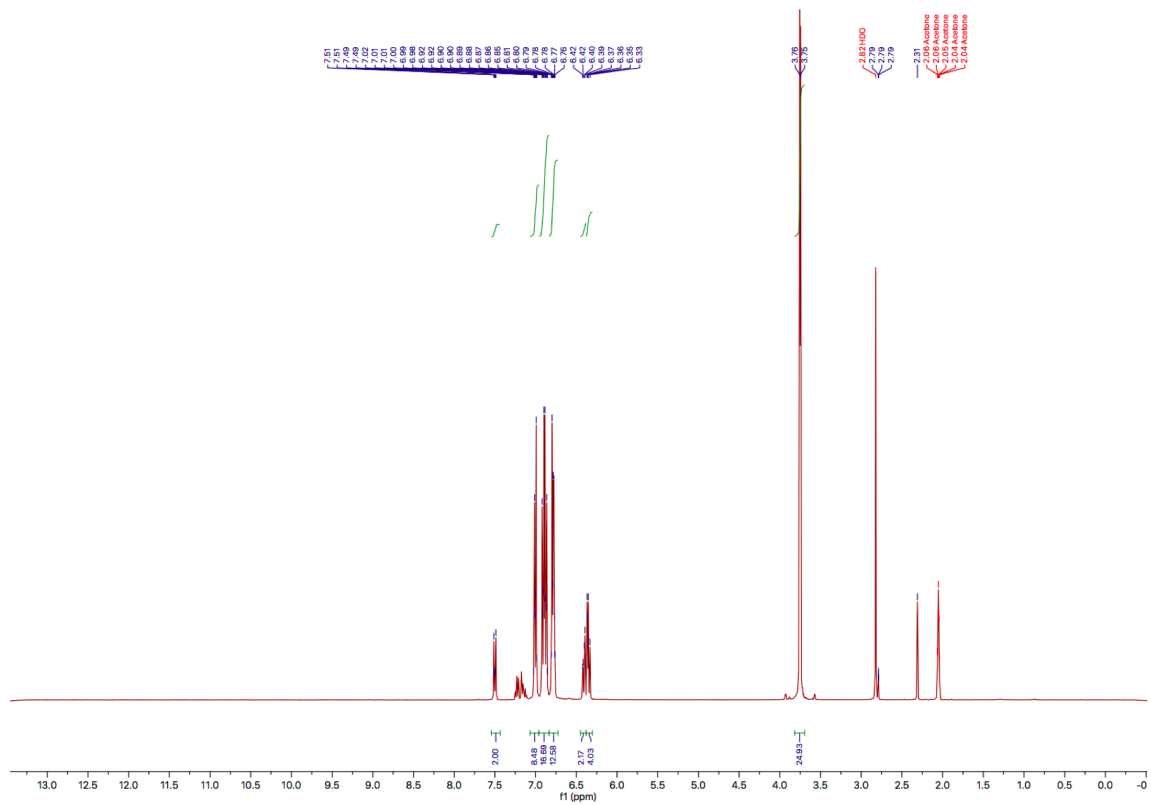


Figure A4-5 ^1H NMR of HTM-FX' in acetone- d_6 at ambient temperature.

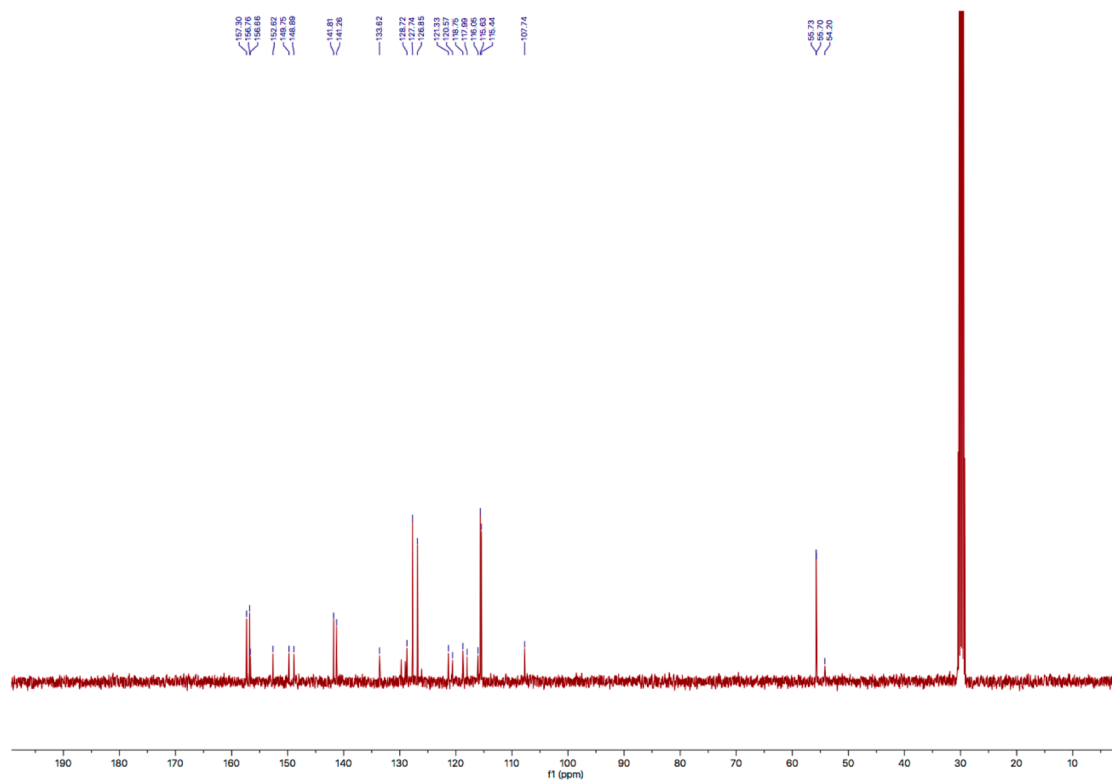


Figure A4-6 $^{13}\text{C}\{^1\text{H}\}$ NMR of **HTM-FX'** in acetone- d_6 at ambient temperature.

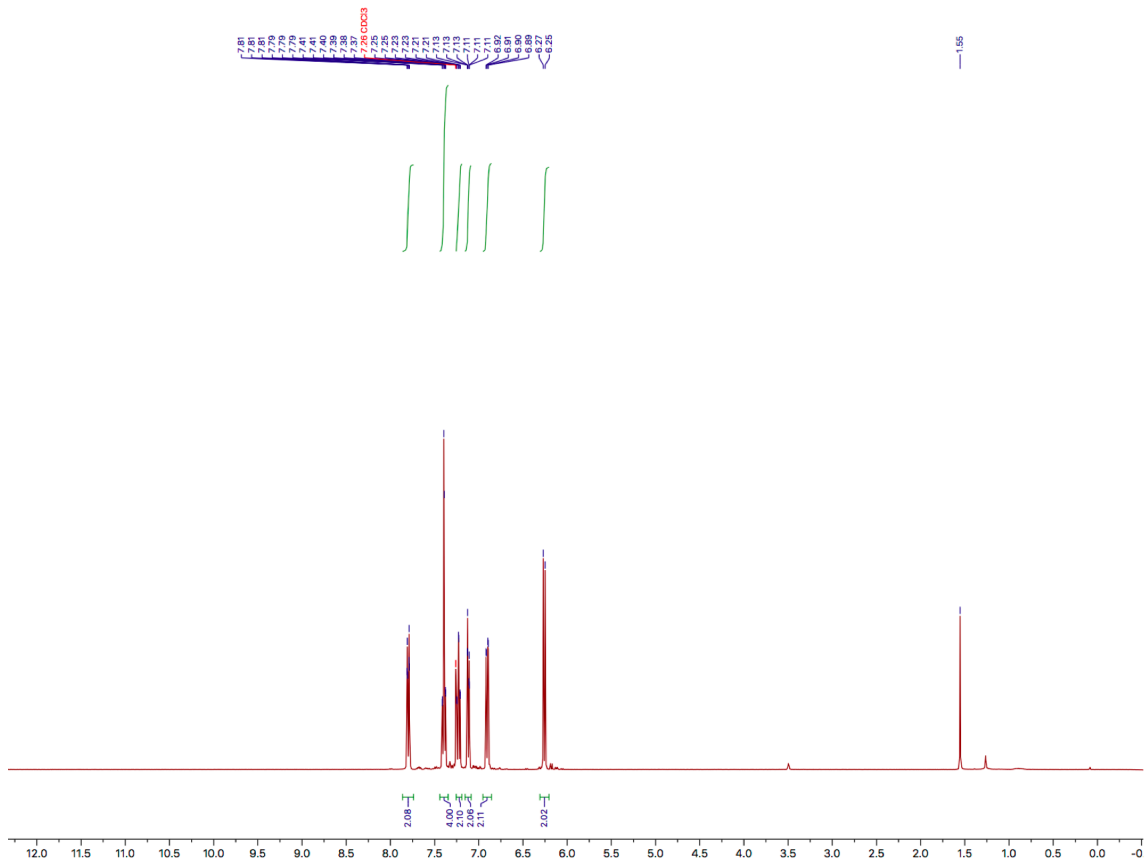


Figure A4-7 ^1H NMR of **Br2-X'** in CDCl_3 at ambient temperature

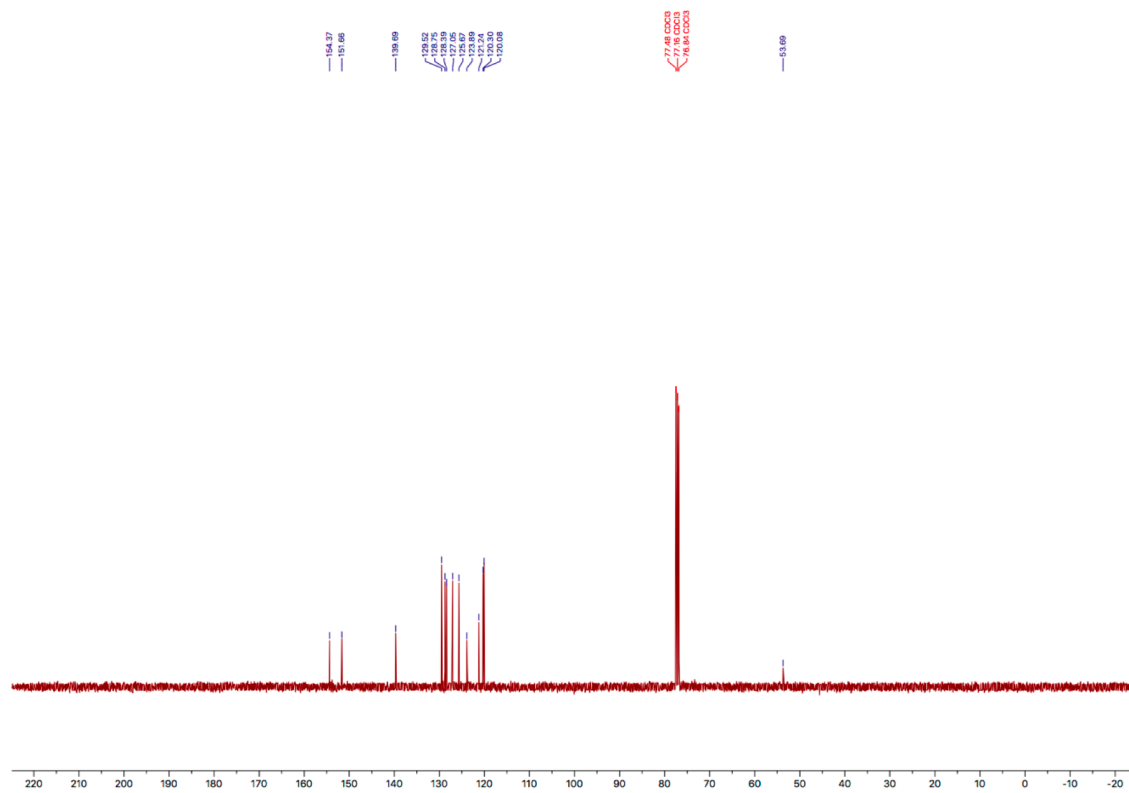


Figure A4-8 $^{13}\text{C}\{^1\text{H}\}$ NMR of **Br2-X'** in CDCl_3 at ambient temperature.

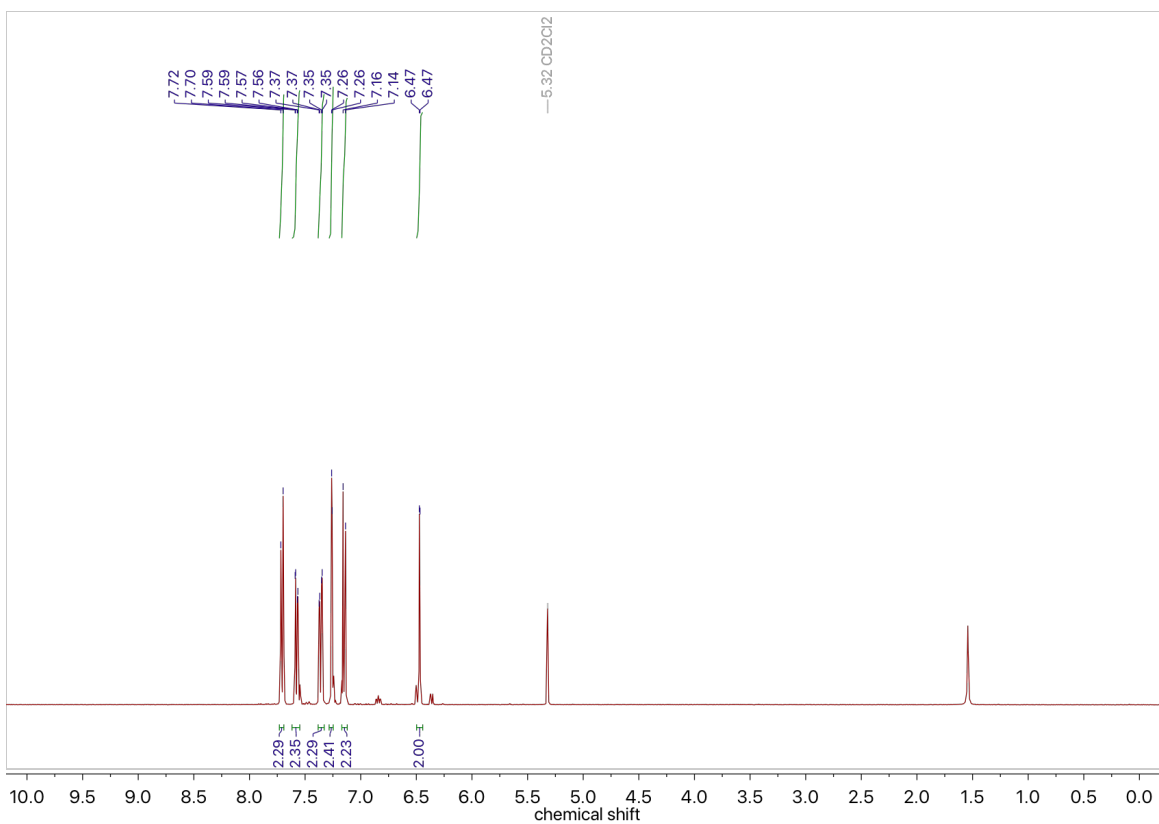


Figure A4-9 ^1H NMR of **Br4-FX'** in CD_2Cl_2 at ambient temperature.

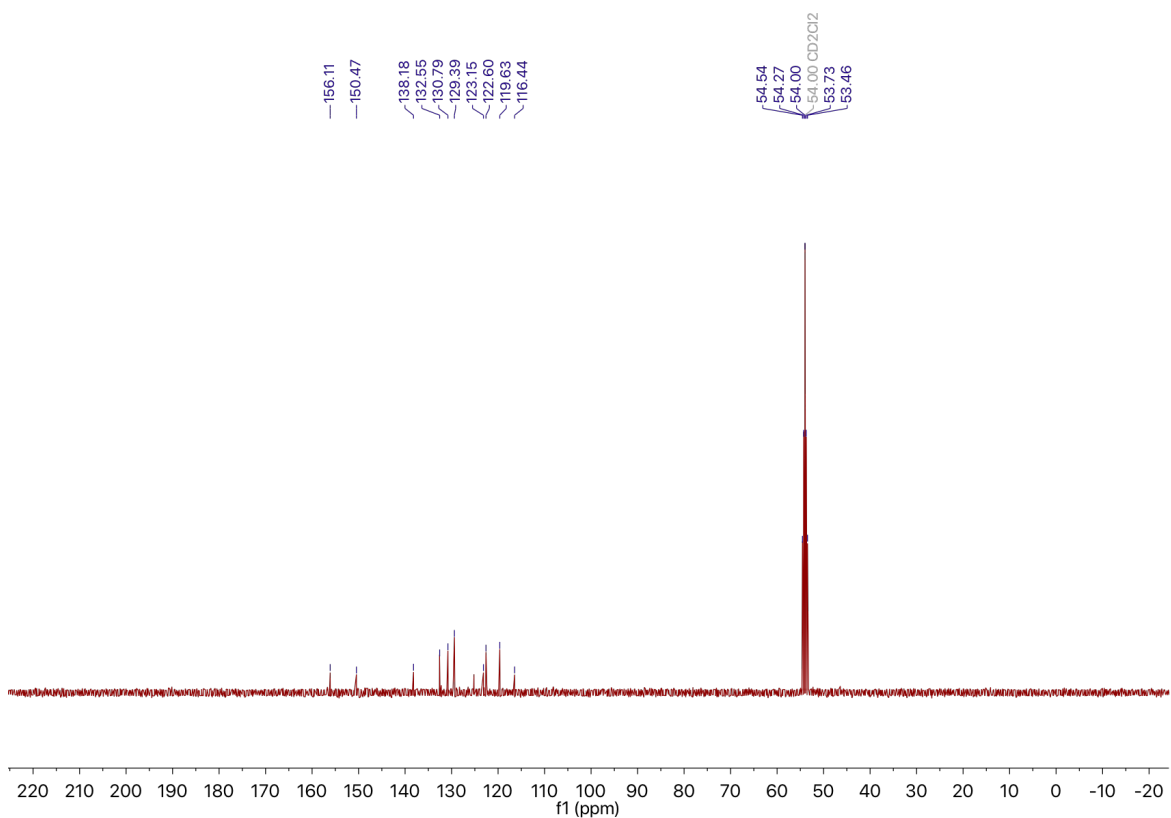


Figure A4-10 $^{13}\text{C}\{^1\text{H}\}$ NMR of **Br4-FX'** in CD_2Cl_2 at ambient temperature.

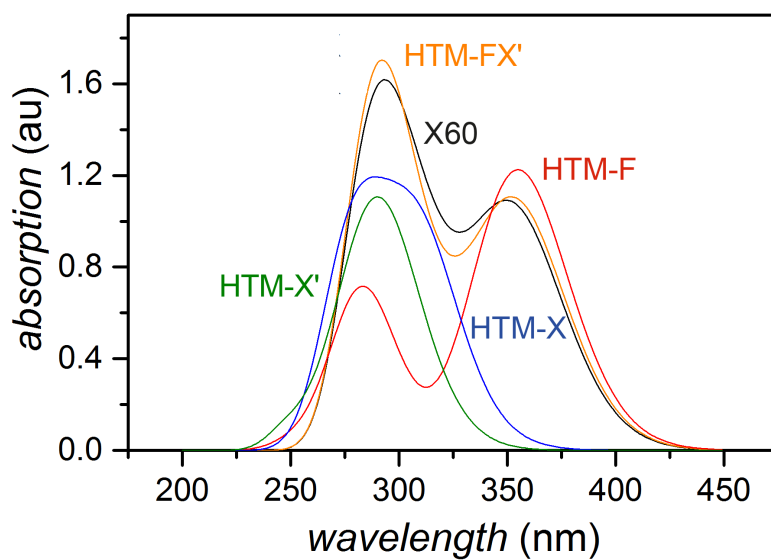


Figure A4-11 Theoretical UV-Vis spectra of the **HTM** series, calculated at the TD-CAM-B3LYP/def2-TZVP level of theory, based on the lowest 15 excited states. A linewidth of 0.3 eV is used, before plotting in units of nm.¹⁵⁵

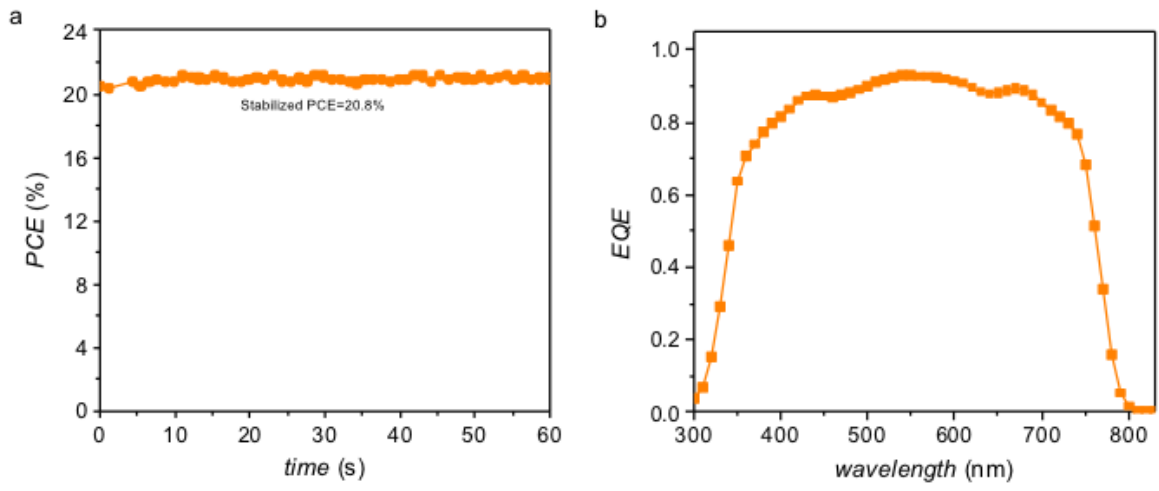


Figure A4-12 (a) MPP and of champion **HTM-FX'** device and (b) EQE curve of solar cell.

Appendix 3: Chapter 5

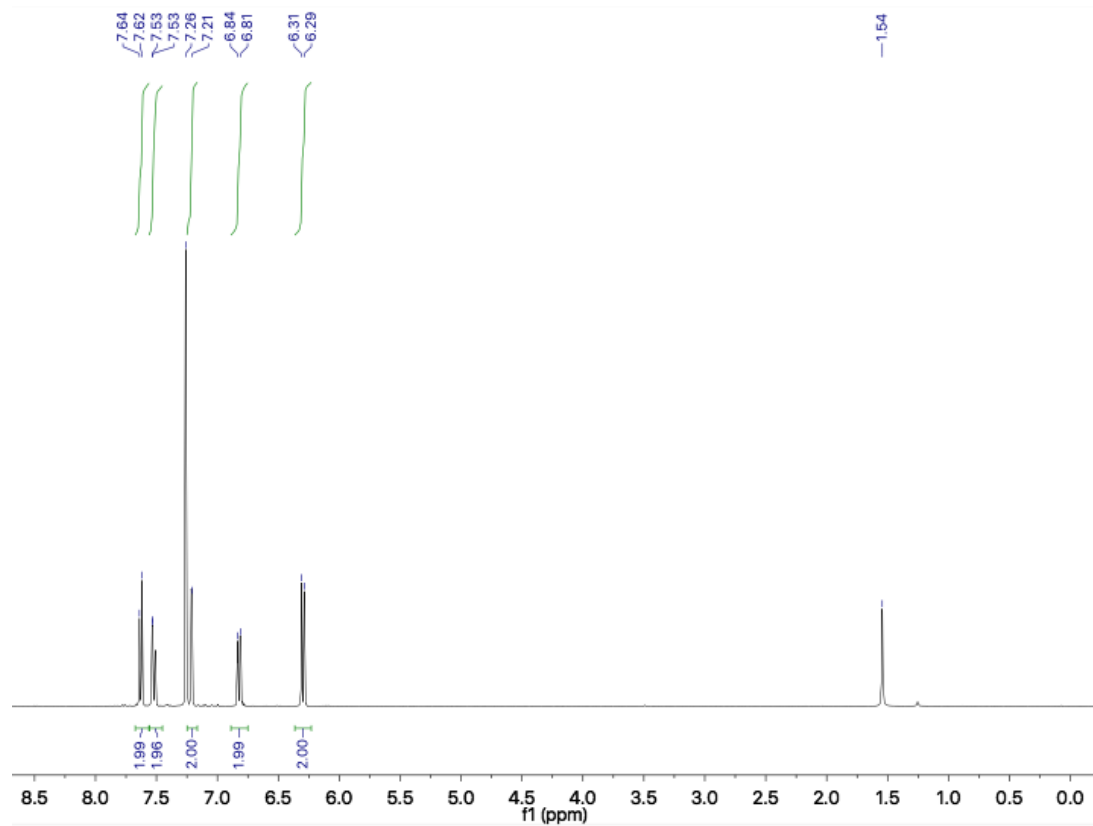


Figure A5-1 ^1H NMR of $\text{Y}_2\text{Br}_2\text{Cl}$ in CDCl_3 at ambient temperature.

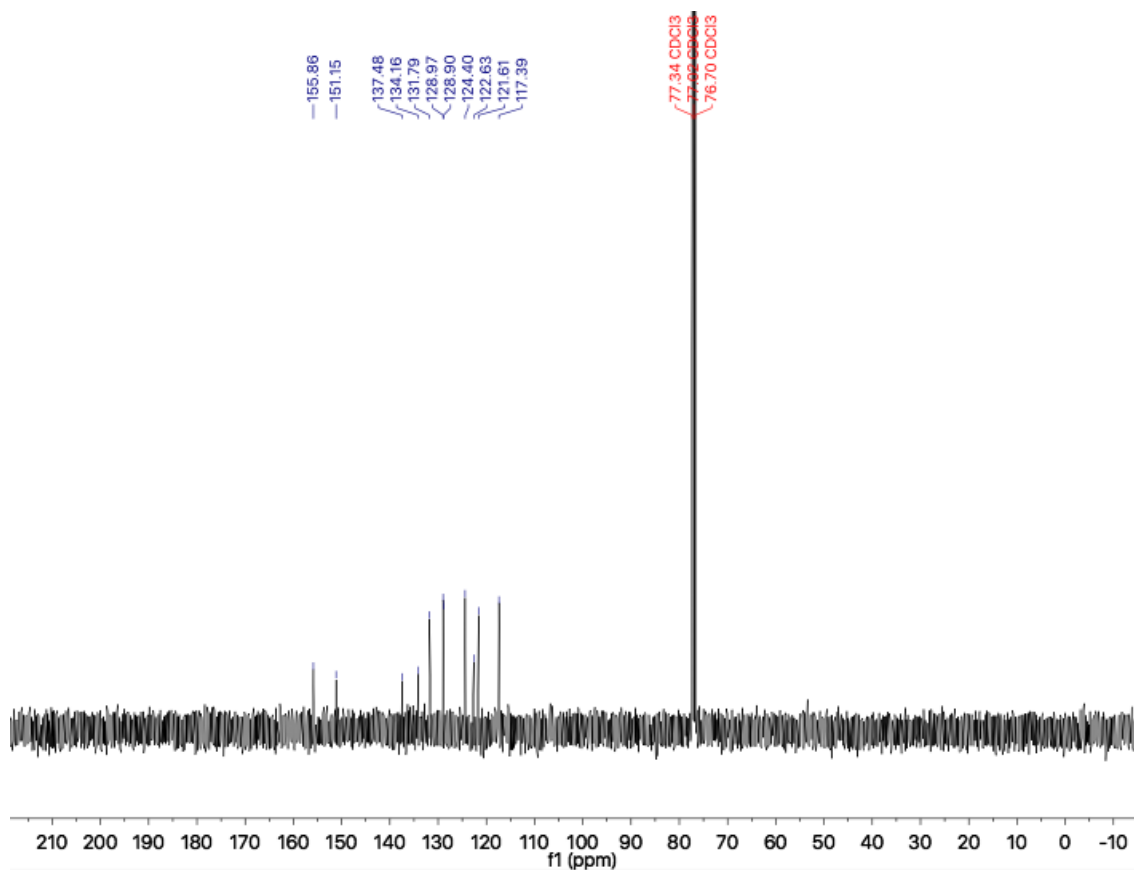


Figure A5-2 ^{13}C NMR of $\text{Y}_2\text{Br}_2\text{Cl}$ in CDCl_3 at ambient temperature.

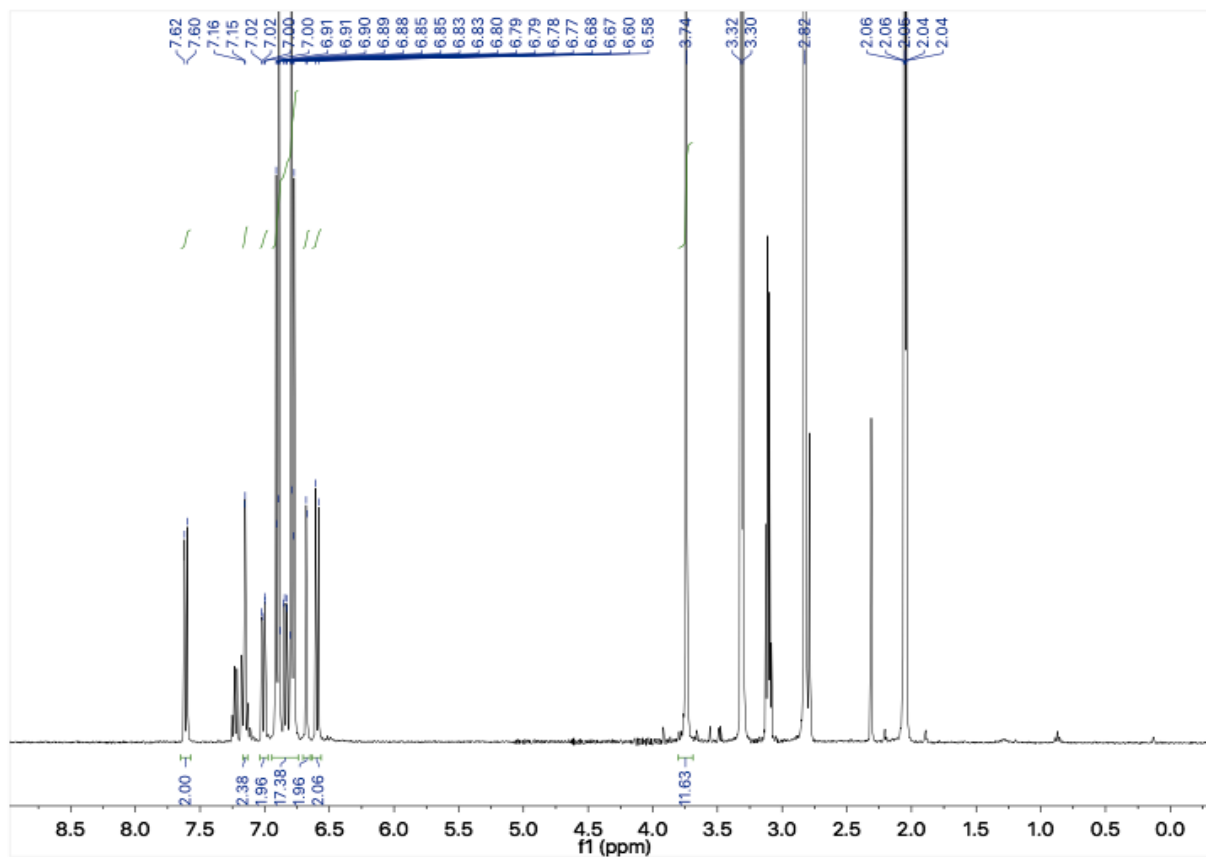


Figure A5-3 ¹H NMR of Y59-Cl in CDCl₃ at ambient temperature.

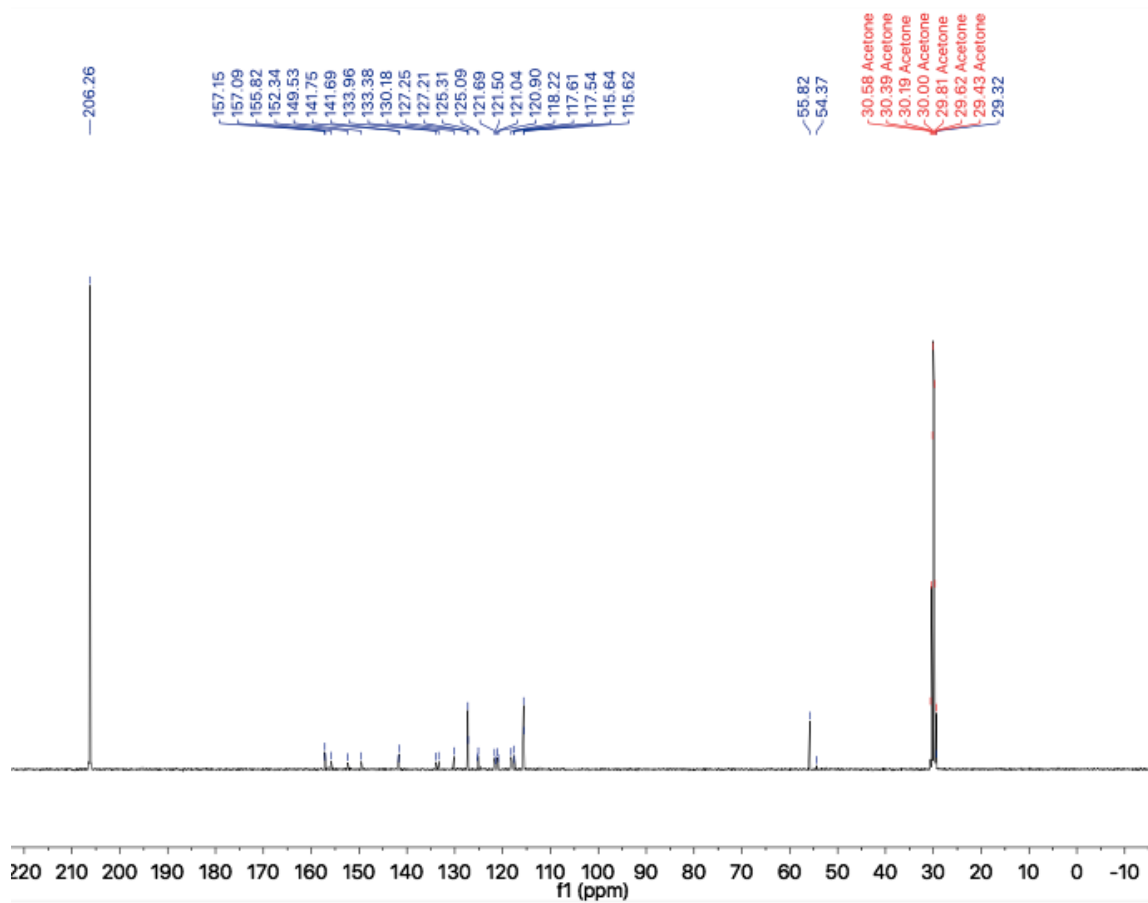


Figure A5-4 ^{13}C NMR of **Y59-Cl** in CDCl_3 at ambient temperature.

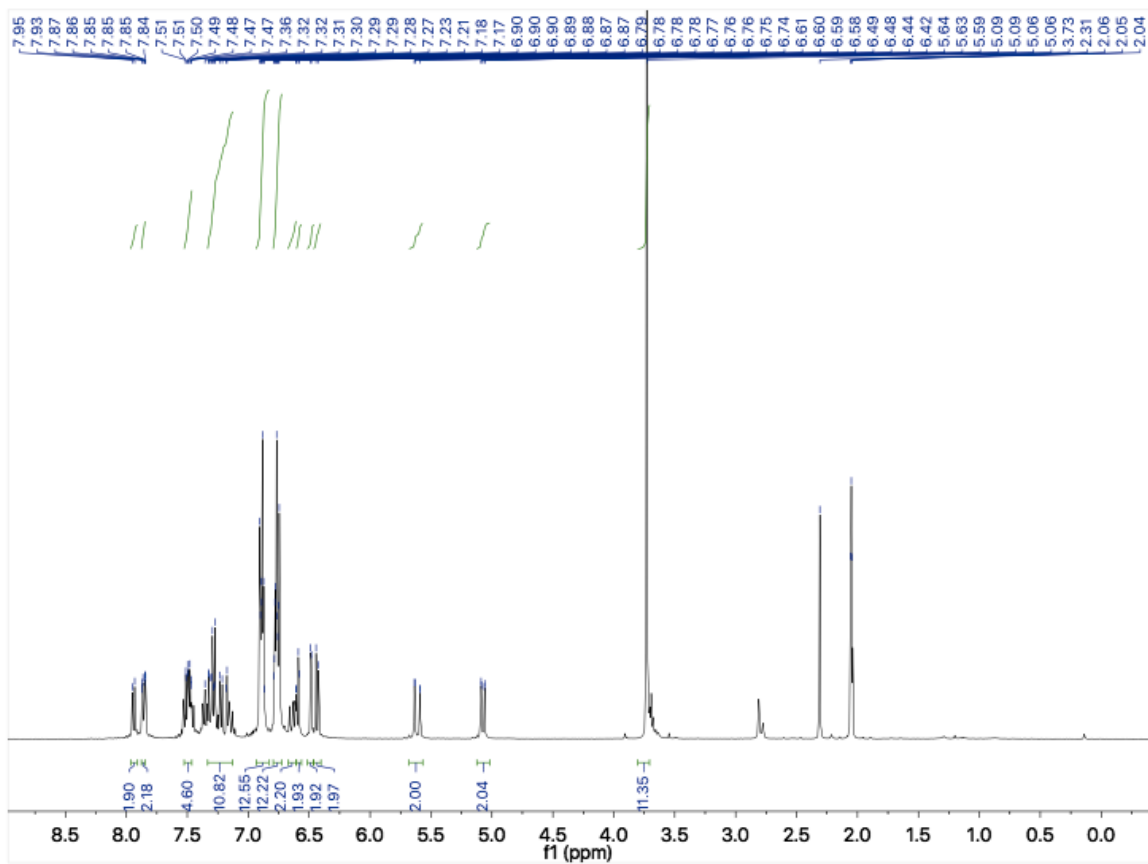


Figure A5-5 ^1H NMR of spiro-VNPB in CDCl_3 at ambient temperature.

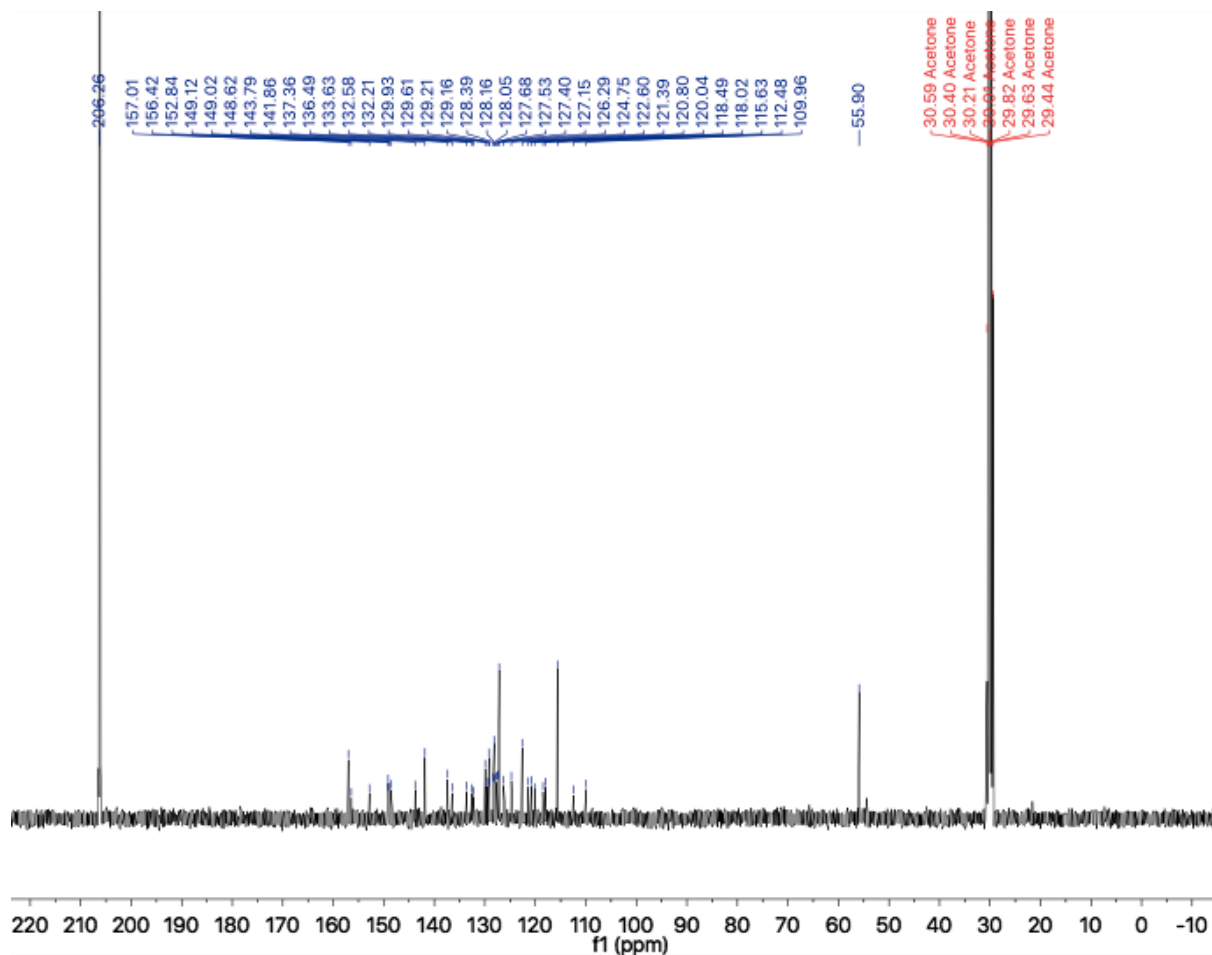


Figure A5-6 ^{13}C NMR of spiro-VNPB in CDCl_3 at ambient temperature.

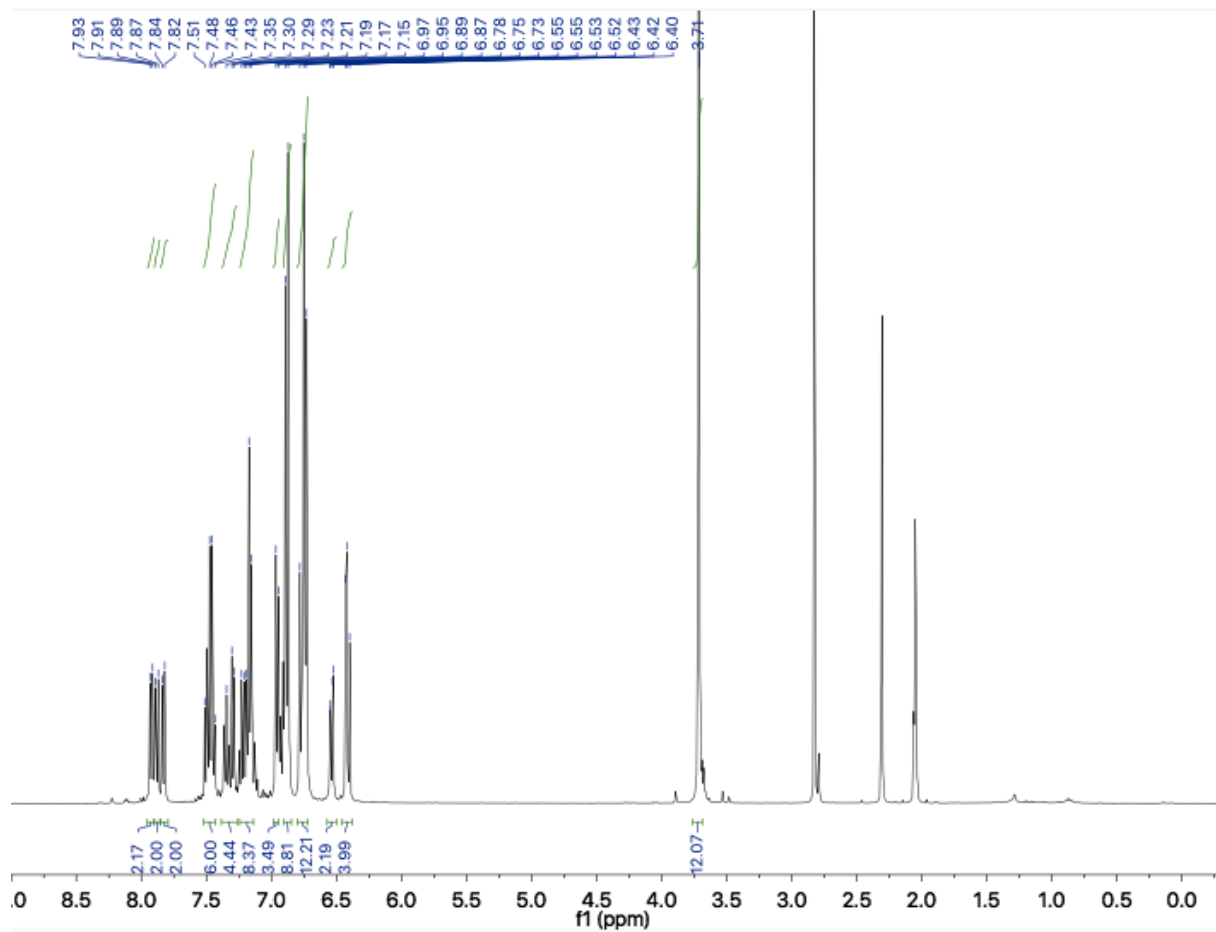


Figure A5-7 ^1H NMR of spiro-NPB in CDCl_3 at ambient temperature.

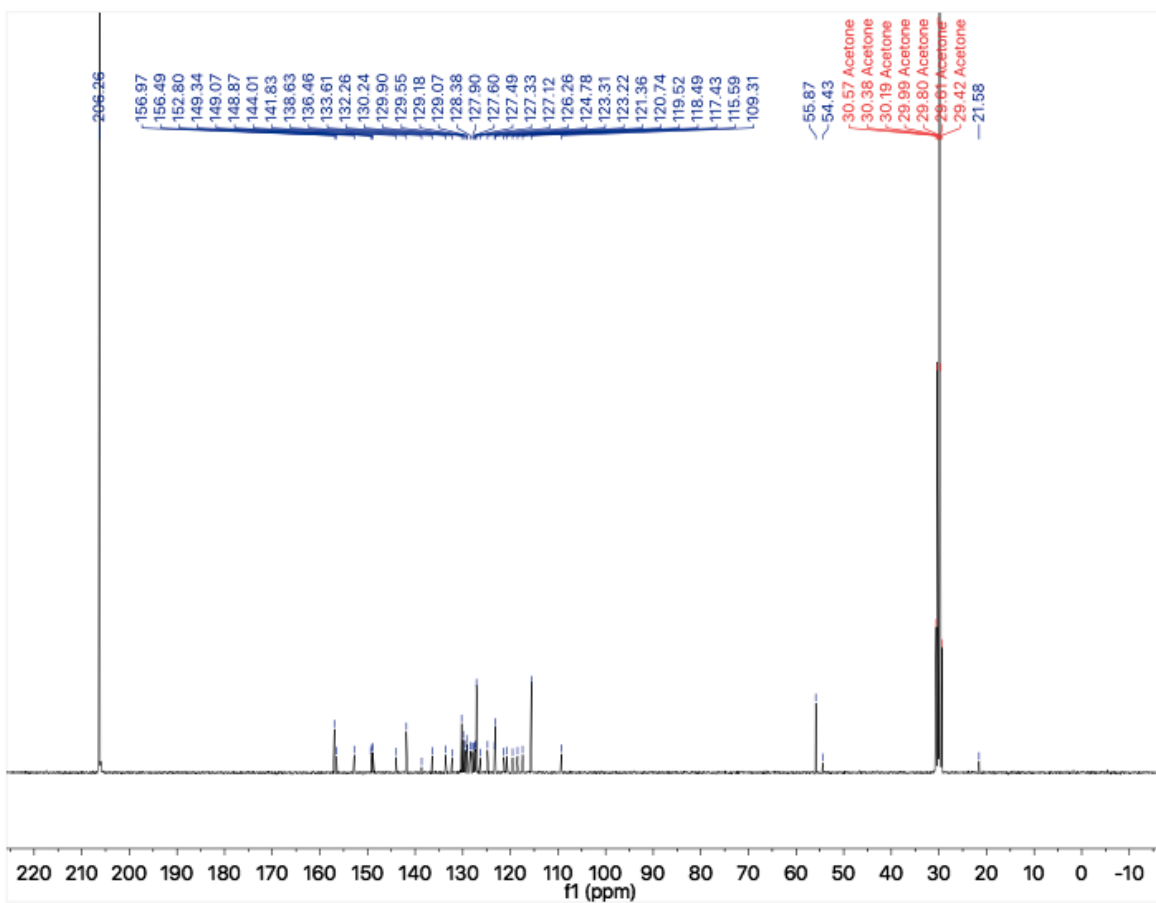


Figure A5-8 ¹³C NMR of spiro-NPB in CDCl₃ at ambient temperature.

Appendix 4: Chapter 6

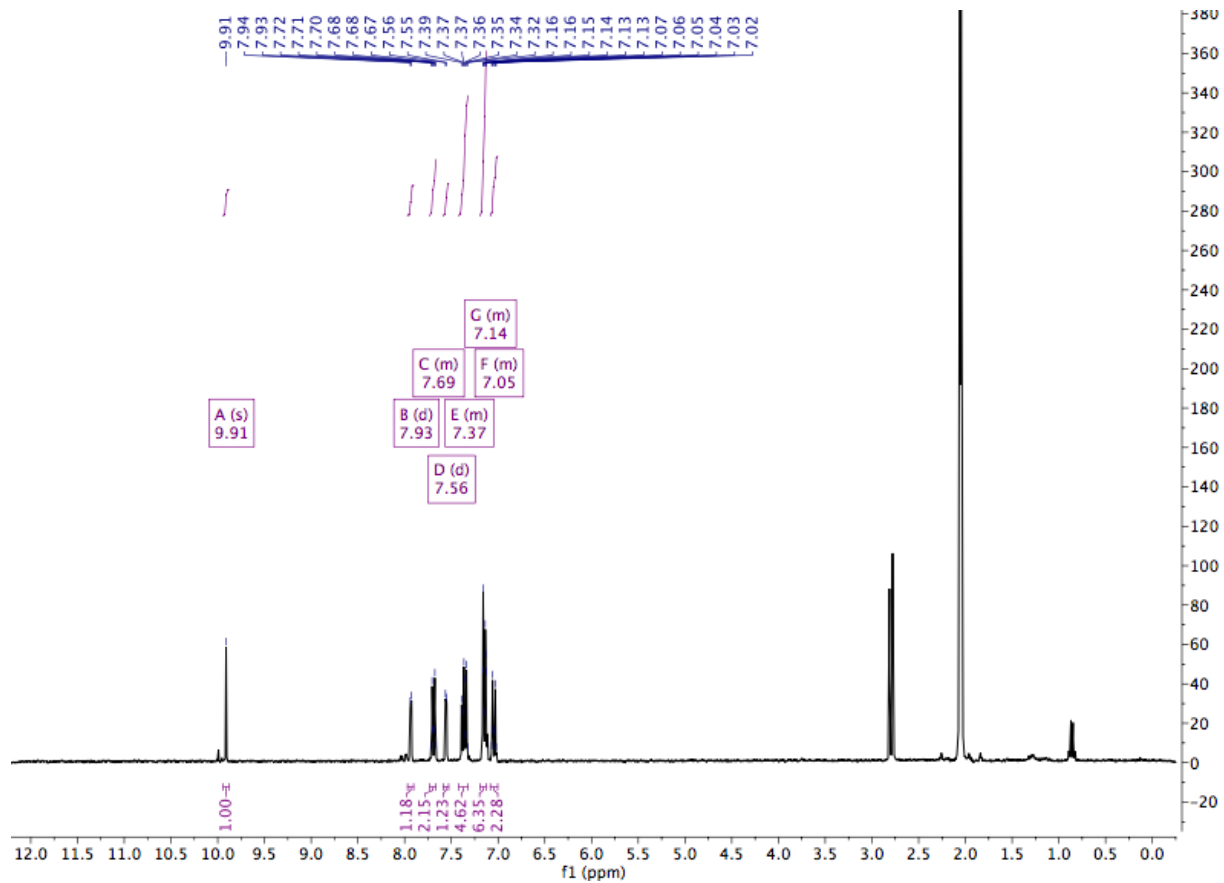


Figure A6-1 ^1H NMR of TPA-1TA in acetone- d_6 at ambient temperature.

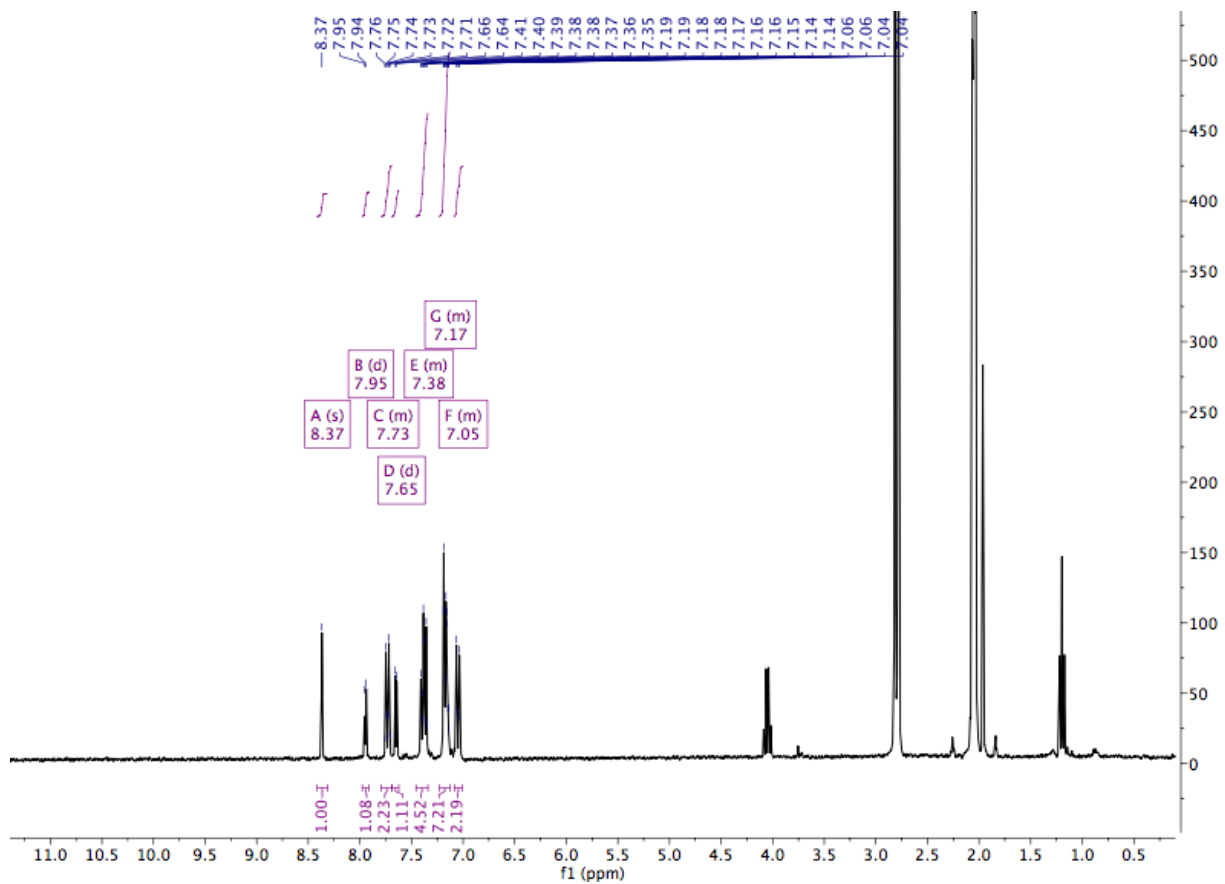


Figure A6-2 ^1H NMR of TPA-1 in acetone- d_6 at ambient temperature.

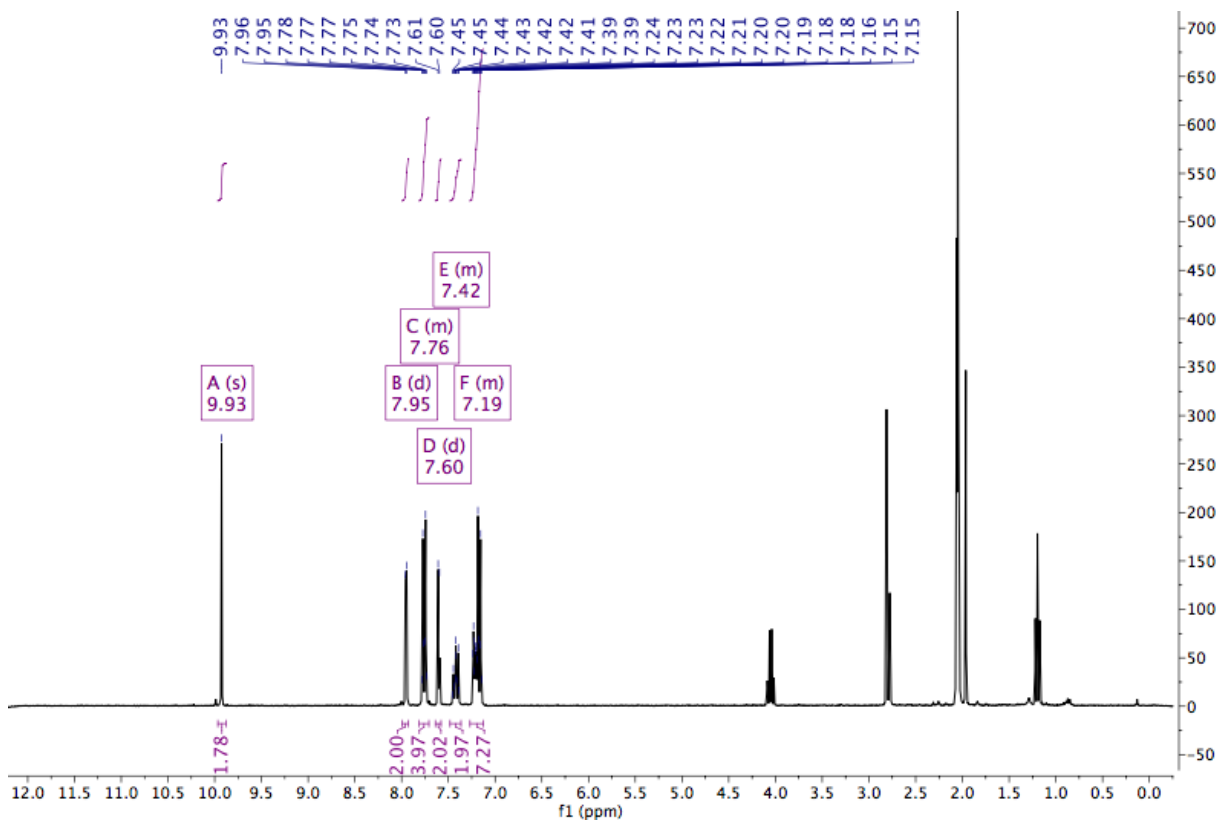


Figure A6-3 ^1H NMR of TPA-2TA in acetone- d_6 at ambient temperature.

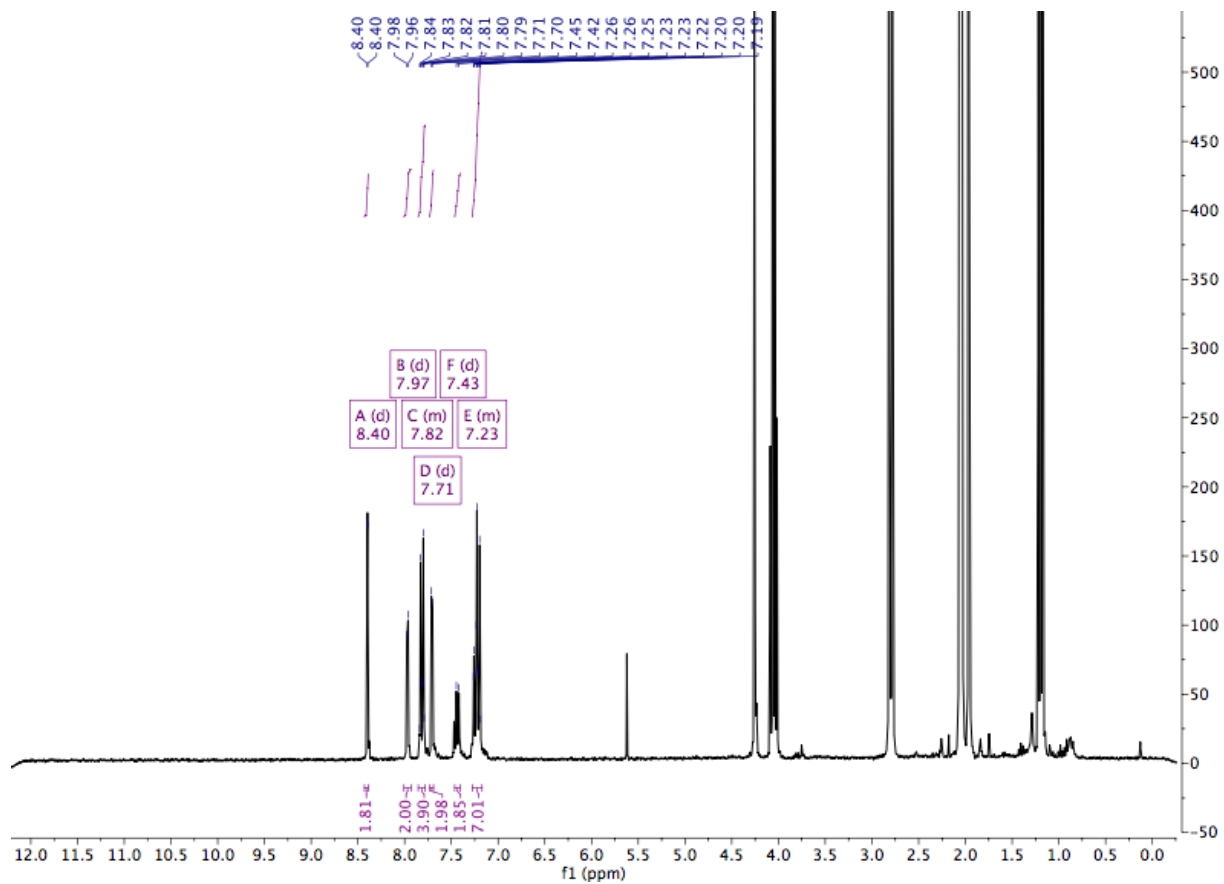


Figure A6-4 ^1H NMR of TPA-2 in acetone- d_6 at ambient temperature.

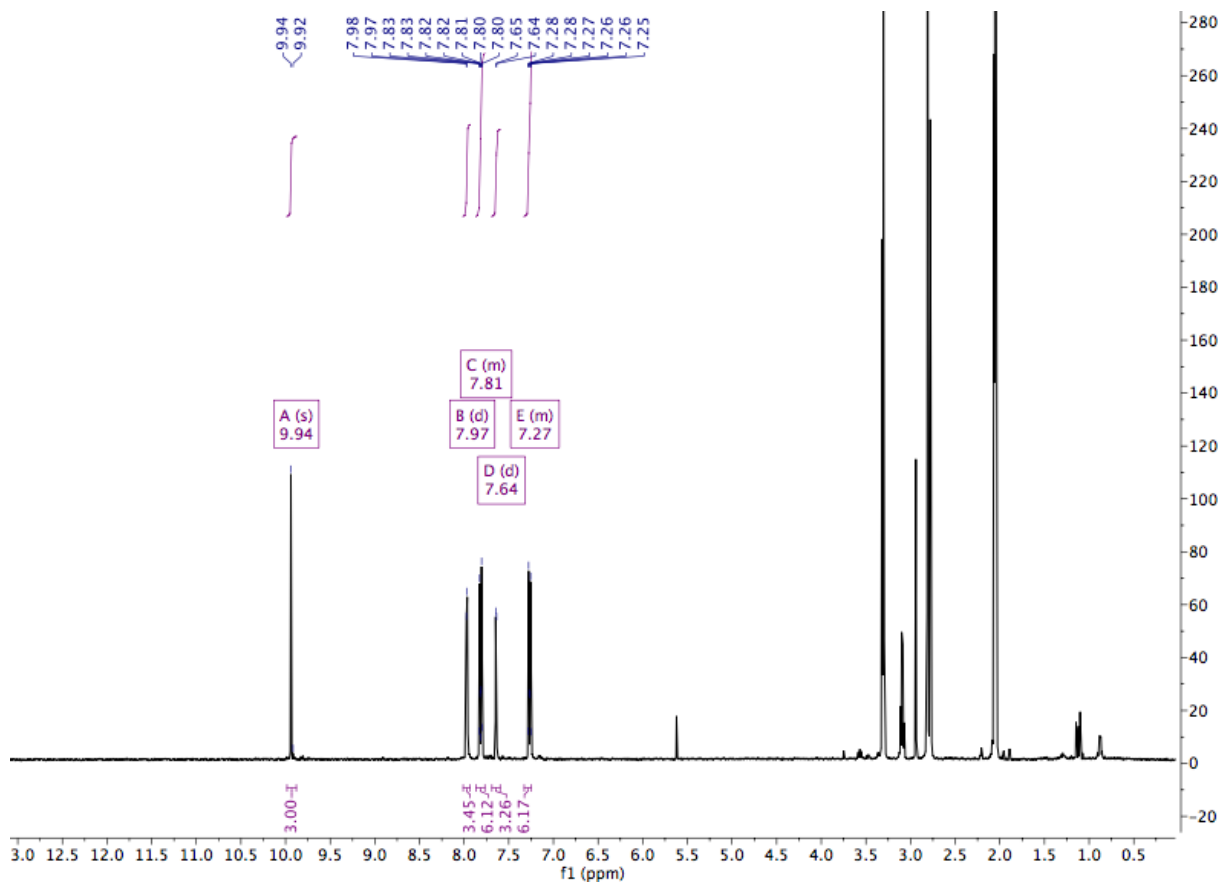


Figure A6-5 ^1H NMR of TPA-3TA in acetone- d_6 at ambient temperature.

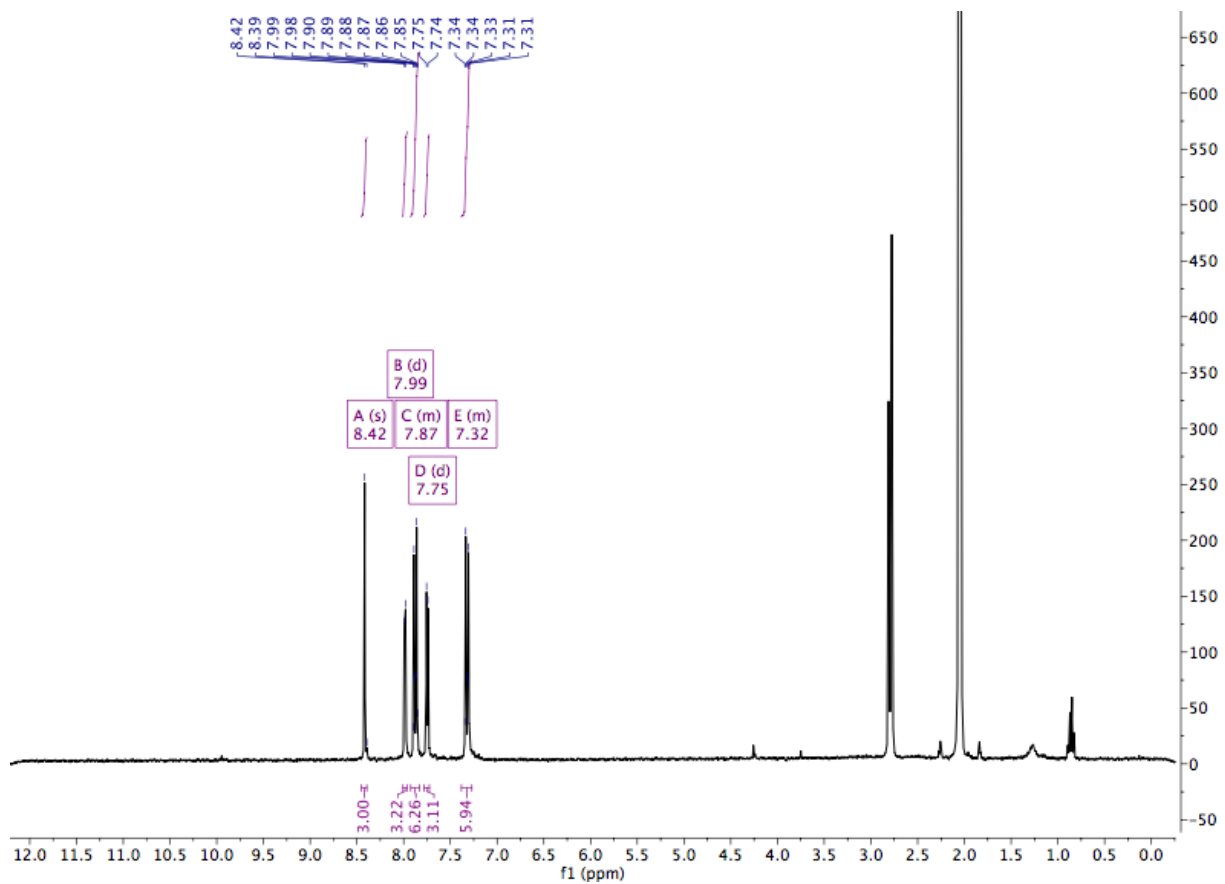


Figure A6-6 ^1H NMR of TPA-3 in acetone- d_6 at ambient temperature.